

On the Statistical Correlation between the Heave, Pitch and Roll Motion of Road Transport Vehicles

Michael Thomas Long B.Eng. (Hons)

College of Engineering and Science, Victoria University

Thesis submitted in fulfilment of the requirements for the degree of Master of Engineering

March 2016

Supervisors:

Professor Vincent Rouillard

Associate Professor Michael Sek

Abstract

A global economy is reliant on the movement of a great variety of goods on a large scale. Because the vast majority of goods are not sufficiently robust, protective packaging is needed to mitigate the adverse effects of shock and vibration that occur during distribution.

In Australia and many other countries the predominant method for the transportation of goods is via a well-developed road network. To date, the vast majority of research into vibrations experienced during road distribution focuses only on the vertical motion of the transport vehicle as it has been shown to be the most severe. However, the pitching and rolling motions of the vehicle can contribute significant energy to the overall excitation of the vehicle and payload, and excite vibratory modes which are not stimulated by vertical vibration alone.

This research focuses on investigating the heave, pitch and roll motions of light transport vehicles, and the relationships which exist between the vibratory modes. Two different approaches were used to investigate the relationships, a series of in-service field experiments and a complementary series of numerical experiments. The field experiments were designed to identify the influence of key parameters upon the relationships. The parameters investigated included; vehicle speed, road roughness, payload mass and payload inertial properties (CG location and MOI). Since the in-service experiments are, to a large extent, uncontrolled, numerical experiments were required to further investigate the vehicle parameters in greater detail. Numerical experiments allowed for controlled investigation of individual parameters which, in practice, are difficult or impossible to vary in isolation.

Data from both field and numerical simulation experiments were analysed statistically. Frequency (Fourier) domain analysis was used to produce Frequency Response Functions relating the heave, pitch and roll response. Statistical distributions and Principal Component Analysis were used to characterise the relationships in the amplitude domain.

The research presented herein found a strong relationship between the vertical acceleration and the pitch angular velocity. A weaker, yet still evident relationship was observed between the vertical acceleration and the roll angular velocity. These relationships were found to exist both in the amplitude and frequency domain. All the parameters tested had an influence on the magnitude of the heave, pitch and roll response of the vehicle. In addition, variations in vehicle speed were found to have some effect of the relationships whereas the overall road roughness was found to have no bearing on the interrelationships between heave, pitch and roll. One

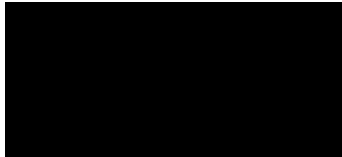
significant finding of this thesis is that the location of the vertical acceleration response measurement, relative to the centre of gravity of the vehicle has a considerable influence on the data.

Finally, the results herein provide a good guide for configuring the target PSD functions and RMS levels for laboratory testing of packaged systems using multi-axis vibration test systems.

Student Declaration

“I, Michael Thomas Long, declare that this Master by Research thesis entitled ‘On the Statistical Correlation Between Heave, Pitch and Roll Motion of Road Transport Vehicles’ is no more than 60,000 words in length including quotes and exclusive of tables, figures, appendices, bibliography, references and footnotes. This thesis contains no material that has been submitted previously, in whole or in part, for the award of any other academic degree or diploma. Except where otherwise indicated, this thesis is my own work.”

Signature:



Date: 31/3/2016

Acknowledgments

I would like to thank my beautiful partner Lily for her love and support over the course of my research.

I would like to thank my principal supervisor Professor Vincent Rouillard for his guidance and encouragement. I would also like to express my warm thanks to my associate supervisor, Associate Professor Michael Sek for his assistance.

I would like to extend my deepest gratitude towards Dr Daniel Ainalis, Dr Matthew Lamb and Mr Julien Lépine. This thesis would have been completed in half the time if it was not for them, although it would not have been half as good.

I would like to thank my parents Anne and Tony as I wouldn't be here without them. I would also like to express thanks to my sister Joanna for being there for me.

Finally, I would like to thank my fingers as I could always count on them. My Legs for always supporting me and to my arms for always being at my side.

Publications

1. **Long M.**, Rouillard, V. & Sek, M. 2013, *Preliminary Investigation of Statistical Relationship between Heave, Pitch and Roll Vibration in Road Vehicles*. Proceedings of the 27th IAPRI Symposium on Packaging, Espoo, Finland.
2. Rouillard, V., **Long, M.** & Sek, M. 2013, *Some Observations on the Heave, Pitch and Roll Motion of Road Transport Vehicles*. Proceedings of the International Transport Packaging Forum ISTA. Orlando, Fl.
3. **Long, M.**, Rouillard, V. & Lamb, M. 2014, *Evaluating the use of Statistical Estimates of Vehicle Geometric and Inertial Properties for Use in Numerical Simulations*. 8th Australian Congress on Applied Mechanics, Melbourne, Australia.
4. **Long M.**, Rouillard, V., Lamb, M. & Sek, M. 2016, *Characterising the heave, pitch and roll motions of road vehicles with principal component and frequency analysis*. Proceedings of the 20th IAPRI World Packaging Conference, Sao Paulo, Brazil.

Table of Contents

Chapter 1 Introduction.....	1
Chapter 2 Background.....	4
2.1 The Role of Protective Packaging in Society.....	4
2.1.1 Protecting the Environment from Protective Packaging	5
2.2 Protective Packaging Optimisation.....	6
Chapter 3 Review of Packaging Testing in Relation to Vehicle Vibrations	10
3.1 Current Packaging Testing Methods.....	11
3.2 Multi-Axial Vehicle Vibrations	14
3.2.1 The Nature of Road Topography	14
3.2.2 Road-Vehicle Interaction	18
3.2.2.1 Non-Vertical Vehicle Vibration.....	18
3.3 Effects of Multi-Axis Vibration on Vehicle Payloads	20
3.4 Literature Review Summary	24
Chapter 4 Hypothesis	25
4.1 Sub-hypothesis	25
Chapter 5 Methodology.....	26
5.1 Approach 1 – Physical Experiments	26
5.2 Approach 2 – Numerical Simulations.....	28
Chapter 6 Physical Experiments: In-Service Measurement	29

6.1 Experimental Setup	29
6.1.1 Instrumentation	34
6.2 Data Analysis Approach	35
6.2.1 Statistical Distribution Analysis.....	36
6.2.2 Fourier Analysis	45
6.3 Experimental Response Survey Results	48
6.3.1 On the Effects of Vehicle Speed	48
6.3.2 On the Effects of the Road	62
6.3.3 On the Effects of Carrying a Payload.....	72
6.3.4 On the Effects of Payload Inertial Properties	82
6.4 Physical Experiments - Concluding Statements.....	93
 Chapter 7 Numerical Model: Development and Parameter Estimation	 95
7.1 Synthetic Road Profile Generation – for Pitch and Roll Motion	96
7.1.1 Current Synthesis Methods	96
7.1.2 Improved Two-Track Road Synthesis.....	98
7.2 Vehicle Model Development	101
7.2.1 Equations of motion	104
7.3 Estimating Vehicle Parameters	108
7.3.1 Mass	108
7.3.2 Stiffness and Damping	112
7.3.3 Centre of Gravity and Moments of Inertia	117

7.3.3.1 Regression analysis of NHTSA Data	118
7.3.4 Concluding Comments for Estimating Vehicle Properties	123
7.4 Chapter Conclusion.....	124
Chapter 8 Numerical Simulation - Results and Discussion.....	126
8.1 On the Effects of Vehicle Speed	127
8.2 On the Effects of Road Roughness	138
8.3 On the Effects of Sprung Mass	148
8.4 On the Effects of Moments of Inertia.....	161
8.5 On the Effects of Wheelbase Length.....	173
8.6 Numerical Simulations Summary	185
Chapter 9 Conclusions and Future Work	188
9.1 Future Work	190
Chapter 10 References.....	191
Appendix A Validation of the Full Car Numerical Model.....	197
A.1 2DoF frequency response function fitting.....	198
A.2 4DoF frequency response function fitting.....	202
A.3 Eigenvalues	208
A.3.1 Case 1: Symmetrical system.....	210
A.3.2 Case 2: Asymmetrical unsprung masses	213
A.3.3 Case 3: Front anti-roll bar	216
A.3.4 Case 4: Asymmetrical unsprung masses with front anti-roll bar.....	219

A.3.5 Case 5: Front and rear anti-roll bars	222
A.3.6 Case 6: Asymmetrical centre of gravity location	224
A.3.7 Eigenvalue analysis conclusion.....	228
Appendix B Complexities with Idealised Multi-Axis Vehicle Vibration	229

Chapter 1

Introduction

This thesis is the first major investigation into the heave, pitch and roll vibratory motion of road vehicles and relationships which may exist between them. Research in this field is lacking, and common sense dictates that some relationships must exist, simply due to the mechanics of the road-vehicle interaction. However, the randomness of the road topography results in a random vibrational response of the vehicle meaning that investigation and description of potential relationships requires a certain level of sophistication. This thesis outlines the approaches taken to investigate potential relationships between the vibratory modes as well as the reasoning behind the study.

Chapter 2 presents a thorough background to this research, the motivation of which is protective packaging optimisation. The role protective packaging plays in a globalised world is explained in detail as well as the ever increasing need for optimised protective packaging solutions for economic and environmental reasons.

Chapter 3 addresses a wide range of issues associated with determining a payload's robustness when subjected to real world vehicle vibrations. A summary of current packaging test methods is given, discussing the advantages and limitations of both field distribution trials and laboratory testing. The second section of the chapter summarises the causes and manifestations of multi-

axial vehicle vibrations. The random irregularities of the road surface are shown to be the main source of excitation for road vehicle vibration. A review of the spectral and statistical make-up of the road surface is given. This section also summarises the research into the non-vertical motions of road transport vehicles, and demonstrates the limited work which has been undertaken in this area. It was shown that the severity of non-vertical motions, for some frequency bands, contain more energy than vertical vibrations, which is the primary focus of most testing methods. Chapter 3 culminates with the impacts that non-vertical excitation has on vehicle payloads. It was shown that the simultaneous excitation of all modes alters the magnitude and location of stresses experienced in payloads, and also that vertical only excitation is unable to excite the mode shapes excited during transport.

Chapter 4 presents the main hypothesis of the research and a number of supporting sub-hypothesis.

Chapter 5 explains the basics behind the approaches used to investigate the research hypotheses. The first section describes using physical experiments as a means to investigate potential links between the heave, pitch and roll vibratory response of vehicles. The second section of the chapter outlines the requirement for a numerical model for a more in-depth investigation. An outline is given for the desired capabilities of the model, it is stated here that it is not the aim of the numerical model to replicate the physical experiments but as a comparative study, with the ability to go further in-depth into the sensitivity analysis of the vehicle parameters.

Chapter 6 outlines the experimental series that was undertaken to explore and investigate relationships between the heave, pitch and roll motions. Section one describes the setup of the experimental series. A significant test schedule is described, with aims to probe the effects of experimental conditions (speed, payload, etc.) on the vehicles vibratory response. The second section of the chapter focused on determining and evaluating metrics that can easily describe relationships between the vibration modes. Traditional methods of analysing vehicle vibrations are assessed including Fourier analysis and statistical distributions. Novel analysis techniques are also investigated.

The third section of chapter 6 compiles the results from the significant vehicle response survey undertaken. The section is divided into four sub-sections with each participant focusing on a separate experimental parameter. The first explores the effects of vehicle speed whilst the second is dedicated to road roughness. The final two sub-sections are dedicated to the effects of carrying a payload, firstly looking into the effects of the added mass (and the accompanying changes to other vehicle parameters) and secondly the impacts of the changing the mass

distribution properties (the centre of gravity height and moments of inertia). Issues are identified with the physical experiment process namely; the uncontrolled nature of the physical experiments, low number of setups possible (due to the time consumptions of each configuration) and the inability to isolate the effects of parameters individually. These issues support the need for a laboratory based investigation.

Chapter 7 deals with the development of a numerical model for analysing multi-dimensional vehicle response. Taking a bottom-up approach, the first section presents a new approach for synthesising dual wheel path road profiles that have a target PSD function as well as a user specified coherence function between the two tracks. The second section of the chapter covers the development of the model itself. The seven degrees of freedom numerical model was based upon modified versions of published equations of motion which were implemented in the Simulink toolbox of Matlab®.

Accurate vehicle parameter estimates are required for realistic simulation results, and is the focus of the third section of chapter 7. A vehicle was partially disassembled to accurately estimate its mass properties. Estimates of the suspension and tyre stiffness were made from load deflection tests, whilst the suspension damping was estimated using the random decrement technique. An improved approach for estimating a vehicle's centre of gravity height and moments of inertia from statistical data is also described. The technique proved to be more accurate than the existing method it is based upon.

Chapter 8 focuses on the results of the sensitivity analysis carried out using the multi-degree of freedom numerical model. The first section of the chapter investigates the impact of vehicle speed. The second explores the impact of road roughness, where only the overall road roughness is varied. The coherence between the left and right wheel paths, and therefore roll excitation, was not investigated. The remaining three sections of the chapter looked into the influence of individual vehicle parameters. The sprung mass (vehicle body plus payload) was varied in isolation, which is not possible using physical experiments. The sprung mass's moments of inertia were also varied in isolation, in greater ranges and fidelity than was possible in the physical experiments. Finally, the impacts of the vehicles wheelbase on its vibratory response are investigated.

Chapter 9 draws the main conclusions from observations on the relationships between heave, pitch and roll of road transport vehicles. Numerous aspects of the work were identified that warrant further development and investigation.

Chapter 2

Background

Protective packaging is the unsung hero of the modern economy, and is the motivation for this research. The role protective packaging plays in a globalised world is explained in detail in this chapter, along with the increasing need for optimised protective packaging in road transport.

2.1 The Role of Protective Packaging in Society

A global economy is reliant on the movement of goods (such as food, electronics and pharmaceuticals) on a large scale. Preservation of these goods throughout the distribution network is handled by a combination of the product's robustness and protective packaging. Effective protective packaging enables products to be shipped over great distances around the world, allowing for the centralisation of processing and manufacturing facilities close to materials and labour, which results in a significant reduction to production costs. Economies can prosper due to the reduced cost and increased robustness of products and allows for greater rates of international export.

It has been estimated that by 2020 the worldwide protective packaging industry will be worth USD\$29.30 billion (Oristep Consulting 2015). This figure, while impressive, pales in

comparison to the amount spent on packaging related materials and machinery, totalling approximately US\$485 billion globally in 2004 (WPO 2008). One reason for such significant expenditure is the benefits to manufacturers, who must ensure that their products reach the consumer intact. During the distribution phase, there are a vast number of hazards products will encounter. While these hazards are complex and difficult to predict, the products, nonetheless, need to be protected against such hazards in order to ensure that they arrive without damage.

The primary goal of protective packaging is to mitigate the effects of shocks and vibrations encountered between the producer and consumer. This is achieved predominantly through cushioning the product with vibration absorbing material, such as foam, loose fill material and air cushions. Engineering a cushioning system requires knowledge of the products' fragility; how tough the product is. Its susceptibility to both shocks (short duration - high amplitude) and vibrations (long duration - low amplitude) must be thoroughly understood. The expected severity of the hazards encountered during distribution must also be known. Assumptions on the severity of the shocks and vibrations ensures that protective packaging designs will not be optimised.

A conservative approach to packaging design, in many cases, leads to over-packaging (Sek 2001). Over-packaging is when the robustness of the product and packaging is greater than the expected hazard level. Excessive protection manifests itself through the inclusion of more cushioning material than needed. Over-packaging is difficult to identify as the product reaches its destination intact, however it can be costly. The cost of over-packaging is far greater than the price of the excess cushioning material itself. Excess cushioning material results in an increased package volume, reducing the palletised quantity. This in turn increases the number of pallets required to transport the same number of units, resulting in more trucks on the road. Increased truck numbers results in increases in traffic, accelerated road deterioration and pollution (Cebon 1989; Janic 2007). Protective packaging is often a single use item and disposed of by the end user, therefore over-packaging can lead to increased landfill or litter. It has been estimated that the hidden costs associated with over-packaging is 20 times greater than the cost of the excess material itself (Ostergaard 1991). The compounding environmental costs have seen protective packaging come under scrutiny from various governments in recent years.

2.1.1 Protecting the Environment from Protective Packaging

The environmental costs of packaging has compelled governments to impose restrictions on the use of packaging materials (Yam 2010) and recycling targets. Australia fell short of the 2015

target of a 70 % recycling rate for used packaging managing only 61.3 % (APC 2015), the recycling rate dropped from the already stagnant rate of around 64 % from 2012-2014 (APC 2014). This is, however, not representative of the efforts made by both governments and industry. Recycling rates have increased considerably, in 2003 the recycling rate in Australia was approximately 39 % (APC 2014). To address the current recycling rate plateau the Council of Australian Governments (COAG) Standing Council on Environment and Water commissioned a decision regulation impact statement from the National Environment Protection Council (NEPC). The 2014 report (NEPC 2014) evaluated ten different strategies to improve management of packaging waste and litter. One strategy outlined in the report would see a mandatory Advance Disposal Fee (ADF) on all packaging materials. The ADF would be a weight-based fee per tonne of packaging materials, with the rate of the fee dependent on the type of material. Revenue from the ADF would be earmarked for funding various packaging recycling and litter reduction initiatives. If implemented, the onus would be on the packaging manufacturers and brand owners to optimise the amount of packaging in order to reduce the applicable taxation. It is clearly evident that significant economic and social savings can be made by reducing the prolificacy of excessive packaging.

2.2 Protective Packaging Optimisation

While protective packaging is essential, several problems associated with excessive packaging have been identified. To reduce the economic and social losses, extra packaging material can be reduced by means of optimising the protective packaging. A holistic approach must be taken when optimising protective packaging systems; that is to say that both the product and the packaging must be optimised together to withstand with the expected hazards of the distribution environment.

The broadly adopted approach to engineering an optimised product/package combination is the Six-Step Method (Root 1997):

- I. Evaluate and quantify distribution hazards
- II. Determine product robustness
- III. Increase product robustness
- IV. Characterise protective packaging material
- V. Design protective packaging
- VI. Test and validate product/package against synthesised distribution hazards

Figure 2-1 illustrates the possible outcomes of total product/packaging robustness. Importantly, the Six-Step Method promotes that idea that the optimal level of robustness is a function of both the product and packaging.

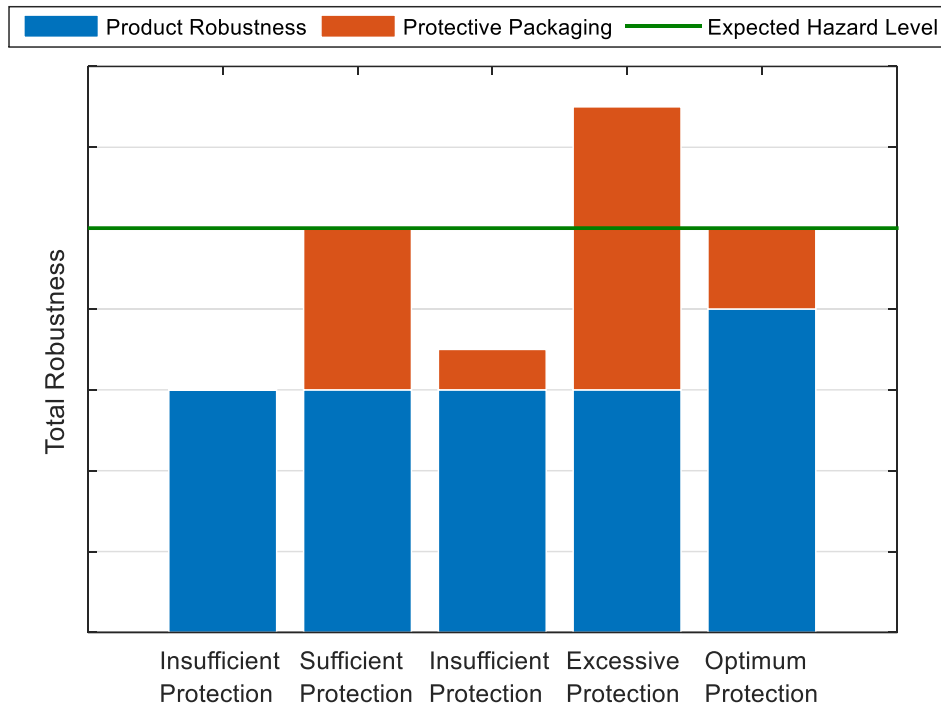


Figure 2-1: Possible product robustness situations for a given hazard level (Root 1997).

Optimising a product/packaging combination is generally guided by the economical trade-offs between the product and packaging design, illustrated in Figure 2-2. While only two cost functions are shown as an example, the actual costs of the packaging and product damage results in the use of many cost functions. Costs such as tax expenditure may also need to be taken into account (e.g. ADF). The cost of increasing the product's robustness must be considered; this can include the cost of R&D and extra material, but may be offset by greater brand reputation (e.g. "Built Ford Tough" (Kohli *et al.* (2013)). Either way a thorough knowledge of the expected hazard level is key to the optimisation process.

Product distribution is largely dominated by three transport modes: road, rail, and sea. Of these modes of transport, road is by far the most prolific (67 %) within Australia (BITRE 2010). It is currently projected that 243 billion tkm of freight will travel on Australian roads in 2016, this is predicted to increase by 50 % (Figure 2-3) to 342 billion tkm by 2030 (BITRE 2010). The abundant use of road transport means that road-borne vibrations are of great importance to optimising the product/packaging system.

The socioeconomic costs associated with protective packaging use and disposal have been shown to be considerable. A strong case is presented for investing resources into further research and development of improved techniques for protective packaging optimisation. In order to achieve a significant level of protective packaging optimisation, a comprehensive knowledge of the nature of vehicle vibrations is required.

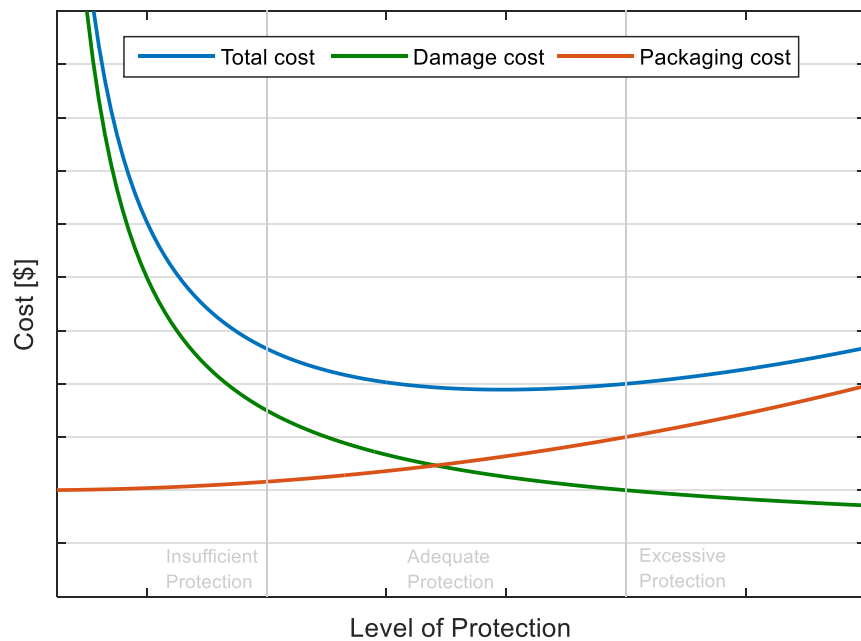


Figure 2-2: Economic cost function for package / product optimisation. (Reproduced from Rouillard 2006)

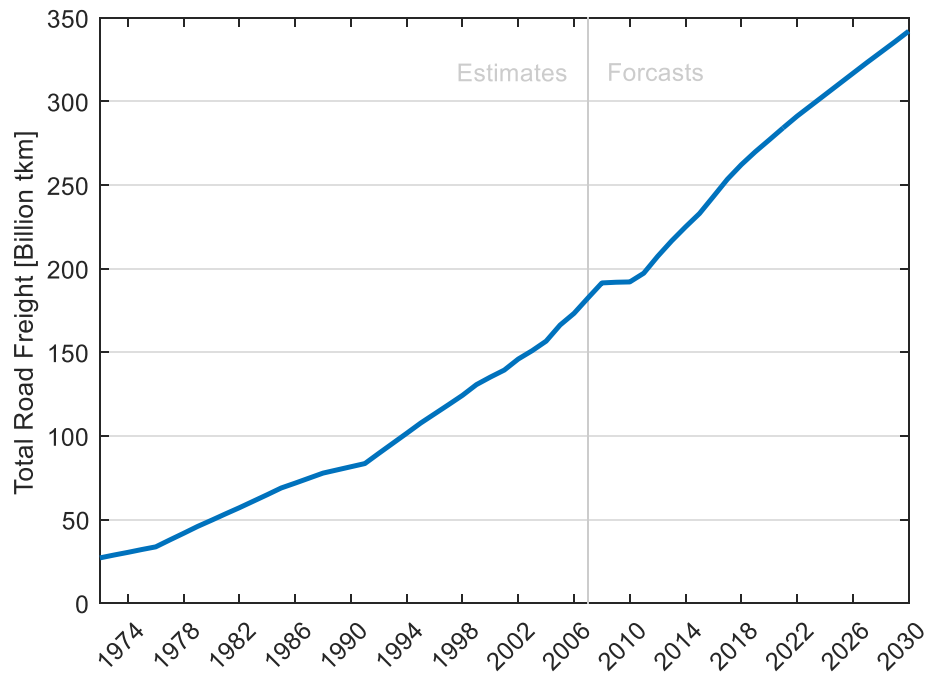


Figure 2-3: Growth in road freight transport in Australia. Source: Bureau of Infrastructure, Transport and Regional Economics 2010.

Chapter 3

Review of Packaging Testing in Relation to Vehicle Vibrations

This Chapter presents a thorough review of vehicle vibrations and their effects on payloads. The first section provides a brief overview of current packaging testing methods, focusing on trial shipments and laboratory simulation. Several limitations are identified for both methodologies, namely the difficulties surrounding packaging optimisation.

The second section of this chapter focuses on the vehicle vibrations experienced during distribution. The section begins with an overview of the statistical and spectral nature of road topography, the principal source of road vehicle vibrations. The section then moves onto vehicle-road interactions, focusing on research into the manifestations of vehicle vibrations other than heave (vertical).

The final section of this chapter presents a summary of research undertaken on the effects of multi-axis vibration on payloads. A full spectrum of payloads is included, ranging from simple structures and electronics to fully palletised loads.

3.1 Current Packaging Testing Methods

Manufacturers wishing to validate or improve their current protective packaging designs, in relation to vehicle vibrations, have two primary options; trial shipments (distribution trials) or laboratory simulation of the transport environment. When selecting the appropriate method for optimisation, a compromise must be made between time, cost and the knowledge gained from the testing procedure.

In most situations, trial shipments are the most cost efficient approach and provide a good representation of the distribution environment; however, there are several limitations. The distribution environment is random in nature and trial shipments are effectively 'playing the percentages' when it comes to obtaining vibration data for a representative trip. Statistically speaking a trial shipment should be close to an average trip; although it may be excessively smooth or rough; both of which are detrimental to the packaging optimisation process. To minimise the effects of the randomness, a series of trial shipments may be undertaken, but this also significantly increases the cost of the approach.

Trial shipments are generally examined prior to departure and on arrival for product damage, however if damage is observed it is difficult to determine when it occurred, making time to failure estimates difficult to establish. Failure may have occurred at the beginning of the test or close to the completion of the test. Video surveillance can be implemented to circumvent this issue, but this increases the cost of performing the trial shipments increases.

Furthermore, the mechanics by which the damage has occurred cannot be established with simple trial shipments. It can be difficult to determine if failure occurred due to a high magnitude shock, continuous vibration of road transport or other factors (such as rapid deceleration or cornering). While both the vehicle's and payload's dynamic motion can be recorded using specialised equipment, the collection, analysis and interpretation of the data requires an in depth knowledge of signal analysis and vibrations, as well as the dynamic characteristics of the shipment.

Transportation trials provide the most realistic representation of the distribution environment, however the shortcomings associated with trial shipments limit its use in engineering and optimising protective packaging systems. The alternative testing method, which is better suited to packaging optimisation, is through the use of laboratory simulations of road vehicle vibrations. The vehicle vibrations, shocks and translational accelerations (braking and cornering) can all be replicated within the laboratory using different testing apparatus. The

following review centres on the simulation of vehicle vibrations, which has evolved significantly from its inception (Lépine *et al.* 2015).

To date, the vast majority of procedures used to simulate vehicle shock and vibration focus only on vertical motion. Currently, two main approaches are used for simulating broadband random vehicle vibrations. The first approach involves the computation of a target PSD from in-service vibration response data under the desired environmental conditions, while the second involves the use of generic PSD functions based on previous vibration surveys. Both processes are described and used in many standards, such as American Society for Testing and Materials (ASTM) D4728, ASTM D4169, International Safe Transit Association (ISTA) 3E and 3H, United States Department of Defence (MIL-STD) 810G, International Standards Organisation (ISO) 13355 and International Electrotechnical Commission (IEC) 60068-2-64.

Laboratory simulation allows for the precise control over the excitation of the payload, which offers several benefits for protective packaging optimisation. Firstly, the severity of the excitation can be varied whilst maintaining the same spectral shape, allowing the engineer to accurately determine a payload's robustness. The ability to precisely control the excitation also allows for the use of time compression, which increases the test severity to reduce test time, although its validity is strongly debated by many authors (Charles 1993; Rouillard 2008; Rouillard & Sek 2000; Shires 2011).

Notably, payload condition monitoring is greatly improved with laboratory simulation and continuous visual inspection of all sides of the payload is easily facilitated during testing. Furthermore, the laboratory setting allows for simpler data recording systems and real time data analysis. Using real time analysis it is possible to observe damage as the payload's dynamic characteristics change, the payload's frequency response function can be utilised to track the development of fatigue in the payload (Lamb *et al.* 2012).

It should be noted that laboratory simulation of vibration is not without its own drawbacks. Firstly, it must be used in conjunction with other tests to ensure the packaging is robust to withstand shocks and other loading scenarios. The spectral shape and intensity of the vibration are also very important, as PSD profiles based upon surveys of the actual environment provide a better representation of the expected conditions than those from the standards.

Generally, laboratory vibration simulation is limited to vertical excitation. This is due to two main factors: 1) it is well supported in the literature that the vertical component of vehicle vibrations contain the most energy, and 2) the technological limitations associated with

measuring and replicating multi-axial vehicle vibrations in the laboratory. The focus on only vertical vibration has so far resulted in no protective packaging test standards requiring simultaneous multi-axis excitation.

It is, however, becoming increasingly clear that the seemingly gentle pitching and rolling motions of road vehicles (Figure 3-1) do have an impact on payload damage. Technological advances in vibration tables have led to the development of multi-axis shaker tables, an example of which is shown in Figure 3-2. Many varieties of multi-axis shaker tables can reproduce the three axes of translational vibration, as well as rotation about each axis, offering up to six degrees of freedom. Using these advanced systems, replication of realistic vehicle vibration in the laboratory is now possible, however research into vehicle vibration, other than the vertical axis, is in its infancy. This means that operators of multi-axis vibration tables have a limited knowledge of what they are trying to replicate. An improved understanding of real world (multi-axial) vehicle vibration is needed to make better use of these systems.

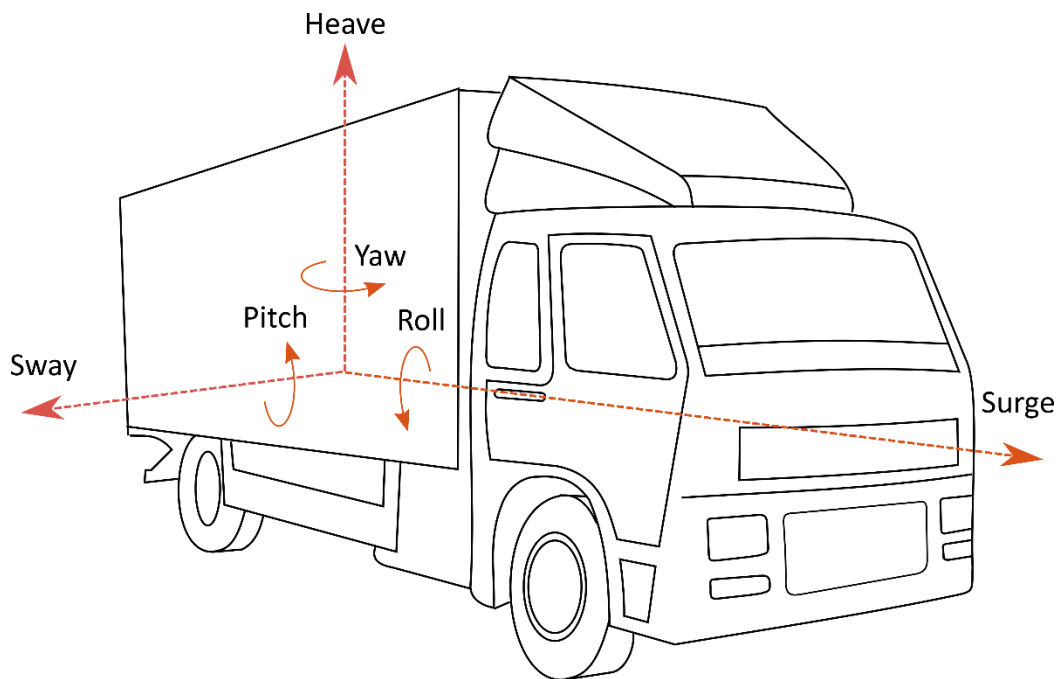


Figure 3-1: An illustration of a vehicles six degrees of freedom.



Figure 3-2: A photograph of a six degree of freedom multi-axis shaker table produced by Moog Inc. (Sourced from moog.com)

3.2 Multi-Axial Vehicle Vibrations

Complex motions are created within ground vehicles when they travel over the irregular surface of the pavement; the irregularities in the surface means the resulting vehicle vibrations are complex and random. Consequently, to fully understand the statistical nature and spectral characteristics of vehicle vibrations an in-depth knowledge of the nature of road topographies is needed.

3.2.1 The Nature of Road Topography

It is well established that road profiles, defined as the vertical deviation of the road surface along an axis parallel to the direction of travel, are random in nature (Dodds & Robson 1973). Variation in pavement condition (surface finish and localised damage) and type result in most roads being highly non-stationary (Heath 1989), although short sections have been shown to be stationary (Heath 1989; Rouillard *et al.* 1996; Bruscella *et al.* 1999). Pavements are also likely to contain a significant number of large amplitude, short wavelength, transient events (e.g. pot holes, train tracks, etc.) (Bruscella *et al.* 1999).

One of the first approaches aimed at characterising the spectral properties of pavement elevation profiles began with Houbolt *et al.* (1955) and continued on by Houbolt (1962) who proposed a

mathematical model for representing the Power Spectral Density (PSD) function of surface profiles for airport runways:

$$G(n) = A \cdot (2\pi n)^{-2} \quad 3-1$$

Where G is the vertical surface elevation spectral density, n is the spatial frequency in cycles per unit length (m) and A is the roughness magnitude parameter in m^3/cycle . This model was also shown to describe the surface profiles of highways by Quinn & Zable (1966) and La Barre *et al.* (1969).

Numerous variations of Houbolt's model, along with other models, have been proposed over the years. However, in general, the spectral amplitude of the elevation has been found to be inversely proportional to the squared spatial frequency squared:

$$G(n) \propto n^{-2} \quad 3-2$$

This general finding is used by the ISO who developed standard ISO8608 (ISO 1995) to classify road roughness based on its spectral function. This standard, and most mathematical models, only represent the average power spectral density of the pavements, and should exclude any transient events.

The PSD function alone is insufficient to completely characterise a longitudinal pavement elevation profile, the statistical characteristics is also required. For laboratory synthesis of road elevation profiles it is generally assumed that the profile is stationary (constant RMS) and has a Gaussian distribution. When transient events are excluded it has been shown that pavement elevation profiles across many countries are random in nature with a distribution often assumed to be Gaussian, despite evidence to the contrary (Cebon 1999, p. 21).

Many authors over the years have found that the statistical distributions of pavement elevation profiles can deviate from Gaussian (Heath 1989; Rouillard *et al.* 1996; Bruscella *et al.* 1999; Otari *et al.* 2011; Griffiths 2012). Bruscella (1997) analysed 415 km of road elevation profiles and found that they significantly deviated from a Gaussian distribution. Rouillard (2006, p. 23), commenting on the work of Bruscella *et al.* (1999), noted that the majority of the moving kurtosis values were approximately three, suggesting that sections of roads may approximate a Gaussian distribution if they are transient free.

The aforementioned methods for characterising road elevation profiles only describe an infinitely thin (very small) cross section of the road surface, however when considering the entire vehicle (multiple wheel paths), a knowledge of the complete road surface is required. To characterise a complete road surface a significant number of the cross sections must be known (measured); a notoriously laborious process. To simplify the characterisation process Dodds and Robson (1973) investigated the possibility of assuming the pavement surface is isotropic (statistical properties are independent of coordinate system rotation) and homogeneous (statistical properties are independent of coordinate system translation). Assuming an isotropic and homogeneous surface allows for the use of a single PSD function to describe the entire road surface. Dodds and Robson (1973) found that it is reasonable to suggest that road surfaces are both isotropic and homogeneous. Exploring these findings further, Heath (1988; 1989) observed that for smooth roads the assumptions of isotropy and homogeneity are acceptable, although Heath observed that rarely was the entire road surface homogeneous and isotropic. Heath (1989) found that the assumptions did not hold for particularly rough roads.

Kropac and Múčka (2008) agreed that isotropy is a valid assumption from analysing the left and right wheel paths of roads in the USA and finding negligible difference between the wheel paths. Section C.5.2 of ISO8608 (ISO 1995, p.18) states that it is convenient to assume the road surface is isotropic and to 'accept the coherence function resulting from using this assumption'. Despite this recommendation, it is unwise to accept the resulting coherence as it may result in one wheel being on the crest of a wave (such as a hill) while the other may be in a trough (valley). It is therefore expected that there must exist a relationship between the spatial frequency (n) and the coherence (γ^2) between the left and right wheel paths (eqn. 3-3) to maintain the superelevation of the road.

$$\lim_{n \rightarrow 0} n = \lim_{\gamma^2 \rightarrow 1} \gamma^2 \tag{3-3}$$

Sayers (1986) found that, for very long wavelengths (low spatial frequencies), the observed wheel paths are almost identical, while at very short wavelengths (high spatial frequency), the coherence of the wheel paths fall to zero as the roughness becomes a function of the surface texture. As such, a roll profile (z_ϕ) exists for any two given wheel paths and is equal to a point-by-point subtraction of the two paths (z_L & z_R), shown in Equation 3-4(Sayers 1986).

$$z_{\varphi} = \frac{(z_L - z_R)}{2}$$

3-4

For low spatial frequencies the wheel tracks are nearly identical resulting in a PSD of the roll profile approaching zero. The tendency for the corresponding elevations of the differing wheel paths to become less correlated at high spatial frequencies causes a relatively higher magnitude in the roll profile. This must be taken into account when synthesising road elevation profiles and Sayers (1986) states that either the cross-spectral density function or the coherence between the profiles is needed in conjunction with a PSD function for accurate replication.

Můčka (2015) conducted an in-depth review of several published models of left-right wheel path coherence functions. The models were compared to 3,492 calculated coherence functions from measured road elevation profiles obtained under the Long-Term Pavement Performance (LTPP) programme data sets. Ammon and Bormann's (1991) model (eqn. 3-5) was found to be the most accurate by Můčka, illustrated in Figure 3-3.

$$\left[1 + (1.497\Omega)^{1.427} \right]^{-0.555}$$

3-5

Where Ω is the angular spatial frequency (rad/m).

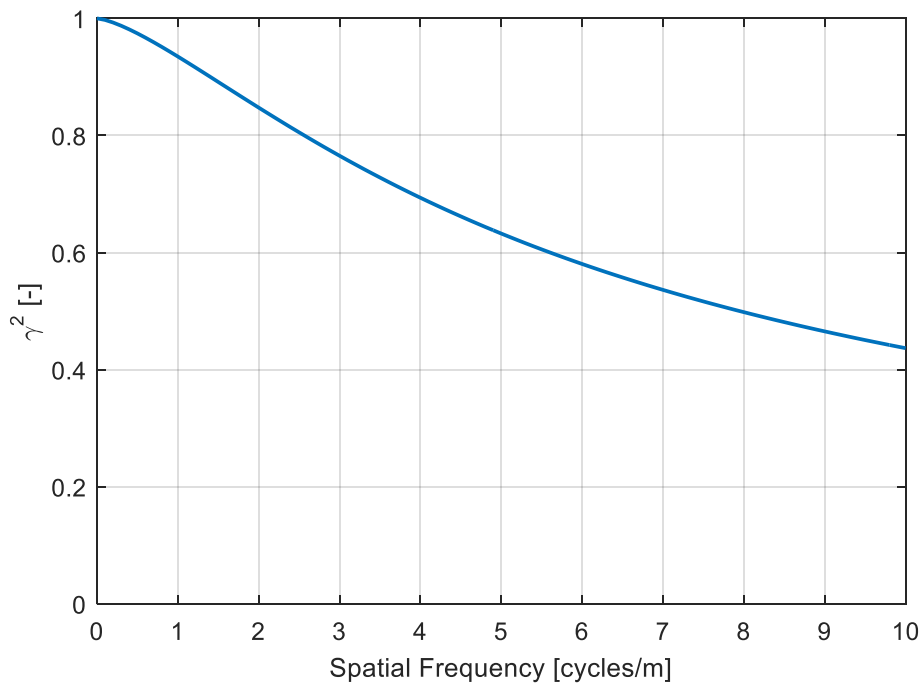


Figure 3-3: Dual wheel path coherence model proposed by Ammon and Bormann (1991).

With a sufficient understanding of the nature of road topography it is possible to move onto the complex motions induced as a vehicle traverses the irregular road surface.

3.2.2 Road-Vehicle Interaction

The vertical vibration response of road vehicles, and its laboratory simulation, is a heavily researched area. On the other hand, limited research has been conducted into the non-vertical motions of road transport vehicles. This section is focused on the research and characterisation of non-vertical vehicle vibratory motion.

3.2.2.1 Non-Vertical Vehicle Vibration.

The body of a vehicle is able to not only translate along three orthogonal directions (vertical, lateral and longitudinal), but also rotate about each of these axis (roll, pitch and yaw). It should be noted that not all of these vibratory modes can be excited by the unevenness of the road surface.

Longitudinal acceleration may be experienced during braking and accelerating, however the road surface cannot directly excite this motion. Similarly, the vehicles body may be subject to a lateral acceleration during cornering (tangential acceleration), but the road-vehicle interaction cannot directly initiate this.

Vibratory lateral and longitudinal accelerations experienced within vehicles is manifested through the effects of the pitching and rolling motion of the body. At points above (or below) the centre of gravity the pitching and rolling motion is transformed into longitudinal and lateral acceleration respectively. The amplitudes of longitudinal accelerations are directly proportional to the height above the centre of gravity and the pitch response amplitude (Gillespie 1985), therefore the longitudinal acceleration will increase with the height of the measurement point. Likewise, the same phenomena occurs with lateral acceleration and the roll response. This is a particular area of concern when transporting tall palletised payloads and necessitates the use of dunnage, or lateral restraint systems, to limit or prevent this from occurring.

The same mechanisms that allow the pitching and rolling motions to transfer into longitudinal and lateral vibrations also augments the levels of vertical vibration experienced in the vehicle; proportionally increasing as the distance from the centre of gravity increases. Bernad *et al.* (2011) measured the response of partially loaded trucks and observed higher acceleration

levels in the rear of the load platform than above the rear axle, highlighting the importance of measurement location.

Singh *et al.* (1992) studied the levels of vertical, longitudinal and lateral vibration using a large transport truck. They found that below 10 Hz the levels of lateral and longitudinal vibration is much less than the level of vertical vibration. However, they estimated that the non-vertical acceleration at the top of the trailer could be as much as 81 times greater than their measured results twelve inches above the trailer bed, assuming full rigid body motion.

A vehicle's pitching motion is a response to the different vertical responses between the front and rear of the vehicle. The vertical response from both vehicle ends is of comparable amplitudes regardless of the vehicle's length, however for shorter wheelbase vehicles this results in larger pitch angles (Gillespie 1985).

Chonhenchob *et al.* (2012) conducted a study into the levels of lateral, longitudinal and vertical vibration of light transport vehicles. Comparisons on the ride quality of each vehicle type was drawn from the acceleration response results. The authors used arbitrary measurement locations, which were not consistent between the vehicles and made any comparison difficult to make. Furthermore, the excitation was also not consistent between vehicles as each travelled over different routes and at varying speed; rendering the results worthless.

Bernad *et al.* (2011) set out to investigate the non-vertical motions of road transport vehicles, including angular accelerations. Two vehicles were used for the study; a two-axle truck and a two-axle pup trailer towed behind a three-axle truck. The vehicle response was measured using six accelerometers for full kinematic reconstruction. Bernad *et al.* (2011) found that, not unexpectedly, the vertical vibration contained the most energy of the three translational accelerations. The yaw rotational acceleration levels were significantly lower than the pitch and roll motions, which were of similar levels. Spectral analysis was limited to low frequencies to ensure that the assumption of rigid body motion was maintained. Analysis of the PSD functions showed that vibrations in the 7-8 Hz range are subject to contribution from all axes.

It is clear from the review of research presented here, that the vibrations experienced during road transport are complex and vary considerably from the vertical only excitation used in the current standardised test methods. The impact of the non-vertical vibrations must be further investigated and evaluated in order to justify their inclusion in future revisions of test standards.

3.3 Effects of Multi-Axis Vibration on Vehicle Payloads

Protective packaging testing is designed to replicate vehicle vibrations in a controlled manner and potentially induce product damage, which can be manifested in a variety of ways. Product damage can occur in the form of scuffing and denting to full product failure. Being able to quantify the effects of non-vertical vibration is difficult, since different loading scenarios are affected by the pitching and rolling motion differently. Any difference between the effects of vertical only and multi-axial excitation will therefore be treated as potentially significant.

To explore the difference between single and multi-axis excitation, Gregory *et al.* (2008), exposed a simple structure (mass atop a beam) to single axis and multi-axis excitation. Three separate single axis tests were compared to simultaneous three axis excitation and full 6DoF excitation. Finite element analysis revealed that the maximum Von Mises stress and location were different between the single axis and multi-axis excitations. Physical experiments using a 6DoF (20-2000 Hz excitation with no correlation between the inputs) electro-dynamic shaker showed a 'significant difference' in the acceleration response of the mass and in the measured strain in the beam between the cases. The change in magnitude and location indicate that potential failure modes can be different between single axis excitation in the laboratory and the real world.

Ernst *et al.* (2015) investigated the robustness of electronic components. The specimen characterised was a four layer FR-4 fibreglass/epoxy circuit board with six insertion mounted inductors, mounted to a 6DOF electro-dynamic shaker using two aluminium fixtures. Failure was defined as a break in continuity between the board and component, with any damaged component replaced upon failure (to maintain board dynamics) until the six original inductors had failed. The excitation used was a truncated version (Cut off frequency reduced from 2000 Hz to 320 Hz) of the U.S. Navy's manufacturing screening programme P-9492 (NAVMAT 1979). Four excitation configurations were tested: vertical, horizontal (perpendicular to the inductor pin direction), combined incoherent (0.1 coherence) vertical-horizontal and combined coherent (0.9 coherence) vertical-horizontal. The average time to failure differed considerably with the type of excitation, reducing from 5:54 (h:min) under horizontal excitation to just 0:55 when subjected to the combined incoherent excitation.

Ernst *et al.* (2015) compared the measured and calculated damage accumulation rates (DAR) of electrical components exposed to multi-axis excitation, and found that the widely accepted approach of using linear superposition would drastically overestimate the durability of the

components. The linear superposition of the separate single axis tests represents the hypothetical DAR if there are no interactions between the axes, and are excited simultaneously. The calculated DAR ($11.0 \times 10^3 \text{ s}^{-1}$) overestimated the electrical components durability more than a factor of two when compared to the combined incoherent excitation ($24.2 \times 10^3 \text{ s}^{-1}$) the test is designed to represent. Under the combined coherent excitation the DAR further increased to $3.09 \times 10^3 \text{ s}^{-1}$. Ernst *et al.* (2015) explained that the large difference between the hypothetical and measured DARs is due to linear superposition's inability to describe the inherently nonlinear behaviour of the component's movement. This affects packaging two-fold, as not only may the products be nonlinear but the protective packaging (both cushioning and box) can be as well (Lamb & Parker 2015).

A product's resistance to multi-axis vibration can be influenced by many factors, one of which is product orientation. Peterson (2012) investigated the effects that product orientation has on a product's robustness when exposed to vibration with varying degrees of freedom. The test specimens used in the study were digital alarm clocks, chosen because of their price, ease of fixturing and the large number of failure modes. The clocks were considered representative of a large number of different electronic devices because of the broad range of components included; they generally include an LED, LCD, circuit board, and wiring. Tests included combinations of mounting directions (upside down and upright) and differing modes of vibrations including single axis, combined translational, and combined translational with rotation. The excitation used for the tests was a modified version (limited by displacement) of the ground vehicle vibration profile from MIL-STD 810G (2008). Although the profile is based on measured data, no phase relationship is used between the different axes. Peterson found that the product's orientation to the vibration made a significant difference and that three single axis tests do not correlate to a combined excitation. The low number of tests (per experiment) and the poor production quality (different failure modes under the same conditions) of the devices tested means that the research is far from conclusive. However, it does show that time to failure and failure modes are dependent on the product's orientation and excitation type, showing a need for realistic multi-axis testing.

Stacked packaging units can exhibit several resonances, including those associated to bending modes, which cannot be excited by vertical vibration alone. Translational accelerations will excite bending modes however the degree to which they are excited is much less than when excited by rotational accelerations (Bernad *et al.* 2011). Bernad *et al.* (2010) investigated the dynamics of stacked paperboard packaging units. Three configurations of stacked paperboard units were studied; five units column stacked, five units column stacked and strapped and 40

units palletised (2 x 2 x 10). The payloads were excited with white noise (4 – 80 Hz) in all translation axes and in the z-rotation (about the vertical axis) simultaneously. Three excitation RMS levels were used (0.04, 0.06 and 0.11 g) in order to attempt to excite all possible modes before operational modal analysis was performed on the measured response. While the stacked paperboard units were found to be non-linear, interestingly the X and Y-bending modes were at a lower frequency than the compression mode for all cases studied.

In general, packaging is designed for large vertical loads and because of this the alignment between packaging units is essential. Misalignment between packaging units (particularly when column stacked) does not allow for the effective transfer of these loads. Batt (2010) observed significant differences in load stability (even when stretch wrap and strapping were used) between only vertical and multi-axis vibration. No observable instability was experienced with the vertical (0.20 g RMS) only excitation. Low level lateral and longitudinal vibrations (0.11 and 0.07 g RMS respectively) and the same vertical vibration level saw box misalignments as high as two inches occur after only three minutes of testing. While a packaged unit's susceptibility to misalignment is dependent on its design (such as location tabs), this highlights potential problems with stacked unit vibration modes and resonance, and the need to consider lateral and longitudinal loading.

Bending modes in stacked packaging units were observed by Griffiths *et al.* (2011) when comparing the damage caused to apples by single and multiple degree of freedom excitation. During experiments to compare the effect of loading configuration, Griffiths *et al.* (2011) observed a sway motion of a single column stack that was not present in a four column stack, demonstrating that payload layout and dynamics are important considerations in multi-axis testing. Using time history replication, damage (measured using the equivalent bruise index) increased by approximately 60 % between vertical only and multi-axis (vertical, pitch and roll) excitation.

Whilst investigating the difference in damage between single and multi-axis excitation, Griffiths *et al.* (2011) also explored the difference between time history replication and Gaussian synthesis from PSD functions. The PSD functions were generated from the measured time history and a new signal with the same spectral characteristics was generated. Griffiths *et al.* found that the tests conducted using the Gaussian signals resulted in more damage for both single and multi-axis excitation. Griffiths *et al.* concluded that the excess damage caused by the Gaussian excitation was equivalent to the damage experienced with multi-axis vibration, and therefore single axis Gaussian excitation is sufficient. The authors clarify this by stating that the results are valid for a single product and that the need for multi-axis testing should be assessed

on a case by case basis, or that the failure (or damage) modes for each product-packaging system must be considered. The metric used to quantify the damage to the apples is only dependent on the amount of bruising, so different damage mechanisms caused by the vertical vibration and multi-axial vibrations can produce similar results. For situations where real world damage can only be replicated by certain vehicle motions, the need for multi-axial excitation increases.

As mentioned earlier in this chapter, no standard test method exists that specifically requires simultaneous multi-axis vibration, however manufactures may still develop internal multi-axis transport vibration test standards to assess their products. For example, Bernad *et al.* (2012) developed a bespoke accelerated multi-axis vibration test schedule for a distribution company. The response of three shipments with different trailer designs (M1, M2 and M3) were measured traveling along a 1000 km stretch of road with an equal split of highways and national roads. Bernad *et al.* found that the trailer stiffness and inertia significantly influenced the roll and vertical vibration PSD functions. It was believed that the bending stiffness of the trailer and its implications in the natural frequencies of the bending modes were the cause. A time replication approach was used when developing the test to maintain the phase shift between the different degrees of freedom and to include the high energy events that would be removed in a PSD based test. The vibration test schedule consisted of three stages:

- Stage I – A 15 and 10 minute section of M1 and M3 respectively is repeated six times (2.5 hours total)
- Stage II – A combined 10 minute signal of M1 and M3 is repeated three times with the signal artificially magnified each time (30 minutes)
- Stage III – The signal is magnified once more and repeated three times (30 minutes)

The test schedule developed by Bernad *et al.* (2012), like all time compressed tests, evaluates harshness using techniques derived from metallic material fatigue. The harshness becomes dependent on a constant (α) used in the calculations, as no value has been scientifically determined the selected value was overly conservative. The time compression allows the first two stages to be equally as demanding as the 1000 km journey; with stage III doubling the test harshness. The addition of stage III is designed to avoid over packaging. A comparison of damage between laboratory tested and field samples was carried out to validate the test method, with the results considered satisfactory.

3.4 Literature Review Summary

This literature review has addressed a wide range of issues associated with determining a payload's robustness when subjected to real world vehicle vibrations. A summary of current packaging test methods was given, discussing the advantages and limitations of both field distribution trials and laboratory testing. This revealed that trial shipments, despite being the most realistic method, suffer from the randomness of the distribution environment and may be excessively moderate or severe. Also, the difficulties associated with data capture and analysis are a significant limitation when considering this approach for protective packaging optimisation. Laboratory simulation sacrifices some realism for improvements in control over the excitation and the ability to monitor the product-package system. Over the years, advances in technology have allowed for laboratory simulation to regain some realism through multi-axis excitation, however research into non-vertical vibration components is, to date, limited.

The second section of the review summarised the causes and manifestations of multi-axial vehicle vibrations. The random irregularities of the road surface were shown to be the main source of excitation for road vehicle vibration. The spectral nature of road profiles was revealed to be highly non-stationary, although short sections of road have been shown to be stationary. The review showed that pavement profiles have been found to be generally non-Gaussian, but can be Gaussian over short distances.

The review summarised the research into the non-vertical motions of road transport vehicles, and demonstrated the limited (and often imprecise) work which has been undertaken in this area. The transformation of pitching and rolling motions into longitudinal and lateral motions was discussed. It was shown that the severity of non-vertical motions varied with frequency and, for some frequency bands, contained more energy than vertical vibrations.

The review culminates with the impacts non-vertical excitation has on individual components, assemblies and palletised payloads. It was shown that the simultaneous excitation of all modes alters the magnitude and location of stresses experienced in payloads. Furthermore, the time to failure was also found to significantly vary. Finally, the use of vertical only excitation for laboratory testing is unable to excite the mode shapes excited during transport of palletised loads. The development of a bespoke multi-axis testing standard was discussed, and good agreement between laboratory testing and real world failures was observed.

Chapter 4

Hypothesis

The principal hypothesis of this thesis is that a statistical correlation exists between the heave, pitch and roll vibratory motions of a wheeled vehicle traveling over uneven pavements.

4.1 Sub-hypothesis

Two further sub-hypothesis will also be considered:

1. These relationships, if they exist, manifest themselves as functions of amplitude and frequency.
2. These relationships, if they exist, are a function of the road, vehicle speed and dynamic parameters, namely the vehicles geometric properties, vehicle moments of inertia and payload mass.

Chapter 5

Methodology

The hypotheses will be investigated using two approaches:

1. Undertake a series of field experiments, in which the on-the-road response of vehicles will be measured.
2. Develop a numerical model of a generic 4-wheeled vehicle with variable parameters and conduct a sensitivity analysis study to investigate the parameters impact on the vehicle's vibratory response.

5.1 Approach 1 – Physical Experiments

The field experiments are designed to identify relationships between the heave, pitch and roll vibratory motion of the vehicle and to investigate the influence of vehicle parameters upon the relationships. The parameters to be investigated include; vehicle speed, road roughness, payload mass and payload inertial properties (CG location and MOI).

Vehicle speed, road roughness, and payload mass are easily varied. To vary the payload inertial properties a modular palletised payload will be used. Wooden pallets will be used to support

lead weights at various heights above the vehicle tray (changing the centre of gravity and total vehicle moments of inertia), while retaining the same overall payload mass.

Many options exist to measure the heave, pitch and roll vibratory response of the vehicle, vertical vibration will be measured using an accelerometer, as is common practice. Traditional piezoelectric accelerometers (charge mode or IEPE) and their associated conditioning hardware are cumbersome and not well suited to on-the-road testing. Micro-electromechanical system (MEMS) accelerometers are robust, accurate and offer frequency ranges suitable for measuring vehicle vibration, and will therefore be utilised.

An accelerometer array can be used to measure pitch and roll vibratory motion, however sensor placement becomes critical and may intrude into the payload area. Furthermore, the need to have exact phase matching between sensors over the whole frequency range of interest make this approach unattractive. MEMS gyroscopes directly measure angular velocity and offer the same advantages as MEMS accelerometers. Inertial measurement units (IMU) are a single unit containing three orthogonally orientated accelerometers and three orthogonally orientated gyroscopes. A MEMS IMU was selected due to the aforementioned advantages of MEMS sensors and the prevalence of high quality, affordable units.

There are a myriad of possibilities to analyse the vertical acceleration and angular velocity response data obtained from the experiments. It is difficult to precisely fix at this early stage without having data on the kinds of analysis that can be used, some analysis techniques that will be explored to see if they yield relevant information are:

- Vehicle response time histories
- Moving RMS time histories
- Statistical distributions
- RMS scatter plots
- Joint distribution functions
- Principal component analysis
- Fourier analysis

The different analysis techniques will be evaluated to find which techniques are the most useful to describe the relationships between the heave, pitch and roll vibratory motions. These analysis techniques will then be used in conjunction with the numerical model for a more focused sensitivity analysis.

5.2 Approach 2 – Numerical Simulations

Since the on-the-road experiments are, to a large extent, uncontrolled, cumbersome and expensive to undertake, a parallel series of numerical experiments is required to further investigate the various vehicle parameters in greater detail. The numerical simulations require a validated four wheeled vehicle numerical model to carry out a significant number of simulated experiments on synthetic roads. The principal benefit of using a numerical model is the controlled investigation into the influence of individual vehicle parameters which, in practice, are difficult or impossible to vary.

The numerical model will be a seven degree of freedom (7DoF) linear model producing direct estimates of vertical acceleration, and pitch and roll angular velocities. No nonlinearities will be included in the model, such as wheel bounce and complete suspension compression (bottoming out). The model will be validated by specific DoFs aspects and comparing the frequency response functions (transmissibility) to those of known models. The natural frequencies of the different degrees of freedom will be calculated from the systems eigenvalues for further validation of the numerical model.

The model will be excited using synthetically generated road elevation profiles. The profiles will be generated from power spectral density (PSD) functions taken from ISO 8608 (ISO 1995), the methodology outlined in the standard will be modified to allow the left and right wheel paths to be synthesised with a user-defined coherence function between them. Realistic parameter values for the numerical model will be procured by various means, including; physical measurement, estimation, and taken directly from literature. The numerical model response data will be analysed using the same analysis techniques used for the physical experiments.

It is important to note that it is not the aim of the numerical model to replicate the physical experiments. This section of the research is designed as a comparative study, with the ability to go further in-depth into the sensitivity analysis of the vehicle parameters

Chapter 6

Physical Experiments: In-Service Measurement

The complexity of road-vehicle interactions means that any investigation into possible relationships between vertical vibration, pitch and roll is not straightforward. This chapter describes a series of physical experiments undertaken to evaluate and identify any correlation between these modes of vibration. The experiments involved measuring the response of two typical light transport vehicles in operation (on-the-road experiments). An Inertial Measurement Unit (IMU) was used to measure the vertical acceleration and the pitch and roll angular velocities of the transport vehicles chassis. The vehicle's response was measured while it was travelling at a variety of nominally constant speeds and under different payload configurations. The measured data was then analysed using Fourier analysis and statistical distributions to identify any potential relationships between them.

6.1 Experimental Setup

The physical experiments consisted of driving two light transport vehicles over a range of roads under different payload configurations and nominally constant speeds. The vehicles used for the physical experiments were a Toyota Hilux utility vehicle and a Toyota Hiace transport van, referred to as UTE1 and VAN1, respectively. The vehicles were chosen as they represent typical

light transport vehicles. An overview of each vehicles' properties are given in Table 6-1, and photographs of each vehicle are shown in Figure 6-1 and Figure 6-2, respectively.

Table 6-1: Properties of the vehicles used for the physical experiments.

	VAN1	UTE1
Model	Toyota Hiace	Toyota Hilux
Description	Small transport van	Small utility vehicle
Tare / Capacity [kg]	1,440 / 700	1460 / 1240
Suspension (Front)	Coil springs + telescopic dampers	Coil springs + telescopic dampers
Suspension (Rear)	Leaf springs + telescopic dampers	Leaf springs + telescopic dampers
Wheelbase [m]	2.60	3.09
Track width [m]	1.43	1.51
Personnel	2	2



Figure 6-1: A photograph of the Toyota Hiace (VAN1) used for the physical experiments.



Figure 6-2: A photograph of the Toyota Hilux (UTE1) used for the physical experiments.

Selecting appropriate roads for the experiments requires many considerations to be taken into account. Roads are selected primarily due to their board spectral bandwidth, in that they are moderately rough, ensuring that the vehicles are sufficiently excited. The length of the road must also be considered when conducting Fourier analysis as the total time of the response signal impacts on the frequency resolution and the number of possible spectral averages. For tests requiring nominally constant speed the roads must also be free from any features that would affect the diver's ability to maintain the desired operating speed. This includes roundabouts, traffic lights, rail way crossings, sharp corners, inclines and descents (depending on the vehicle, payload and speed), as well as other road users.

The first road selected is route C704, a 44 km dual lane country road between Bacchus Marsh and Geelong, shown in Figure 6-3. The second route selected is route C325 between Sunbury and Romsey, north of Melbourne. Route C325 is a 26 km dual lane country road, shown in Figure 6-4. Finally, a 10 km stretch of Bulban road was also selected for the on-the-road experiments. This section of road is a rough dual lane country road between Werribee and Little River (Figure 6-5).

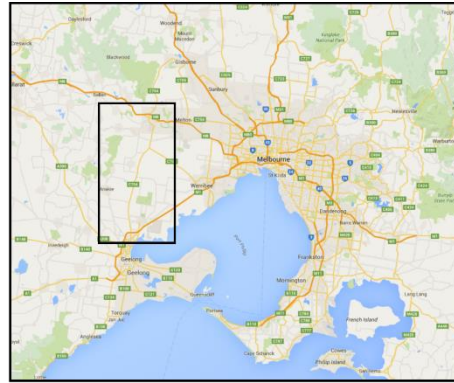
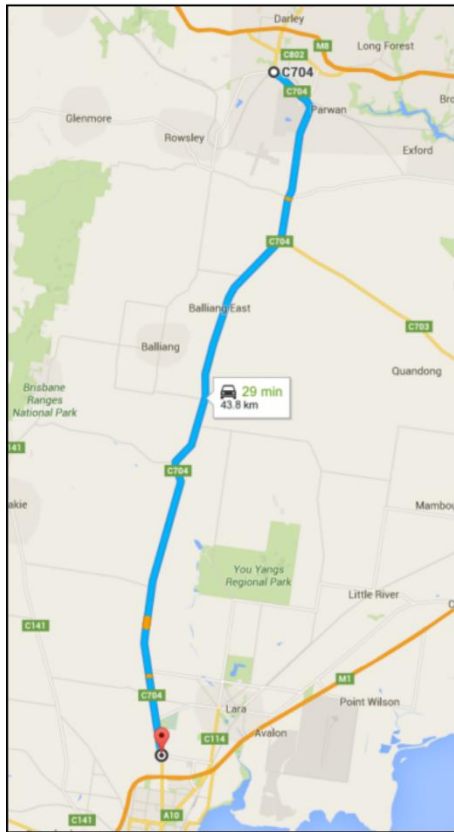


Figure 6-3: Map showing the location of Route 1 (C704) between Bacchus Marsh and Geelong. © Google

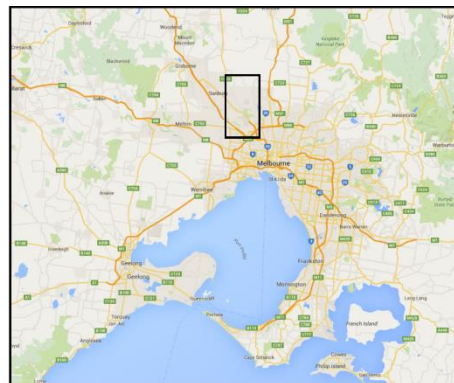
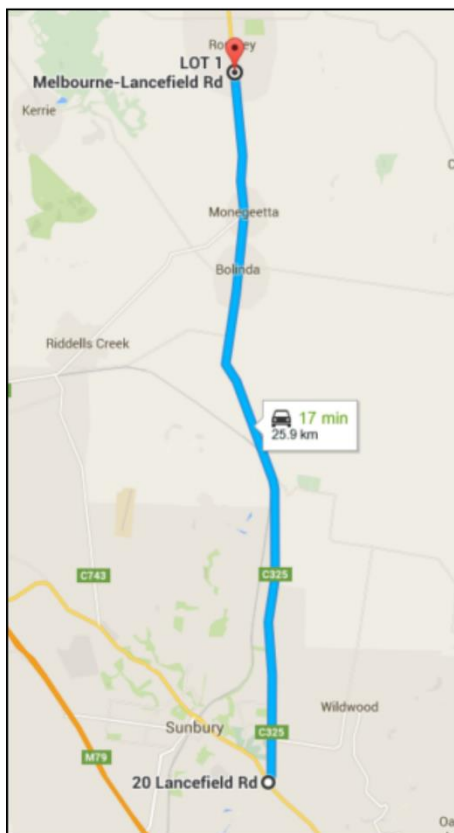


Figure 6-4: Map showing the location of Route 2 (C325) between Sunbury and Romsey. © Google

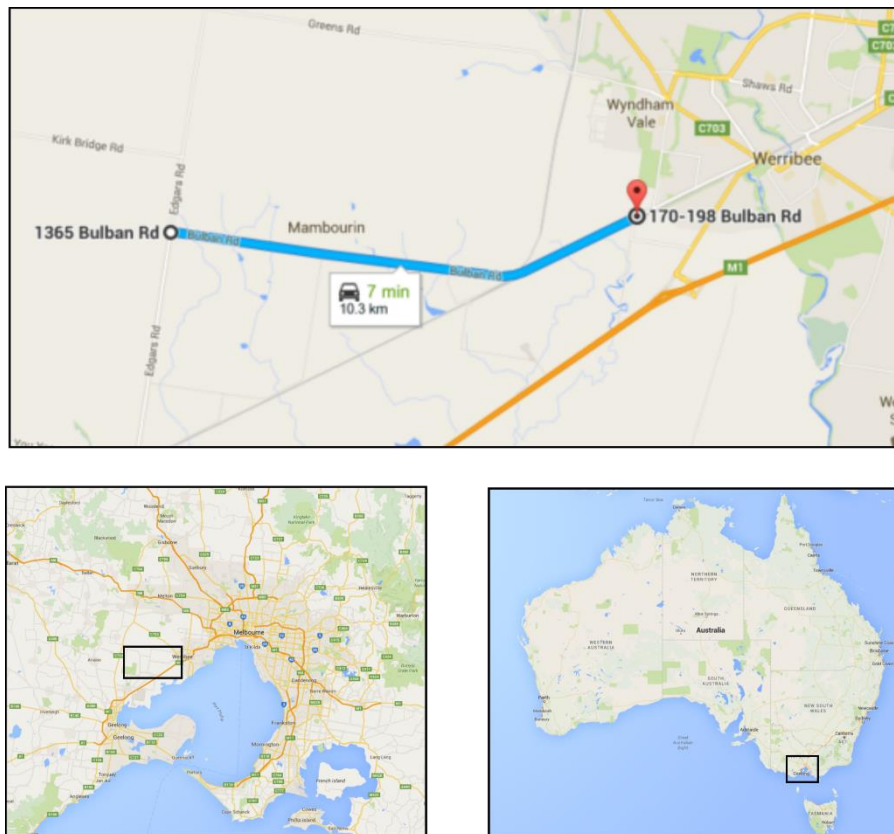


Figure 6-5: Map showing the location of Bulban road between Werribee and Little River. © Google

Table 6-2: Description of routes used for the physical experiments.

ID	Location	Length	Type	Pavement
Route 1	Bacchus marsh - Geelong	44 km	Dual lane country road	Moderately rough
Route 2	Sunbury – Romsey	26 km	Dual lane country road	Moderately rough
Route 3	Werribee – Little River	10 km	Dual lane country road	Moderately rough

The physical experiments were designed to investigate the relationships between the vertical vibration and pitch and roll. As such, ways of quantifying the relationships needs to be found, before a sensitivity analysis can be performed, to investigate the impacts of individual parameters. Experiments were set up to investigate the effects of road selection (and ultimately roughness), vehicle speed, payload mass, and payload mass distribution (CG height and MOI). An investigation into the effects of vehicle design (wheelbase, mass, etc) is deemed impractical with physical experiments, as too many variables change between vehicles and it becomes significantly difficult to isolate the effects of individual parameters. The test schedule for the on-the-road experiments are shown in Table 6-3.

Table 6-3: Test schedule for the physical experiments

ID	Vehicle	Route	Payload [kg]	Payload Height [% of maximum]	Speed [km/h]	Number of Runs
1.1	VAN1	1	-	-	60	2
			-	-	70	2
			-	-	80	2
			-	-	90	2
1.2		2	-	-	80	2
			-	-	90	2
			-	-	100	2
2.1			-	-	70	2
					80	2
					90	2
					100	2
2.2	UTE1	3			70	1
					80	1
					90	1
					100	1
2.3			570	50	70	1
					80	1
					90	1
					100	1
2.4				100	70	1
					80	1
					90	1
					100	1

6.1.1 Instrumentation

The response of the vehicle was measured with a Gladiator Technologies MRM 10 Analog inertial measurement unit (IMU). The IMU features a tri-axial accelerometer with a range of ± 2 g per axis. The IMU's gyroscopes have a range of ± 300 $^{\circ}/s$ (± 5.2 rad/s) about each axis. Only vertical acceleration, and pitch and roll angular velocity was recorded for the experiments A National Instruments USB-6009 analogue to digital converter (ADC) was used to sample the analogue output of the IMU before it was recorded directly to the computer using a custom Matlab® script.

The IMU was recorded at 1000 Hz. However upon inspecting the data it was observed that the analogue output was an analogue signal that was reconstructed by a digital to analogue converter (DAC) within the IMU with an update rate of 100 sec^{-1} . When sampled using the ADC at 1000 Hz the signal would hold the same value for 10 sample before changing. This was overcome by filtering the data before analysis. The down sampling meant that the effective

sample rate was 100 Hz. Despite this loss in sampling frequency, it was found to be sufficient as a vehicle's rigid body vibration has been shown to typically fall within the 0-25 Hz bandwidth (Gillespie 1992)

The IMU was mounted to a 100 kg steel mass and placed on the rear of VAN1. During the on-the-road experiments, the IMU was monitored by a passenger and no separation from the vehicle was observed. The sensor was secured directly to the tray of UTE1, using a non-elastic adhesive.

Measurements were taken directly above the rear axle when using VAN1. For experiments using UTE1 the measurements were taken on the tray, behind the cabin. This was to ensure that the payload, when used, would be directly above the rear axle.

6.2 Data Analysis Approach

Exploring the relationships between vertical vibration, pitch and roll, through physical experiments is incredibly involved, not only from the number of experiments required, but also the sheer number of ways that the data can be represented and analysed. It is important that any relationship can be shown or summarised as clearly as possible. This section will outline the analytical thought process that was followed to identify the metrics that are used to compare all the experimental results in the remainder of this chapter and the results of the numerical model shown in the following chapter.

6.2.1 Statistical Distribution Analysis

Figure 6-6 shows a typical time history of the vertical acceleration, pitch and roll angular acceleration recorded; in this case for VAN1 travelling along Route 1 at a nominally constant speed of 60 km/h. All three measured signals are clearly broad-band and appear to be marginally non-stationary. More importantly similar changes in the amplitude are observed across all signals. That is to say that a change in the level of vertical vibration sees a corresponding change in the level of pitch and roll motion.

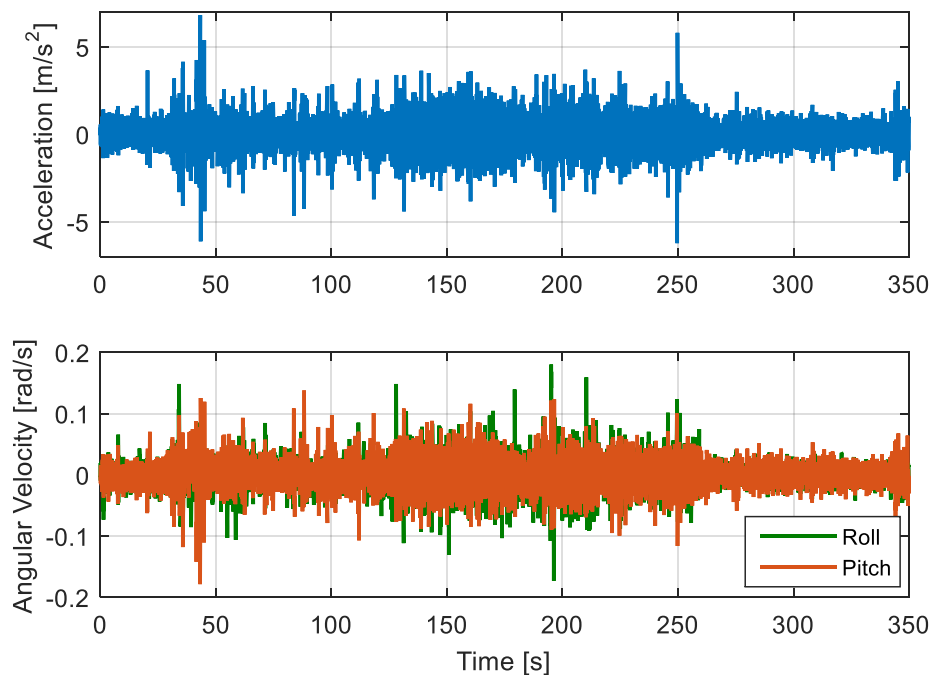


Figure 6-6: Time history of vertical acceleration (top) and pitch and roll angular velocity (bottom) of VAN1 travel along Route 1 at 60 km/h.

Figure 6-7 and Figure 6-8 show the probability density functions (PDF) for the time histories of the vertical acceleration and pitch and roll angular velocities of the signals respectively. The kurtosis of the PDFs is higher than normally distributed data (Gaussian), with negligible skewness. This is expected as the road surface, as discussed previously, can be described as a sequence of Gaussian segments (Rouillard 2006) and the vehicles suspension is operating within its linear (approximately) region.

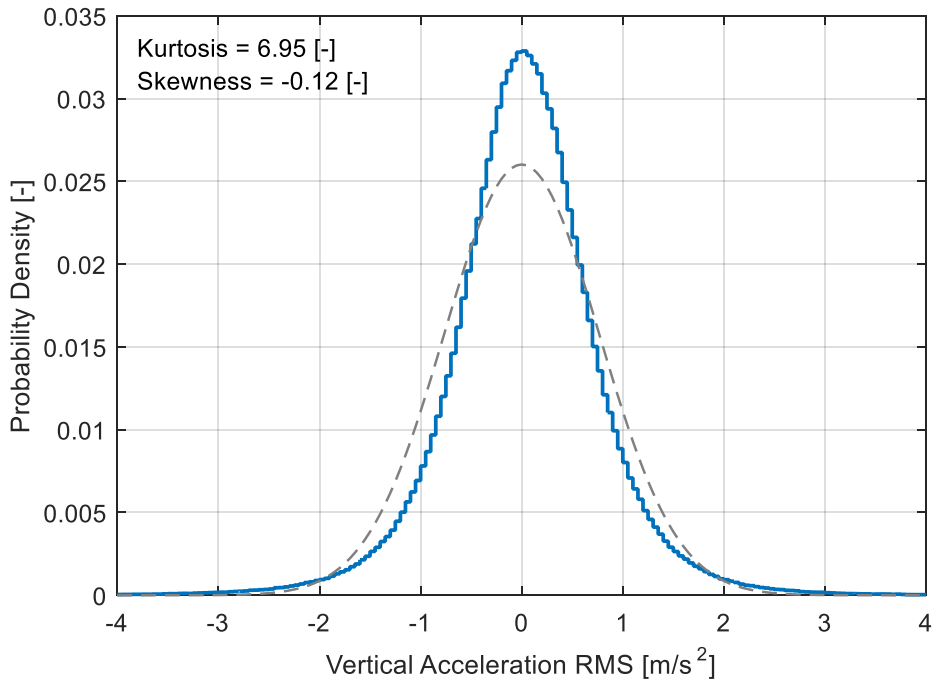


Figure 6-7: Probability density function of the vertical acceleration time history from VAN1 traveling along Route 1 at 60 km/h with Gaussian fit (grey).

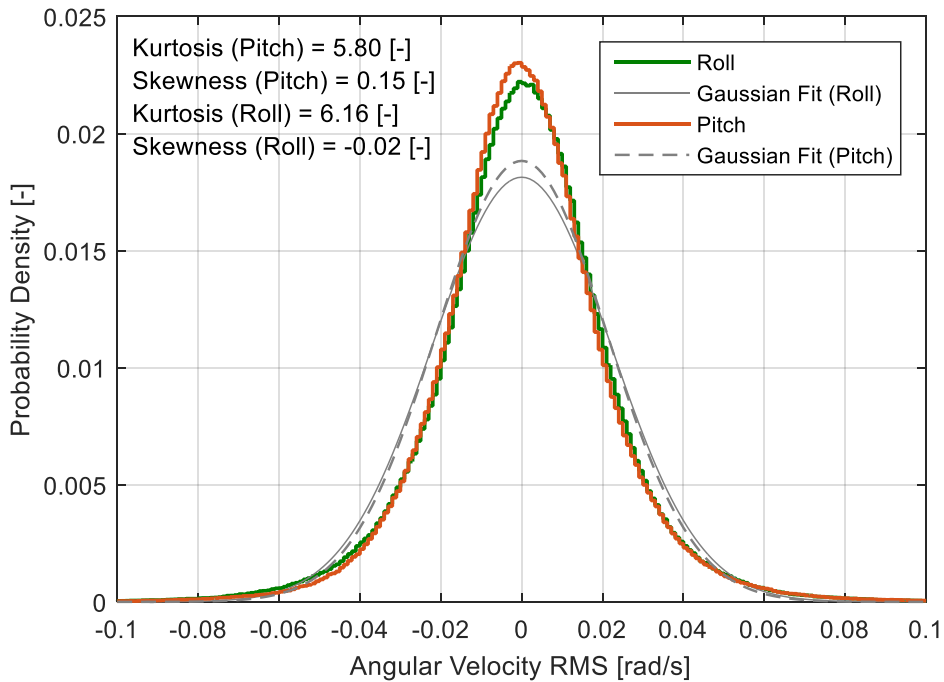


Figure 6-8: Probability density function of the pitch and roll angular velocity time history from VAN1 traveling along Route 1 at 60 km/h.

The corresponding changes in levels of vertical acceleration, pitch and roll is better observed in the RMS time history shown in Figure 6-9. The moving RMS was calculated using a two-second window with maximum overlap (see Rouillard (2006) for the effect of window size and overlap on moving RMS). At approximately 270 seconds a clear drop in the RMS is observed in the vertical acceleration, accompanied by a corresponding drop in the RMS pitch and roll angular velocity is observed. At 340 seconds the RMS increases across all signals. This lower RMS section aligned with a section of road that had been recently resurfaced. These results show that there is some type of correlation between the RMS level of vertical vibration, pitch and roll. The ratios between the RMS of vertical vibration, pitch and roll can be used to describe relationships between the vibratory modes also. It should be noted here, that in all future figures vertical vibration will be represented by shades of blue, pitch in shades of red, and roll in shades of green, for ease of identification.

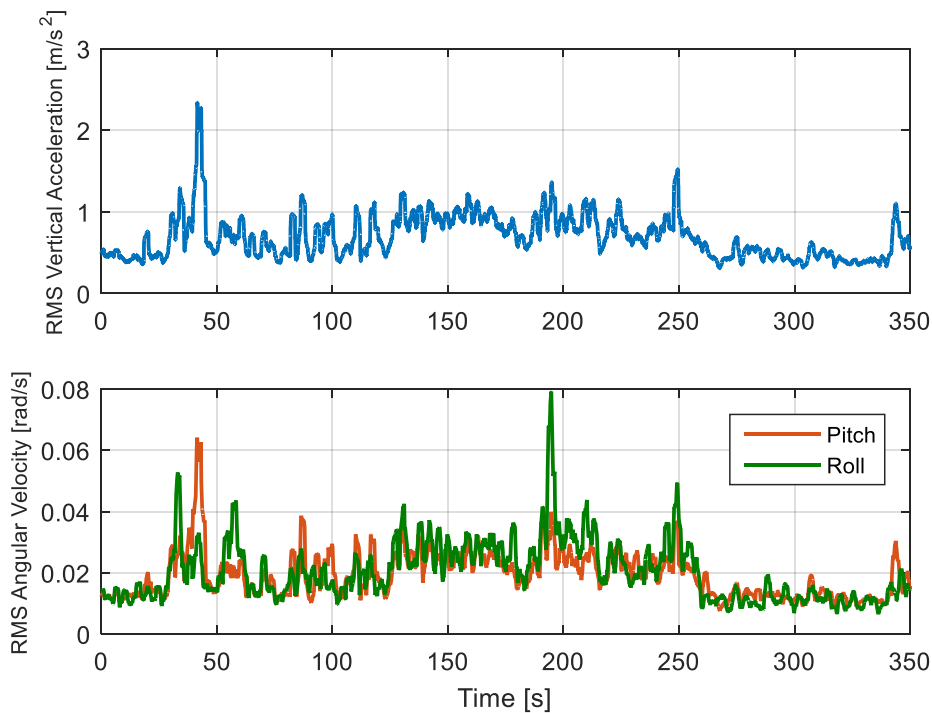


Figure 6-9: RMS time history of vertical acceleration (top) and pitch and roll angular velocity (bottom) for VAN1 traveling along Route 1 at 60 km/h. Moving RMS was calculated with a two second window with maximum overlap.

Figure 6-10 shows the scatter plot of the RMS signal of pitch and roll angular velocity against the RMS signal of the vertical acceleration for VAN1 traveling on Route 1 at 60 km/h. It should be noted that the data has been decimated for clarity. The plot shows a reasonably strong linear relationship between the level of pitch and vertical vibration. A weaker, but still evident, relationship is observed between the roll and vertical vibration.

Plotting the RMS of the pitch and roll angular velocities against the RMS signal of the vertical acceleration forms a particularly strong metric as the data cloud may be affected in many ways; the range values of both axes can change, the gradient and apparent y-intercept of the data cloud can also vary. Cloud density and distribution about a line of best fit may also change. The RMS error (RMSE) of a fitted linear model is also significant as it represents the standard deviation (σ) of the data about that axis. The coefficient of determination (R^2), a measure of how well a line of best fit fits, can also vary.

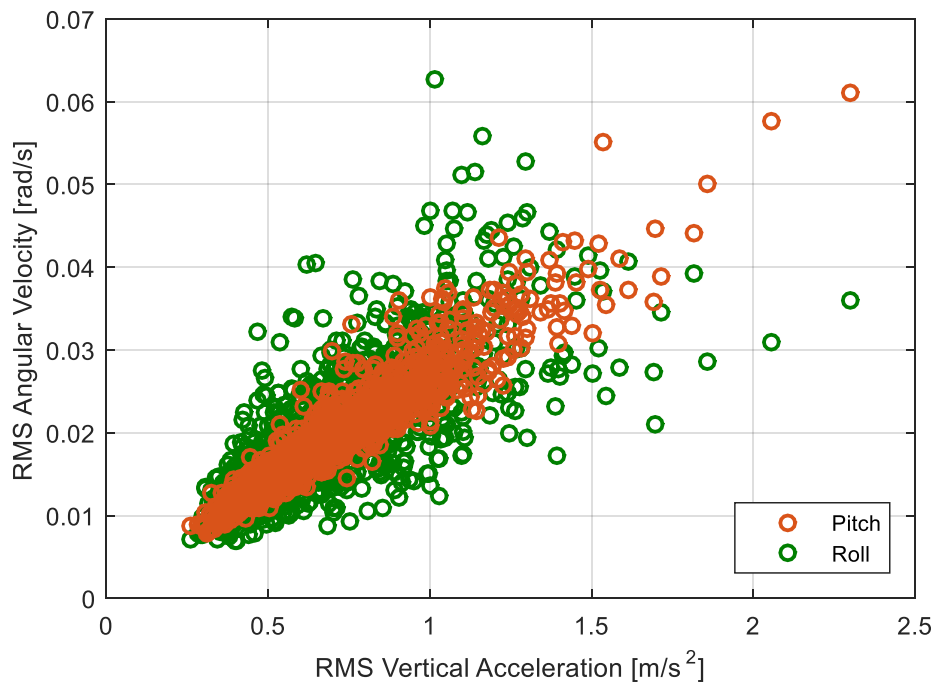


Figure 6-10: RMS scatter plot for VAN1 traveling on Route 1 at 60 km/h.

Continuing the analysis of the RMS time histories, distributions of each vibratory mode can be calculated, Figure 6-11 shows an example of a vertical acceleration RMS time history distribution. It is important to remember that the bin size influences the appearance of the distribution significantly, both in density and shape. For this reason, all PDFs shown herein have a bin size of 0.05 m/s^2 for vertical acceleration and 0.001 rad/s for the pitch and roll angular velocity, unless otherwise stated. The shape of the PDF of the vertical vibration RMS approximates a Chi distribution. The Chi distribution is the square root of the sum of squares of independent random variables having a standard normal distribution (Evans *et al.* 2001) As the vertical acceleration RMS is the square root of the sum of squares of the raw vertical acceleration it makes sense that it would take this shape, as the vertical acceleration PDF approximates a normal distribution as shown earlier (Figure 6-7). The maximum probability density, mode (most frequently occurring value) and the standard deviation of the distribution are all possible points of comparison.

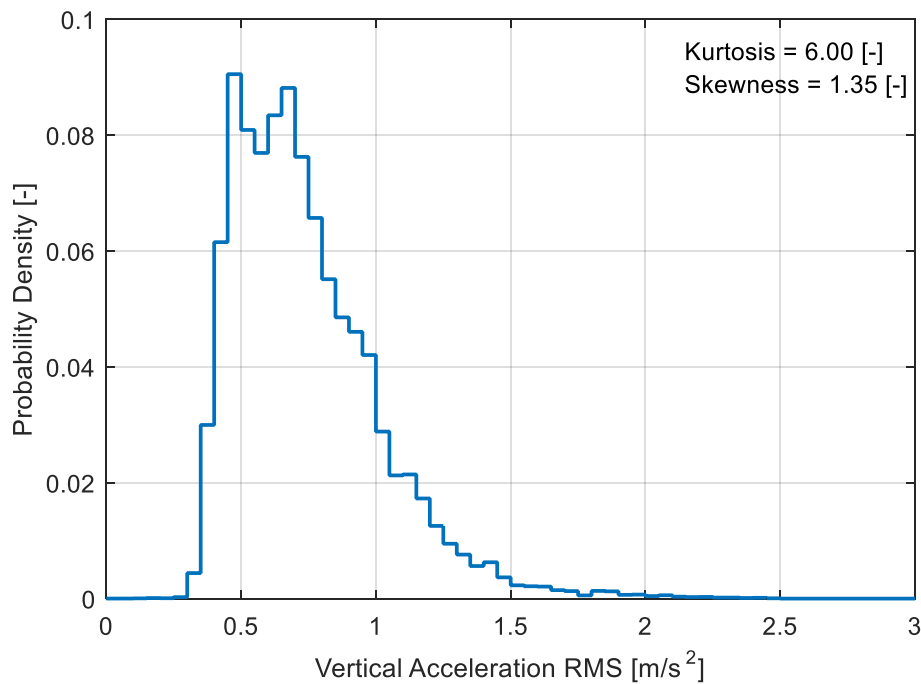


Figure 6-11: Probability density function of the RMS vertical acceleration from VAN1 traveling along Route 1 at 60 km/h.

Figure 6-12 shows PDFs of the pitch and roll angular velocities RMS, again the shape of the PDF approximates a Chi distribution. It is interesting to observe that the PDFs for both pitch and roll angular velocities are very similar, this may differ by changing the system properties.

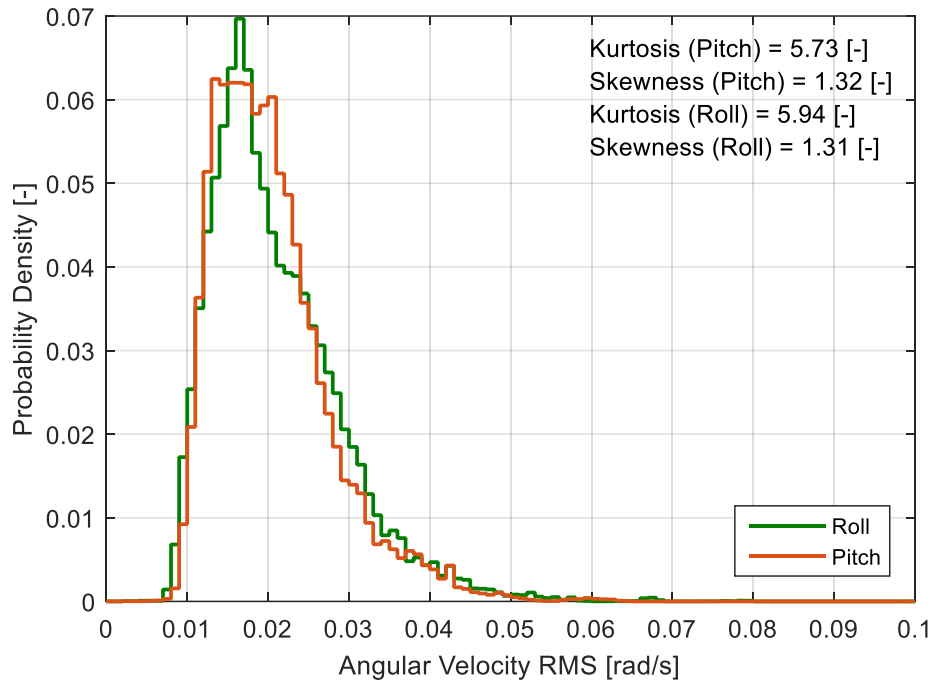


Figure 6-12: Probability density function of the RMS pitch and roll angular velocities from VAN1 traveling along Route 1 at 60 km/h.

As mentioned previously, the density of the RMS data cloud may vary. This is not evident in the RMS scatter plots due to the number of overlapping data points. Figure 6-13 shows the bivariate histogram for the vertical acceleration RMS and pitch angular velocity RMS, where the colour map represents the probability density. It should be noted that many data points exist outside of the coloured region, however their density is too low to register on the colour scale.

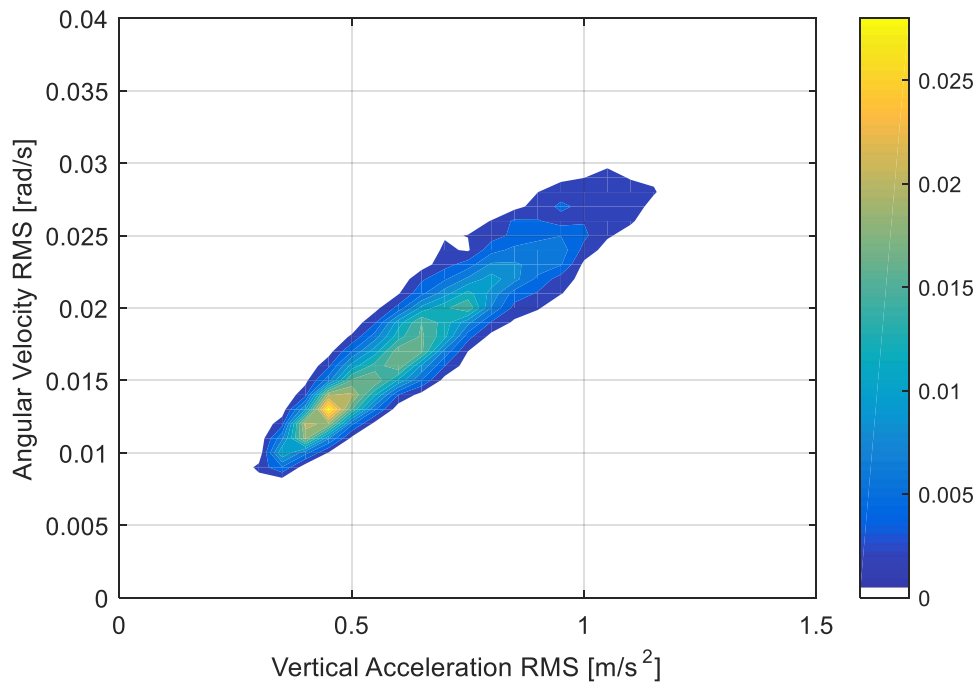


Figure 6-13: Bivariate distribution of the pitch RMS scatter data for VAN1 on Route 1 traveling at 60 km/h.

Principal component analysis (PCA) was the final statistical analysis tool used to identify and describe the relationships between the vibration signals. PCA results in the rotation of the data to its primary axes using its eigenvectors shown in Figure 6-14, effectively removing the gradient from the data cloud. PCA does not translate the data, only the mean slope is removed to centre the data about the x axis. The units after using PCA become quite complex in these cases as they become a factor of the vertical acceleration, angular velocities and the angle of rotation, causing them to change for each case, for this reason they are left undefined. An example of PCA-adjusted data is shown in Figure 6-15.

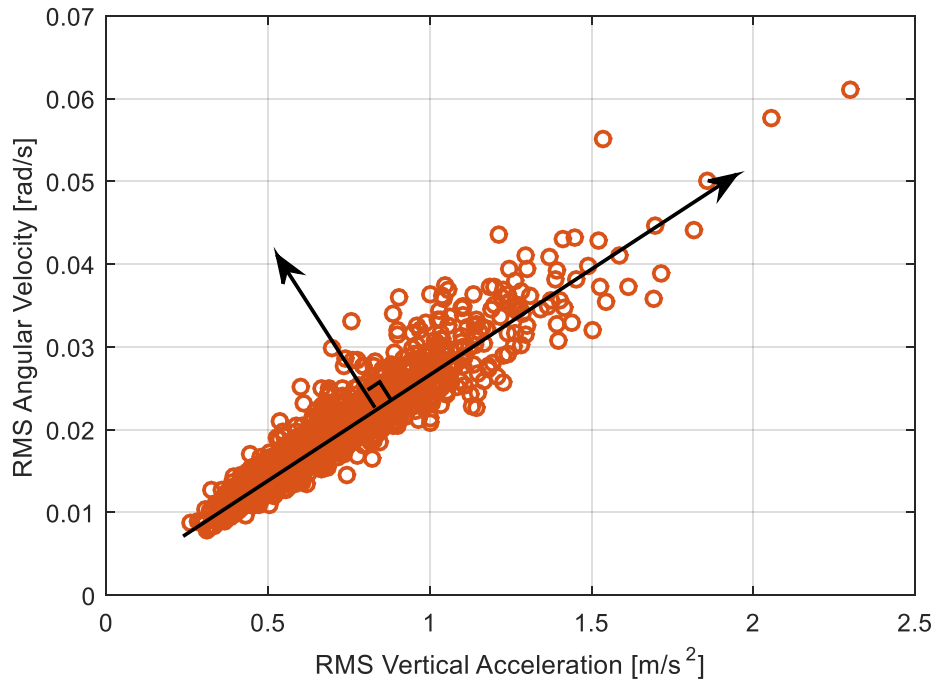


Figure 6-14: Principal components indicated on the pitch angular velocity vs vertical acceleration moving RMS scatter plot for VAN1 on Route 1 traveling at 60 km/h.

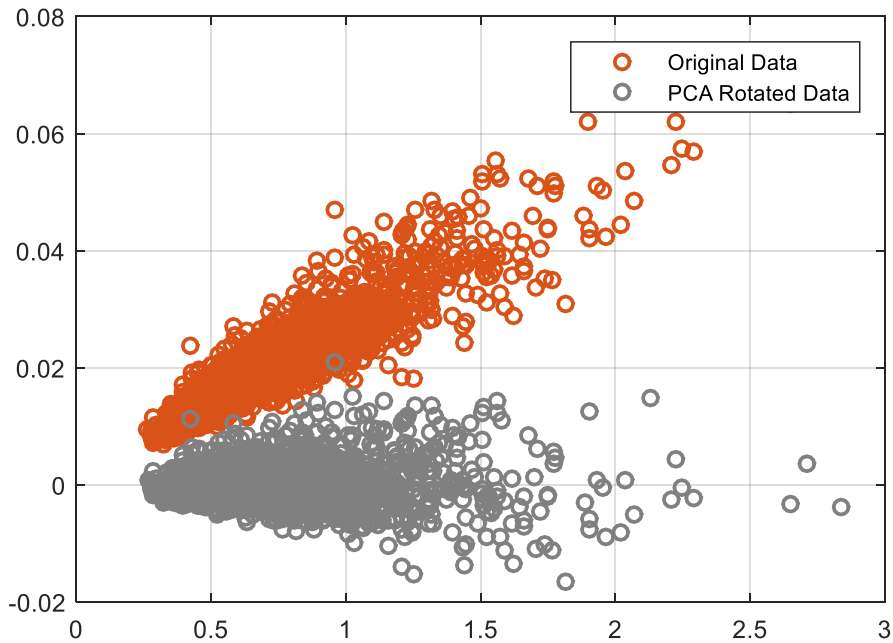


Figure 6-15: Principal component analysis performed on the pitch angular velocity vs vertical acceleration moving RMS scatter plot for VAN1 on Route 1 traveling at 60 km/h.

Despite the problems associated with PCA units, PDFs are still a good point of comparison between different system configurations. Rotating the data using PCA allows for the calculation of PDFs about each axes. A PDF taken parallel to the principal axis represents the distribution about the linear relationship, characterising the strength of the relationship. Figure 6-16 shows an example of a PDF taken along the principal axis from a PCA-adjusted RMS scatter plot. These PDFs show that the relationship between angular velocity and vertical acceleration is much stronger for pitch than for roll. It should be remembered that the RMSE of the linear models fitted to the RMS scatter plots is equal to the standard deviation of these distributions.

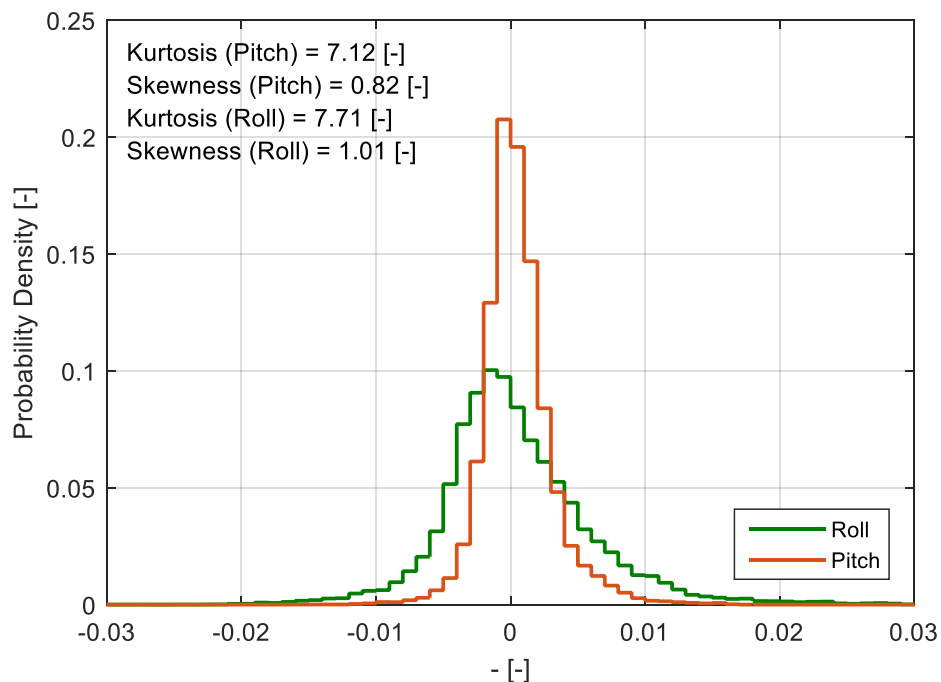


Figure 6-16: Probability density function along the principal axis from PCA-rotated pitch and roll angular velocity vs vertical acceleration moving RMS scatter plot for VAN1 traveling on Route 1 at 60 km/h.

Figure 6-17 shows the PDF taken perpendicular to the principal axis from the PCA-rotated RMS scatter plots. It is significant to note that the pitch and roll PDFs fall almost directly atop of one another. This is not entirely unexpected due to the bin size of the PDF coupled with the vertical acceleration levels being of a significantly higher magnitude than the pitch and roll angular velocities. As such, the distribution of the PCA-adjusted data is almost identical to the distribution of the RMS vertical acceleration PDF, and therefore does not offer any improvement in describing the relationships between the modes of vibration.

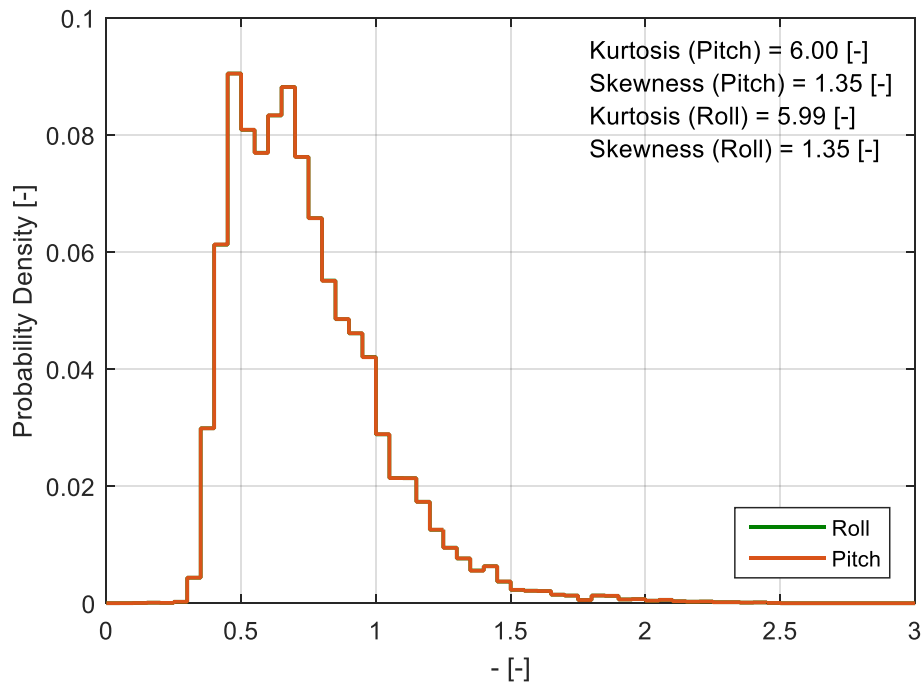


Figure 6-17: Probability density function taken perpendicular to the principal axis from PCA-rotated pitch and roll angular velocity vs vertical acceleration moving RMS scatter plot for VAN1 traveling on Route 1 at 60 km/h.

6.2.2 Fourier Analysis

The previous section investigated the statistical nature of the vehicles heave, pitch and roll response, this section will centre on different Fourier analysis techniques. Fourier analysis is the most widely-used approach to analyse vehicle vibrations, providing insight into the frequency content of the vibrations. Figure 6-18 shows an example of a Power Spectral Density (PSD) function of the vertical acceleration response of a vehicle. The series of peaks occur at the different natural frequencies of the system. The first peak at approximately 2.5 Hz corresponds to the bounce natural frequency of the vehicle's body. The subsequent peaks around 10 and 20 Hz relate to other components of the vehicle, most likely the front and rear unsprung masses. The near-harmonic event at 8.5 Hz was found to be caused by wheel imbalance. Figure 6-19 and Figure 6-20 show the PSD functions for the pitch and roll angular velocities, respectively. With their primary peaks representing the vehicles fundamental frequency for that vibratory modes. The area under the PSD is equal to the RMS^2 of the signal for that bandwidth. The number of averages (N_{AVE}) and frequency resolution (Δf) are dependent on the record length and sub-record length respectively.

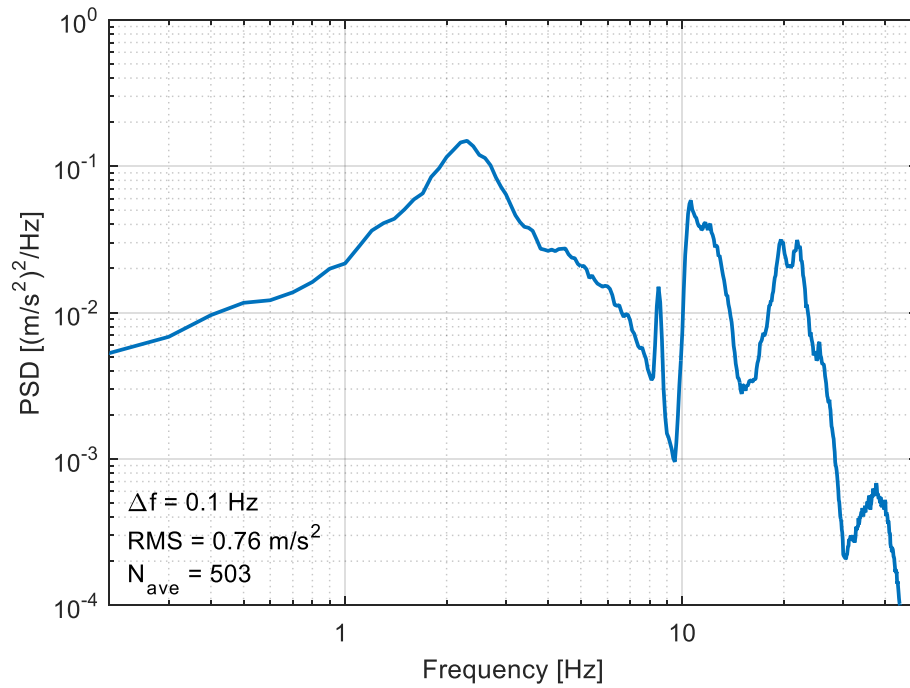


Figure 6-18: Power spectral density function of the vertical acceleration for VAN1 traveling along Route 1 at 60 km/h.

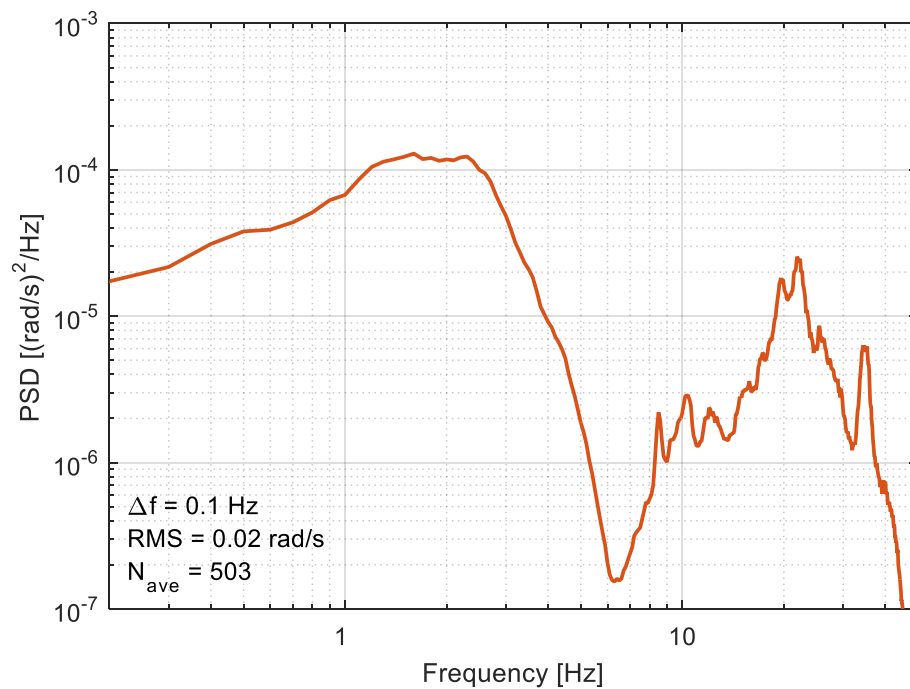


Figure 6-19: Power spectral density function of the pitch angular velocity for VAN1 traveling along Route 1 at 60 km/h.

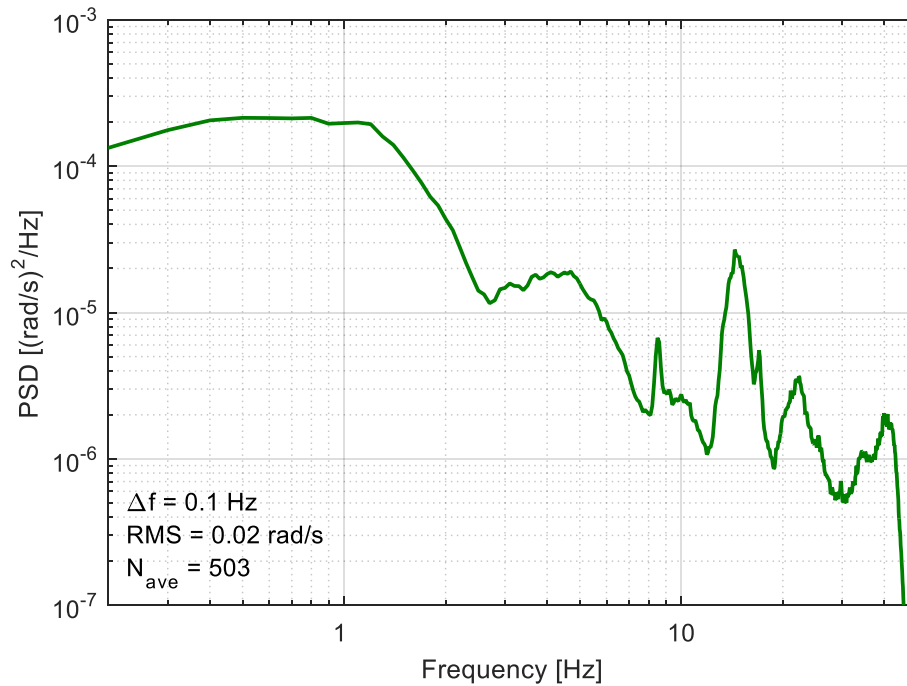


Figure 6-20: Power spectral density function of the roll angular velocity for VAN1 traveling along Route 1 at 60 km/h.

The PSD functions alone can provide considerable information about the vehicle systems. The effects of sprung mass, vehicle speed and road topography on the shape and overall power of the vertical acceleration PSD function are well established. Conversely, the effect of these parameters on the pitch and roll PSD functions has not been the focus of significant research.

In trying to identify any correlation that exists between the vertical vibration, pitch and roll, knowing that a natural frequency has shifted or that the RMS has reduced is insufficient. A way to describe the relationship between the modes of vibration is needed, therefore a frequency response function (FRF) was employed. Traditionally FRFs have been used to describe the relationship between the excitation and response of a system in the same unit (transmissibility), however they can be used to describe different unit excitation-response combinations, such as receptance (force-displacement). The FRFs shown in Figure 6-21 are calculated by taking the vertical acceleration as the excitation and pitch and roll angular velocity as the response. Changes in shape as well as translational movement of the curve can indicate changes in the relationships. The area under the curve (AUC) of the function can be used to quantify changes.

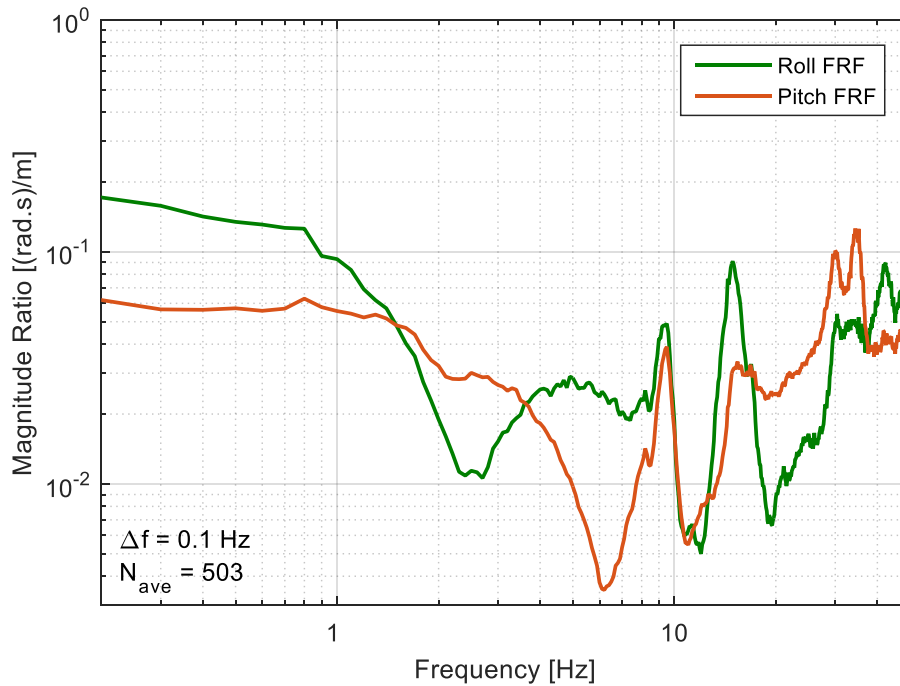


Figure 6-21: Frequency response functions for pitch and roll angular velocity against vertical acceleration for VAN1 traveling along Route 1 at 60 km/h.

6.3 Experimental Response Survey Results

The remainder of this chapter focuses on the results of the significant vehicle vibration response survey described in section 6.1. The analysis will focus on investigating four different vehicle/experiment parameters; vehicle speed, the road selection, payload mass and payload mass distribution characteristics.

It is important to remember that the results and conclusions contained herein are specific to the vehicles and conditions tested, and are not representative of all of all vehicles and payload configurations. Due to the nature of the figures, occasionally only selected results are displayed for comparison to facilitate the interpretation of the results.

6.3.1 On the Effects of Vehicle Speed

The effective road roughness, experienced by a vehicle, is a function of both the road roughness and the vehicle speed. A roads roughness is specified in the spatial domain (section 3.2.1), however when a vehicle traverses a road at speed the displacement spectrum is transformed into the frequency domain. In the frequency domain, the spectrum is translated to the right as speed

increases, as the frequency band of interest does not change (0-25 Hz) this has the same effect as the spectrum translating up, or increasing in roughness.

The following results show the response of VAN1 traveling along Route 1 and Route 2 (configurations 1.1 and 1.2) and UTE1 in both an unloaded (2.1) and loaded (2.4) configurations. Experiments were conducted at nominally constant speeds (± 5 km/h) ranging from 60 to 100 km/h.

Figure 6-22 and Table 6-4 display how the pitch:heave and roll:heave over all RMS ratios vary with speed. The top graph shows the ratio between RMS pitch angular velocity (P_{RMS}) and RMS vertical acceleration (H_{RMS}), whilst the bottom graph shows the ratio between RMS roll angular velocity (R_{RMS}) and RMS vertical acceleration. A reasonably strong linear relationship can be observed between vehicle speed and the pitch-heave ratio relationship for configurations 1.1 and 1.2, the relationship appears to be independent of the road roughness (the only difference between the two configurations). A fitted linear model, using both configurations, returns a gradient of -1.99×10^{-4} and returns a R^2 of 0.94. The pitch:heave ratios for configurations 2.1 and 2.4 fluctuate randomly within a small range for the varying speeds. The roll-heave ratios appear to be independent of speed as they also fluctuate randomly within a narrow band.

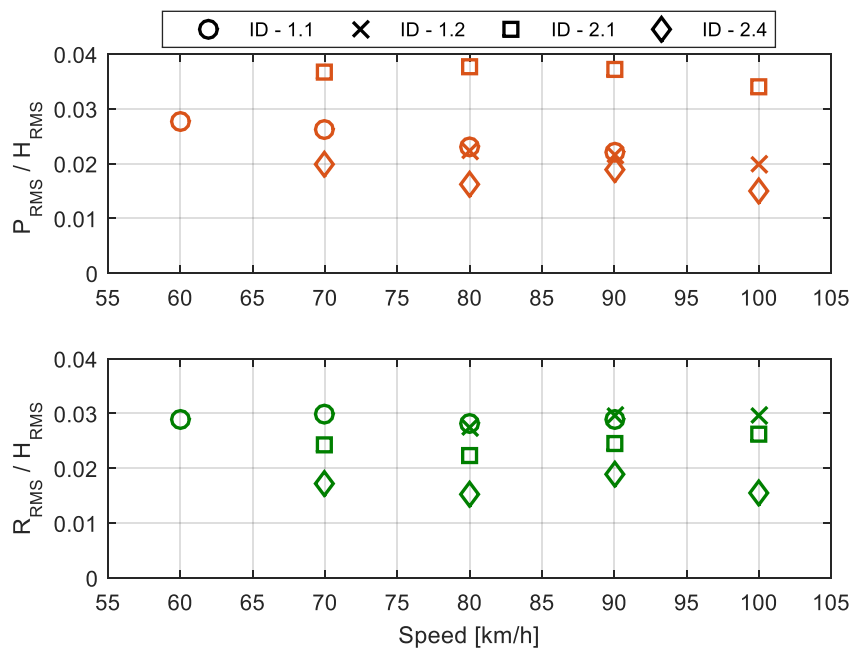


Figure 6-22: The effects of speed on the ratio between the pitch RMS and heave RMS (top) and the ratio between the roll RMS and heave RMS (bottom).

Table 6-4: A table summarising the RMS ratios for multiple vehicles traveling on multiple roads at nominally constant speeds.

ID	Speed [km/h]	H_{RMS} [m/s²]	P_{RMS} [rad/s]	R_{RMS} [rad/s]	P_{RMS}/H_{RMS} [(rad.s)/m]	R_{RMS}/H_{RMS} [(rad.s)/m]
1.1	60	0.7682	0.0213	0.0221	0.0277	0.0288
	70	0.8518	0.0222	0.0255	0.0261	0.0299
	80	0.9681	0.0223	0.0273	0.0230	0.0282
	90	1.0562	0.0232	0.0305	0.0220	0.0289
1.2	80	0.9969	0.0221	0.0273	0.0222	0.0274
	90	1.0126	0.0218	0.0300	0.0215	0.0296
	100	1.1645	0.0231	0.0346	0.0198	0.0297
2.1	70	1.1536	0.0424	0.0279	0.0368	0.0242
	80	1.3428	0.0505	0.0299	0.0376	0.0223
	90	1.3117	0.0488	0.0320	0.0372	0.0244
	100	1.3250	0.0451	0.0349	0.0340	0.0263
2.4	70	1.4764	0.0292	0.0253	0.0198	0.0171
	80	1.7783	0.0289	0.0272	0.0163	0.0153
	90	1.5676	0.0298	0.0294	0.0190	0.0188
	100	2.0373	0.0307	0.0313	0.0151	0.0154

The IMU was located directly above the rear axle for the experiments which used VAN1 (1.1 and 1.2), however for experiments using UTE1 (2.1 and 2.4) the IMU was located forward of the rear axle, closer to the centre of gravity. The reduction in distance to the centre of gravity reduces the tangential component of the pitch (and roll) angular acceleration. This directly influences the relationships between the vibratory modes, as a smaller component of the vertical acceleration is produced by pitch and roll. This effects the RMS levels, and subsequently the RMS ratios, helping explain the stronger correlation between the RMS ratios for VAN1 than UTE1.

Figure 6-23, Figure 6-24 and Figure 6-25 show a comparison of the RMS distributions for VAN1 traveling between 60 and 90 km/h. Figure 6-23 displays the vertical acceleration RMS PDF, a significant change in the distribution occurs with the changing speed. As speed increases the RMS distribution becomes more spread out, indicated by an increase in the standard deviation of the data. This change in standard deviation changes linearly with speed, as shown in the bottom graph of Figure 6-23. The mode (most frequent value) increases with speed, as expected from the increased excitation roughness.

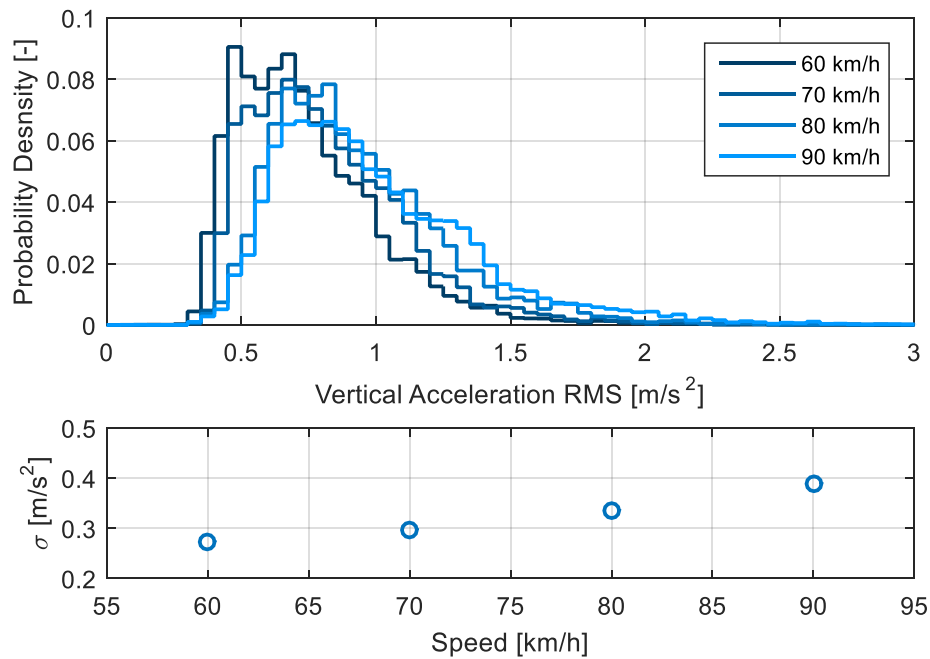


Figure 6-23: A comparison of the probability density function of the moving RMS vertical acceleration (2 second window, maximum overlap) for VAN1 on Route 1 traveling at speeds between 60 and 90km/h (top) and a comparison of the standard deviation at each speed (bottom).

Figure 6-24 displays the pitch angular velocity RMS PDFs for VAN1 traveling at multiple nominally constant speeds along Route 1. The pitch response distribution varies slightly with speed compared to the heave response. A migration towards higher RMS levels is observed and the maximum probability density increases slightly as speed increases. The spread of the RMS pitch response remains consistent though all speeds, with only slight variation in the standard deviation between the experiments.

PDFs of the roll angular velocity RMS for VAN1 traveling at multiple nominally constant speeds are show in Figure 6-25. Compared with the pitch response the variation in the mode and standard deviation of the roll RMS are more pronounced with changes in vehicle speed.

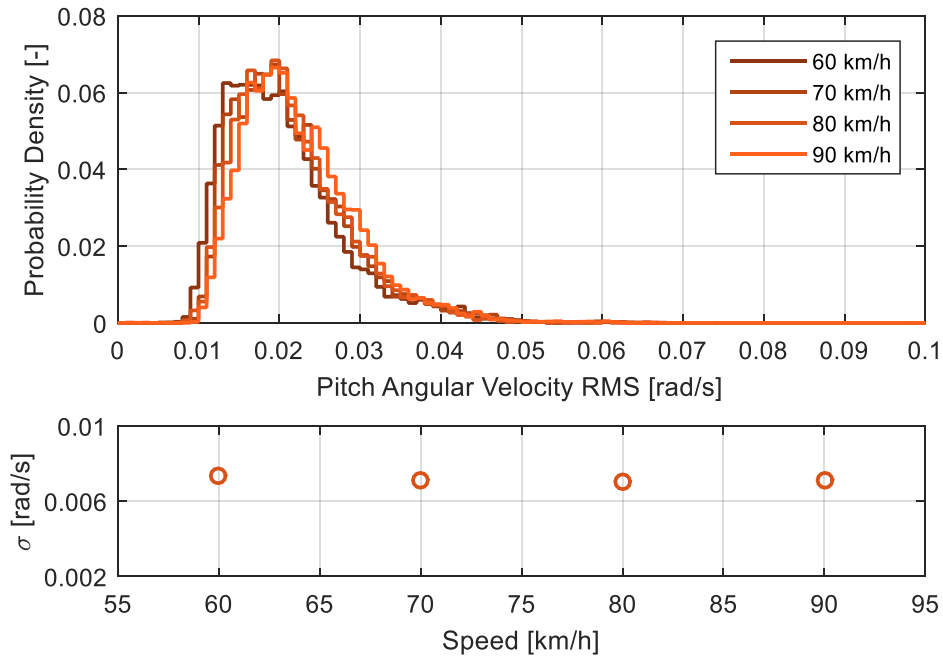


Figure 6-24: A comparison of the probability density function of the moving RMS pitch angular velocity (2 second window, maximum overlap) for VAN1 on Route 1 traveling at speeds between 60 and 90km/h (top) and the standard deviation at each speed (bottom).

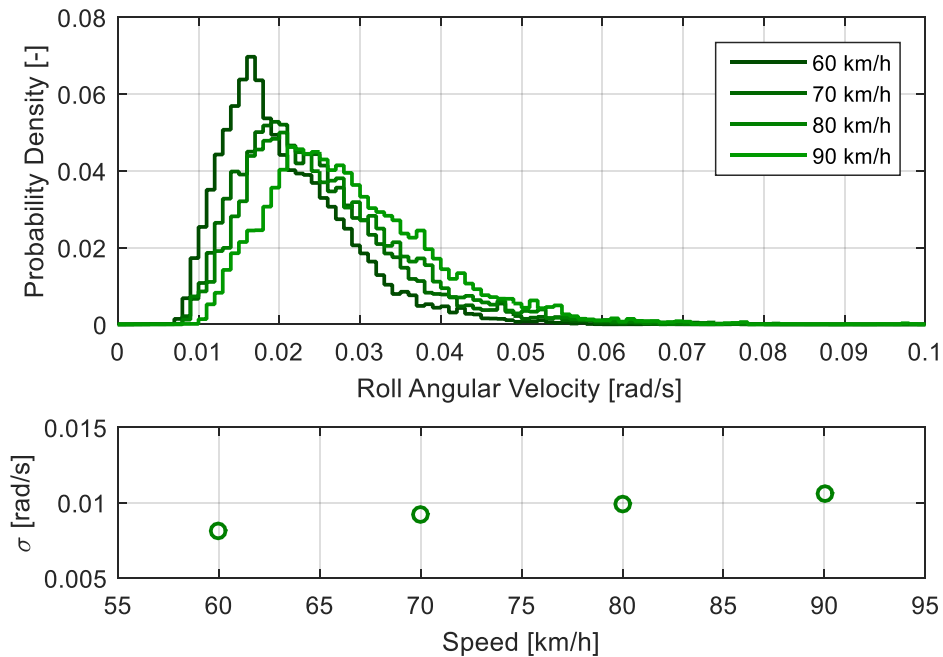


Figure 6-25: A comparison of the probability density function of the moving RMS roll angular velocity (2 second window, maximum overlap) for VAN1 on Route 1 traveling at speeds between 60 and 90km/h (top) and the standard deviation at each speed (bottom).

Figure 6-26 shows the bivariate histograms for the vertical acceleration and pitch angular velocity RMS response. A clear change in density is observed, with that of the lower speed being more concentrated. It should be again noted that the colour map does not show all of the data points, due to their probability density being too low. As speed increases the data cloud translates to the right and up, representing higher occurrences of larger vertical accelerations and pitch angular velocity values (although the maximum and minimum values remain similar for the pitch response, their frequency of occurrence decreases). A change of gradient also occurs with speed.

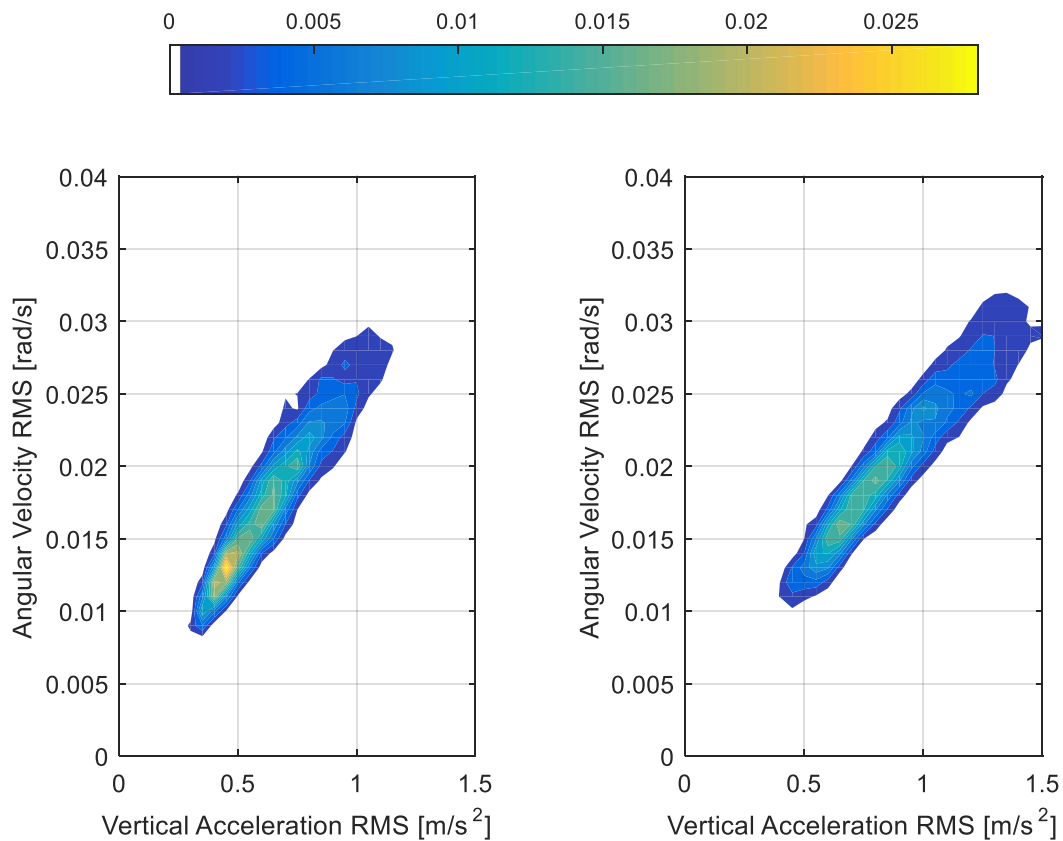


Figure 6-26: Comparison of vertical acceleration - pitch angular velocity moving RMS bivariate histograms of VAN1 traveling along Route 1 and 60 km/h (left) and 90 km/h (right).

Table 6-5 contains the properties of linear models fitted to the heave vs. pitch RMS data clouds for the experiments. The gradient for configurations 1.1 and 1.2 varies linearly with speed as show in Figure 6-27, with the trend continuing across both configurations, the same as the RMS ratios. R^2 values are quite high, showing that the relationship is highly linear. The RMS error (RMSE) is low and consistent, again demonstrating the highly linear relationship. As the Y-intercept tends to be around zero, the gradient tends to be approximately equal to the RMS ratios shown previously.

Table 6-5: Summary of the linear models fitted to the pitch vs heave RMS scatter plots.

Configuration ID	Speed [km/h]	Gradient	Y-Intercept	R ²	RMSE
1.1	60	0.0252	0.0019	0.8743	0.0026
	70	0.0229	0.0027	0.9028	0.0022
	80	0.0198	0.0031	0.8922	0.0023
	90	0.0172	0.0052	0.8918	0.0023
1.2	80	0.0206	0.0016	0.9082	0.0022
	90	0.0176	0.0041	0.9068	0.0021
	100	0.0152	0.0057	0.9040	0.0023
2.1	70	0.0321	0.0055	0.9133	0.0039
	80	0.0357	0.0024	0.9138	0.0050
	90	0.0350	0.0026	0.8415	0.0066
	100	0.0290	0.0065	0.8304	0.0055
2.4	70	0.0145	0.0076	0.5844	0.0045
	80	0.0160	-0.0004	0.4825	0.0064
	90	0.0132	0.0091	0.6662	0.0038
	100	0.0142	0.0010	0.4418	0.0064

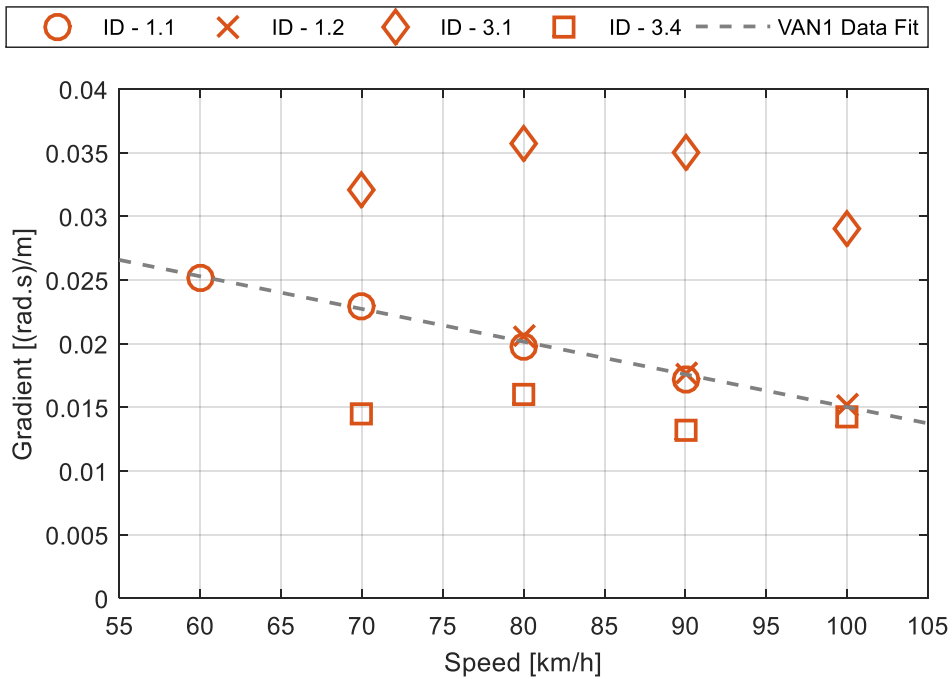


Figure 6-27: A comparison of the heave-pitch RMS scatter plot gradient as speed varies.

Figure 6-28 shows a comparison of the bivariate histograms for vertical acceleration and RMS roll angular velocity. Once more, a clear drop in maximum density occurs with an increase in speed. The data cloud translates up and right as heave and roll levels increase. This drop in density and translation can be connected to the changes in the distributions of the individual modes of vibrations.

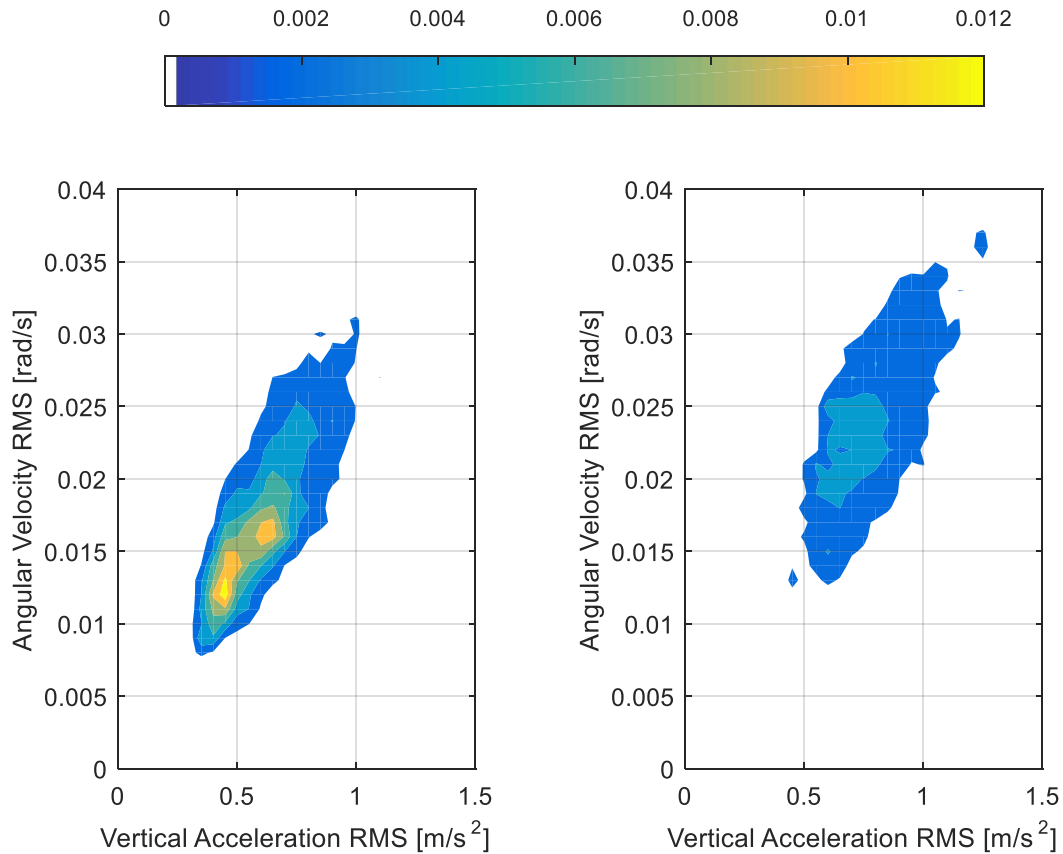


Figure 6-28: Comparison of vertical acceleration - roll angular velocity moving RMS bivariate histograms of VAN1 traveling along Route 1 and 60 km/h (left) and 90 km/h (right).

A summary of linear models fitted to the data clouds is shown in Table 6-6. A small fluctuation in gradient is exhibited across all speeds. This is better observed in Figure 6-29. The R^2 values are much lower when compared to the heave-pitch fitted linear models, suggesting that the modes of vibration are less correlated. The RMSE of the fitted linear models increases with speed signifying the relationship between heave and roll levels becomes less correlated as speed increase.

Table 6-6: Summary of the linear models fitted to the roll vs heave RMS scatter plots.

Configuration ID	Speed [km/h]	Gradient	Y-Intercept	R ²	RMSE
1.1	60	0.0212	0.0052	0.5078	0.0057
	70	0.0219	0.0062	0.4957	0.0066
	80	0.0200	0.0073	0.4513	0.0074
	90	0.0176	0.0113	0.4143	0.0081
1.2	80	0.0242	0.0023	0.5343	0.0076
	90	0.0231	0.0060	0.5430	0.0080
	100	0.0207	0.0098	0.5216	0.0093
2.1	70	0.0195	0.0051	0.6280	0.0058
	80	0.0173	0.0063	0.5788	0.0067
	90	0.0201	0.0051	0.6086	0.0070
	100	0.0243	0.0019	0.6335	0.0077
2.4	70	0.0129	0.0053	0.2899	0.0075
	80	0.0114	0.0059	0.2336	0.0079
	90	0.0164	0.0029	0.4353	0.0076
	100	0.0146	0.0004	0.3140	0.0086

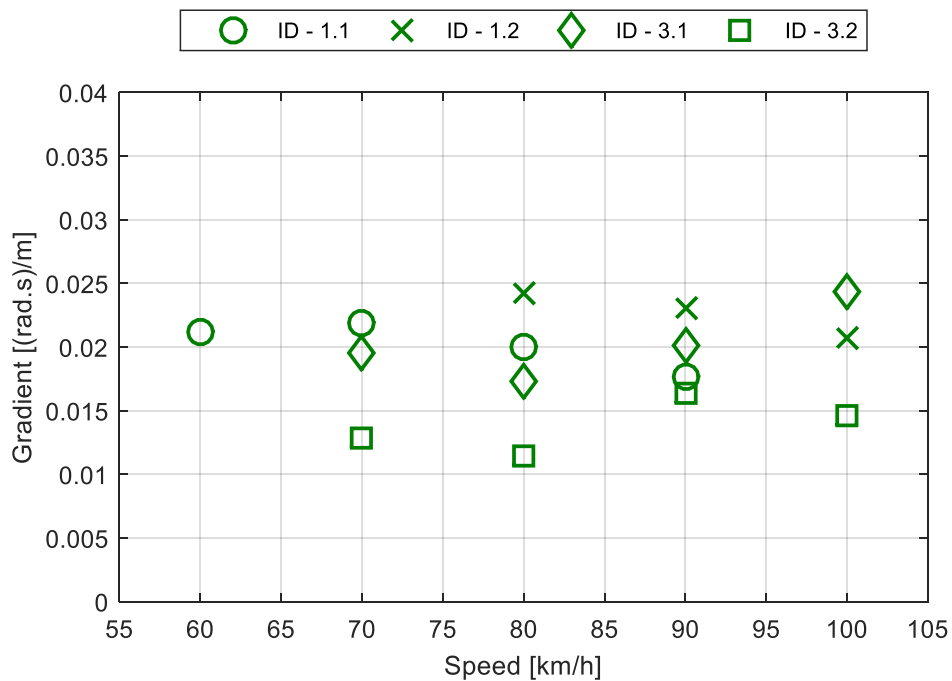


Figure 6-29: A comparison of the heave-roll RMS scatter plot gradient as speed varies.

Principal component analysis reveals more of the relationship between heave and the angular motions. Figure 6-30 shows the distribution about the principal axis of the PCA-adjusted pitch-heave data for VAN1 traveling along route 1 at speeds between 60 and 90 km/h. The PDF of the pitch-heave data remains similar, indicating that the pitch responses distribution along the fitted linear model is relatively independent of speed. The standard deviation remains consistent for all speeds, indicating the independence of the relationship with respect to speed.

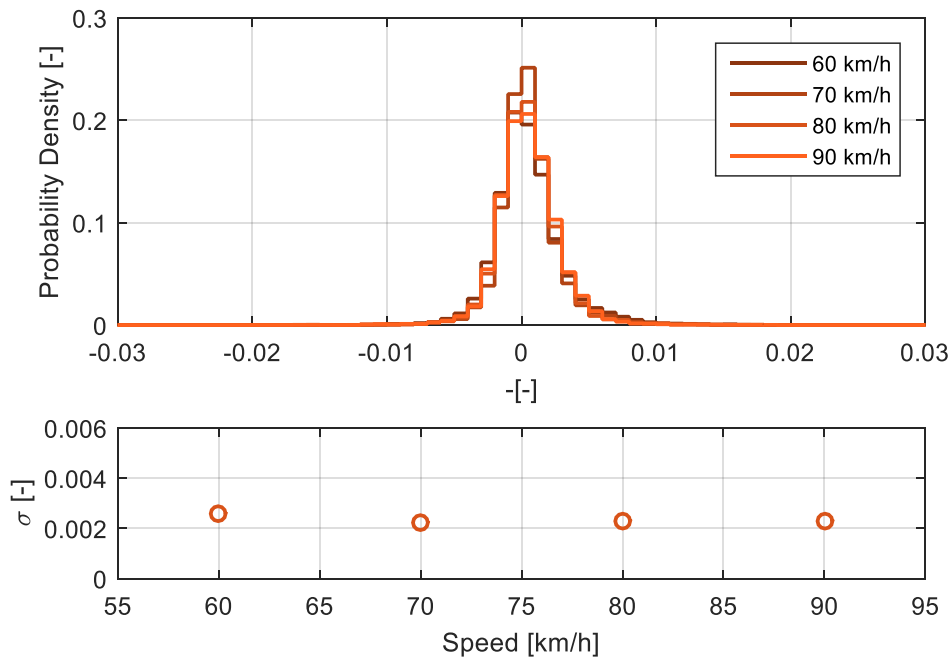


Figure 6-30: A comparison of the probability density functions along the principal axis from the PCA-adjusted vertical acceleration vs pitch angular velocity moving RMS scatter plot for VAN1 on Route 1 traveling at speeds between 60 and 90km/h (top) and change in standard deviation with speed (bottom)

As speed increases roll PDF becomes far more dispersed, manifesting as an increase in standard deviation, as seen in Figure 6-31. The increase in standard deviation is once again consistent with the increase in speed. This is also shown previously in Table 6-6 as the RMS error from the linear fits is equivalent to the standard deviation.

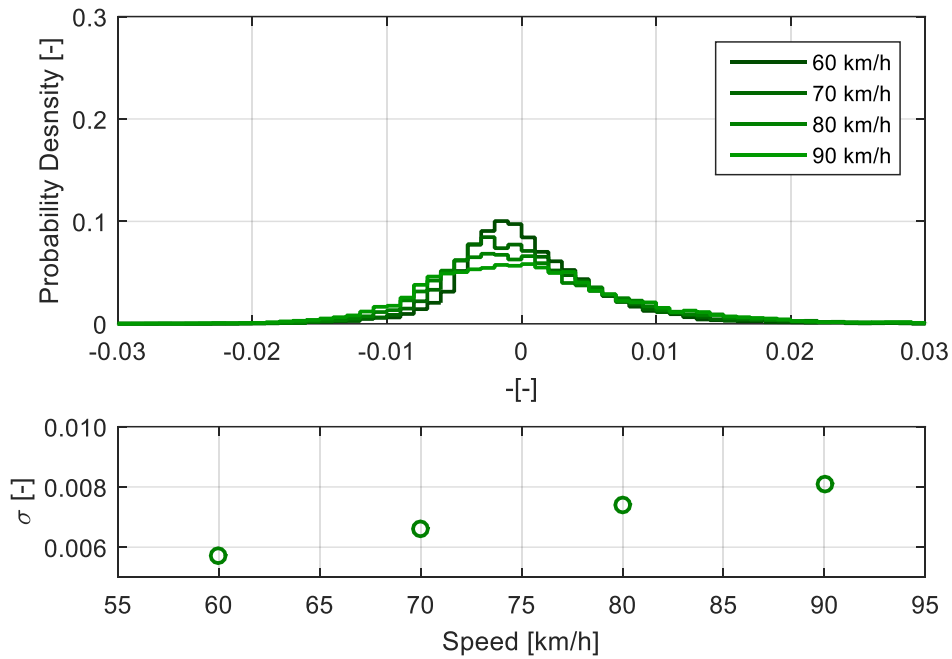


Figure 6-31: A comparison of the probability density functions along the principal axis from the PCA-adjusted vertical acceleration vs roll angular velocity moving RMS scatter plot for VAN1 on Route 1 traveling at speeds between 60 and 90km/h (top) and change in standard deviation with speed (bottom)

Figure 6-32, Figure 6-33 and Figure 6-34 show the PSD functions for heave, pitch and roll response respectively of VAN1 traveling along route 1 and numerous constant speeds. The RMS vertical acceleration increase with speed which is well documented. The RMS levels of pitch and roll angular velocities remain consistent across all speeds. It is of note that the two secondary peaks in the heave PSD function (11 and 22 Hz) align with the secondary peaks within the pitch PSD function, it is believed that the cause of this is the coupling between the heave and pitch vibrational modes.

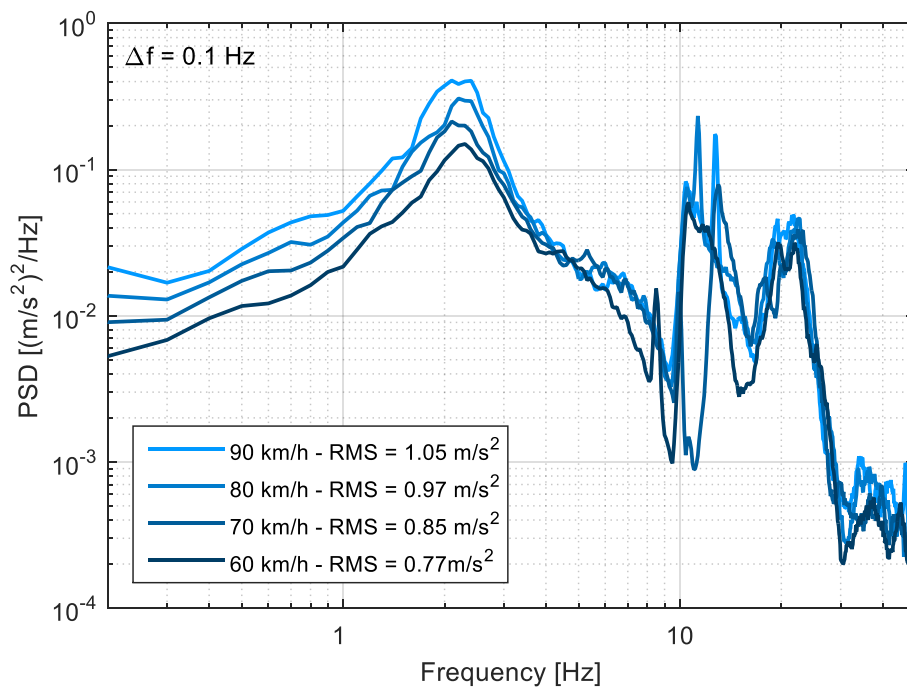


Figure 6-32: A comparison of the vertical acceleration PSD functions for VAN1 on Route 1 traveling at multiple speeds.

The effects of wheelbase filtering can be observed in the pitch PSD function (Figure 6-33) in the troughs located between 6 and 9 Hz. The wheelbase filter frequencies of the specific speed and wheelbase combinations align with the troughs in the pitch PSD functions. The filtering is not evident in the vertical vibration PSD because of the location of the sensor. Wheel imbalance can also be tracked across the speeds, best observed in the roll PSD function, shown Figure 6-34.

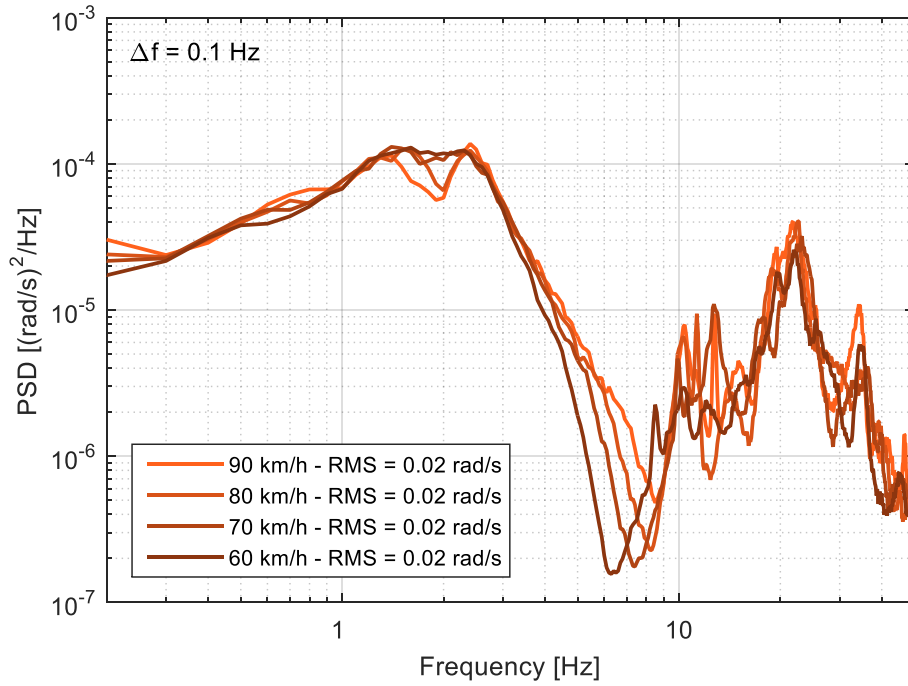


Figure 6-33: A comparison of the pitch angular velocity PSD functions for VAN1 on Route 1 traveling at multiple speeds.

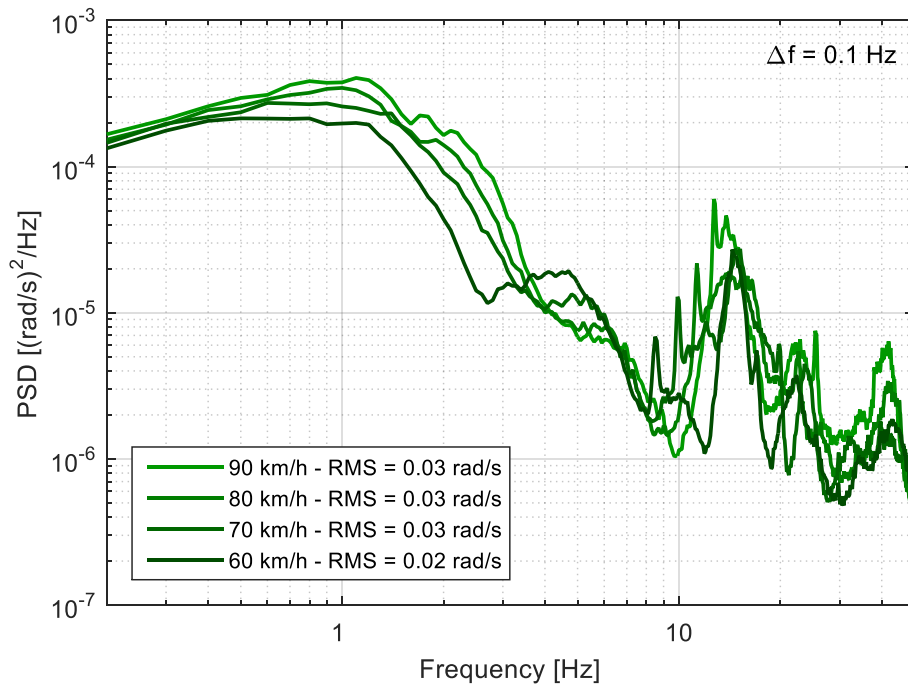


Figure 6-34: A comparison of the roll angular velocity PSD functions for VAN1 on Route 1 traveling at multiple speeds.

The frequency response functions calculated between the vertical vibration and the pitch and roll response are shown in Figure 6-35 and Figure 6-36. The FRFs vary significantly with speed indicating that the change in power is not proportional between the vibratory modes. The flat sections at the beginning of the pitch FRFs evident across all speeds until approximately 1.5 Hz indicates that the pitch angular velocity being a constant factor of the vertical acceleration at low frequencies. The initial flat sections of the FRFs reduce in magnitude until reaching the natural frequency of the sprung mass. The same phenomenon is not evident in the roll FRFs, which remain similar across all speeds.

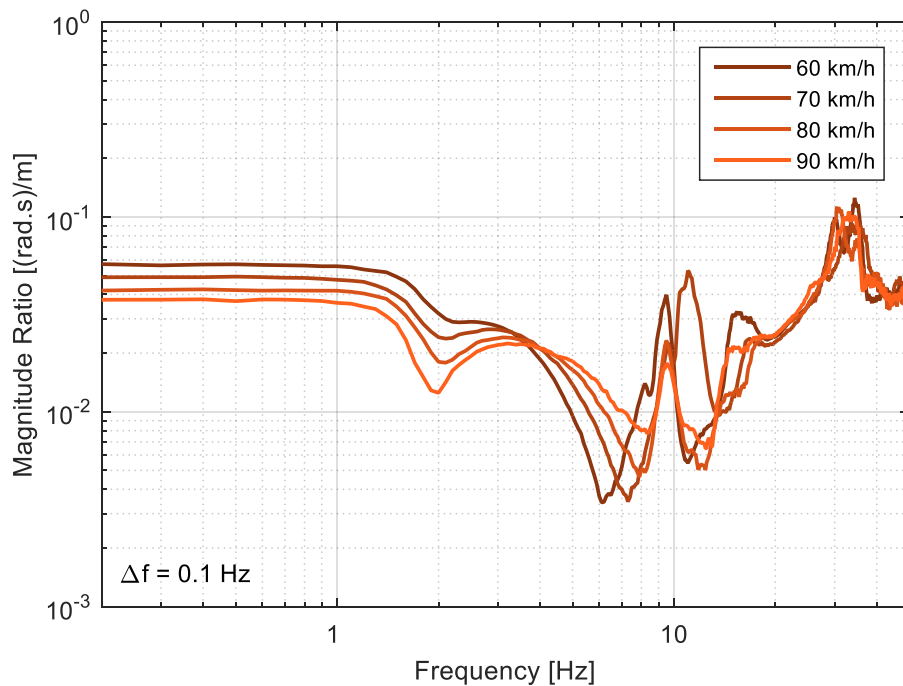


Figure 6-35: A comparison of the frequency response functions between the pitch angular velocity and vertical acceleration for VAN1 on Route 1 traveling at 60 and 90km/h.

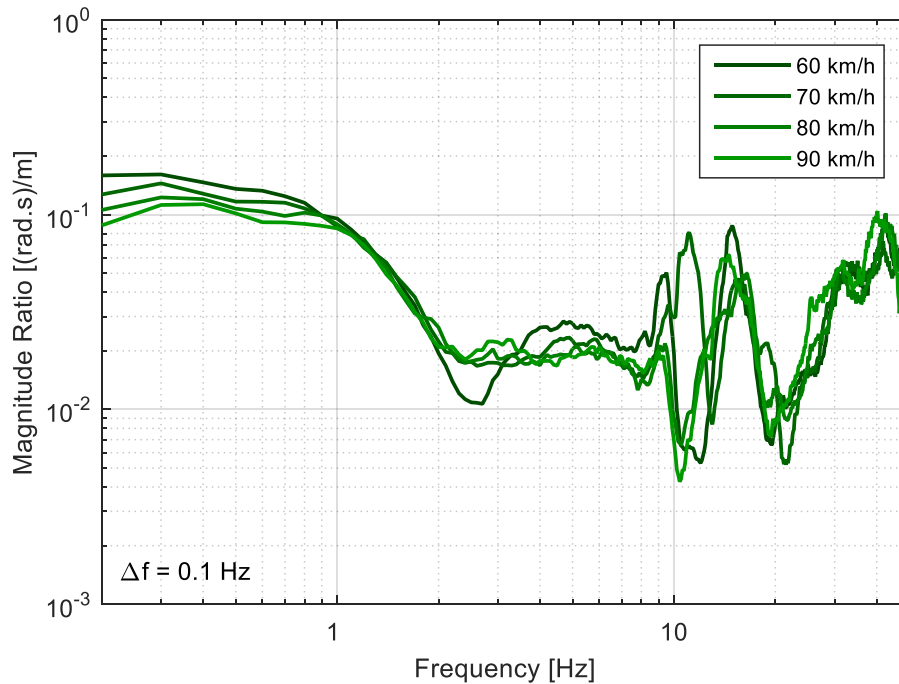


Figure 6-36: A comparison of the frequency response functions between the roll angular velocity and vertical acceleration for VAN1 on Route 1 traveling at 60 and 90km/h.

6.3.2 On the Effects of the Road

To investigate the effects of road topography on the vehicle's response VAN1 was driven at a nominally constant speed along Route 1 (Bacchus Marsh to Geelong) and Route 2 (Sunbury to Romsey). Both roads were subjected to single track topography mapping (Ainalis 2014) around the same time period when the results were collected. The topography mapping revealed that Route 1 was marginally smoother than Route 2, however both roads fall within the B classification according to ISO standards.

Table 6-7 contains a summary of the RMS values obtained from Routes 1 and 2. The vertical acceleration RMS is higher for Route 2, however the pitch and roll RMS remains similar between the different routes. This results in a slight reduction (when compared to the previous section) in the pitch-heave ratios for Route 2, the rougher of the two roads. This is consistent with the results from Section 6.3.1 where an increase in speed (and therefore effective road roughness) was met with a reduction in the pitch-heave ratio. The roll-heave ratio was also reduced however the reduction was small and within the range of the varying speed experiments.

Table 6-7: A table summarising the RMS ratios for VAN1 traveling on multiple roads at 80 km/h.

ID	Route	H_{RMS} [m/s ²]	P_{RMS} [rad/s]	R_{RMS} [rad/s]	P_{RMS}/H_{RMS} [(rad.s)/m]	R_{RMS}/H_{RMS} [(rad.s)/m]
1.1	1	0.9681	0.0223	0.0273	0.0230	0.0282
1.2	2	0.9969	0.0221	0.0273	0.0222	0.0274

A comparison of the RMS vertical acceleration distributions of Routes 1 and 2 are shown in Figure 6-37. A significant difference in the maximum probability density is observed between the routes, although the mode remains similar between the roads. The standard deviation remains consistent between the routes, varying only slightly.

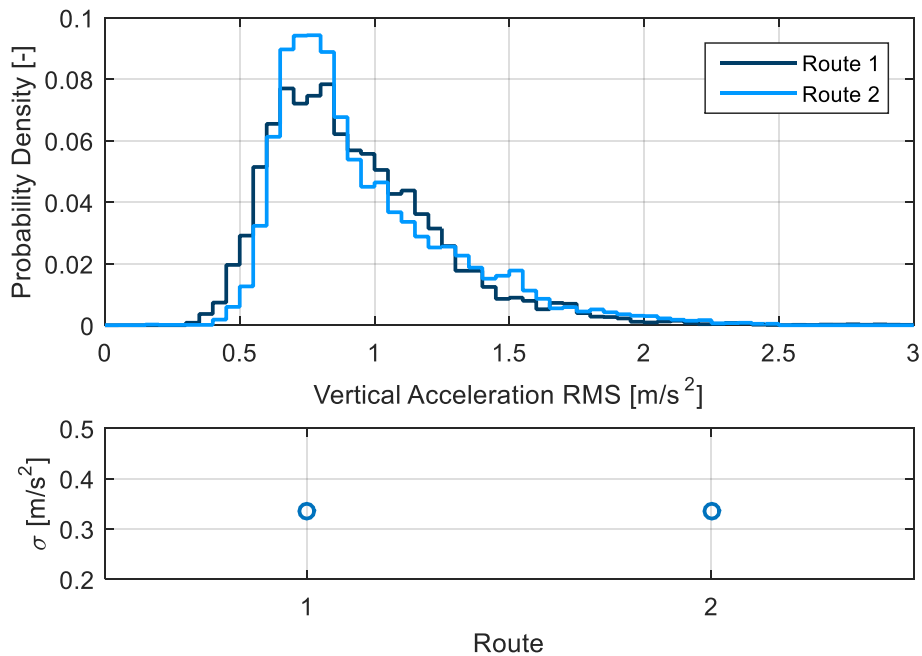


Figure 6-37: A comparison of the probability density function of the RMS vertical acceleration (2 second window, maximum overlap) for VAN1 on Route 1 and 2 traveling at 80km/h (top) and a comparison of the standard deviation on each route (bottom).

Figure 6-38 shows the difference in distribution of the pitch RMS angular velocity when traveling along the Routes 1 and 2. Route 2 once again has a higher maximum probability density, although this is accompanied with a lower mode than Route 1. Route 2 has a marginally larger standard deviation than Route 1.

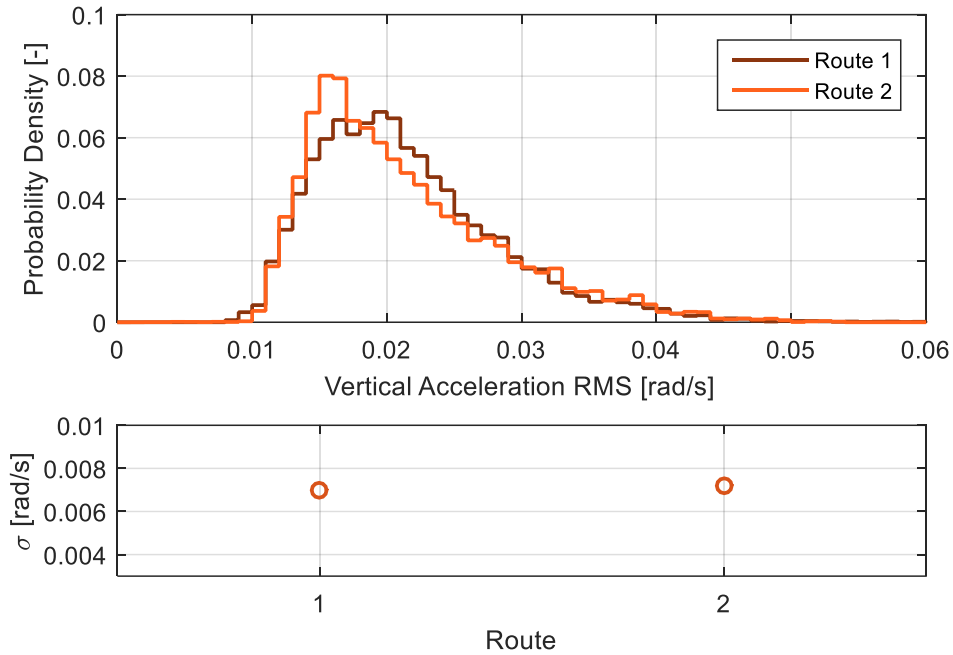


Figure 6-38: A comparison of the probability density function of the RMS pitch angular velocity (2 second window, maximum overlap) for VAN1 on Route 1 and 2 traveling at 80km/h (top) and a comparison of the standard deviation on each route (bottom).

Figure 6-39 shows a comparison of the roll RMS angular velocity PDFs between Routes 1 and 2 when traveling at 80 km/h. The maximum probability density of the roll response remains consistent between the two roads, however the mode of Route 1 is higher than Route 2, indicating that the roll excitation of Route 1 is rougher more frequently. The standard deviation of Route 2 is considerably higher than for Route 1. This is consistent with the results from section 6.3.1, where an increase in effective road roughness causes an increase in the standard deviation of the roll RMS. Unfortunately, it is difficult to determine if this is due purely to the increase in road roughness or if Route 2 has a greater roll excitation due to the road surface topography.

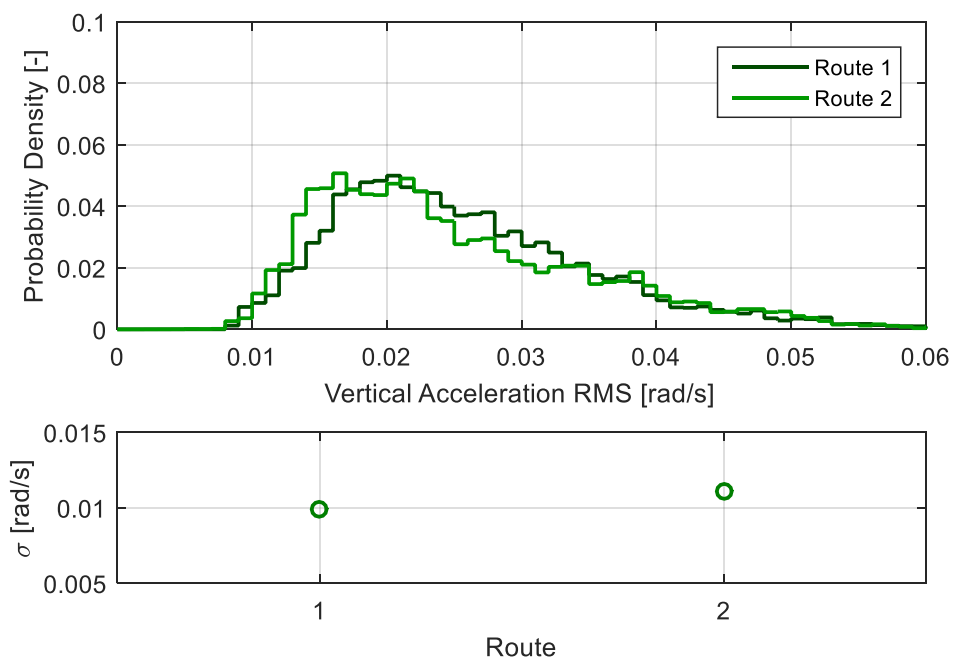


Figure 6-39: A comparison of the probability density function of the RMS roll angular velocity (2 second window, maximum overlap) for VAN1 on Route 1 and 2 traveling at 80km/h (top) and a comparison of the standard deviation on each route (bottom).

A comparison of the heave-pitch bivariate histograms is shown in Figure 6-40. A clear change in probability density occurs between the two roads. This is consistent with the higher probability density of the RMS pitch distribution of Route 2 (shown in Figure 6-38). The gradient appears similar between the two roads, fitted linear models support this observation, with the gradient of both histograms being approximately 0.02 (rad.s)/m. Table 6-8 contains a summary of the linear regression performed on the data. The RMSE for both cases is very similar, demonstrating the strong relationship between heave and pitch, the high R^2 values also indicate that this relationship is of a linear nature.

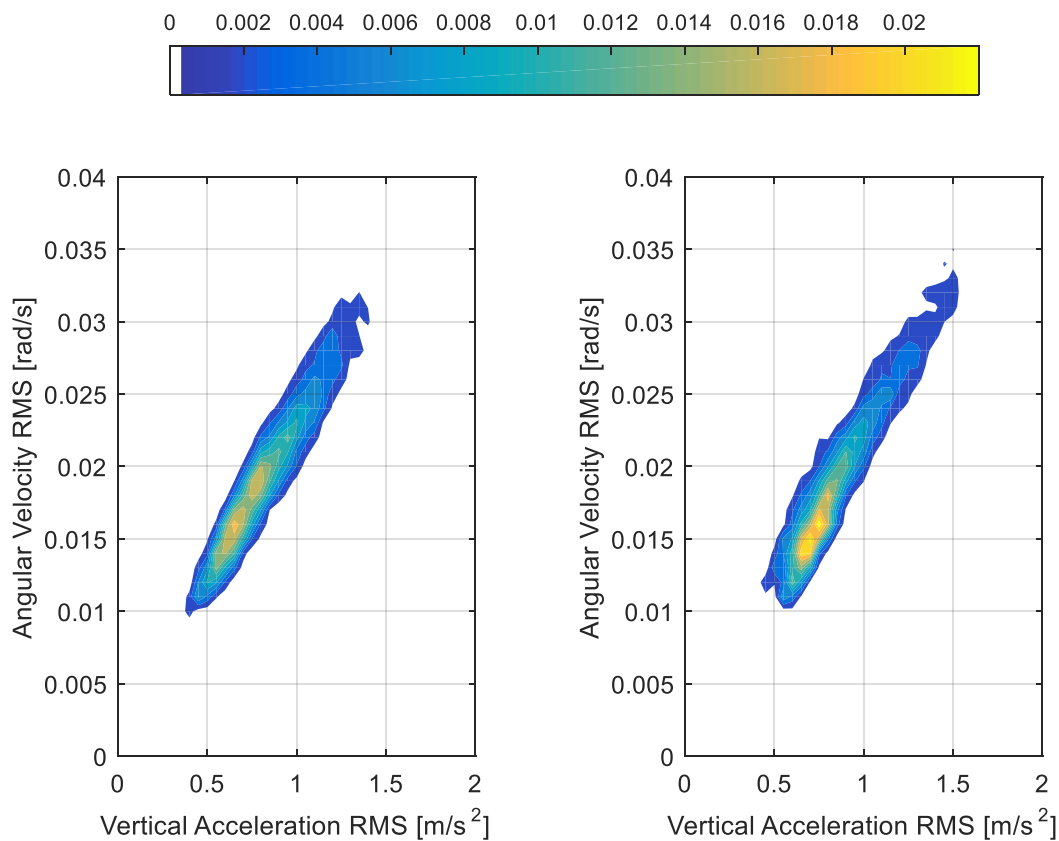


Figure 6-40: Comparison of vertical acceleration - pitch angular velocity bivariate histograms of VAN1 traveling along Route 1 (left) and Route 2 (right) at 80 km/h.

Table 6-8: Summary of the effects of road type upon the pitch vs heave RMS scatter plot.

ID	Route	Gradient	Y-Intercept	R^2	RMSE
1.1	1	0.0198	0.0031	0.8922	0.0023
1.2	2	0.0206	0.0016	0.9082	0.0022

The heave-roll bivariate histograms, shown in Figure 6-41, indicate that the roll response data is more dispersed from Route 1 than Route 2. The histograms reveal that Route 2 as a higher frequency of occurrence of simultaneously high levels of heave and roll than Route 1. A change in gradient of the relationship is observed between the two roads, although the R^2 coefficients returned from the fitted linear models are poor (as shown in Table 6-9), indicating that the relationship is quite weak. The RMSE is comparatively high (to the heave-pitch) but still consistent between the routes.

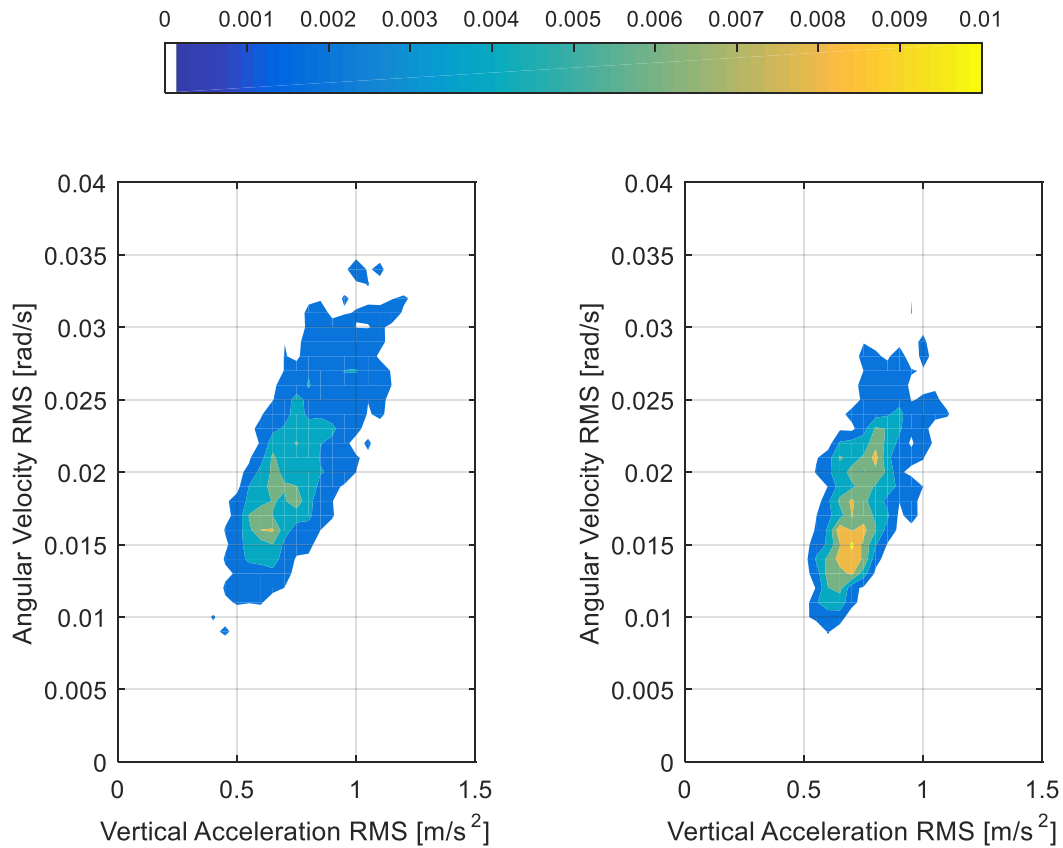


Figure 6-41: Comparison of vertical acceleration - roll angular velocity bivariate histograms of VAN1 traveling along Route 1 (left) and Route 2 (right) at 80 km/h.

Table 6-9: Summary of the linear models fitted to the roll vs heave RMS scatter plots.

ID	Route	Gradient	Y-Intercept	R^2	RMSE
1.1	1	0.0200	0.0073	0.4513	0.0074
1.2	2	0.0242	0.0023	0.5343	0.0076

Figure 6-42 displays the distributions of the heave-pitch (top) and heave-roll (bottom) PCA-adjusted RMS scatter plots for Route 1 and Route 2. Between both routes only a slight change in the distribution of the roll-heave relationship is observed, with both routes having a similar standard deviation (7.5×10^{-3}), remembering that the RMSE of the fitted linear models is equal to the standard deviation. Similarly, the heave-pitch distributions have similar standard deviations (2.2×10^{-3}), but the maximum probability density is lower for Route 2.

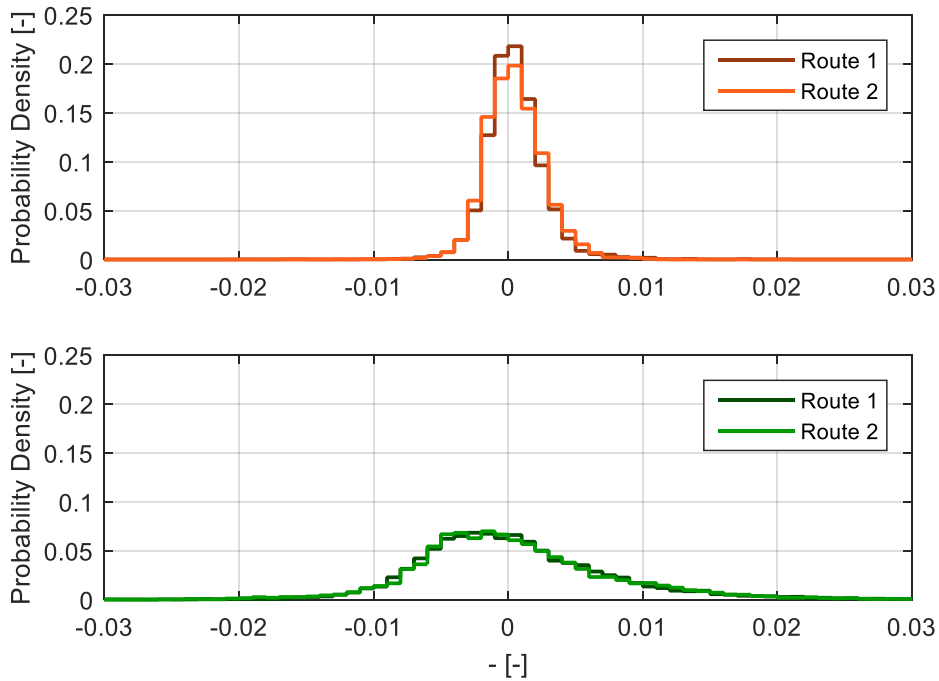


Figure 6-42: A comparison of the probability density function along the principal axis from the PCA-adjusted vertical acceleration vs pitch (top) and roll (bottom) angular velocity RMS scatter plot for VAN1 traveling along Routes 1 and 2 at 80 km/h.

Figure 6-43, Figure 6-44 and Figure 6-45 show the PSD functions for heave, pitch and roll respectively. As mentioned previously Route 2 has higher road surface displacement PSD function than Route 1. This is manifested as a higher RMS vertical acceleration response for the vehicle, when traveling on Route 2. RMS values of pitch and roll remain similar between the routes. The spectral shape for all modes of vibration remains comparable for both routes, however slight differences are visible at all frequencies, due to the logarithmic scale.

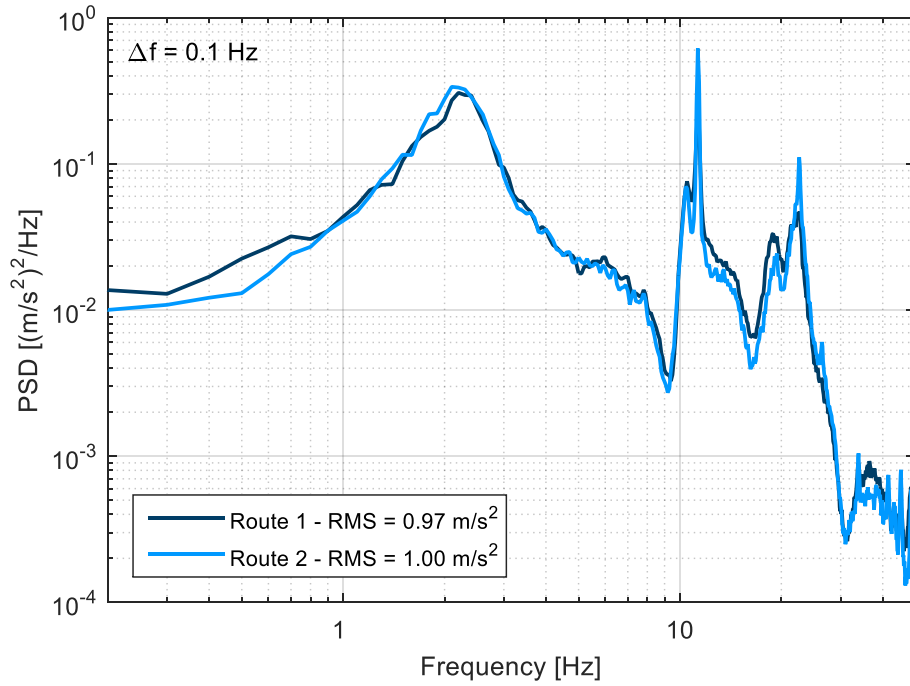


Figure 6-43: A comparison of the vertical acceleration PSD functions for VAN1 traveling along Routes 1 and 2 at 80 km/h.

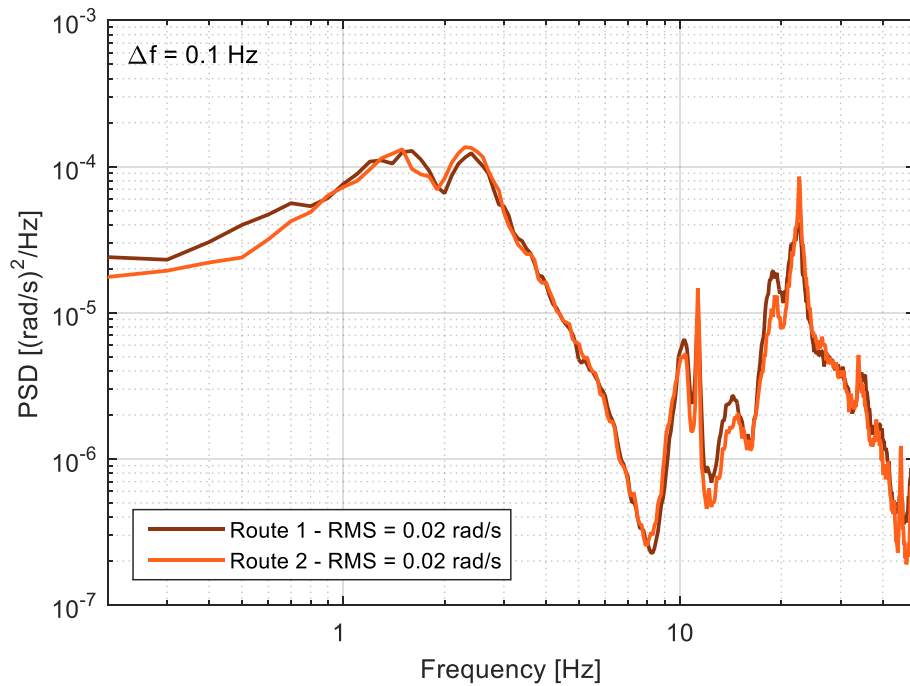


Figure 6-44: A comparison of the pitch angular velocity PSD functions for VAN1 traveling along Routes 1 and 2 at 80 km/h.

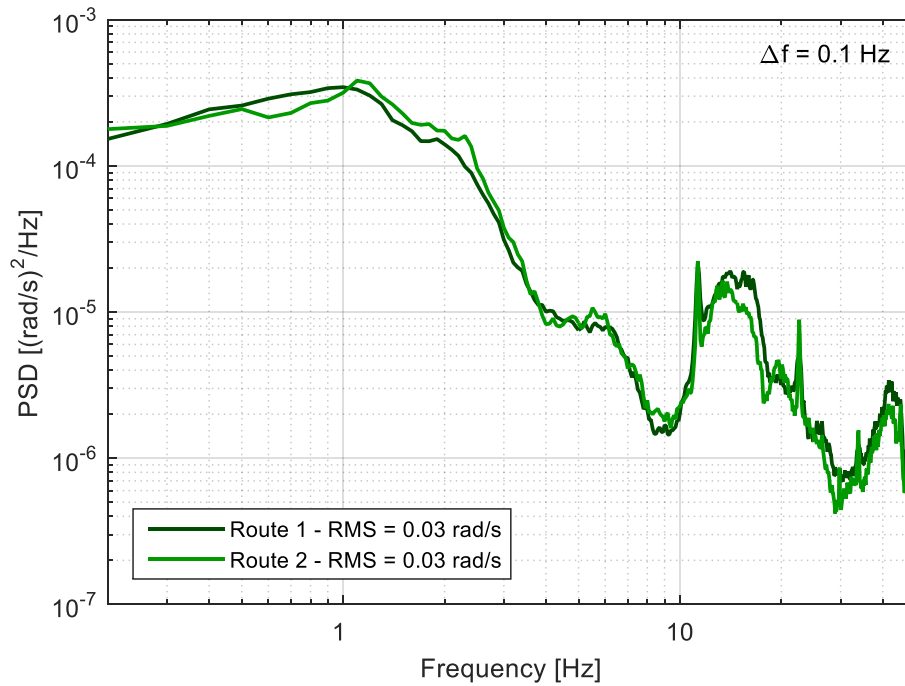


Figure 6-45: A comparison of the roll angular velocity PSD functions for VAN1 traveling along Routes 1 and 2 at 80 km/h.

Figure 6-46 shows that the FRF of taken between the vertical acceleration and pitch angular velocity is independent of road roughness (for small changes). The difference in roughness between Routes 1 and Route 2 did not manifest in a significant change to the appearance of FRF, however the AUC shows a slight difference. The AUC increases from 46.33 for Route 1, to 51.35 for Route 2. Similar differences AUC values occur in the heave-roll FRFs, shown in Figure 6-47, with Route 1 having an AUC of 48.16 and Route 2 returning a value of 53.87. Larger AUC vales indicate a lower ratio between the vibratory modes. The similar AUC values show that when roads are truly random, as are the two roads, they have no influence on the heave, pitch and roll relationships.

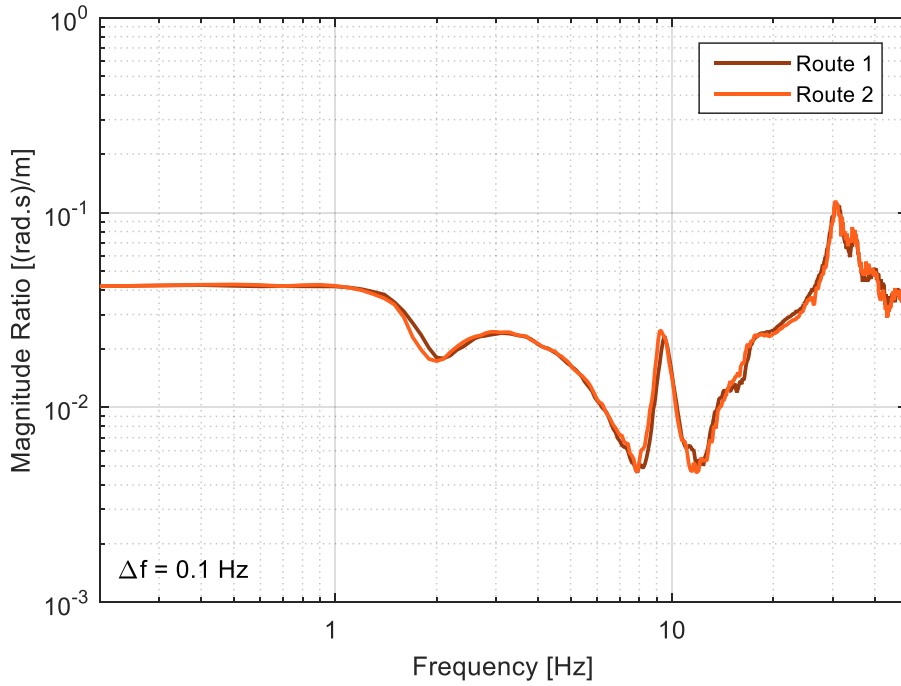


Figure 6-46: A comparison of the frequency response functions between the pitch angular velocity and vertical acceleration for VAN1 traveling along Routes 1 and 2 at 80 km/h.

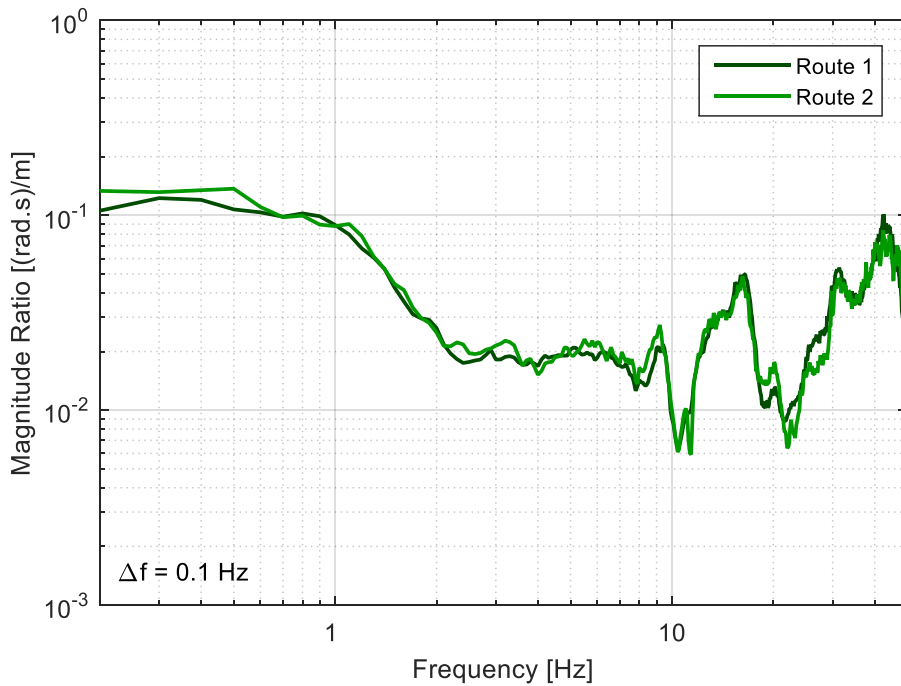


Figure 6-47: A comparison of the frequency response functions between the roll angular velocity and vertical acceleration for VAN1 traveling along Routes 1 and 2 at 80 km/h.

6.3.3 On the Effects of Carrying a Payload

Anybody who has driven a transport vehicle knows the drastic effects the payload can have on a vehicle's handling and performance. Adding a payload influences many vehicles properties; the sprung mass, CG location and MOI change, as wells as the vehicle's acceleration, braking and cornering performance. As it is prohibitively difficult to isolate the effects of payload mass alone using physical experiments, this section focuses on the effects that the addition of a payload, as a whole, has on the heave, pitch and roll relationships. An estimation of the change in vehicle properties is shown in Table 6-10, the process used to estimate the values is shown in section 7.3.3.

Table 6-10: Summary of the estimated mass and inertial properties of the sprung mass for the different loading configurations.

ID	Payload [kg]	CG location [m]			MOI [kg.m ²]		Sprung Mass [kg]
		F-B	L-R	height	I _x	I _y	
2.1	0	1.16	0.75	0.69	474	2681	1256
2.2	570	1.75	0.75	0.92	827	4465	1826

To investigate the effects of the addition of a payload, UTE1 was driven along Route 3 at 70 km/h, firstly unloaded (0 kg payload) and then carrying a 570 kg palletised payload directly over the rear axle. A summary of the pitch:heave and roll:heave RMS ratios is contained within Table 6-11. A significant drop in both the pitch:heave and roll:heave ratios occurs with the addition of the 570 kg payload.

Table 6-11: A table summarising the RMS ratios for the different loading configurations of UTE1 traveling along Route 3 at 70 km/h.

ID	Payload [kg]	H _{RMS} [m/s ²]	P _{RMS} [rad/s]	R _{RMS} [rad/s]	P _{RMS} /H _{RMS} [(rad.s)/m]	R _{RMS} /H _{RMS} [(rad.s)/m]
2.1	0	1.1536	0.0424	0.0279	0.0368	0.0242
2.2	570	1.4378	0.0274	0.0251	0.0191	0.0175

The distributions of the moving RMS vertical acceleration for both configurations are shown in Figure 6-48. A significant increase in the mode occurs with the addition of the payload, however this is met with a decrease in the maximum probability density. Despite this, the standard deviation remains consistent when both loaded and unloaded.

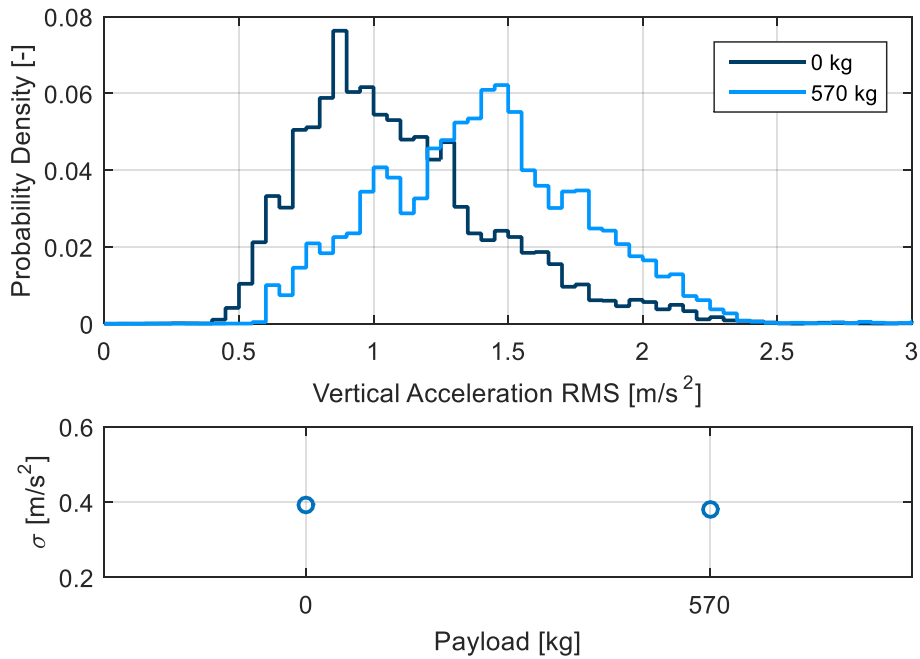


Figure 6-48: A comparison of the probability density functions of the RMS vertical acceleration (2 second, window maximum overlap) for UTE1 traveling along Route 3 (at 70 km/h) carrying a 0 kg payload and a 570 kg payload (top) and a comparison of the standard deviation for each payload (bottom).

Similarly, the distributions of pitch RMS angular velocity (Figure 6-49) changes drastically with the addition of the 570 kg payload. The mode decreases significantly when the payload is added, and so does the standard deviation, as the distribution becomes skewed towards lower levels of pitch response.

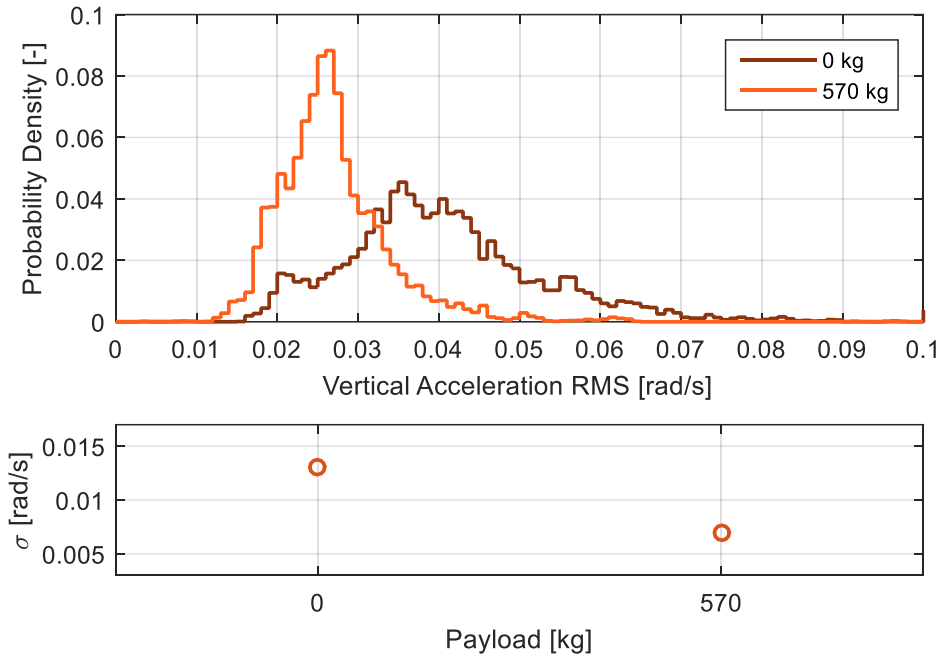


Figure 6-49: A comparison of the probability density function of the RMS angular velocities (2 second, window maximum overlap) of pitch and roll for UTE1 traveling along Route 3 (at 70 km/h) carrying a 0 kg payload and a 570 kg payload (top) and a comparison of the standard deviation for each payload (bottom).

The distribution of the roll RMS angular velocity (Figure 6-49) does not change as significantly as the heave and pitch distributions. A decrease in maximum probability density is observed however the mode remains similar. The standard deviation does decrease, although not to the same level the pitch response.

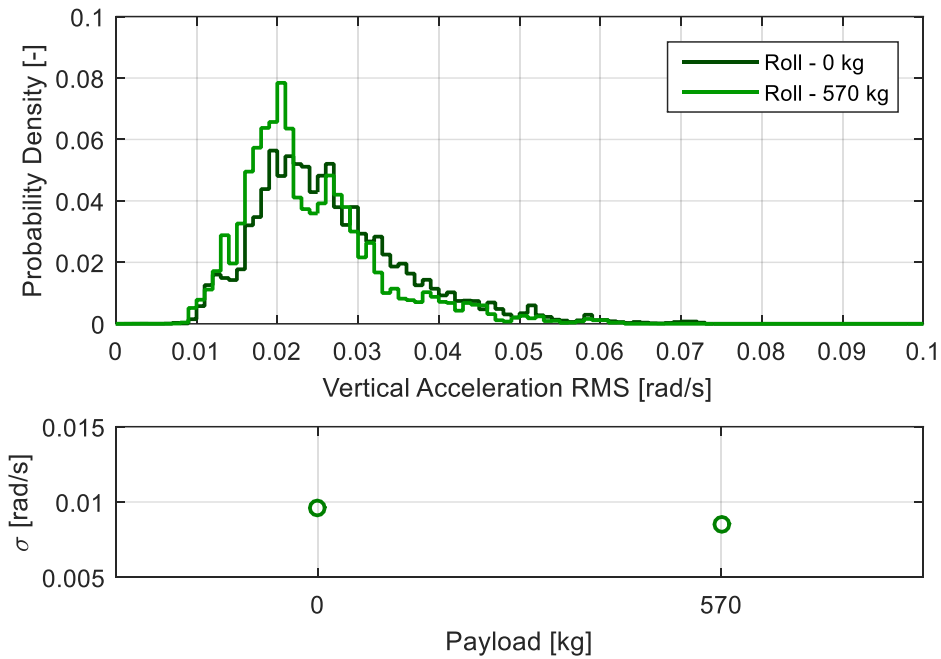


Figure 6-50: A comparison of the probability density function of the RMS angular velocities (2 second, window maximum overlap) of pitch and roll for UTE1 traveling along Route 3 (at 70 km/h) carrying a 0 kg payload and a 570 kg payload (top) and a comparison of the standard deviation for each payload (bottom).

Figure 6-51 displays a comparisons of the bivariate histograms for UTE1 traveling along Route 3 unloaded (left) and caring a 570 kg payload (right). A significant change in slope is observed dropping from 32.1 to 12.7 (mrad.s)/m. When unloaded the fitted linear model returns a high R^2 value of 0.91 however with the addition of the load this falls to 0.48, the RMSE increases concurrently. A summary of the fitted linear models is shown in Table 6-12. The cause of these changes is difficult to identify from the physical experiments due to the payload varying many vehicle characteristics.

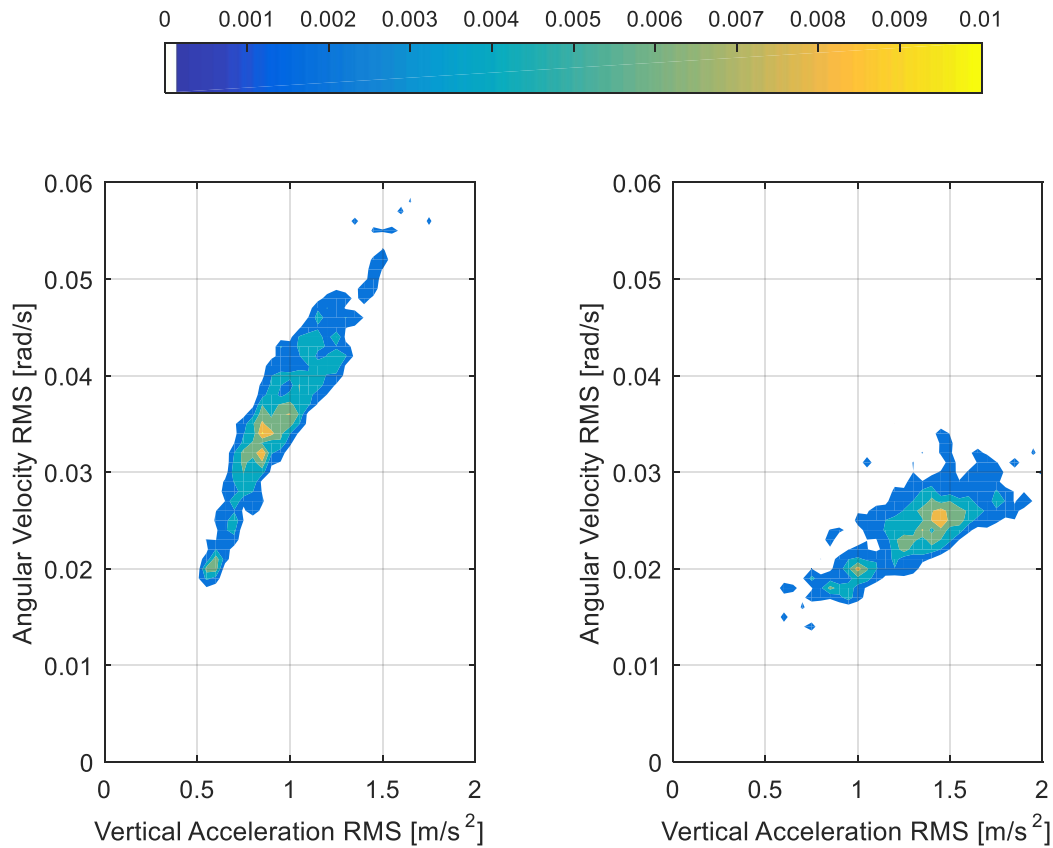


Figure 6-51: Comparison of vertical acceleration - pitch angular velocity bivariate histograms of UTE1 traveling along Route 3 at 70 km/h with 0 kg payload (left) and a 750 kg (right).

Table 6-12: Summary of the linear models fitted to the pitch vs heave RMS scatter plots.

ID	Payload [kg]	Gradient	Y-Intercept	R^2	RMSE
2.1	0	0.0321	0.0055	0.9133	0.0039
2.2	570	0.0127	0.0089	0.4811	0.0050

The heave-roll bivariate histograms, shown in Figure 6-52, have deteriorated considerably from the comet dust trail-esque distributions from the road and speed experiments. Similarly to the heave-pitch bivariate histogram, the gradient of the heave-roll RMS data cloud reduces, however the R^2 values of the fitted linear models are incredibly low (Table 6-13) indicating that the data cannot be represented by a linear model with as much confidence.

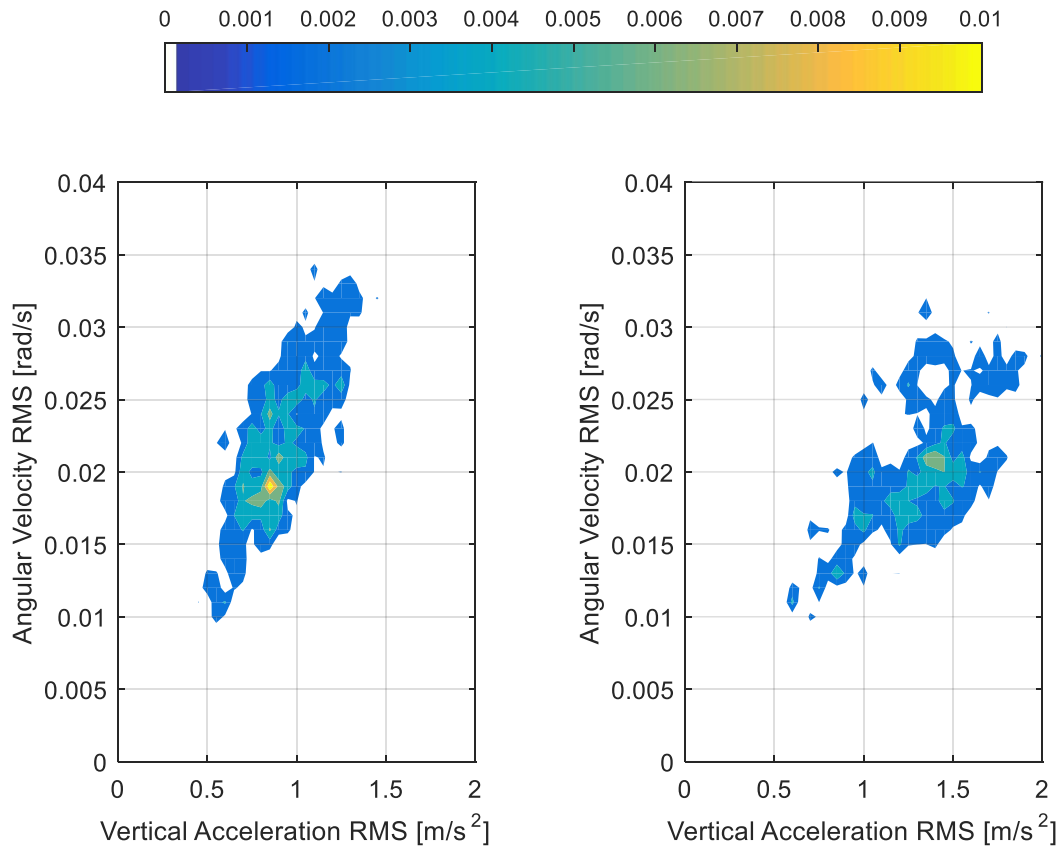


Figure 6-52: Comparison of vertical acceleration - roll angular velocity bivariate histograms of UTE1 traveling along Route 3 at 70 km/h with 0 kg (left) and a 750 kg (right) payload.

Table 6-13: Summary of the linear models fitted to the roll vs heave RMS scatter plots.

ID	Payload [kg]	Gradient	Y-Intercept	R^2	RMSE
2.1	0	0.0195	0.0051	0.6280	0.0058
2.2	570	0.0122	0.0067	0.2976	0.0071

The distributions of the PCA-adjusted data is shown in Figure 6-53. For all case the addition of the 570 kg payload saw a slight decrease in the median RMS. The standard deviation also increased marginally with the addition of the payload.

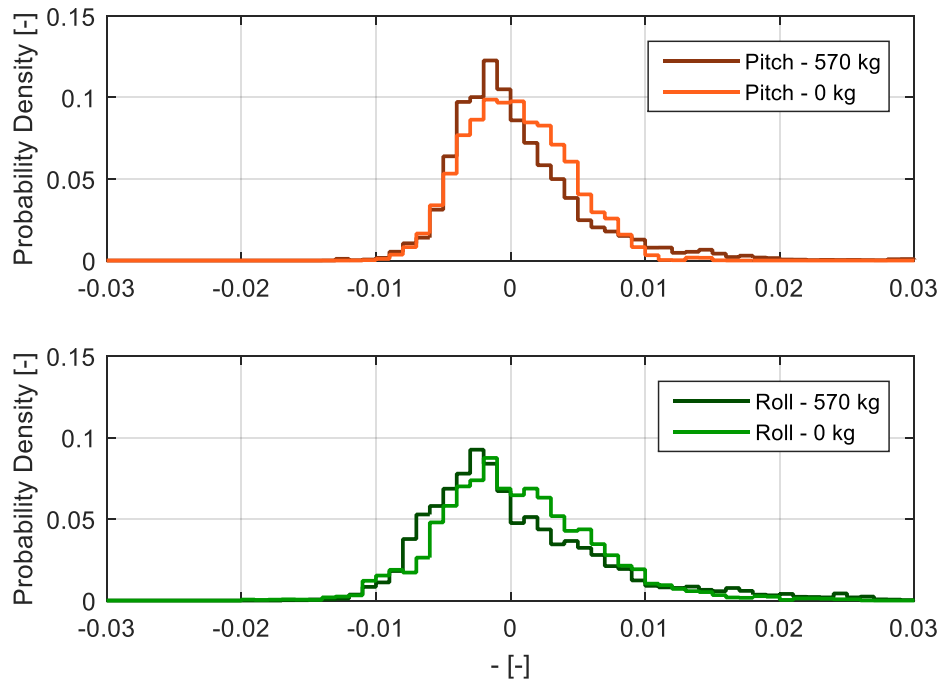


Figure 6-53: A comparison of the probability density function along the principal axis from the PCA-adjusted vertical acceleration vs pitch (top) and roll (bottom) angular velocity RMS scatter plot for UTE1 traveling along Route 3 at 70 km/h carrying a 0 kg payload and a 570 kg payload.

The PSD functions of the vertical acceleration from Configurations 2.1 and 2.4 are shown in Figure 6-54. When unloaded UTE1 is excessively damped (ζ is large) as it is designed to be optimally damped when carrying a payload, this is one possible explanation of the significantly higher energy contained within the 2-20 Hz band, remembering that rigid-body ride vibration falls within the 0-25 Hz bandwidth (Gillespie 1992). The prominent peak observed at around 40 Hz with the 570 kg payload on board is believed to be caused by resonance of the load tray. The higher RMS of the loaded configuration is due to this higher frequency content.

The pitch angular velocity PSD function, shown in Figure 6-55, shares the same characteristics as the vertical acceleration PSD function. Significantly more energy is contained above 2 Hz when unloaded, however the higher energy band extends to 35 Hz. Again a peak is observed at 40 Hz when loaded.

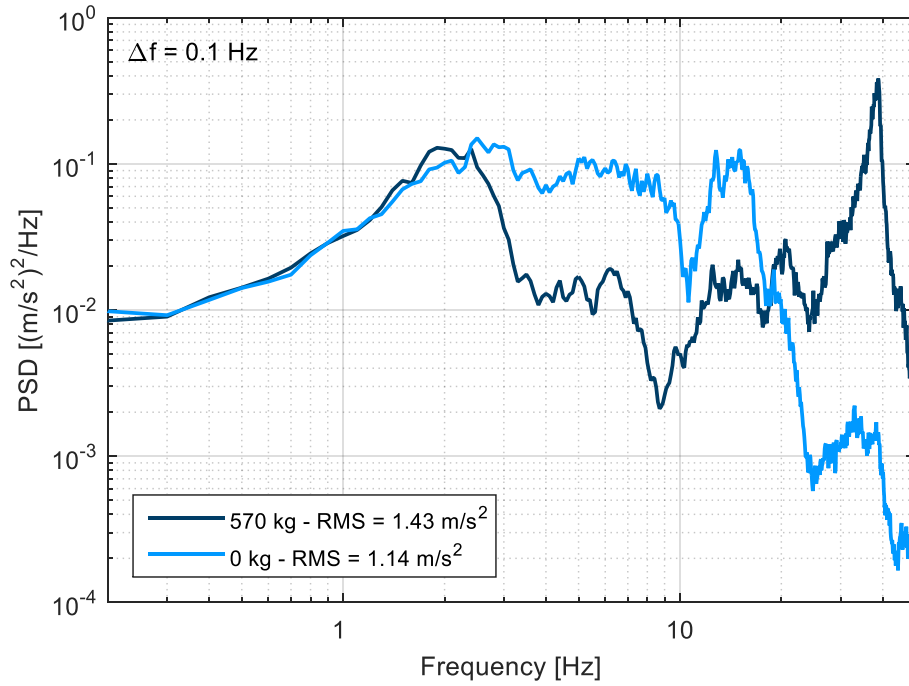


Figure 6-54: A comparison of the vertical acceleration PSD functions for UTE1 traveling along Route 3 (at 70 km/h) carrying a 0 kg payload and a 570 kg payload.

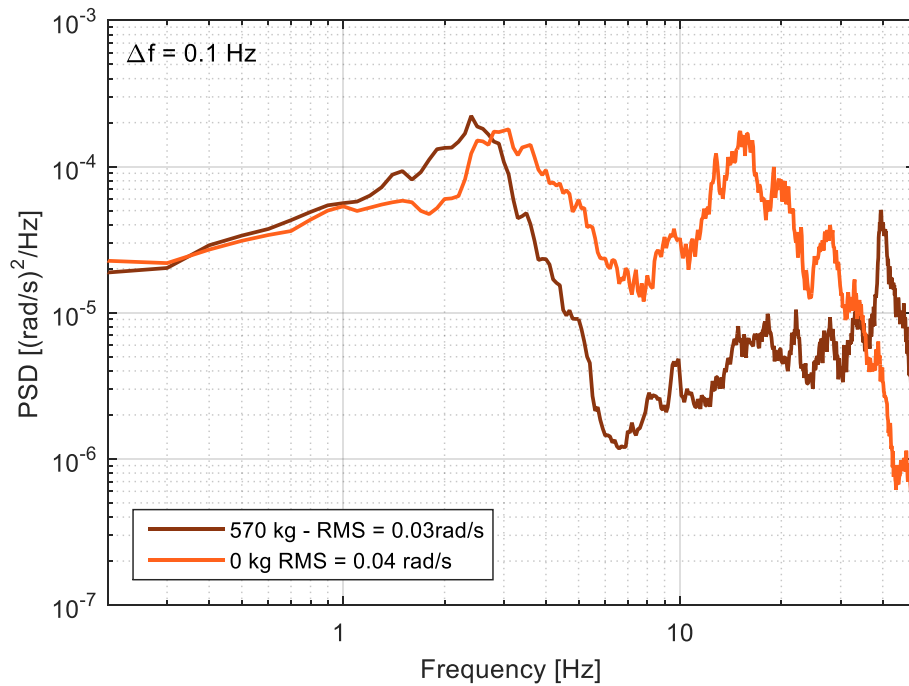


Figure 6-55: A comparison of the pitch angular velocity PSD functions for UTE1 traveling along Route 3 (at 70 km/h) carrying a 0 kg payload and a 570 kg payload.

Figure 6-56 shows a comparison of the roll angular velocity PSD functions for the two configurations. Once more the unloaded configuration contains higher energy at lower frequencies (approximately 1.5– 5 Hz), although the difference between the configurations is not as large.

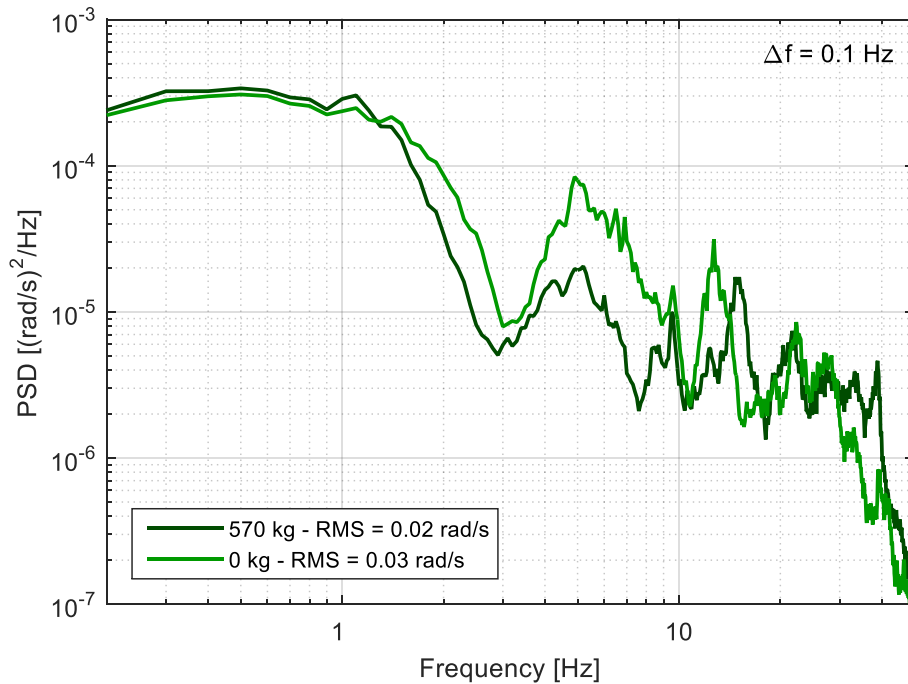


Figure 6-56: A comparison of the roll angular velocity PSD functions for UTE1 traveling along Route 3 (at 70 km/h) carrying a 0 kg payload and a 570 kg payload.

Figure 6-57 and Figure 6-58 show a comparisons of the heave-pitch and heave-roll FRFs respectively. In both cases the FRFs remain the same below 1 Hz however above that the FRFs share little similarity. This demonstrates that the addition of the payload affects each vibratory mode differently. This is not unexpected due to the large number of vehicle characteristics adding a payload changes.

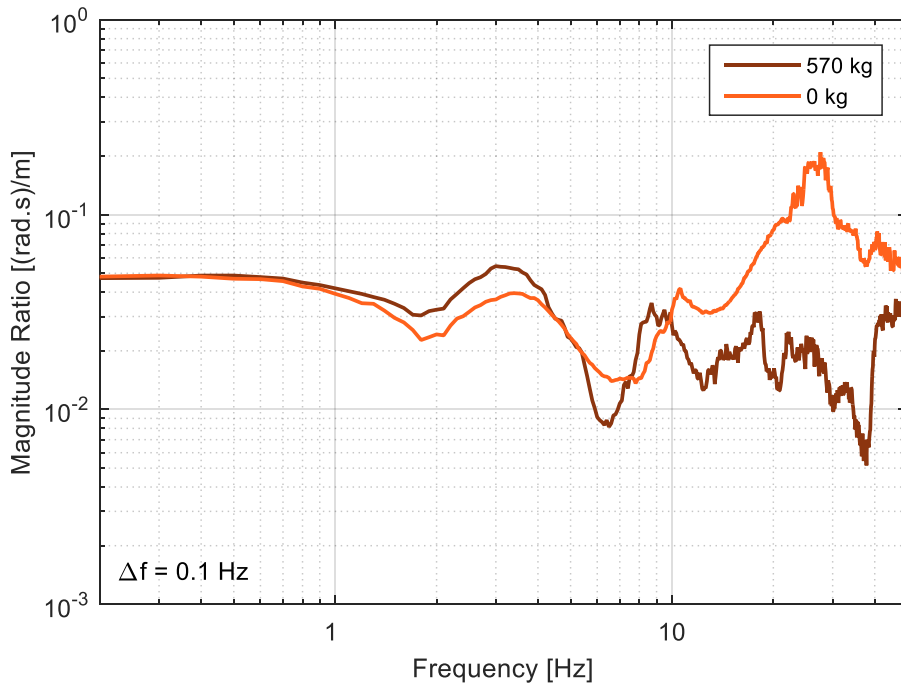


Figure 6-57: A comparison of the frequency response functions between the pitch angular velocity and vertical acceleration for UTE1 traveling along Route 3 (at 70 km/h) carrying a 0 kg payload and a 570 kg payload.

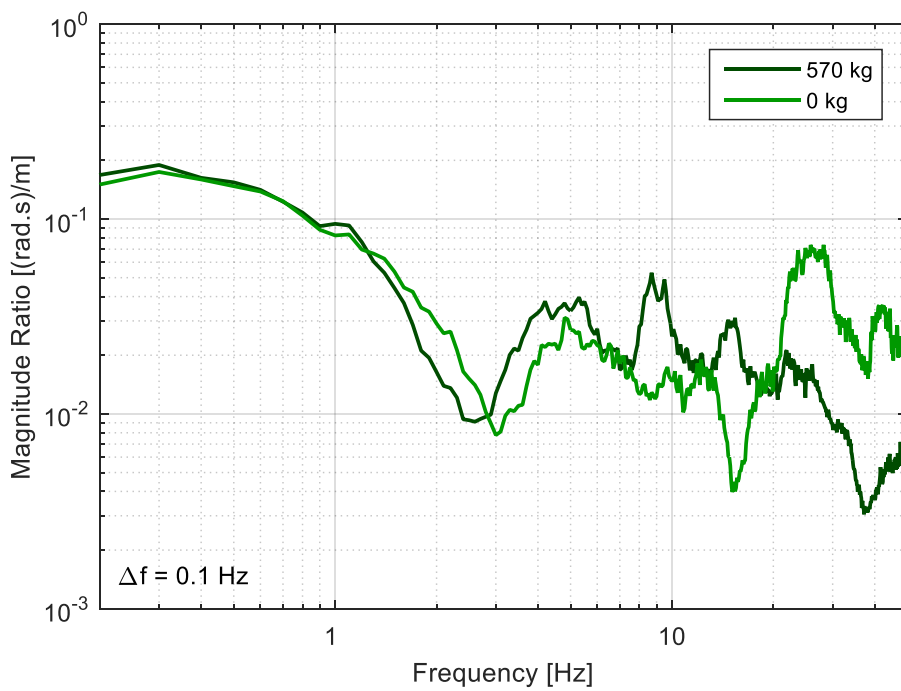


Figure 6-58: A comparison of the frequency response functions between the roll angular velocity and vertical acceleration for UTE1 traveling along Route 3 (at 70 km/h) carrying a 0 kg payload and a 570 kg payload.

6.3.4 On the Effects of Payload Inertial Properties

To isolate some of the effects encountered when adding a payload to the vehicle, a series of experiments were undertaken where only the vehicles moments of inertia and CG height varied. The experimental setup can be seen in Figure 6-59, varying the mass distribution properties was achieved by using approximately 300 kg of lead weights (indicated with the highlighted red box) and a number of wooden pallets. The lead weights were spaced up and down using the pallets, with the remaining pallets placed on top to maintain the same payload mass. Estimates of the vehicles inertial characteristics is shown in Table 6-14. Although changes in I_x and I_y are small, they were the largest changes possible that was deemed safe.



Figure 6-59: Photograph of the experimental setup for varying the payloads inertial properties. Red box highlights 300 kg of lead weights.

Table 6-14: Estimates of the inertial properties of the sprung mass for each configuration

ID	CG height [m]	Pallets Bellow	I_x - Roll [kg.m ²] (%)	I_y - Pitch [kg.m ²] (%)
2.2	0.92	1	827 (0)	4465 (0)
2.3	0.95	3	878 (6)	4517 (1)
2.4	0.98	5	959 (16)	4598 (3)

Table 6-15 contains a summary of the RMS characteristics of the three experimental runs. Despite the sequential increase in centre of gravity height and moments of inertia there is no consistent increase in the RMS ratios. Both the pitch-heave and roll-heave ratios remaining similar for all configurations.

Table 6-15: A table summarising the RMS ratios for the different loading configurations of UTE1 traveling along Route 3 at 70 km/h.

ID	CG height [m]	H _{RMS} [m/s ²]	P _{RMS} [rad/s]	R _{RMS} [rad/s]	P _{RMS} /H _{RMS} [(rad.s)/m]	R _{RMS} /H _{RMS} [(rad.s)/m]
2.2	0.92	1.4378	0.0274	0.0251	0.0191	0.0175
2.3	0.95	1.5414	0.0325	0.0259	0.0211	0.0168
2.4	0.98	1.4764	0.0292	0.0253	0.0198	0.0171

Figure 6-60 shows a comparison of the RMS vertical acceleration distributions for different configurations. Across all CG heights the distributions remain similar with slight variations in the median RMS level. The standard deviation remains similar through all configurations.

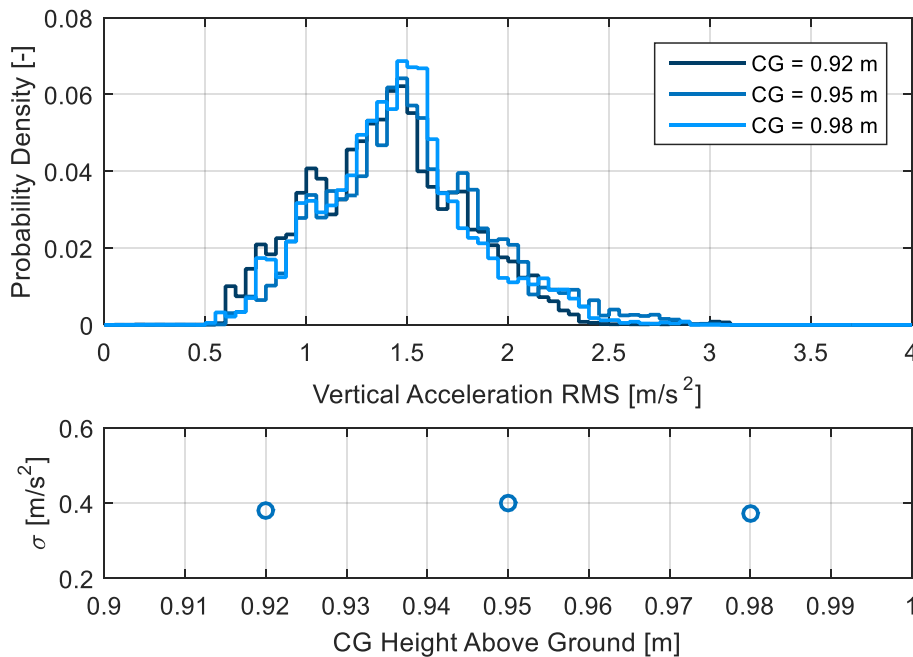


Figure 6-60: A comparison of the probability density functions of the RMS vertical acceleration (2 second, window maximum overlap) for UTE1 traveling along Route 3 (at 70 km/h) carrying a 570 kg payload with varying CG heights (top) and a comparison of the standard deviation for each height (bottom).

Significant differences are apparent between the RMS pitch angular velocity distributions (Figure 6-61) when the CG height is varied. These changes do not change consistently as the CG height is raised. The maximum probability density is similar between the 0.98 m and 0.95 m CG heights, although the mode is different. The mode is the same for the 0.98 and 0.92 m CG heights but the maximum probability density is increased. The standard deviation also varies between the configurations randomly.

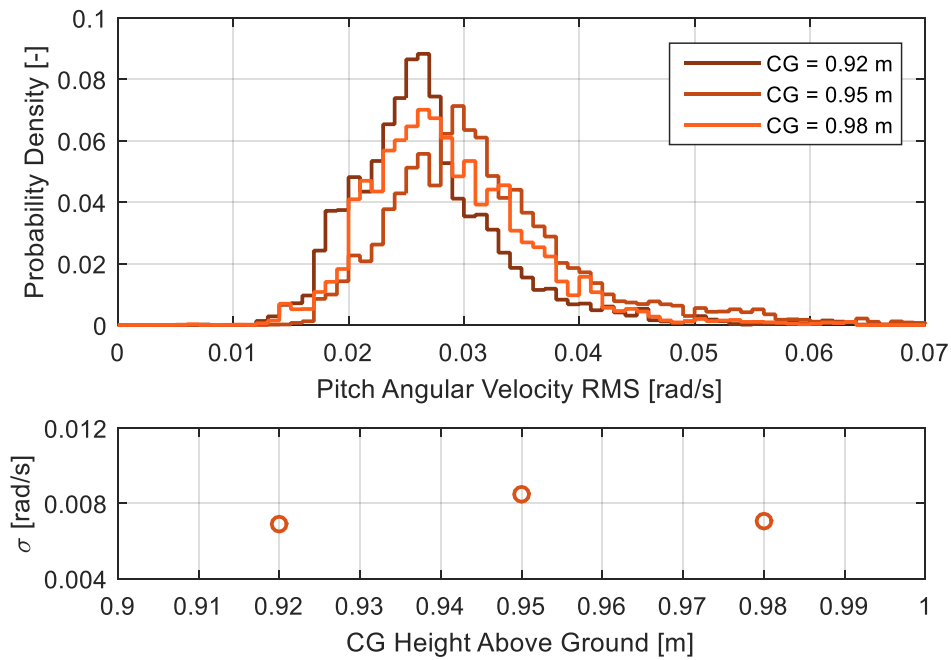


Figure 6-61: A comparison of the probability density functions of the RMS pitch angular velocity (2 second, window maximum overlap) for UTE1 traveling along Route 3 (at 70 km/h) carrying a 570 kg payload with varying CG heights (top) and a comparison of the standard deviation for each height (bottom).

The distribution of the roll angular velocity moving RMS remained similar with the change in CG height, as shown in Figure 6-62. The mode remained the similar between the configurations, although the standard deviation varied inconsistently.

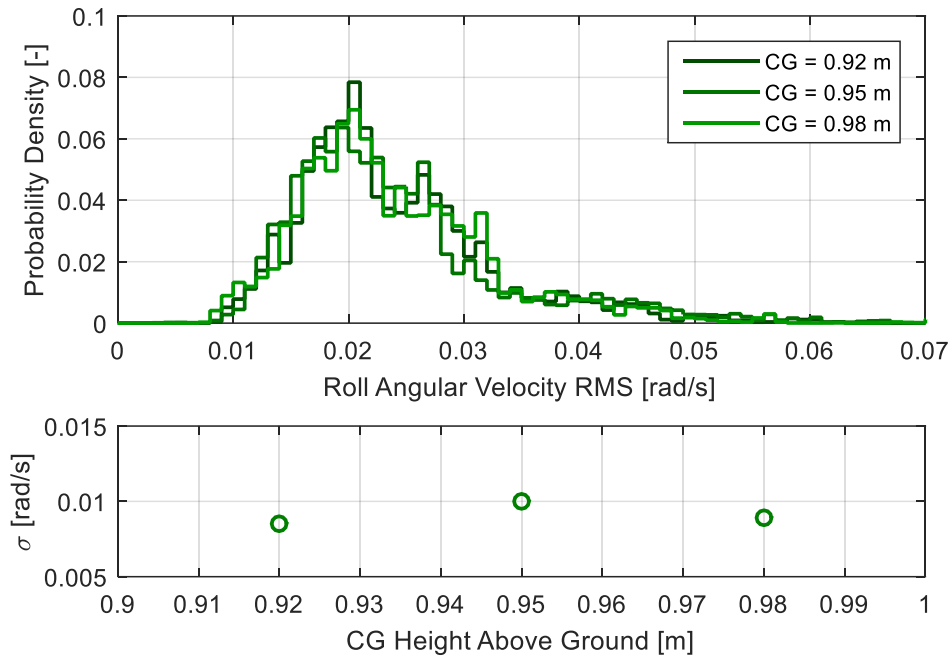


Figure 6-62: A comparison of the probability density functions of the RMS roll angular velocity (2 second, window maximum overlap) for UTE1 traveling along Route 3 (at 70 km/h) carrying a 570 kg payload with varying CG heights (top) and a comparison of the standard deviation for each height (bottom).

A comparison of the heave-pitch bivariate histograms for configurations 2.2 and 2.4 is shown in Figure 6-63. In both cases the range of vertical acceleration remains similar, with the cloud shifting towards higher levels of pitch angular velocity with the higher CG of configuration 2.4. A change in gradient is seen between the two configurations, however the slope change appears arbitrarily across the different configurations as seen in Table 6-16. A summary of the fitted linear models is shown in Table 6-16, for all configurations the linear estimates are poor, indicated by the R^2 values. The RMSE remains similar between the experiments.

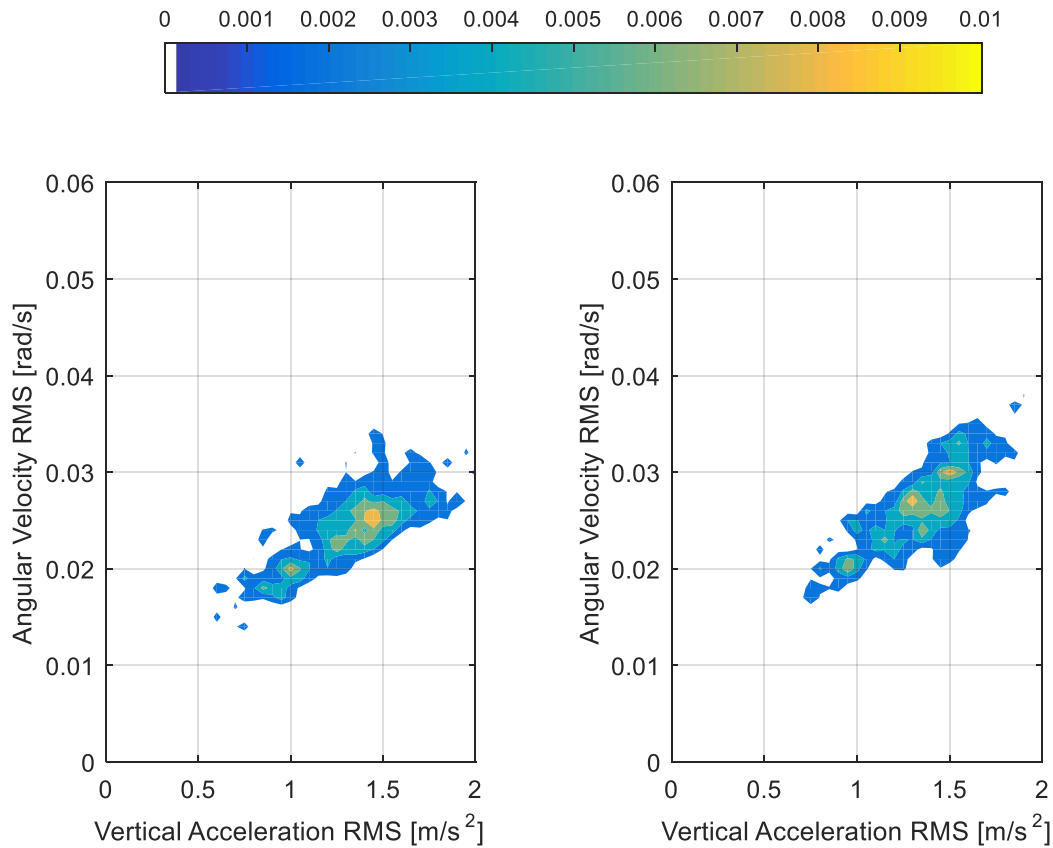


Figure 6-63: Comparison of vertical acceleration - pitch angular velocity bivariate histograms of UTE1 traveling along Route 3 (at 70 km/h) carrying a 570 kg payload with minimum centre of gravity height (left) and maximum centre of gravity height (right).

Table 6-16: Summary of the fitted linear models of the heave-pitch RMS scatter plot for differing payload mass distributions.

ID	CG height		Y-Intercept	R^2	RMSE
	[m]	Gradient			
2.2	0.92	0.0127	0.0089	0.4811	0.0050
2.3	0.95	0.0165	0.0069	0.6036	0.0053
2.4	0.98	0.0145	0.0076	0.5844	0.0045

The heave-roll bivariate histograms remain similar between the configurations, as shown in Figure 6-64. It is difficult to discern the slope of the relationship visually due the scattered appearance, fitted linear regression models also struggle; returning extremely poor R^2 values. A summary of the linear regression models is shown in Table 6-17. The estimated gradients fluctuate randomly across the three tests, although this may be a result of the poor accuracy of the models.

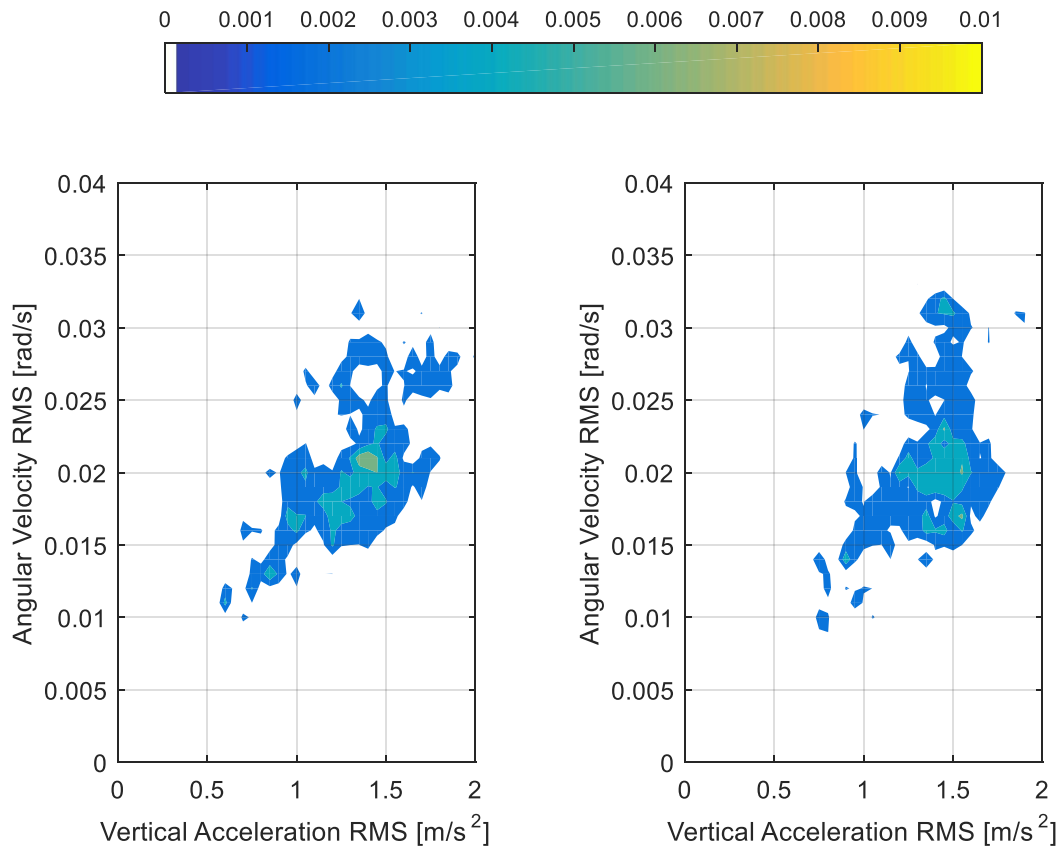


Figure 6-64: Comparison of vertical acceleration - roll angular velocity bivariate histograms of UTE1 traveling along Route 3 (at 70 km/h) carrying a 570 kg payload with minimum centre of gravity height (left) and maximum centre of gravity height (right).

Table 6-17: Summary of the fitted linear models of the heave-roll RMS scatter plot for differing payload mass distributions.

ID	CG height [m]	Gradient	Y-Intercept	R^2	RMSE
2.2	0.92	0.0122	0.0067	0.2976	0.0071
2.3	0.95	0.0143	0.0026	0.3316	0.0081
2.4	0.98	0.0129	0.0053	0.2899	0.0075

The inability to fit accurate linear models to the data cloud impacts the use of PCA as it also relies upon linear representation of the data. Figure 6-65 shows a comparison of the PCA-adjusted heave-pitch distributions for the differing CG heights. A small variation in the standard deviation occurs with the change in CG height.

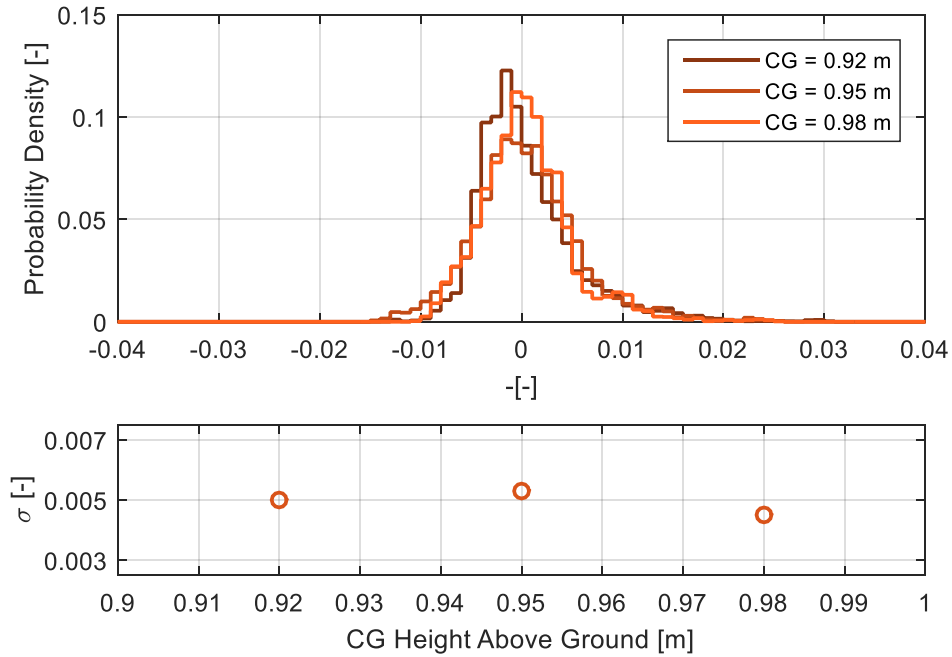


Figure 6-65: A comparison of the probability density function along the principal axis from the PCA rotated vertical acceleration vs pitch angular velocity RMS scatter plot for UTE1 traveling along Route 3 (at 70 km/h) carrying a 570 kg payload with differing centre of gravity heights (top) and change in standard deviation CG height (bottom)

Figure 6-66 shows a comparison of the PCA-adjusted heave-roll distributions for the differing CG heights. Once more the standard deviation of the data fluctuated inconsistently with the changing heights. The maximum probability density remain similar between the 0.95 and 0.98 m CG heights, however the 0.92 m configuration was greater.

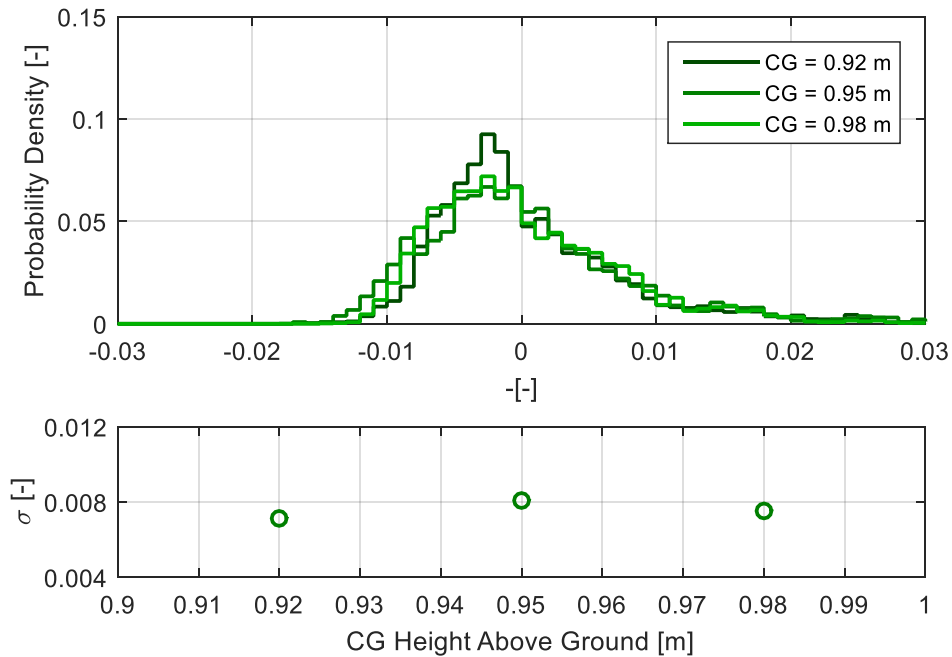


Figure 6-66: A comparison of the probability density function along the principal axis from the PCA rotated vertical acceleration vs roll angular velocity RMS scatter plot for UTE1 traveling along Route 3 (at 70 km/h) carrying a 570 kg payload with differing centre of gravity heights (top) and change in standard deviation CG height (bottom)

The inconsistent nature of the results may have been caused by the variations in the inertial parameters not being sufficiently large enough, their influence on the system may have been drowned-out by small variations in experimental speed and wheel path. Although the payload was secured to the vehicle, it was not rigidly mounted (idealised) to the vehicle, as such, it is possible that some degree dynamic coupling between the vehicle and payload was evident.

Fourier analysis of the experimental runs did not reveal any significant differences from the varying centre of gravity heights. The vertical acceleration PSD functions, shown in Figure 6-67, showed that the spectra shape remains similar between all of the configurations, with configuration 2.3 (0.95 m) having the highest RMS. Distinct levels are observable in the trough between the primary and secondary peak (4-5 Hz) of the PSD function and may be correlated to the change in inertial properties.

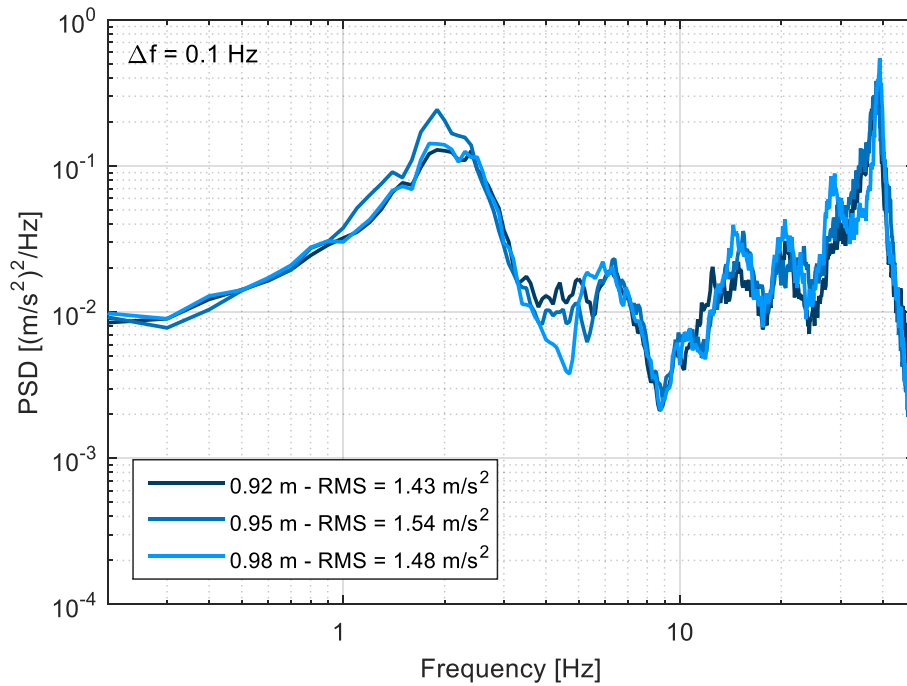


Figure 6-67: A comparison of the vertical acceleration PSD functions for UTE1 traveling along Route 3 (at 70 km/h) carrying a 570 kg payload with differing centre of gravity heights.

Figure 6-68 and Figure 6-69 show the pitch and roll angular velocity PSD functions respectively. For all modes of vibration no discernible relationship can be linked between CG height (and MOI) and the RMS or spectrum shape, with all changes appearing to be arbitrarily.

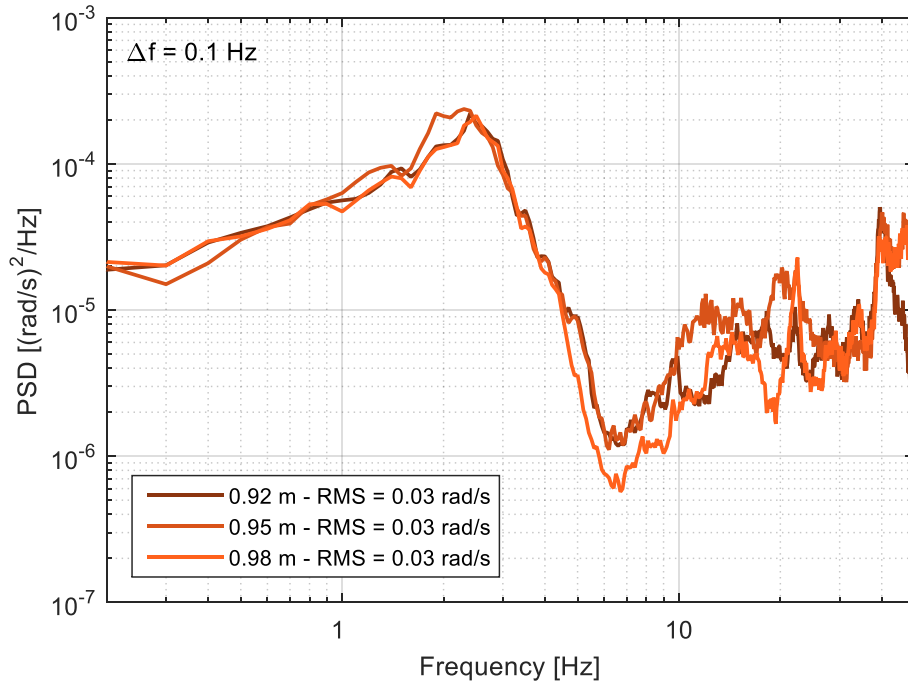


Figure 6-68: A comparison of the pitch angular velocity PSD functions for UTE1 traveling along Route 3 (at 70 km/h) carrying a 570 kg payload with differing centre of gravity heights.

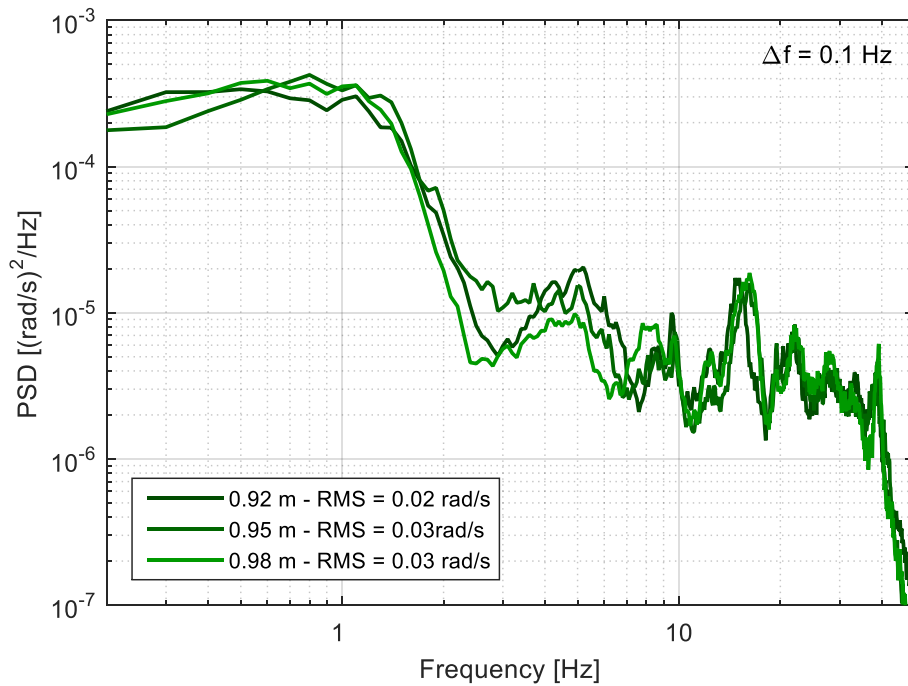


Figure 6-69: A comparison of the roll angular velocity PSD functions for UTE1 traveling along Route 3 (at 70 km/h) carrying a 570 kg payload with differing centre of gravity heights.

The pitch frequency response functions (Figure 6-70) reveals that the seemingly random fluctuations of the heave and pitch PSD functions are correlated below 3 Hz. For all vibratory modes this is frequency bandwidth is high enough to cover the first resonant frequency. Above 3 Hz the FRFs diverge, with only the basic shape remaining comparable.

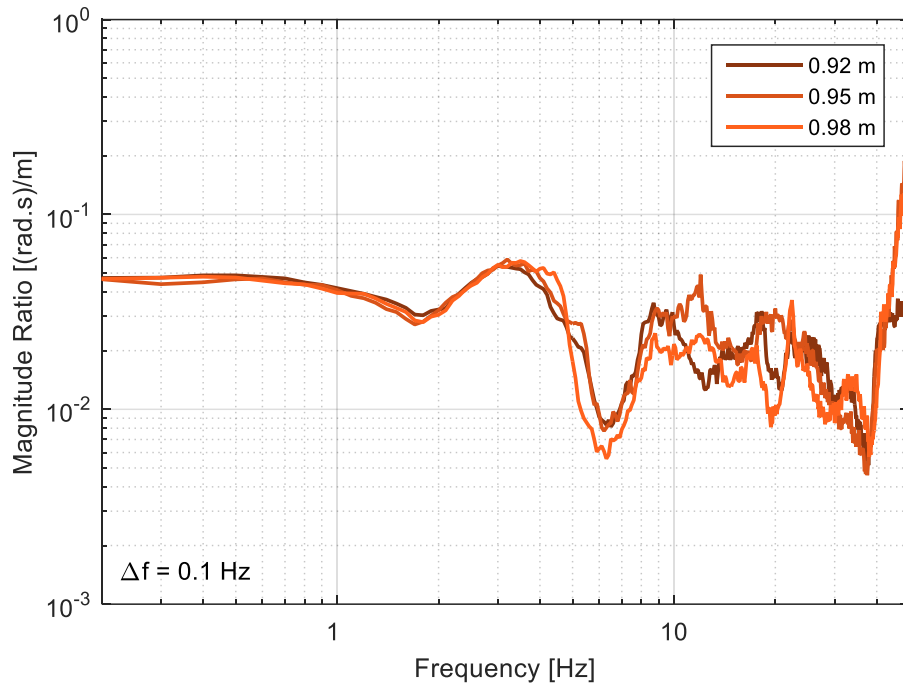


Figure 6-70: A comparison of the frequency response functions between the pitch angular velocity and vertical acceleration for UTE1 traveling along Route 3 (at 70 km/h) carrying a 570 kg payload with differing centre of gravity heights.

Figure 6-71 shows the FRF between the vertical and roll vibratory motions for the different CG heights. The shape of roll FRFs remain similar across all frequencies although the magnitude ratio fluctuates independently of the CG height.

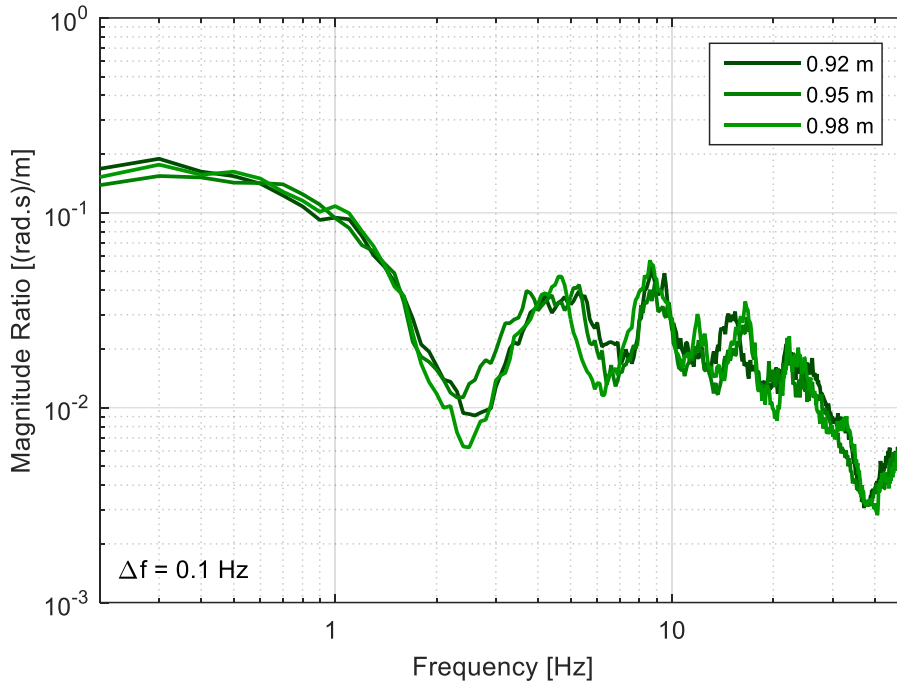


Figure 6-71: A comparison of the frequency response functions between the roll angular velocity and vertical acceleration for UTE1 traveling along Route 3 (at 70 km/h) carrying a 570 kg payload with differing centre of gravity heights.

6.4 Physical Experiments - Concluding Statements

This series of experiments was undertaken to explore and investigate potential relationships between the heave, pitch and roll motions of various vehicles as they traversed irregular terrain. An in-depth analysis of the vehicles multiple vibratory modes was performed. Tried and true methods of analysing vehicle vibrations were used including Fourier analysis and statistical distributions. To further investigate potential correlations between heave, pitch and roll some novel analysis techniques were implemented namely; bivariate histograms, principal component analysis (allowing for further analysis using statistical distributions) and frequency response functions between different vibratory modes. The experiments were designed to probe the effects of vehicle speed, road type, payload, and payload mass characteristics.

The experiments showed that strong relationships exist between the heave and pitch vibratory modes, being evident in the bivariate histograms and PDFs obtained from the PCA-adjusted data. It was found that when using PCA the distribution perpendicular to the principal axis fitted almost identically with the distribution of the RMS vertical acceleration. It was concluded that this was due to the vertical acceleration being more than one order of magnitude higher than the angular velocities of the pitch and roll motions, resulting in it effectively being the principal component. PDFs along the principal axis presented the strength of the relationship between the modes of vibration. The comparatively low standard deviation and high maximum probability density of the heave-pitch data show a stronger relationship than the heave-roll in all experiments.

The newly-implemented analysis techniques all indicated that the heave-pitch relationship is much stronger than the heave-roll relationship. However, the uncontrolled nature of the physical experiments, low number of possible configurations (due to the time-consuming aspect of each configuration) and the inability to isolate the effects of parameters individually make it difficult to draw conclusions on the influence of some of the system parameters. For this reason a validated numerical model was used to carry out a more in-depth investigations into the correlations between the heave, pitch and roll response of transport vehicles.

Chapter 7

Numerical Model: Development and Parameter Estimation

The physical experiments in Chapter 6 showed a strong correlation between the levels of vertical and pitch vibration, as well as a weaker relationship between the levels of vertical and roll vibration. Assessing the impact of the vehicle's various parameters, such as vehicle geometry and payload location, on these relationships using physical experiments is a challenging and time consuming process. This is due to not only the number of experiments required, but also the difficulty in isolating the effects of individual parameters. For this reason the physical investigation was limited solely to evaluating the effects of vehicle speed, road roughness and payload. The significant amount of time and resources needed to examine only these parameters using on-the-road experiments limited the experiments to a small number of variations. To further investigate the vehicle's dynamic behaviour it was decided to develop a numerical model in order to conduct an in-depth sensitivity analysis. A good numerical model has many advantages over physical experiments; namely the ability to easily isolate the effect of individual parameters and to rapidly conduct a large range of experiments, under a broad variety of conditions.

A full car, seven degree of freedom, numerical model was developed. It was paramount that the numerical model be validated in order to ensure the accuracy of the results. The development

process of full car numerical model is described in this chapter, as well as an explanation of the methods used to estimate the parameter values used within the model. Furthermore, a description of the processes used to synthetically generate dual wheel path road elevation profiles with a predefined left-right wheel path coherence function to excite the system is also presented.

7.1 Synthetic Road Profile Generation – for Pitch and Roll Motion

An accurate description of the road topography is necessary for vehicle simulation purposes. Simplified vehicle simulations using a quarter car model require only a single excitation input representing one wheel path. When the response of the pitch and roll modes of vibration is of concern, separate wheel paths and time delays between the front and rear wheels need to be considered. In these cases, not only does the statistical properties of each wheel path need to be known, but the cross-correlation of the vertical displacement between the left and right wheel paths is also required.

7.1.1 Current Synthesis Methods

Since the irregularities of a road surface are random, trying to completely replicate a road surface is impossible. It is possible however, to generate a surface with the same statistical properties, provided that some characteristics of the road are known and general assumptions are made. If a pavement elevation profile is treated like any other continuous random signal, it can be broken down into a series of sinusoidal signals of varying amplitude and phase in accordance to the Fourier series.

ISO standard 8608 (ISO 1995) is used to classify pavements into roughness classes based on the power of the displacement PSD, as shown in Figure 7-1. The ISO standard divides roads into classes ranging from A (very good) to G (ungraded). In order to synthesize a random road profile, it is assumed that the process conforms to a Gaussian distribution; that is, the phase spectrum is distributed uniformly. For synthesis, a uniformly-distributed phase spectrum needs to be created before being combined with the PSD function prior to the use of the inverse (Fast) Fourier transform (IFFT) to generate an artificial longitudinal road profile.

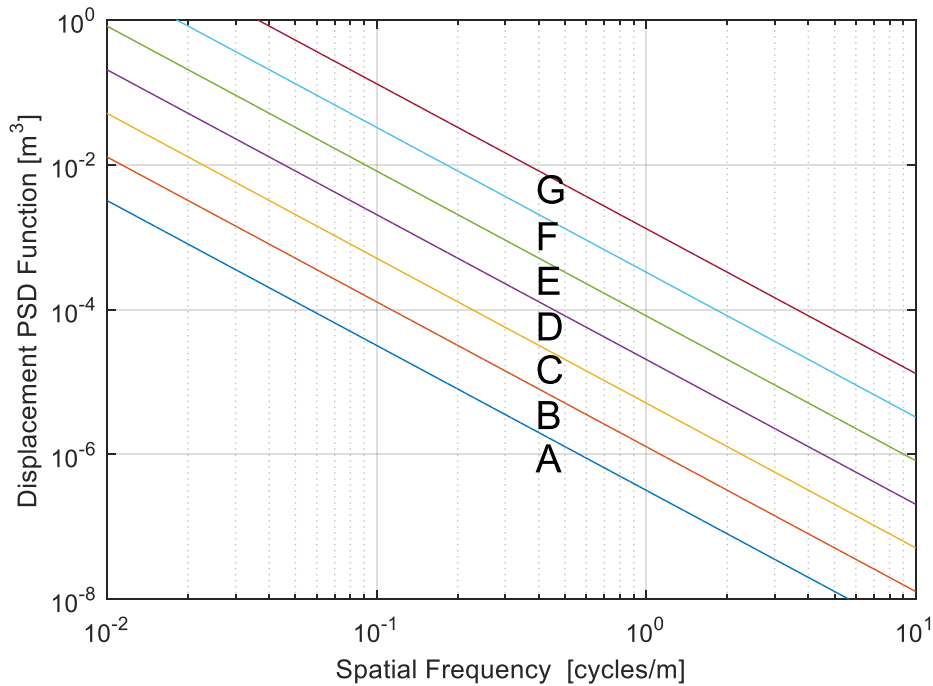


Figure 7-1: ISO8608 road classification PSD level

Exciting the pitch and roll modes of vibration requires different signals be applied to each wheel. It is generally agreed that the front and rear wheels of a vehicle will travel over the same road surface with a delay equal to the wheelbase divided by the vehicle's speed. For dual wheel path synthesis, the standard (ISO 1995) recommends the convenient assumption that the road surface is isotropic, and that all profiles along a given stretch of road, irrespective of orientation and location, have the same properties, and to use the coherence function resulting from this assumption. This is a significant problem when looking at roll vibrations, as the coherence between the differing wheel paths is directly related to the level of roll input. As discussed earlier in section 3.2.1, for very long wavelengths the wheel paths are observed to be nearly identical (highly correlated), while at very short wavelengths the correlation between the left and right wheel paths approaches zero (roughness becomes a function of texture). The correlation function between the left and right wheel paths is explored in the following section.

7.1.2 Improved Two-Track Road Synthesis

In order to maximise the accuracy of numerical simulations a realistic excitation function is needed, particularly when roll vibrations are of interest. From the literature review, it was found by Múčka (2015) that the Ammon and Bormann (1991) model was the most accurate. This model was chosen as the target coherence function for the synthesised road elevation profiles and is shown in Equation 7-1, Ω is the angular spatial frequency (rad/m).

$$\left[1 + (1.497\Omega)^{1.427} \right]^{-0.555} \quad 7-1$$

Dual wheel path road elevation profiles with a specific coherence function between them were synthesised using a process similar to that described by Xiandong *et al.* (2015). The simple process requires only a target PSD function, a target coherence function and two randomly generated phase signals. The left wheel path is synthesised using the same process outlined previously, however the right wheel path requires an extra step, explained in Figure 7-2. To synthesise the right wheel path two signals must be combined. To generate the first sub-signal, the target PSD function is multiplied by the target coherence function and an IFFT process is performed using the same phase signal as the left wheel path. The second sub-signal is generated using the target PSD function multiplied by the residual $(1 - \gamma_{Target}^2)$ and a new phase signal, the two sub signals are then added together creating the right wheel path.

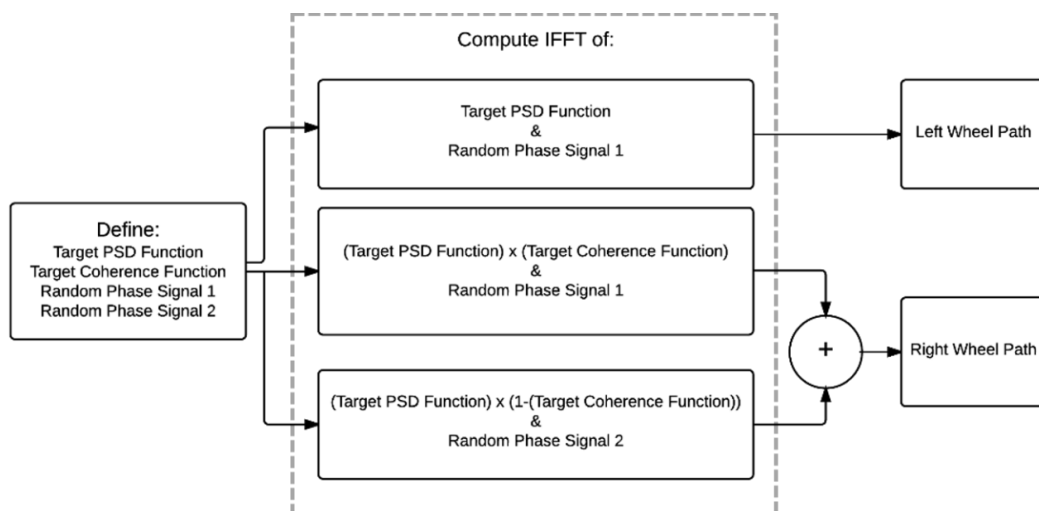


Figure 7-2: Process for constructing dual wheel path elevation profiles with target coherence and PSD functions.

This synthesis method can be used with any target coherence function, it was initially intended to use the coherence model proposed by Ammon and Bormann (1991), shown to be the most accurate (Múčka 2015), for the numerical simulations. However, initial tests yielded significantly lower roll response than the physical experiments. Ainalis (2014, p.148) obtained dual wheel path road elevation profiles of Route 1 (Bacchus Marsh to Geelong), measured in-situ, from a local road authority. Ainalis presented the coherence function between the wheel paths as well as PSD functions for both. A significant difference can be observed between Ammon and Bormann's model and the coherence function published by Ainalis in Figure 7-3. An exponential function was fit to the in-situ measured coherence function (equation 7-2) and used as the target coherence for the road synthesis.

$$\gamma^2 = 1.049 \cdot \exp(-10.54 \cdot n)$$

7-2

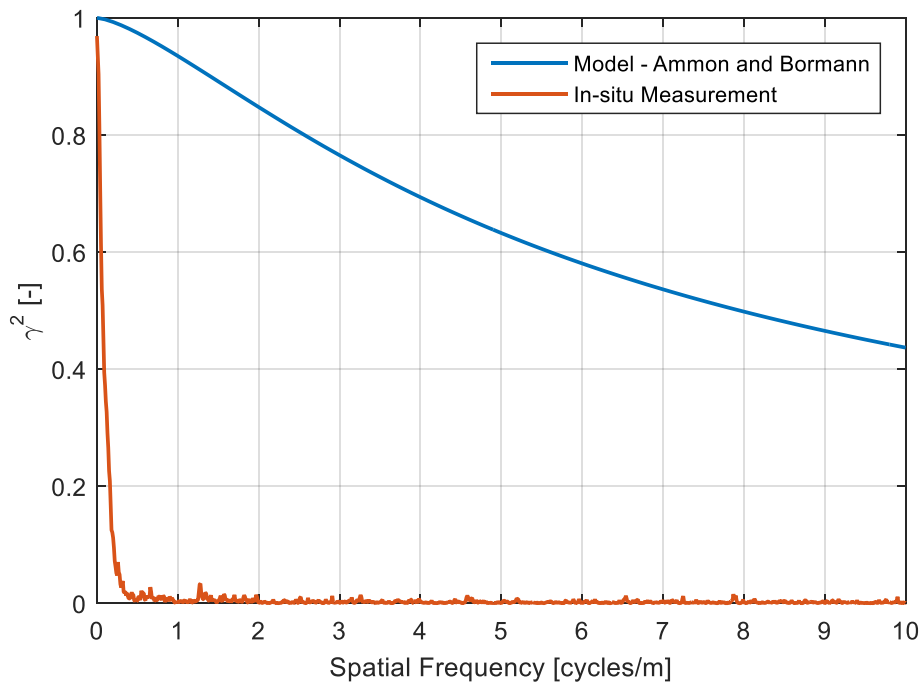


Figure 7-3: Comparison of the coherence model proposed by Ammon and Bormann (1991) and in-situ measurement (Ainalis 2014) of Route 1 between Bacchus Marsh and Geelong.

Figure 7-4 displays the coherence function for the left and right wheel paths and the target coherence function, an exponential model fitted to the published coherence function of Route1. The coherence function of the generated road signal is in excellent agreement with the target model.

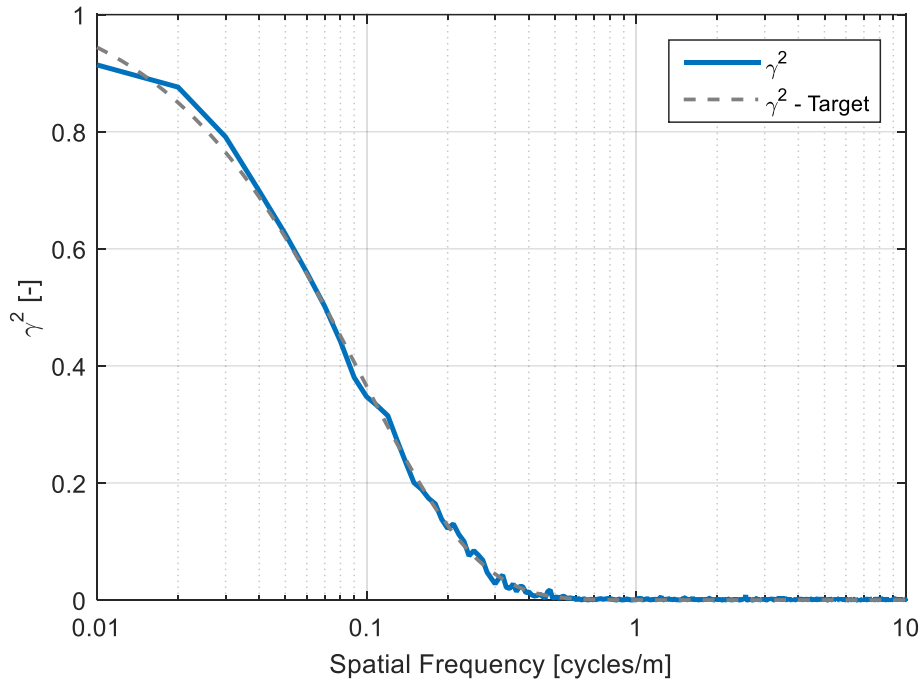


Figure 7-4: Comparison of the target coherence model and the coherence function between the synthesised left and right wheel paths.

Figure 7-5 displays the left and right wheel paths synthesised using this method. The top figure shows a 25 m cropped section of a class ‘A’ road elevation profile and it can be seen that both wheel paths follow the same profile for longer wavelengths, maintaining the superelevation of the road. The bottom figure displays a 5 m section of road where a longitudinal shift between shorter wavelengths is evident. In this example both the left and right wheel paths have the same RMS, however it is not uncommon for one wheel path to be rougher than the other, as one track wears more rapidly than the other. Ainalis (2014, p.148) found that there was a difference in roughness between the two wheel paths for Route 1. A difference of approximately eight percent in RMS was calculated between the wheel paths, this difference will be incorporated into the final synthesised road elevation profiles used in the simulations.

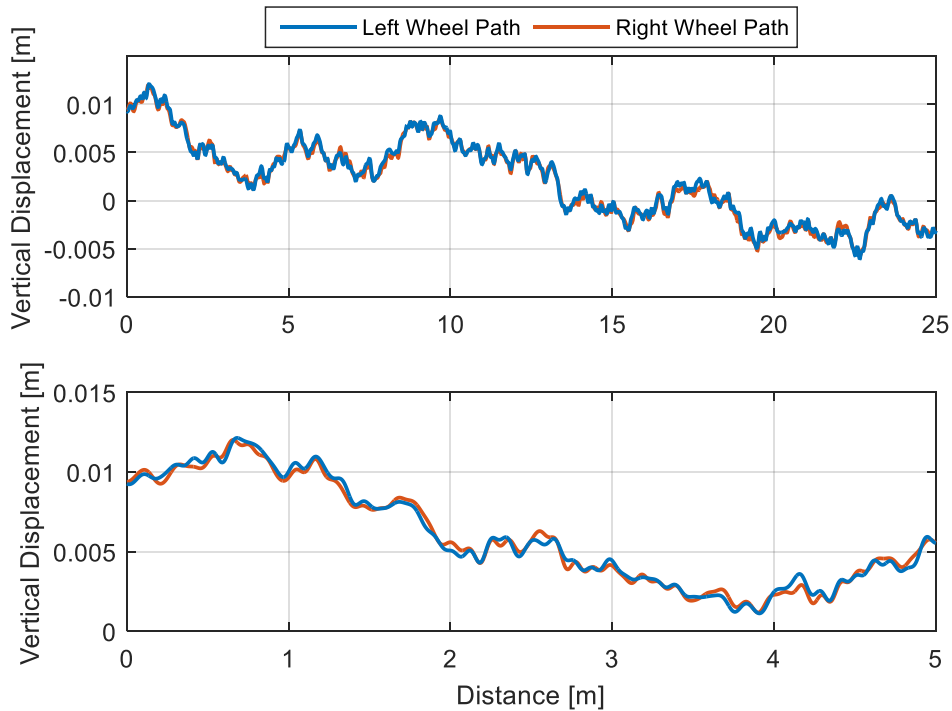


Figure 7-5: Synthesised dual wheel path road elevation profiles.

Generating road elevation profiles with a specified coherence function ensures that the excitation produced is more realistic, however the profile is still not completely representative of an actual road. From the literature review it was shown that road elevation profiles can be considered random with an approximately Gaussian probability distribution (Cebon 1999, p. 21), however they have repeatedly been shown to be nonstationary (Otari *et al.* 2011; Griffiths 2012). Although research has been conducted into the nonstationarity of road elevation profiles, it is still in its infancy. Synthesis of a nonstationary dual wheel path road elevation profile with a specified coherence function and target PSD was determined to be beyond the scope of this thesis. The linear character of the developed numerical model shown in the following section means that it would not benefit significantly from a nonstationary excitation signal.

7.2 Vehicle Model Development

For many years the de-facto approach for vehicle dynamic simulation has been the quarter car model, due to its technical and computational simplicity. It is, however, limited in its applications due to the over-simplification of a vehicle to a single-input-single-output SISO system. More complex vehicle models have been developed, from half car models (Gillespie 1985) to quite complex 21DoF tractor-semi trailer models (Cebon 1999).

A full car (four wheeled) model was decided upon to allow pitch and roll motions whilst still being relatively simple compared to a complete tractor-trailer model. Figure 7-6 shows a representation of the full car vibrating model, a main body mass (sprung mass) sits upon four spring and damper sets, representing the vehicle's suspension. Each suspension spring and damper is attached to a wheel/hub mass (unsprung mass) which in-turn is attached to a tyre spring and damper. The vertical vibration (heave), pitching and rolling motion of the main body mass are the primary interests of this study.

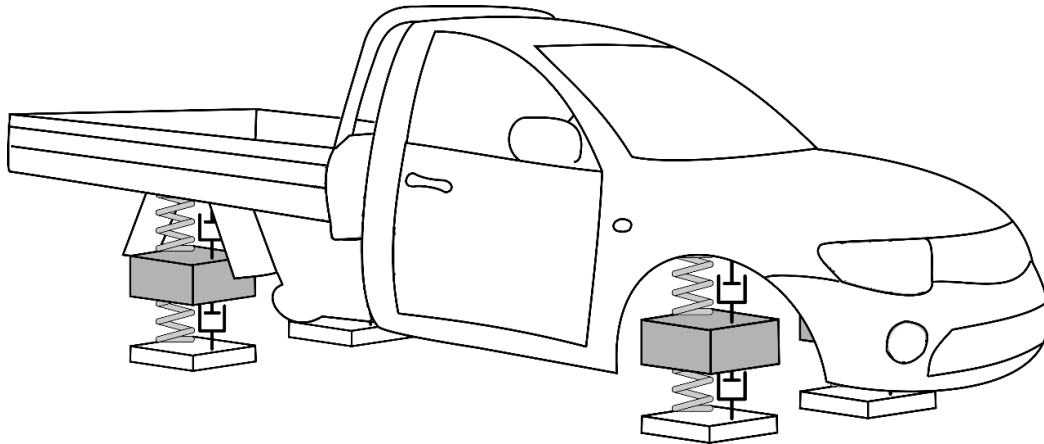


Figure 7-6: An illustration of the full car vibrating model.

Although more complex than the quarter car model, several simplifications were required for the full car model. The tyres and suspension are represented by linear springs with no compression or extension limits. Although this can be implemented within the numerical model it was deemed unnecessary due to the additional level of complexity required to identify suitable limits for each vehicle set up and the very small likelihood of extreme values being encountered.

Similarly, the tyre and suspension damping is represented by linear viscous dashpots. The characterisation of automotive dampers is not straightforward due to their complex nature and previous studies have shown their properties to be dependent on not only the velocity but also the direction of travel and displacement (Ainalis *et al.* 2015). Non-linear analysis is beyond the scope of the research and, for a comparative study such as this, a linear approximation is sufficient.

Figure 7-7 shows a schematic of the system, several variables are used within the numerical model with a summary of terms shown in Table 7-1. Also shown in Figure 7-7 is a breakdown of the coordinate system, where pitch (θ) is taken around the lateral axis of the vehicle, and roll (ϕ) is measured around the longitudinal axis.

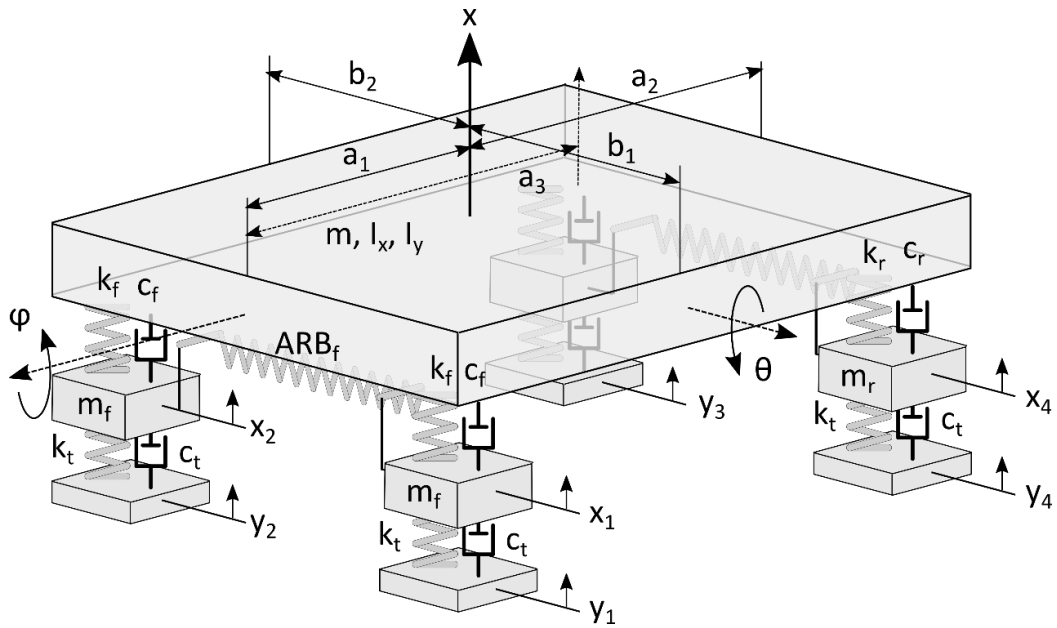


Figure 7-7: An illustration of the full car model with each of the parameters shown.

Typically, engine vibrations propagate into the vehicle body during operation. To mitigate this, the engine and drivetrain are isolated from the body by rubber mounts in most vehicles. These vibrations, present in physical experiments, are of no significance to the research and as such the engine and drive train are represented as a lumped mass. The mass and moments of inertia of the engine and drivetrain are included in the properties of the sprung mass in the numerical model.

Table 7-1: List of variable names, units and brief description, used within the numerical model.

Symbol	Unit	Name	Description
m	kg	Body mass	Mass of the body of the vehicle, including the occupants and the payload.
I_y	kg.m ²	Pitch moment of inertia	Moment of inertia in the pitch plane of the body of the vehicle
I_x	kg.m ²	Roll moment of inertia	Moment of inertia in the roll plane of the body of the vehicle
m_f, m_r	kg	Unsprung mass	Mass of the wheel assembly on each corner. Normally consisting of wheel rim, tyre, hub/upright assembly, brake rotor and calliper, and a percentage of the suspension system and drive shafts. Mass usually varies from front to back, but is generally the same left to right.
a_1, a_2	m	Longitudinal centre of mass distance	Distance from the centre of mass to the front and to the rear wheels.
a_3	m	Longitudinal measurement point	Synthetic measurement location.
b_1, b_2	m	Lateral centre of gravity distance	Distance from the centre of mass to the right and to the left wheels.
k_t	N/m	Tyre stiffness	Spring stiffness of the tyres.
c_t	kg/s	Tyre damping	Tyre damping coefficient.
k_f, k_r	N/m	Suspension stiffness	Effective suspension stiffness taking suspension geometry into account.
c_f, c_r	kg/s	Suspension damping	Effective suspension damping coefficient taking suspension geometry into account.
ARB_f, ARB_r	N.m/rad	Anti-roll bar stiffness	Stiffness of the front and rear anti-roll bars.

7.2.1 Equations of motion

The fundamental basis of the numerical model is a series of Equations of Motion (EoM) that define the dynamic interactions of the vehicle's masses, springs and dampers. Published EoM are available, although it can be problematic trying to find a model that has the same variables in the same arrangement corresponding to a specific model configuration. EoM can be

established from first principles, however this can be time consuming and requires some level of expertise.

Employing a pragmatic approach, the EoMs used were modified versions of those published by Jazzar (2013). Jazzar's (2013) system was slightly more simplistic than desired, with no tyre damping or a rear anti-roll bar. Slight modifications of the equations were made to include these omissions and are shown below ([7-3]-[7-9]).

$$\begin{aligned}
& m\ddot{x} + c_f(\dot{x} - \dot{x}_1 + b_1\dot{\phi} - a_1\dot{\theta}) + c_f(\dot{x} - \dot{x}_2 - b_2\dot{\phi} - a_1\dot{\theta}) + c_r(\dot{x} - \dot{x}_3 - b_1\dot{\phi} + a_2\dot{\theta}) \\
& + c_r(\dot{x} - \dot{x}_4 + b_2\dot{\phi} + a_2\dot{\theta}) + k_f(x - x_1 + b_1\phi - a_1\theta) + k_f(x - x_2 - b_2\phi - a_1\theta) \\
& + k_r(x - x_3 - b_1\phi + a_2\theta) + k_r(x - x_4 + b_2\phi + a_2\theta) \\
& = 0
\end{aligned} \tag{7-3}$$

$$\begin{aligned}
& I_x\ddot{\phi} + b_1c_f(\dot{x} - \dot{x}_1 + b_1\dot{\phi} - a_1\dot{\theta}) - b_2c_f(\dot{x} - \dot{x}_2 - b_2\dot{\phi} - a_1\dot{\theta}) \\
& - b_1c_r(\dot{x} - \dot{x}_3 - b_1\dot{\phi} + a_2\dot{\theta}) + b_2c_r(\dot{x} - \dot{x}_4 + b_2\dot{\phi} + a_2\dot{\theta}) + b_1k_f(x - x_1 + b_1\phi - a_1\theta) \\
& - b_2k_f(x - x_2 - b_2\phi - a_1\theta) - b_1k_r(x - x_3 - b_1\phi + a_2\theta) + b_2k_r(x - x_4 + b_2\phi + a_2\theta) \\
& + ARB_f \left(\phi - \frac{x_1 - x_2}{b_1 + b_2} \right) + ARB_r \left(\phi - \frac{x_4 - x_3}{b_1 + b_2} \right) \\
& = 0
\end{aligned} \tag{7-4}$$

$$\begin{aligned}
& I_y\ddot{\theta} - a_1c_f(\dot{x} - \dot{x}_1 + b_1\dot{\phi} - a_1\dot{\theta}) - a_1c_f(\dot{x} - \dot{x}_2 - b_2\dot{\phi} - a_1\dot{\theta}) \\
& + a_1c_r(\dot{x} - \dot{x}_3 - b_1\dot{\phi} + a_2\dot{\theta}) + a_2c_r(\dot{x} - \dot{x}_4 + b_2\dot{\phi} + a_2\dot{\theta}) - a_1k_f(x - x_1 + b_1\phi - a_1\theta) \\
& - a_1k_f(x - x_2 - b_2\phi - a_1\theta) + a_2k_r(x - x_3 - b_1\phi + a_2\theta) + a_2k_r(x - x_4 + b_2\phi + a_2\theta) \\
& = 0
\end{aligned} \tag{7-5}$$

$$\begin{aligned}
& m_f\ddot{x}_1 - c_f(\dot{x} - \dot{x}_1 + b_1\dot{\phi} - a_1\dot{\theta}) - k_f(x - x_1 + b_1\phi - a_1\theta) \\
& - ARB_f \frac{1}{b_1 + b_2} \left(\phi - \frac{x_1 - x_2}{b_1 + b_2} \right) + k_t(x_1 - y_1) + c_t(\dot{x}_1 - \dot{y}_1) \\
& = 0
\end{aligned} \tag{7-6}$$

$$\begin{aligned}
& m_f\ddot{x}_2 - c_f(\dot{x} - \dot{x}_2 + b_2\dot{\phi} - a_1\dot{\theta}) - k_f(x - x_2 + b_2\phi - a_1\theta) \\
& + ARB_f \frac{1}{b_1 + b_2} \left(\phi - \frac{x_1 - x_2}{b_1 + b_2} \right) + k_t(x_2 - y_2) + c_t(\dot{x}_2 - \dot{y}_2) \\
& = 0
\end{aligned} \tag{7-7}$$

$$\begin{aligned}
& m_r \ddot{x}_3 - c_r (\dot{x} - \dot{x}_3 - b_1 \dot{\phi} + a_2 \dot{\theta}) - k_r (x - x_3 - b_1 \phi + a_2 \theta) & 7-8 \\
& - ARB_r \frac{1}{b_1 + b_2} \left(\phi - \frac{x_4 - x_3}{b_1 + b_2} \right) + k_t (x_3 - y_3) + c_t (\dot{x}_3 - \dot{y}_3) \\
& = 0
\end{aligned}$$

$$\begin{aligned}
& m_r \ddot{x}_4 - c_r (\dot{x} - \dot{x}_4 + b_2 \dot{\phi} + a_2 \dot{\theta}) - k_r (x - x_4 + b_2 \phi + a_2 \theta) & 7-9 \\
& - ARB_r \frac{1}{b_1 + b_2} \left(\phi - \frac{x_4 - x_3}{b_1 + b_2} \right) + k_t (x_4 - y_4) + c_t (\dot{x}_4 - \dot{y}_4) \\
& = 0
\end{aligned}$$

The EoM can then be implemented within a differential equation solver, such as the Simulink toolbox of Matlab®. Figure 7-8 shows the results of this process for the front left corner (Equation 7-6) of the vehicle. Each EoM is constructed in this manner before being linked together.

Once the model has been constructed a synthetic road elevation profile, generated using the procedure described in Section 7.1, can be used to excite the system. As the excitation function is in the spatial domain (samples per metre) the frequency at which the elevation values are sampled determines the vehicles speed within the simulation. The excitation functions (left and right wheel paths, plus time delay for the rear wheels) then pass through the equations, similar to how a road vibration propagate through the tyre, into the suspension before going into the vehicle body. The response of any part of the numerical model can be captured giving a time history of the response of the particular component. For this research the vertical acceleration and pitch and roll angular velocities of the vehicle body were recorded, for direct comparison with the data obtained from the physical experiments the vehicles response can be analysed using the same techniques. Because the excitation function is known further analysis can be undertaken, such as computing the frequency response function.

Before analysis can be conducted on the results from the numerical model it is important that the model is validated. The number of variables and links contained within the numerical model is considerable. It is important to ensure that the model is assembled properly. Several methods for confirming that the numerical model is error-free were utilised, including frequency response function comparison and natural frequency calculations for various parameter sets.

7.3 Estimating Vehicle Parameters

In order to acquire a realistic response from the numerical model, the parameter values used within the model must also be realistic. Accurately measuring all the parameters to create a realistic numerical vehicle model is a challenging task, requiring a significant amount of resources and time. Many parameters of a vehicle can only be known accurately by completely disassembling the vehicle, and conversely other components can return inaccurate values when removed from the system. The following sections explain some of the practical approaches that can be used for estimating a vehicle's parameter values.

7.3.1 Mass

Two different masses are needed to create a numerical model of a vehicle; the sprung (vehicle chassis/body) and unsprung (wheel and axle) masses. As vehicle suspension systems are effectively symmetrical left to right, it is safe to assume that the unsprung masses are the same left to right. From the front to the back of vehicle, there will be a difference due to the drive train, steering and brake setups. The vehicle's brakes contributes mass directly to its unsprung mass, whereas other components such as suspension control arms will only add a fraction of their mass as they are also attached to the vehicle body. A vehicle's drive type, be it front wheel, rear wheel or all-wheel drive, also adds a fraction of the mass of the differential and other drive components to the respective drive ends unsprung masses.

Vehicle disassembly is not an option in most situations, and in the past some work has been done on estimating the separate mass values in situ. Bixel *et al.* (1995 & 1996), with the help of large-scale testing equipment, were able to estimate the sprung and unsprung masses to a relatively high degree of accuracy. This approach is far from ideal due to the required specialised equipment. A simpler method for estimating vehicle sprung and unsprung masses is by using a partial disassembly method.

Car corner weight scales are used to measure the total mass of the vehicle, as well as each corner individually. Leaving the vehicle on the scales, large stroke car jacks or a two post car hoist can be used to lift the body of the vehicle. In modern vehicles, coil springs and dampers are often in a single assembly with the coil over the damper. This configuration allows for the spring and damper to be easily detached from the body of the vehicle. The suspension can now hang without restriction and allows for the measurement of the unsprung mass. A similar process can be used for leaf-spring and other suspension types. The sprung mass value is simply

the total mass value, measured at the beginning, less the unsprung mass. This process was used to measure the mass values of UTE1.

Figure 7-9 shows a photograph of UTE1 sitting upon the corner weight scales. The vehicle was first lifted using the two post car hoist, then the corner weight scales were placed beneath each wheel before the vehicle was lowered. At this point the vehicle gross weight can be taken, and if desired a driver and passenger can also be added before the measurement is recorded. The combined mass of the driver and passenger can represent a significant change in the mass and mass distribution of the vehicle.

Figure 7-10 is a photograph of the rear suspension and drive line of UTE1. The rear wheels, drum brakes, leaf springs, telescopic dampers, differential and drive axles are all visible. These components, or part thereof, form the total rear unsprung mass when in service. To measure the rear unsprung mass the telescopic dampers were disconnected from the suspension anchor, the area where the drive axle connects to the leaf springs with U-bolts. The rear end of the leaf spring was also disconnected from its shackle, allowing the suspension to droop unrestricted as shown in Figure 7-11. This process was repeated for both sides of the vehicle, due to the solid rear axle. The rear unsprung masses were then measured, before reassembly.

The partial disassembly process was then carried out on the front passenger side wheel assembly. UTE1's front suspension utilised a coil-over-spring configuration. Three nuts were removed to disconnect the assembly from the vehicles body, as shown in Figure 7-12. Unfortunately, due to the suspension design, the assembly could not clear its mounting and allow the suspension to droop without the top suspension control arm being disconnected as well. As only one side of the vehicle was partially disassembled, the front anti-roll bar was also disconnected.



Figure 7-9: Photograph of UTE1 sitting upon the corner weight scales.



Figure 7-10: Photograph of the undercharge of UTE1 showing the rear suspension configuration. The vehicles differential, leaf springs and telescopic dampers are visible.



Figure 7-11: Photograph showing the disconnected rear unsprung mass resting upon the corner weight scale, the sprung mass is supported by a car hoist.



Figure 7-12: Photograph showing the disconnected front coil spring and damper combination. The top suspension wishbone is also disconnected.

The partial disassembly process proved to be an easy method for measuring the sprung and unsprung masses of a vehicle taking only a few hours. Table 7-2 shows the estimated sprung and unsprung masses of UTE1 when partially disassembled. The front unsprung mass is slightly

over-estimated due to the inclusion of the upper control arm and the complete shock-spring combination, however a compromise between what to include and exclude must always be made.

Table 7-2: The sprung and unsprung masses of UTE1 measured using the partial disassembly method.

Vehicle	Toyota Hilux – Single cab
Sprung mass	1,256 kg
Sprung mass (two occupants)	1,428 kg
Front unsprung mass	35 kg
Rear unsprung mass	101 kg

7.3.2 Stiffness and Damping

Due to the complex geometry of vehicle suspension, values of suspension stiffness can vary depending on how it is measured. This is due to the leverage of the suspension arms and angle of the spring itself. Figure 7-13 shows a typical double control arm suspension type, this suspension layout is used in the front suspension of UTE1. This suspension type may appear simple however it can become complex very quickly.

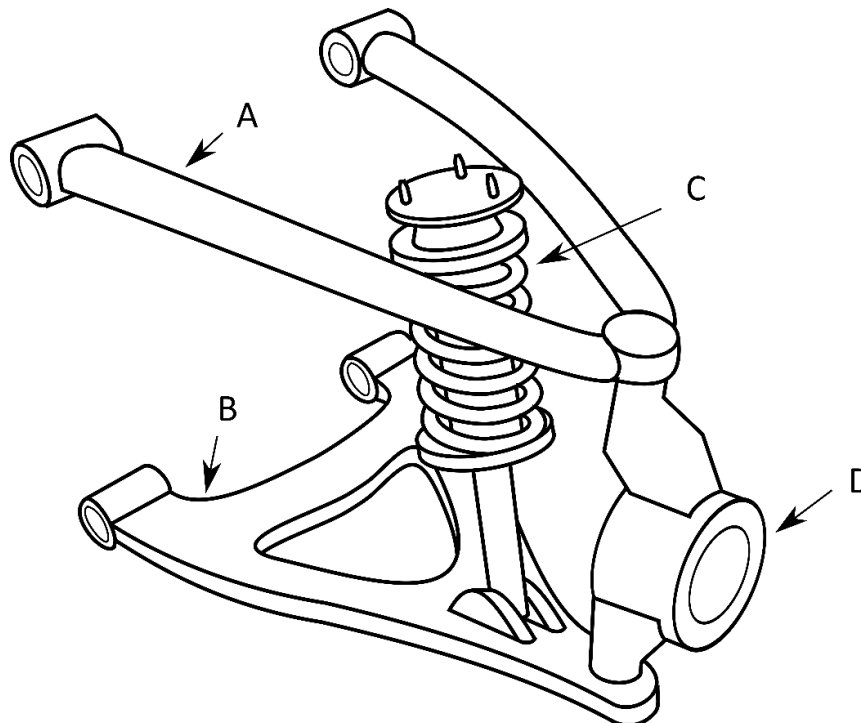


Figure 7-13: Illustration of typical double control arm vehicle suspension. Used in the front suspension of UTE1.

The complexity associated with any suspension system is due to the layout and possible configurations of its components. The upper (A) and lower (B) control arms may or may not be the same length, and also they may or may not be parallel. Changing the configuration of the control arm affects the arc that the wheel hub (D) travels in. This arc can be customised to alter vehicle handling, affecting the amount and the rate at which the spring is compressed. The distance between the wheel hub and coil-damper (C) combination can vary, affecting the amount of leverage from the wheel. The angle of the spring-damper also affects the rate and amount the spring compresses. Finally, the spring itself may be non-linear. Considering all these factors together, the spring stiffness can significantly differ when measured in place or removed from the vehicle.

The complex geometry leads to two spring rates, the effective spring stiffness, and the actual spring stiffness. If the suspension geometry is known, the actual spring stiffness can be measured when removed from the vehicle, the effective spring stiffness can then be calculated. Alternatively the effective spring rate can be measured directly whilst still mounted in the vehicle.

While the vehicle is on the corner weight scales (used to measure the mass), it is possible observe the exact load applied to each corners suspension. Mass can be added to the vehicle body to increase the load on the suspension, and the deflection of the vehicle body and tyre can be measured.

Using this approach the individual suspension stiffnesses of UTE1 were estimated and are shown in Table 7-3. It should be noted that the difference in the tyre stiffness estimates is due to different tyre inflation pressures.

Table 7-3: Estimated suspension stiffnesses of UTE1.

Parameter	Stiffness [kN/m]
Front suspension	43.5
Rear suspension	54.6
Front tyre (240 kPa)	174
Rear tyre (420 kPa)	349

To accompany estimates of the suspension stiffness, estimates of the suspension damping are also required. Many different methods exist to estimate the suspension damping ratio of vehicles. One of the most popular methods outlined by the Council of the European Union (CEU 1996) on tests for heavy vehicle road-friendliness suggests the analysis of the response of

the vehicle to a transient event. The Council of the European Union provides three methods to induce a transient response in a heavy vehicle:

1. Drive the vehicle slowly (constant 5 km/hr) off an 80 mm step (ramp).
2. Pull the chassis down to increase the drive axle tyre force by 50%, then suddenly release.
3. Lift the chassis to increase the spacing between the chassis and drive axle by 80mm, then suddenly release.

Ainalis (2014) conducted an in-depth investigation into these methods using a single wheeled experimental vehicle (physical quarter car). Ainalis utilised two different shock absorbers for the study, the first was a factory fitted shock absorber from a small capacity motorcycle, while the second was a nominally linear replacement shock absorber that was commissioned. Ainalis identified some limitations using the response-only (transient) methods, notably due to the ability to move the vehicle and the specialised equipment needed. Loading the vehicle and lifting the vehicle chassis (methods II. and III.) is possible, however quickly releasing the vehicle was shown to be difficult and requires specialised equipment. The response-only (transient) methods were also, as expected, found to vary in the estimated damping ratios, with a range of 10 % between the ramp test and the lift and release test when using the factory fitted shock absorber. Ainalis also placed the single wheeled experimental vehicle on a large-scale vibration table to test excitation-response methods, however this was deemed impractical for this application.

Looking for a simpler solution, Ainalis (2014) performed a comprehensive study into applying the random decrement technique (Cole 1968 & 1973) to estimate vehicle dynamic characteristics and found promising results. The random decrement signature obtained is “an estimate of the step response of a system and is obtained by averaging sections of the system time response in a particular way such that the components due to random and velocity inputs tend to zero as the number of averages increases” (Siviter & Pollard 1986).

The random decrement signature (Figure 7-14) can then be used to estimate the system’s damping ratio. The instantaneous magnitude of the random decrement signal (calculated using the Hilbert transform) was used to calculate the damping ratio, however many techniques can be used.

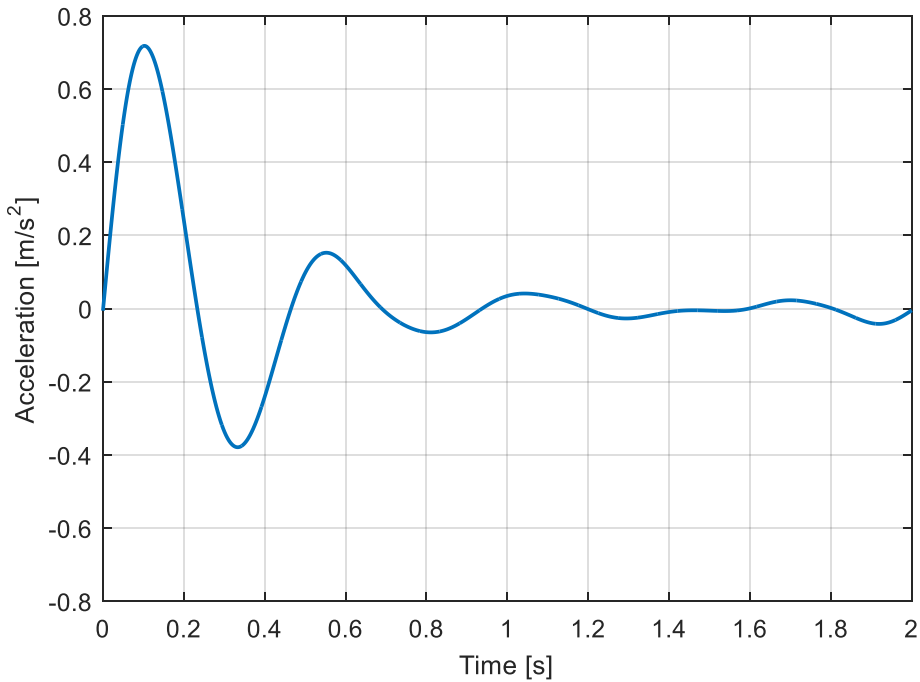


Figure 7-14: Random decrement signature for UTE1 carrying a 570 kg payload traveling at 100 km/h along Bulban road (Route 3)

Table 7-4 shows the estimated damping ratios obtained using the random decrement technique of UTE1 for each of its experimental runs. The damping ratio changes with payload, this is expected as the critical damping coefficient varies with mass. It also varies with speed, not unexpected due to change in suspension loading and the typical non-linearity of factory dampers. The damping coefficients, C_f and C_r , are calculated from the estimates of the proportion of the sprung mass effecting the front and rear suspension.

The high damping encountered when the vehicle was not loaded meant that trying to estimate the damping ratio was challenging, as the usable region of the random decrement signature was short. For this reason the final suspension damping constants, displayed in Table 7-5, are an average of the damping coefficients when the vehicle had a 570 kg payload.

Table 7-4: Estimates of the vehicle damping for UTE1 from the physical experiments

Vehicle	Route	Payload [kg]	Payload Height [% of maximum]	Speed [km/h]	Damping Ratio	C_f [N.s/m]	C_r [N.s/m]
UTE1	3	0	0	70	0.48	3964	3442
				80	0.42	3469	3012
				90	0.44	3634	3156
				100	0.45	3716	3227
		570	33	70	0.32	2643	3413
				80	0.27	2230	2880
				90	0.25	2065	2667
				100	0.32	2643	3413
			66	70	0.30	2478	3200
				80	0.23	1900	2453
				90	0.25	2065	2667
				100	0.26	2147	2773
	100	70	0.25	2065	2667		
		80	0.26	2147	2773		
		90	0.29	2395	3093		
		100	0.29	2395	3093		
	4	0	0	70	0.47	3882	3371
				80	0.43	3551	3084
				90	0.45	3716	3227
				100	0.43	3551	3084

Table 7-5: Estimated damping coefficients from experimental results of UTE1 caring a 570 kg payload.

Parameter	Damping Rate [N.s/m]
Front dampers (C_f)	2264
Rear dampers (C_r)	2925

Tyre dynamic (whilst rotating) stiffness and damping values are more challenging to measure without having to remove the wheel and tyre from the vehicle and use specialised testing machinery. Typical load and deflection measurement techniques to measure the stiffness can be used to estimate the values, as shown previously, however the tyres stiffness and damping characteristics change when the wheel is rotating. The National Highway Traffic Safety Administrations' (NHTSA) publication on pneumatic tyres is a series of articles focused on different aspects of tyre safety, testing and characteristics. The chapter on noise and vibration (Marshal 2006, pp. 364-408) states that a rolling tyre has a relatively stationary spring rate where as a non-rotating tyres' stiffness can vary considerably with deflection. The same behaviour is observed with its' damping characteristics. Representative values of tyre stiffness and damping were listed and are shown in Table 7-6. The damping estimate was used in the

numerical model however the tyre stiffness values obtained from physical measurement were used.

Table 7-6: Typical stiffness and damping values for passenger vehicle tyres.

Parameter	Value
Stiffness	200 kN/m
Damping ratio	0.15

7.3.3 Centre of Gravity and Moments of Inertia

Numerical models require the location of the centre of gravity of the vehicle's sprung mass alone, as such the same problems associated with vehicle disassembly are encountered. An approach to estimate the sprung mass centre of gravity without completely disassembling the vehicle is explored. Bixel *et al.* (1995 & 1996), were able to locate the centre of mass of the body alone, but the scale of specialised equipment required is impractical.

The location of a vehicle's centre of gravity must be considered in three dimensional space. Determining its location in the horizontal plane is straightforward and can be calculated using the vehicles' corner weights. Estimating its height is rather challenging. Although it is not needed for the model itself, the CG height is needed to calculate changes in the moments of inertia (MOI). Estimates can be made by elevating one end of the vehicle by a known amount and measuring the change in mass distribution. While this process works well for light race cars, it is not well suited for larger transport vehicles. The level of mass variation needed to produce a good estimate requires excessive elevation or tilt angles. An alternative method to obtain these estimates is explained in the following section.

Measuring the moments of inertia of a vehicle is by far the most resource intensive parameter to estimate. Considerable research has been conducted in this field, the two main approaches are physical measurement (Winkler 1983; Garrott *et al.* 1988; Riede *et al.* 1984; Rozyn & Zhang 2010) and computer analysis (Bixel *et al.* 1995 & 1996; Allen *et al.* 2003). Physical measurement involves supporting the vehicle on a large swing and allowing it to oscillate freely as a compound pendulum, and its period recorded. The National Highway Traffic Safety administration (NHTSA) has the required equipment to measure the moments of inertia in the pitch, roll and yaw planes, as well as the vehicle's centre of gravity location using this method. The NHTSA produced the Light Vehicle Inertial Parameter Database, which currently includes measurements of 496 different vehicle configurations.

When estimates only need to be in the range of the correct vehicle type (as opposed to a particular model) a much simpler method is possible. The approach relies on the extensive data set recorded by the NHTSA and the assumption that different vehicle subcategories share similar size and mass distributions.

7.3.3.1 Regression analysis of NHTSA Data

The large data set provided by the NHTSA allows for statistical analysis to be performed with a high level of confidence. The wheelbase, average track width, roof height and total vehicle mass were recorded along with the CG location and MOI making it possible to perform linear regression on the data set. The coefficients obtained allow for the CG location and MOI of any vehicle to be estimated if the wheelbase, average track width, roof height and total vehicle mass are all known.

Any statistical analysis performed on the entire data set produces results for an ‘average’ vehicle. However, mass distribution, and moments of inertia of a vehicle are inherently a function of the body size and style, allowing for more accurate analysis to be performed if the vehicle types are known. It is possible to separate the data into specific vehicle types as the NHTSA lists the vehicle make and type, as well as the loading configurations including ballast, number of occupants, drive axle, and fuel level.

As a transport van and two utility vehicles were used for the physical experiments, the data was separated into vehicle type subgroups before linear regression analysis was performed. Of the 496 vehicles, 126 were utility vehicles and 78 were transport vans, incomplete data sets and added ballast were removed dropping the number to 84 and 47 respectively - large enough numbers for acceptable estimates. Regression coefficients obtained by using all 496 data sets returned high coefficient of determination (R^2) values when all vehicles were compared against their measured results seen in Table 7-7, however when the utility and transport vehicles were concentrated on the coefficient reduced considerably in some cases. A comparison between the regression coefficient base (using vehicle specific data sets) and its effect on the goodness of fit is shown in Table 7-7. The results show that moments of inertia, about the pitch and roll axes, can be estimated to acceptable levels for the purposes of this research when data is separated by vehicle type before analysis. Centre of gravity height estimations work reasonably well, while the centre of gravity location from the front axle is the worst performing, it is also the easiest to measure.

Table 7-7: The effects of using all NHTSA vehicle data compared to using vehicle type specific data when calculating linear regression coefficients

Vehicle	Regression coefficient base	CG Distance		MOI pitch R ²	MOI roll R ²
		from front axle	CG height R ²		
All	All	0.685	0.915	0.925	0.898
Utility	All	0.486	0.880	0.905	0.881
	Utility	0.665	0.903	0.926	0.885
Van	All	0.849	0.831	0.821	0.822
	Van	0.880	0.837	0.909	0.858

Figure 7-15 and Figure 7-16 show the regression analysis base data for estimating the vehicle's centre of gravity location behind the front axle and height, respectively. The solid line represents the optimum result, where the predicted value is the measured value. The horizontal distance has the poorest fitting estimates, but as previously mentioned it is the easiest parameter to measure.

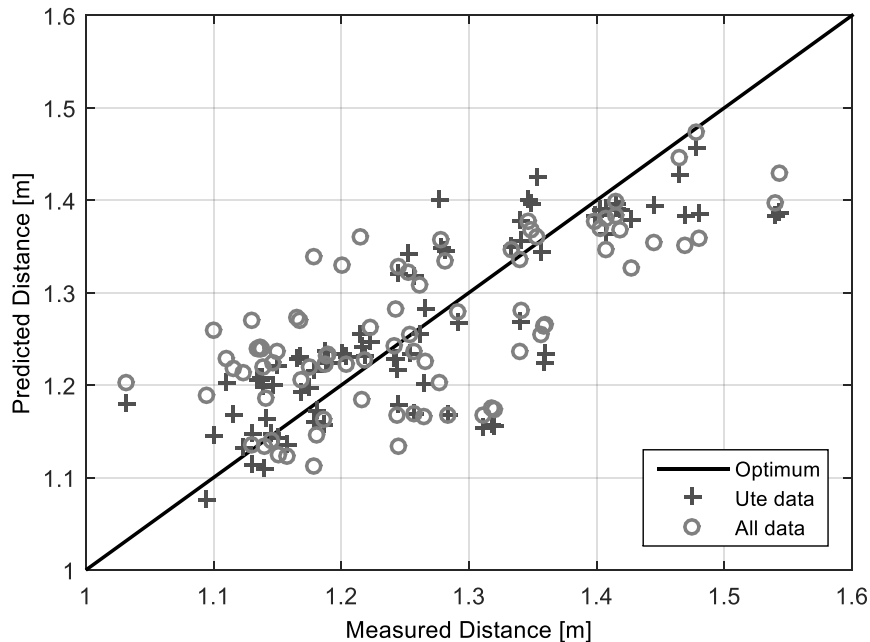


Figure 7-15: A comparison of using the all the NHTSA data versus only the utility vehicle data for calculating the regression coefficients for the horizontal CG location behind the front axle.

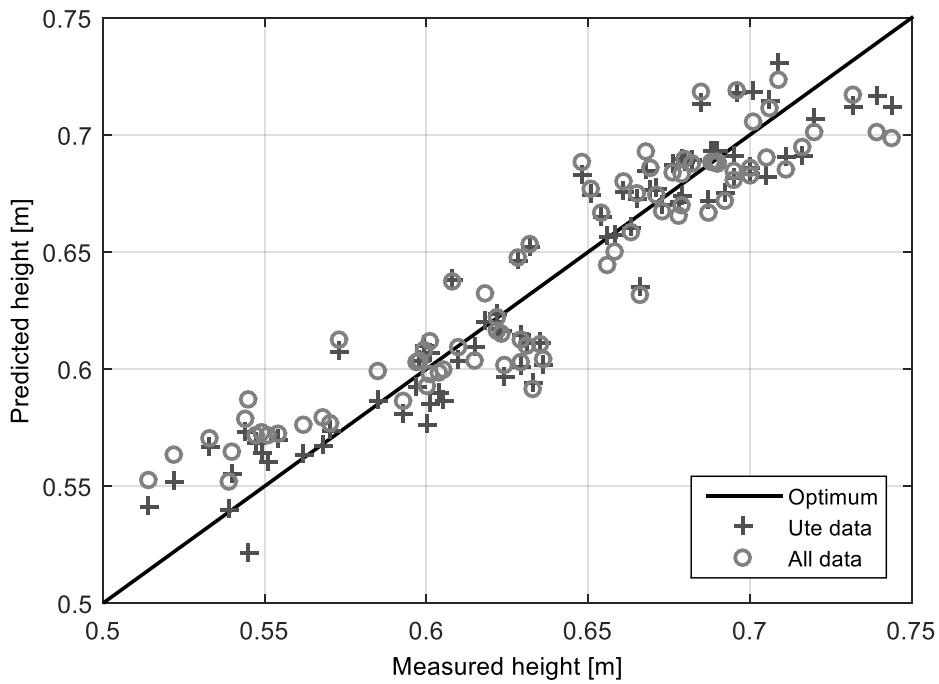


Figure 7-16: A comparison of using the all the NHTSA data versus only the utility vehicle data for calculating the regression coefficients for the CG height.

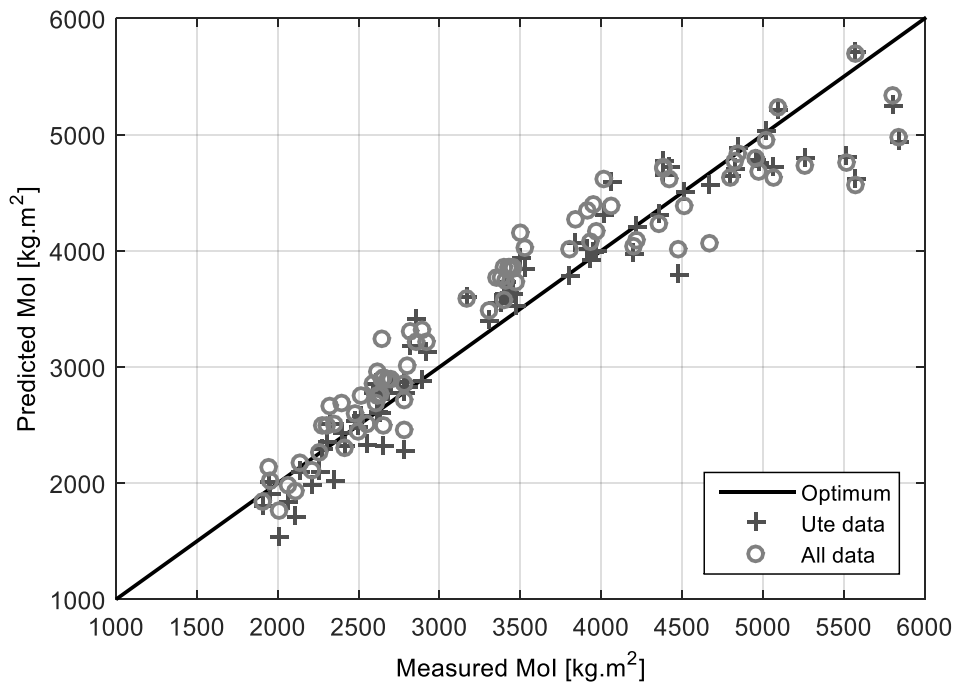


Figure 7-17: A comparison of using the all the NHTSA data versus only the utility vehicle data for calculating the regression coefficients for the pitch MOI.

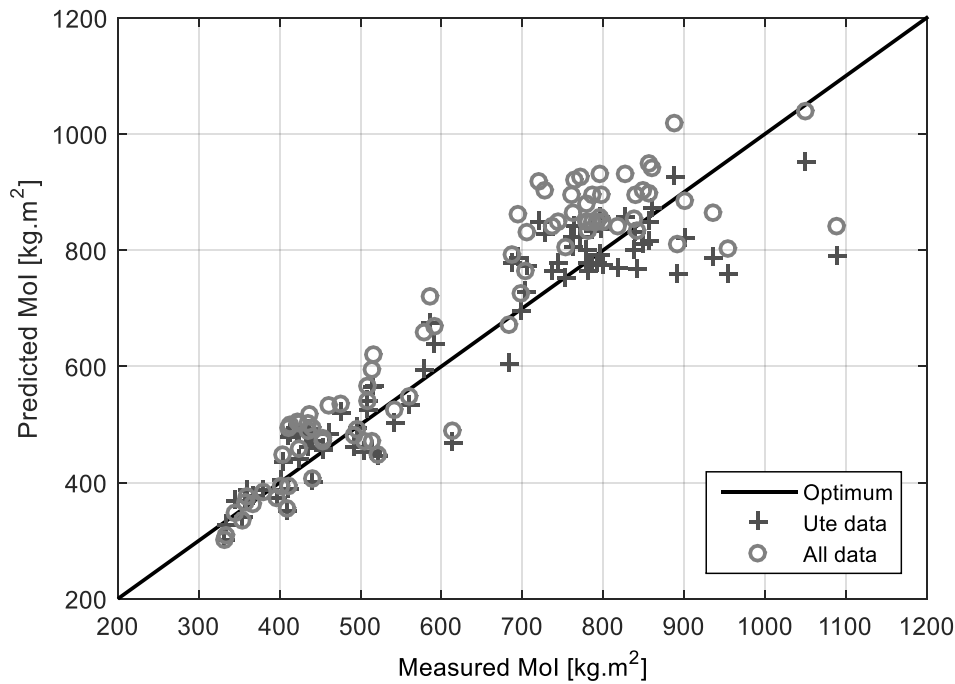


Figure 7-18: A comparison of using the all the NHTSA data versus only the utility vehicle data for calculating the regression coefficients for the roll MOI.

Figure 7-17 and Figure 7-18 show the effects of the regression base on the pitch and roll moments of inertia, respectively. Again focusing the regression analysis data into just the single type of vehicle increases the accuracy of the estimates. The figures have shown the results for only the utility vehicles, however they are representative of the results from the transport van data. The parameter estimates for UTE1 using linear regression are shown in Table 7-8.

Table 7-8: Mass properties of the entire vehicle for UTE1 obtained via linear regression of the NHTSA data statistics and physical measurement.

Parameter	Value
CG height above ground	0.63 m
CG distance from front axle (regression)	1.29 m
CG distance from front axle (measured)	1.36 m
I _{yy} (pitch)	3440 kg.m ²
I _{xx} (roll)	592 kg.m ²

As mentioned previously, numerical models require the CG location and MOI values of the body only. As the results of the NHTSA survey are that of the entire vehicle (body, suspension and wheels/tyres), further analysis is needed to find more accurate values of the body alone. If the unsprung mass values are known (Section 7.3.1), then estimates of their effects on the total

MOI can be made. To negate their effects, it is possible to use the basic geometric principles and the parallel axis theorem.

Figure 7-19 is an illustration of where the CG may be located on a vehicle. The NHTSA measured the horizontal location of the CG from the centre of the front axle, and its height from the ground. In its most basic form the location of the CG of the complete vehicle is a function of the location of the CG of each unsprung mass and the CG of the vehicle body itself. If the CG of the unsprung masses is assumed to be at the centre of the corresponding axle it is possible to solve for the location of vehicles body CG using Equation 7-10, a transposition of the centroid equation. The CG location left to right is unaffected by the unsprung masses, the CG location for the sprung mass is shown in Table 7-9.

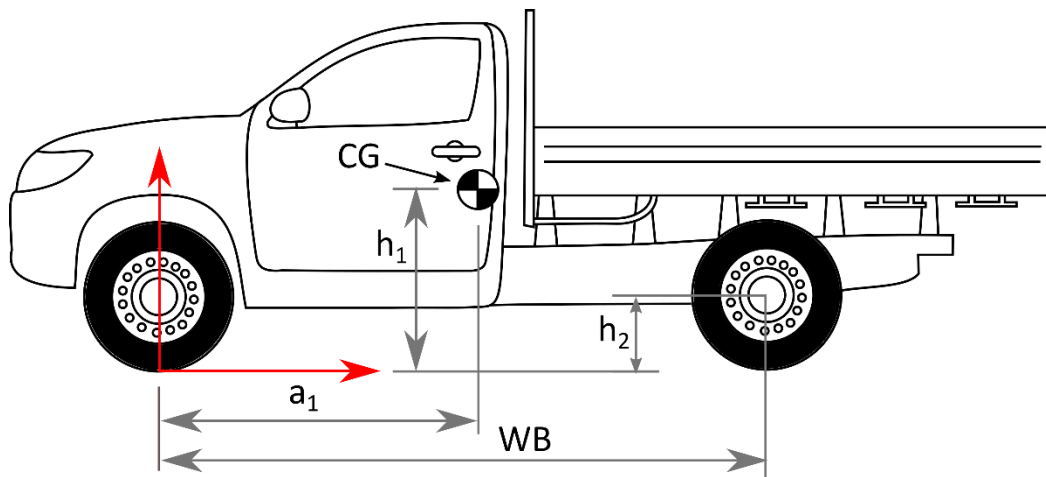


Figure 7-19: An illustration of where the CG may be located on a vehicle

$$CG_x = \frac{2(WBm_r) + a_1m}{m_{total}} \quad 7-10$$

$$CG_y = \frac{2(h_2mf + h_2mr) + h_1m}{m_{total}}$$

Table 7-9: Centre of gravity location of UTE1s' body (sprung mass) alone.

Parameter	Distance [m]
CG distance from front axle	1.16
CG height above ground	0.69
CG distance left to right	0.75

Similarly, the parallel axis theorem can be used to remove the inertial components of the unsprung masses from the overall inertia values. Looking at the pitch plane moment of inertia, the unsprung masses can be treated as point masses located at a distance from the CG. Accuracy

can be increased by treating the unsprung masses as a series of primary objects, such as cylinders and cuboids. However, this increase in accuracy is accompanied by a further complication of determining the masses of each component.

In the roll plane, the unsprung masses need to be treated slightly differently, due to the differential and drive shaft assembly running laterally across the vehicle. In this instance the differential and drive shaft assembly are treated as a circular cylinder, however the wheels and brakes remain as point masses. The MOI for the sprung mass are shown in Table 7-10.

Table 7-10: Moments of inertia about the vehicle body (sprung mass) alone, with the effects of the suspension removed.

Parameter	Inertia [kg.m²]
I _y (pitch)	2681
I _x (roll)	474

Using the focused linear regression analysis and the removal of the effects of the unsprung masses, it is possible to obtain acceptable estimates of a vehicle's inertial properties and CG location from its geometric properties. When transporting freight, the mass, centre of mass and inertial properties of the load combine with that of the vehicle. If the properties of the load are known, new estimates can be made by using the reverse of the above process.

7.3.4 Concluding Comments for Estimating Vehicle Properties

This section has outlined the various methods used to estimate all of the vehicle parameters needed for a numerical model. The intended use for the numerical model is to perform a sensitivity analysis and a comparative study to complement the results of the physical experiments. As such, exact values of the parameters are not required, only reasonable estimates. Trade-offs were made between the accuracy of the results and the difficulty to undertake the measurements.

Several complexities were identified with measuring each vehicle parameter. These ranged from needing to disassemble the vehicle, to not being able to measure the parameters due the scale of the equipment needed. Each problem was overcome at the cost of accuracy in some cases. Table 7-11 contains the complete list of the estimates of all vehicle properties used within the numerical model, as well as the method used to obtain them.

Table 7-11: Table of parameter base values used for the numerical experiments.

Parameter	Value	Estimation Method
Sprung mass	1,256 kg	Physical measurement
Sprung mass (two occupants)	1,428 kg	Physical measurement
Front unsprung mass	35 kg	Physical measurement
Rear unsprung mass	101 kg	Physical measurement
Front suspension stiffness	43.5 kN/m	Physical measurement
Rear suspension stiffness	54.6 kN/m	Physical measurement
Front damping coeff.	2264 N.s/m	Experimental estimate
Rear dampers coeff.	2925 N.s/m	Experimental estimate
Front tyre (240 kPa)	174 kN/m	Physical measurement
Rear tyre (420 kPa)	349 kN/m	Physical measurement
Tyre damping coeff.	1048 N.s/m	Estimate from literature
CG distance from front axle	1.16 m	Physical measurement
CG height above ground	0.69 m	Statistical estimate
CG distance left to right	0.75 m	Physical measurement
I_y (pitch)	2681 kg.m ²	Statistical estimate
I_x (roll)	474 kg.m ²	Statistical estimate
Anti-roll bar stiffness	N.m/rad	Estimate

7.4 Chapter Conclusion

This chapter outlined the processes used to create a numerical model for analysing multi-dimensional vehicle response. The selected vehicle is represented by a 7DoF system, with the heave, pitch and roll response of the sprung mass (vehicle body) being of primary concern.

Taking a bottom-up approach, a synthetic road elevation profile was first generated. Traditional techniques for synthesising wheel paths were improved, with a new technique developed to create dual wheel paths. The newly developed method allows for target PSD functions to be specified as well as a target coherence between the two.

The dual wheel paths were needed to excite the roll motion of the full car numerical model. Pitching motion is excited by having a time delay between the front and rear wheels. The EoM used within the numerical model were modified versions of published equations. The seven degrees of freedom of the numerical model meant that accurate parameter values are needed to obtain a realistic response.

Load-deflection tests were carried out to determine the tyre and suspension stiffnesses. Vehicle damping was estimated using the random decrement technique. The results of the physical experiments were used for the random decrement analysis with acceptable results for this comparative study.

The vehicle was partially disassembled to take measurements of the sprung and unsprung masses. The CG location was also measured at this time, however it could only be measured longitudinally and laterally. The CG height is not required for the numerical model, however it is needed to calculate changes in the moments of inertia.

The vehicles' centre of gravity height and moments of inertia were estimated statistically from a large collection of measured values from the NHTSA. Linear regression was performed on the NHTSAs' Light Vehicle Inertial Parameter Database, and estimates could be obtained as long as the physical dimensions of the vehicle were known. It was found that by arranging and limiting the database to selected vehicle types the accuracy of the results could be increased.

The numerical model requires the moments of inertial and centre of gravity location for the vehicle body alone, excluding the effects of the suspension. Since the NHTSAs' database lists the values for the complete vehicle, some manipulation of the data was required. Having determined the unsprung masses allowed for the parallel axis theorem and other mathematical techniques to be used to remove their effects from the estimates. This resulted in only the moments of inertia and centre of gravity location for the vehicle body. With a validated model and realistic starting values it is now possible to carry out the sensitivity analysis.

Chapter 8

Numerical Simulation - Results and Discussion

The physical experiments identified some potential relationships between the heave, pitch and roll vibratory motion of the vehicles tested. The uncontrolled nature of the experiments, low number of configurations possible and the inability to isolate the effects of individual parameters made it difficult to further explore these potential relationships.

This chapter presents the results from a series of simulations carried out using the numerical model developed in the previous chapter. Five parameters are investigated to assess their impacts on the vehicles vibratory response. The first section assesses the influences of the simulated vehicle speed. The second section shows the results from varying road roughness. The coherence between wheel paths was not investigated as it is outside the scope of the research. The final three sections focus on vehicle parameters, specifically; sprung mass, moments of inertia and vehicle wheelbase.

A 50 km dual wheel-path synthetically-generated B-class road elevation profile is used as the excitation. Simulations were ran at a constant speed of 80 km/h. Vehicle parameters listed in Table 7-11 are used within the numerical model (unless it is the parameter being investigated). The vertical acceleration response was measured directly above the rear axle for all simulations.

8.1 On the Effects of Vehicle Speed

Vehicle speed was varied between 60 and 100 km/h for the following series of simulations. Figure 6-22 and Table 8-1 display how the pitch:heave and roll:heave RMS ratios vary with speed. A slight reduction in the pitch:heave ratio is observed as speed increases. This agrees with the physical experiments which showed the same response to vehicle speed. The roll:heave ratio initially decreases before steadily increasing with speed. As speed is increased the RMS of all vibratory modes also increases.

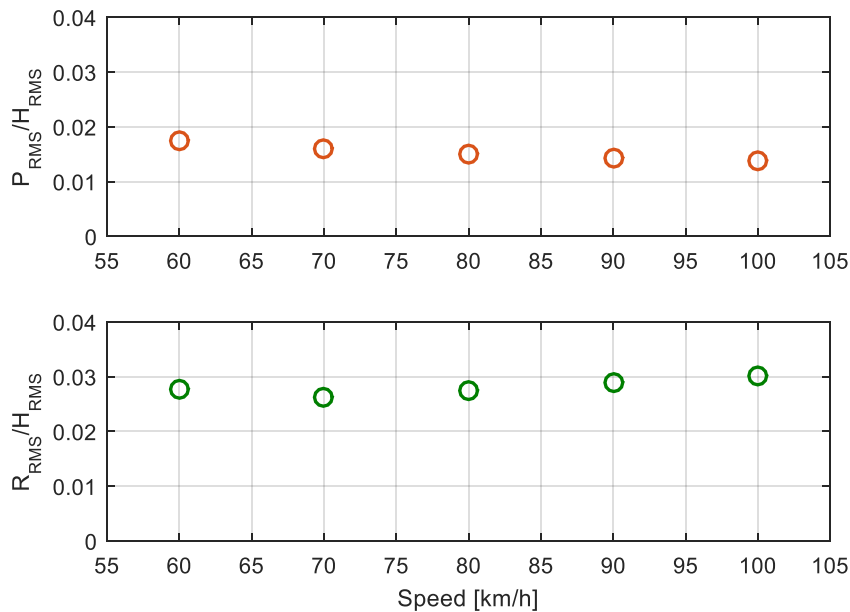


Figure 8-1: The effects of speed on the ratio between the pitch RMS and heave RMS (top) and the ratio between the roll RMS and heave RMS (bottom).

Table 8-1: A table summarising the RMS ratios for the differing simulated speeds.

Speed [km/h]	H_{RMS} [m/s ²]	P_{RMS} [rad/s]	R_{RMS} [rad/s]	P_{RMS}/H_{RMS} [(rad.s)/m]	R_{RMS}/H_{RMS} [(rad.s)/m]
60	1.60	2.80×10^{-2}	4.41×10^{-2}	1.75×10^{-2}	2.76×10^{-2}
70	1.76	2.82×10^{-2}	4.64×10^{-2}	1.60×10^{-2}	2.63×10^{-2}
80	1.91	2.86×10^{-2}	5.24×10^{-2}	1.50×10^{-2}	2.75×10^{-2}
90	2.05	2.92×10^{-2}	5.91×10^{-2}	1.43×10^{-2}	2.89×10^{-2}
100	2.18	2.99×10^{-2}	6.54×10^{-2}	1.38×10^{-2}	3.01×10^{-2}

Figure 6-23 shows a comparison of the vertical acceleration moving RMS PDFs. The increasing speed is met with an increase in mode, as the vertical acceleration tends towards a higher RMS. The maximum probability density decreases and is met with an increase in the standard deviation as speed rises. These traits were also observed within the physical experiments.

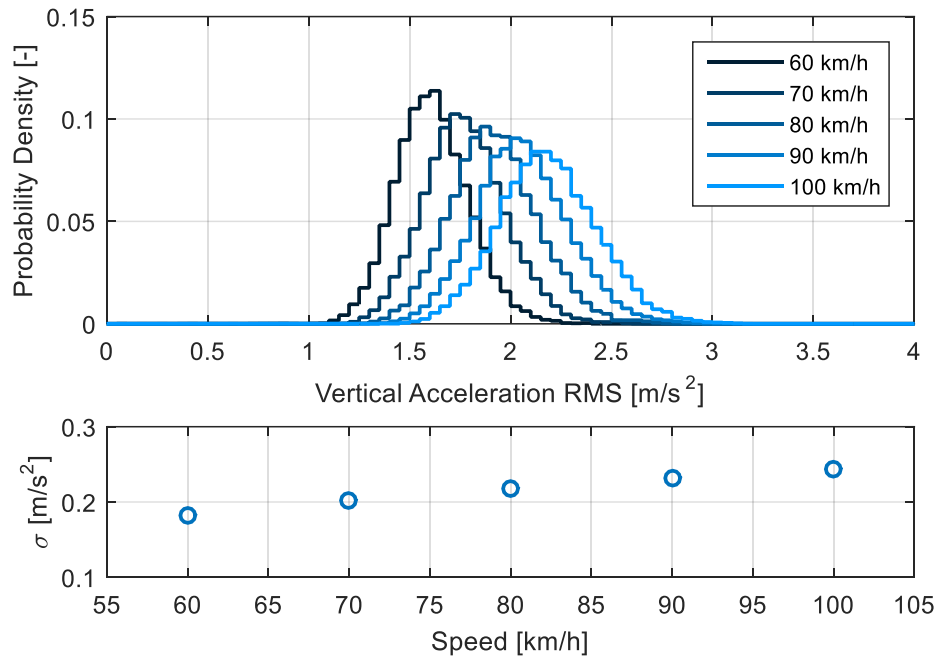


Figure 8-2: A comparison of the of the vertical acceleration moving RMS (2 second window, maximum overlap) PDFs for speeds between 60 and 100km/h (top) and a comparison of the standard deviation at each speed (bottom).

Figure 6-24 displays the pitch angular velocity moving RMS PDFs. The pitch response's distribution varies slightly with speed compared to the heave response. A migration towards higher RMS levels is observed and the maximum probability density fluctuates within a small range. The standard deviation decreases slightly with speed.

PDFs of the roll angular velocity moving RMS are shown in Figure 6-25. As speed is increased, a considerable drop in the maximum probability density is observed, this is coupled with a migration towards higher levels of roll response (mode). The standard deviation also increases consistently with speed as the distributions become more dispersed.

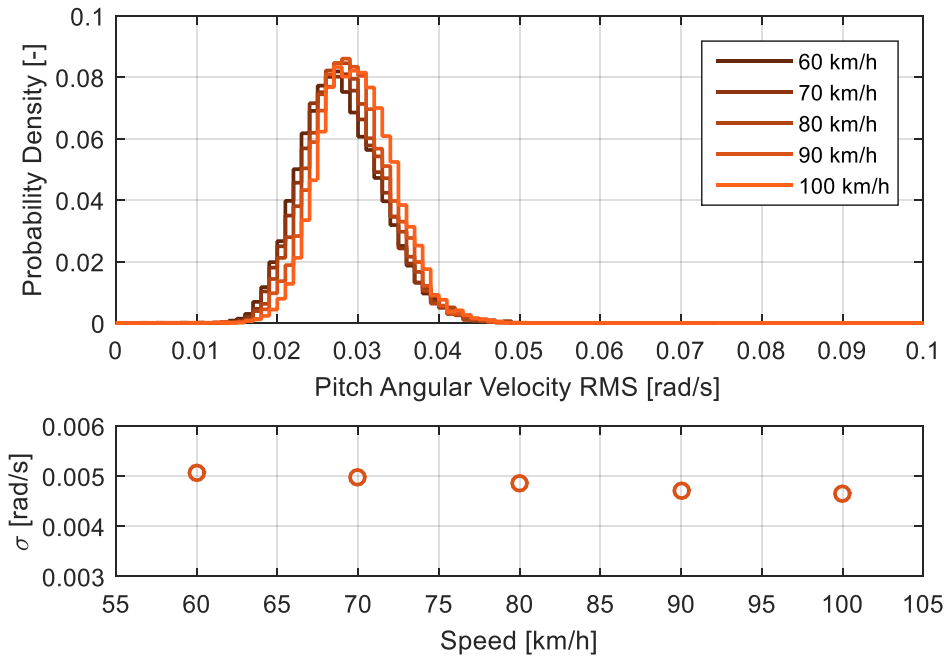


Figure 8-3: A comparison of the of the pitch angular velocity moving RMS (2 second window, maximum overlap) PDFs for speeds between 60 and 100km/h (top) and a comparison of the standard deviation at each speed (bottom).

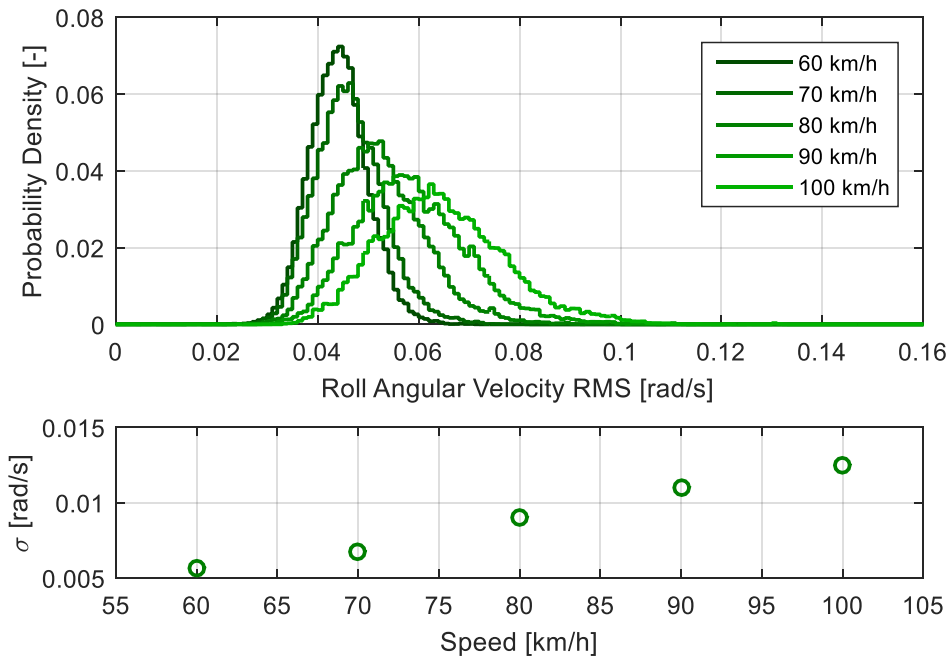


Figure 8-4: A comparison of the of the roll angular velocity moving RMS (2 second window, maximum overlap) PDFs for speeds between 60 and 100km/h (top) and a comparison of the standard deviation at each speed (bottom).

Figure 6-26 shows a comparison of the 60 km/h (left) and 90 km/h (right) heave-pitch bivariate histograms. The data cloud translates towards higher levels of vertical acceleration with the increased speed. The maximum pitch angular velocity remains similar with the increased speed, although range is reduced. The maximum probability density decreases with the higher speed. A change in gradient is also observed.

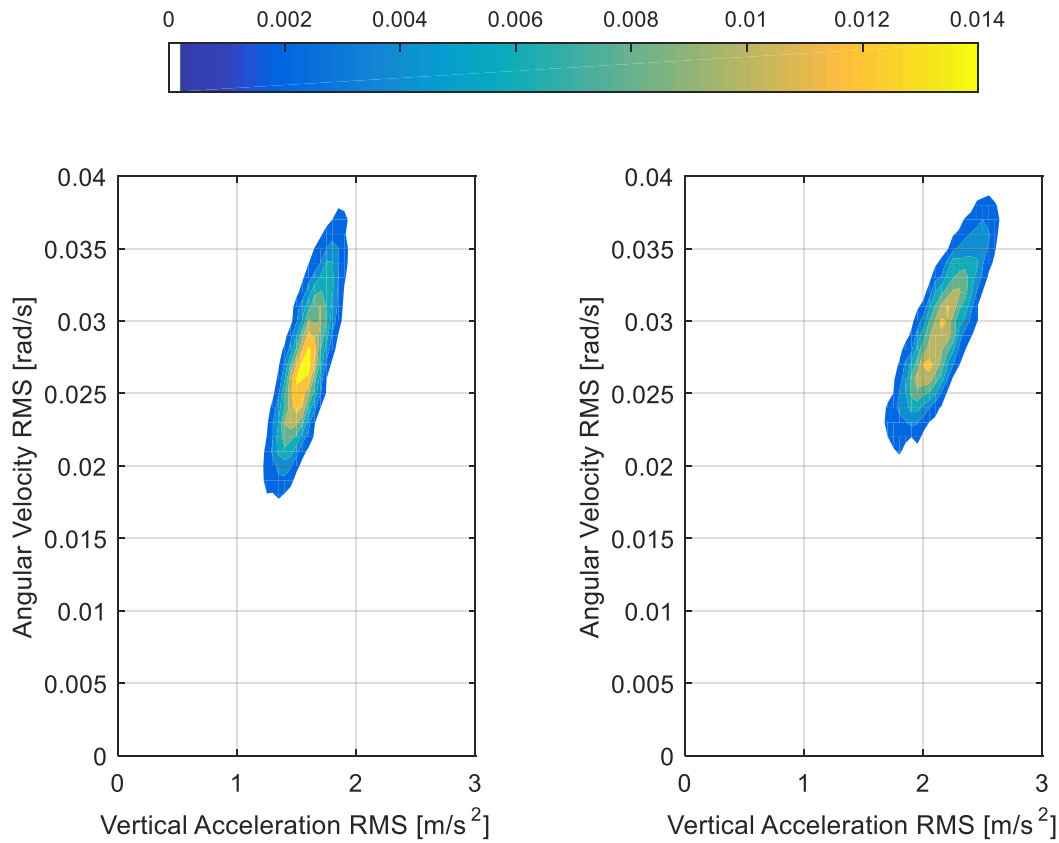


Figure 8-5: Comparison of vertical acceleration-pitch angular velocity bivariate histograms at 60 km/h (left) and 100 km/h (right).

Table 6-5 contains the properties of linear models fitted to the heave vs. pitch RMS data clouds. The gradient varies consistently with speed as show in Figure 6-27, unlike the physical experiments the relationship appears non-linear. R^2 values improve as speed increases, whilst the RMSE (RMS error) is low and improves with speed, indicating that the heave-pitch relationship gets stronger as the speed is increased.

Table 8-2: A table summarising linear models fit to the heave vs pitch RMS scatter plots.

Speed [km/h]	Gradient	Y-Intercept	R^2	RMSE
60	0.0220	-0.0075	0.6220	0.0031
70	0.0199	-0.0071	0.6483	0.0030
80	0.0181	-0.0061	0.6590	0.0028
90	0.0167	-0.0052	0.6698	0.0027
100	0.0158	-0.0046	0.6915	0.0026

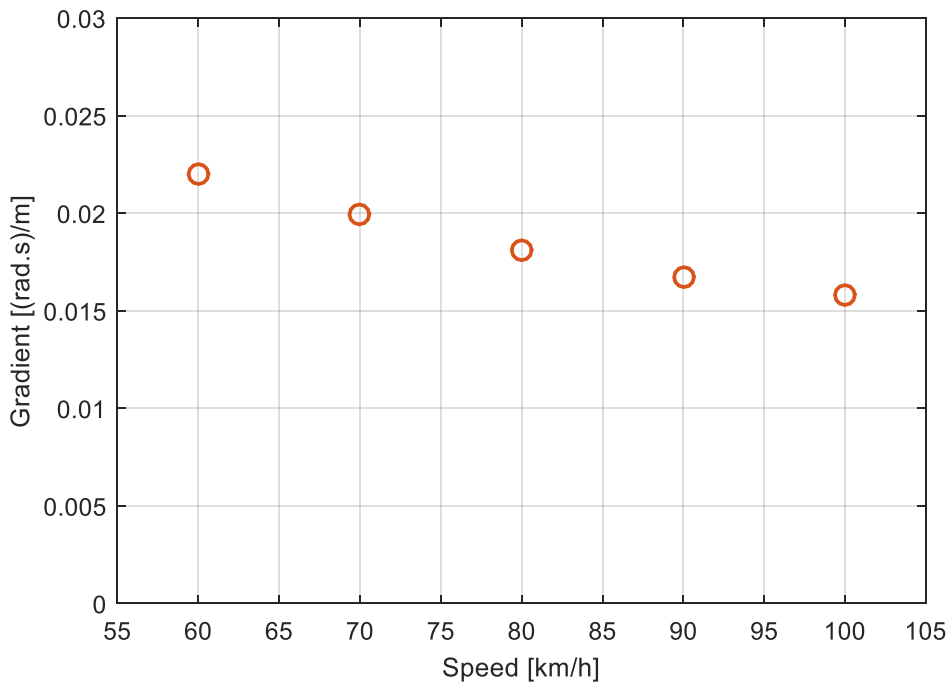


Figure 8-6: A comparison of the heave-pitch RMS scatter plot gradient as speed varies.

Figure 6-28 shows a comparison of the 60 km/h (left) and 90 km/h (right) heave-roll bivariate histograms. The histograms share little similarities with those obtained from the physical experiments, with the comet trail appearance being replaced with a circular distribution. The cause of this is believed to be an unrealistic excitation due to the synthetic road elevation profile, with the roll excitation (elevation difference between the left and right wheel paths) being too severe across the frequency (spatial) band. Although, some conclusions can still be drawn from the results, a significant drop in the probability density is observed with the increase in speed. Also translations towards higher levels of vertical acceleration and pitch angular velocity can be seen.

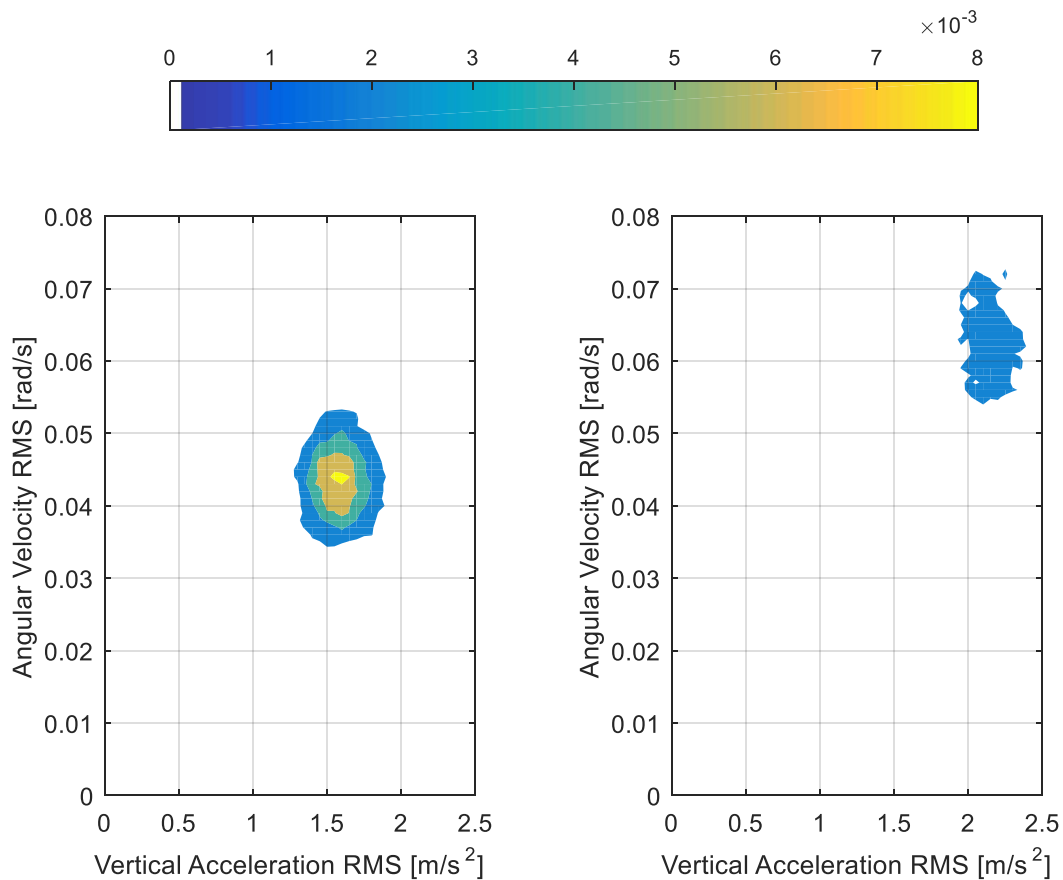


Figure 8-7: Comparison of vertical acceleration-roll angular velocity bivariate histograms at 60 km/h (left) and 100 km/h (right).

Table 8-3 contains a summary of linear models fitted to the heave-roll scatter plots. It is important to remember here that although the bivariate histograms share similarities with the RMS scatter plots, they do not show all data points due to their low probability density. The distribution of the data means that the data cannot be described using a linear model, this is highlighted by the R2 values being near zero for all of the simulations. The gradient (and

change in gradient) can therefore not be used for a point of comparison. Unfortunately, this problem was found to persist through all simulations.

Table 8-3: A table summarising linear models fit to the heave vs roll RMS scatter plots.

Speed [km/h]	Gradient	Y-Intercept	R ²	RMSE
60	0.0000	0.0437	0.0000	0.0057
70	-0.0002	0.0463	0.0001	0.0068
80	-0.0007	0.0530	0.0003	0.0090
90	-0.0005	0.0592	0.0001	0.0110
100	-0.0002	0.0646	0.0000	0.0125

PDFs of the PCA-adjust heave-pitch data (Figure 8-8) show that the distribution about the principal axis remains similar for all speeds. The maximum probability density is reduced as speed increases, this is also met with a consistent, although slight, reduction in the standard deviation.

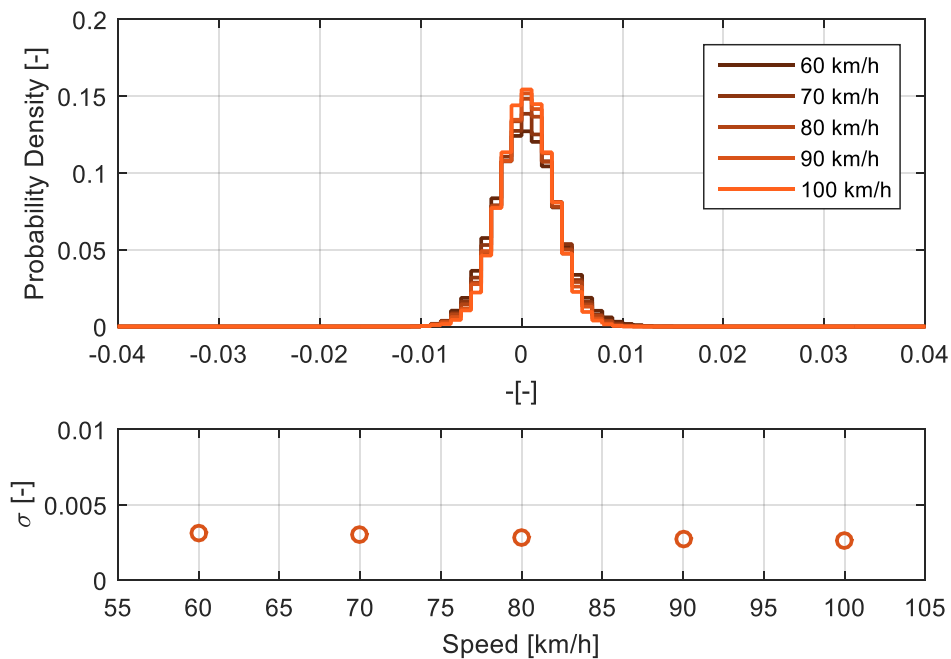


Figure 8-8: A comparison of PDFs taken parallel to the principal axis from the PCA adjusted heave-pitch RMS scatter plots as speed is varied (top) and the change is standard deviation (bottom).

The circular shaped distribution of the of the heave-roll scatter plot still allows for the use of PCA. Figure 6-31 shows a comparison of the PDFs from the PCA-adjusted data. As speed increases the roll PDFs becomes far more dispersed, resulting in an increase in standard deviation. The increase in standard deviation does not appear to vary linearly with the increase in speed. The increased standard deviation is met with a reduction of the maximum probability density.

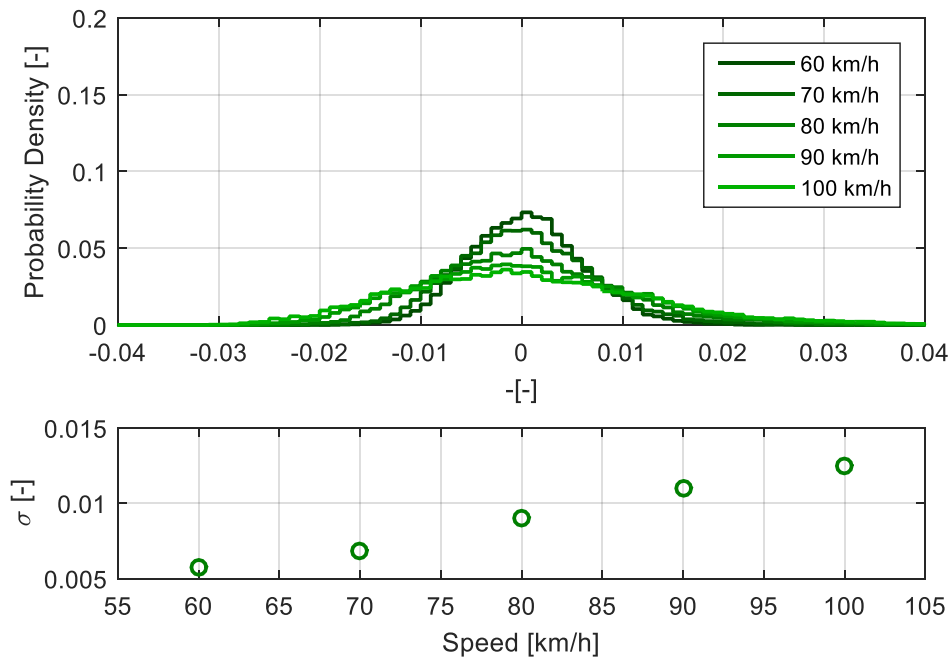


Figure 8-9: A comparison of PDFs taken parallel to the principal axis from the PCA adjusted heave-roll RMS scatter plots as speed is varied (top) and the change in standard deviation (bottom).

Figure 6-32, Figure 6-33 and Figure 6-34 show a comparison of the PSD functions for heave, pitch and roll response respectively. The RMS vertical acceleration increases with speed which is well documented. The ripples in the higher frequency range of the PSD are the remnants of wheelbase filtering that was removed by measuring the vehicles response away from the CG (for more information see Appendix B).

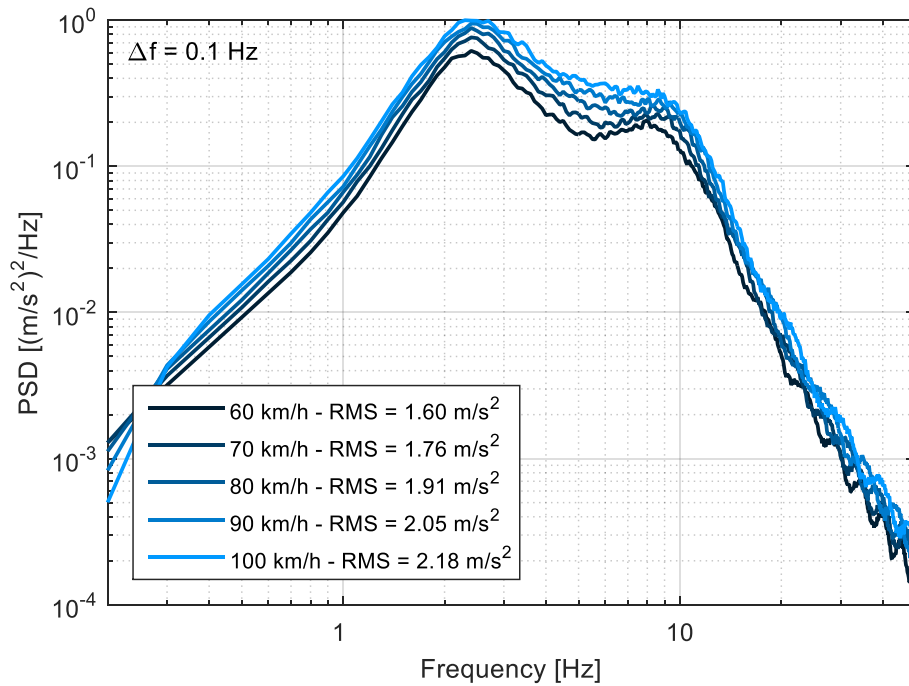


Figure 8-10: A comparison of the vertical acceleration PSD functions at multiple speeds.

Figure 6-33 shows a comparison of the pitch angular velocity PSD. The RMS of the pitch PSDs increases slightly with speed, although this is not reflected within the figure legend. It is interesting that at lower speeds more energy is contained within the lower frequency range (up to the second peak). The effects of wheelbase filtering are evident from approximately 5.4 Hz at 60 km/h.

The roll response PSDs, shown in Figure 6-34, vary considerably more than the other two vibratory modes when the speed is varied. The PSD exhibits severe wheelbase filtering effects, however no research on this effect was found. Some cross-talk appears to occur between the roll and heave vibration, which is not unexpected. The roll response nodes (anti-resonance) do not occur at the same frequencies as those seen the pitch response. The frequencies are similar to those which should occur within the heave response, however they do not match exactly. A significant increase in the RMS occurs as speed increases.

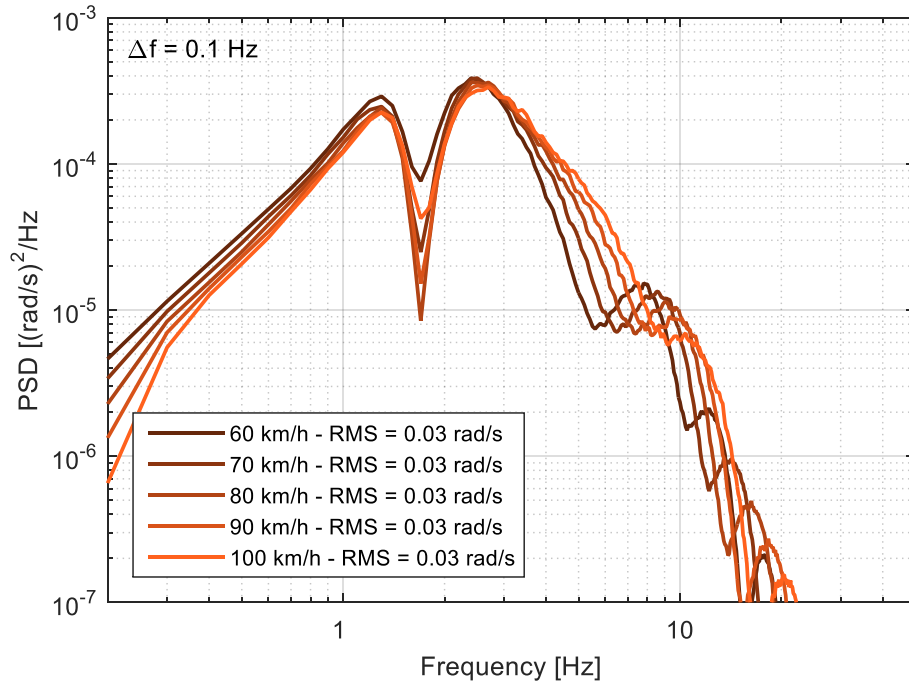


Figure 8-11: A comparison of the pitch angular velocity PSD functions at multiple speeds.

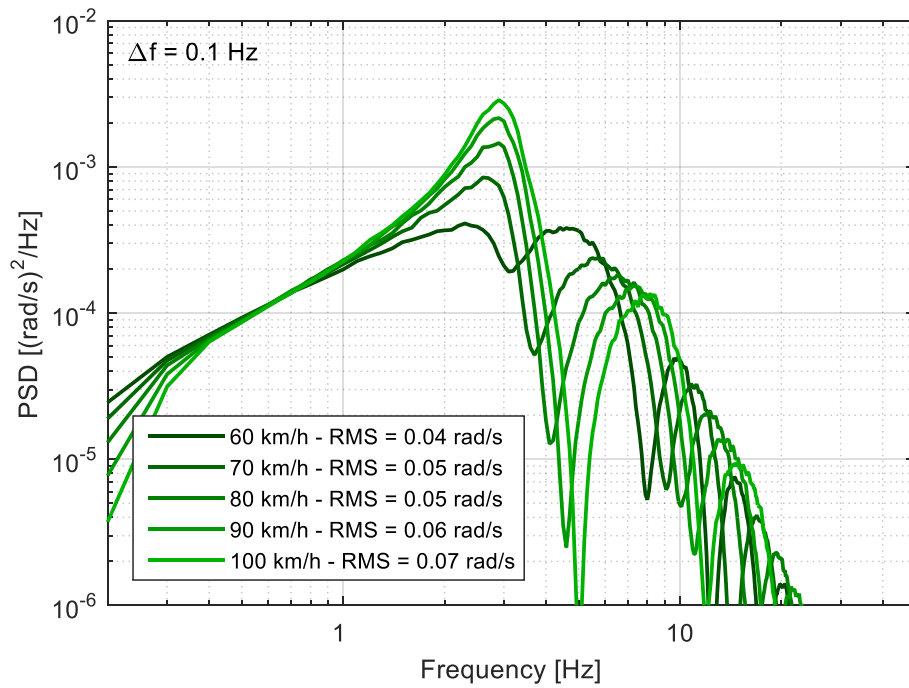


Figure 8-12: A comparison of the roll angular velocity PSD functions at multiple speeds.

The frequency response functions calculated between the vertical vibration and the pitch response are shown in Figure 6-35. The flat sections at the beginning of the pitch FRFs, evident across all speeds, continues until approximately 1.5 Hz, this corresponds with the first peak in the pitch PSD. The secondary peak in the FRF, at around 2.5 Hz also aligns with the second peak in the pitch PSD as well as the primary peak in the Heave PSD. Above 5 Hz the effects of wheelbase filtering take over, with an overall steady decay of $1/f$.

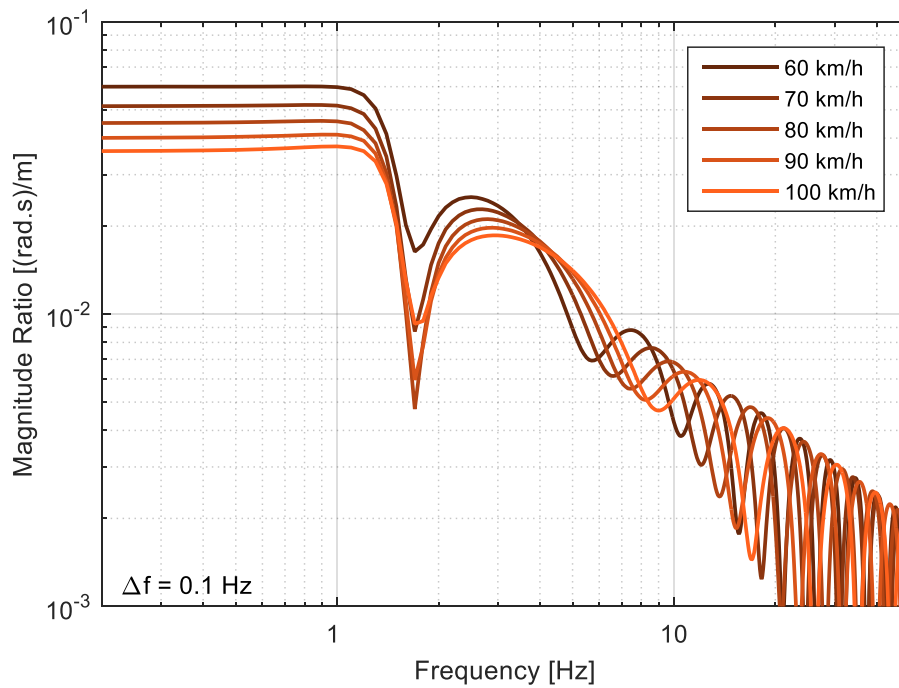


Figure 8-13: A comparison of the frequency response functions between the pitch angular velocity and vertical acceleration as speed varies.

The roll-heave FRFs shown in Figure 6-36 reveal the cross talk between the differing vibratory modes. The magnitude ratio decreases from its initial level until reaching the natural frequency of the roll response, although this also aligns with the natural frequency of the vertical vibration. The slower speeds contain more energy in the lower frequency band, until approximately 1 Hz.

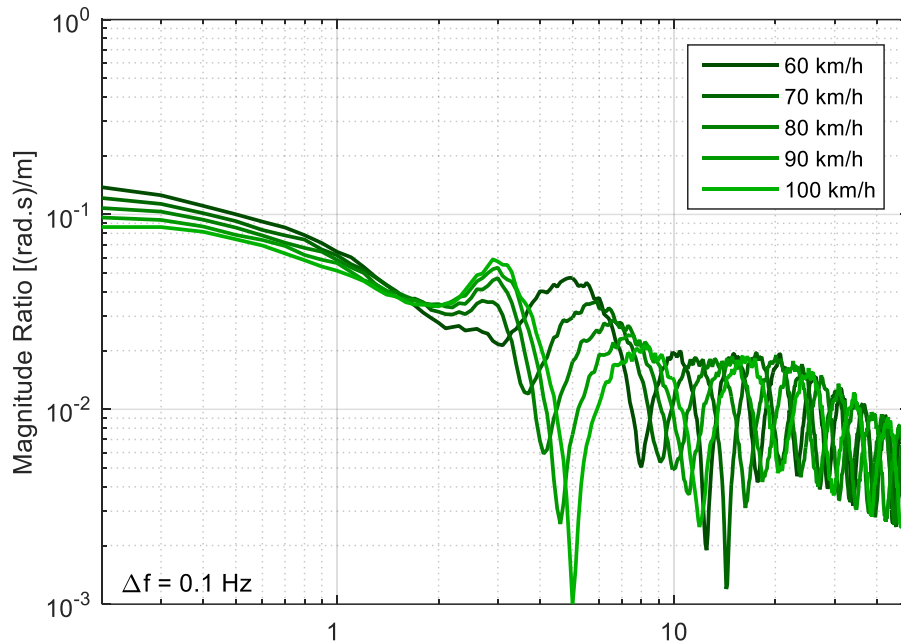


Figure 8-14: A comparison of the frequency response functions between the roll angular velocity and vertical acceleration as speed varies.

8.2 On the Effects of Road Roughness

The following section shows the results for simulations in which the road elevation profile was varied. Road elevation profiles ranging from an A – C classification were used (according to ISO 8608) for the excitation, a summary of the profiles roughness is shown in Table 8-4.

Table 8-4: A table summarising the road classifications elevation RMS.

Road Classification	Elevation RMS
A	5.66×10^{-3} m
B	11.3×10^{-3} m
C	22.6×10^{-3} m

Table 8-5 contains a summary of the RMS ratios for the three roughness classes, for all road classifications the RMS ratio did not vary despite a change in the RMS levels. Meaning that the RMS ratio is solely dependent on the vehicle parameters in these simulations. However, in the simulations all three road elevation profiles have the same spectral shape and the coherence between wheel paths, which is unlikely in reality.

This is significant because, as discussed previously, increasing the vehicle speed has the same effect as making the road rougher (when focusing on a specific frequency bandwidth), but increasing the vehicles speed changes the RMS ratios.

Table 8-5: A table summarising the RMS ratios for the differing road roughness levels

Road Class	H_{RMS} [m/s²]	P_{RMS} [rad/s]	R_{RMS} [rad/s]	P_{RMS}/H_{RMS} [(rad.s)/m]	R_{RMS}/H_{RMS} [(rad.s)/m]
A	0.96	1.43x10 ⁻²	2.61x10 ⁻²	1.50x10 ⁻²	2.73x10 ⁻²
B	1.91	2.87x10 ⁻²	5.21x10 ⁻²	1.50x10 ⁻²	2.73x10 ⁻²
C	3.83	5.74x10 ⁻²	10.4x10 ⁻²	1.50x10 ⁻²	2.72x10 ⁻²

Significant changes occur in the vertical acceleration moving RMS PDFs, as seen in Figure 8-15. A significant change in the mode occurs, increasing with the rougher road surface. A decrease in the maximum probability density occurs as the RMS vertical acceleration becomes more dispersed, which also manifests as an increase in the standard deviation. The same changes in the distribution characteristics are also seen in both the pitch (Figure 8-16) and roll (Figure 8-17) response.

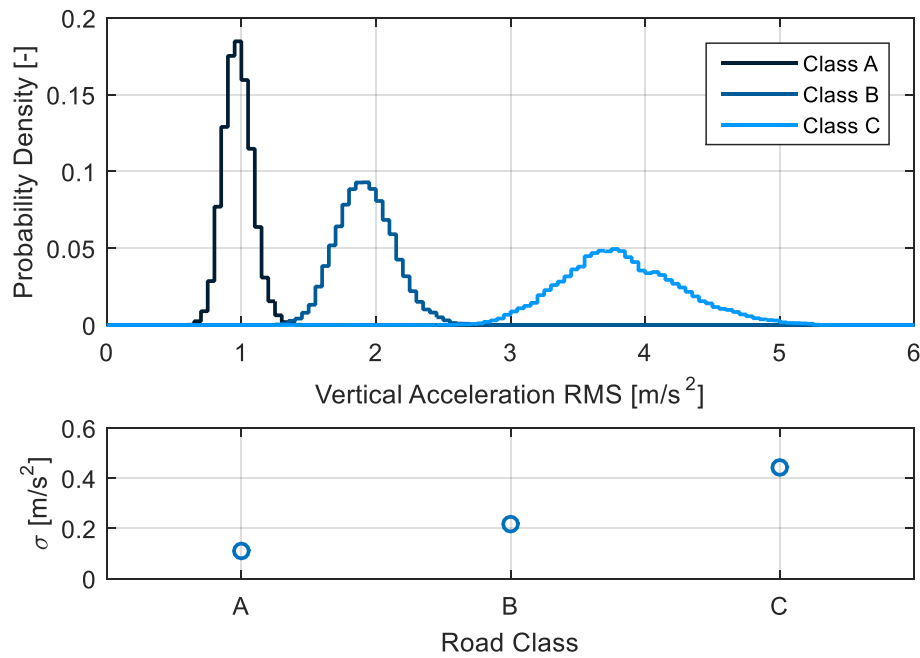


Figure 8-15: A comparison of the of the vertical acceleration moving RMS (2 second window, maximum overlap) PDFs for varying road roughness classes (top) and a comparison of the standard deviation (bottom).

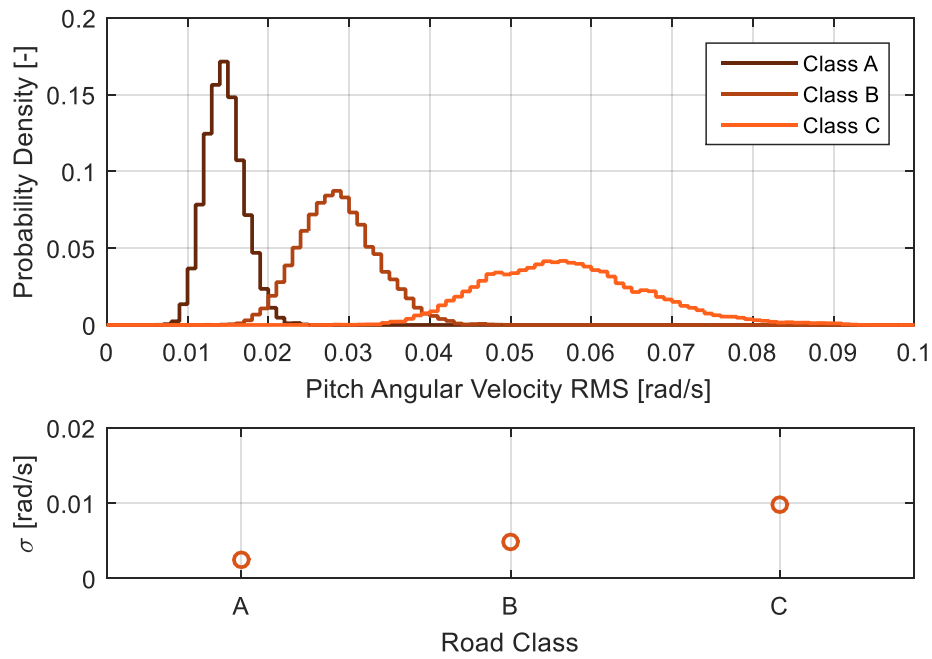


Figure 8-16: A comparison of the of the pitch angular velocity moving RMS (2 second window, maximum overlap) PDFs for varying road roughness classes (top) and a comparison of the standard deviation (bottom).

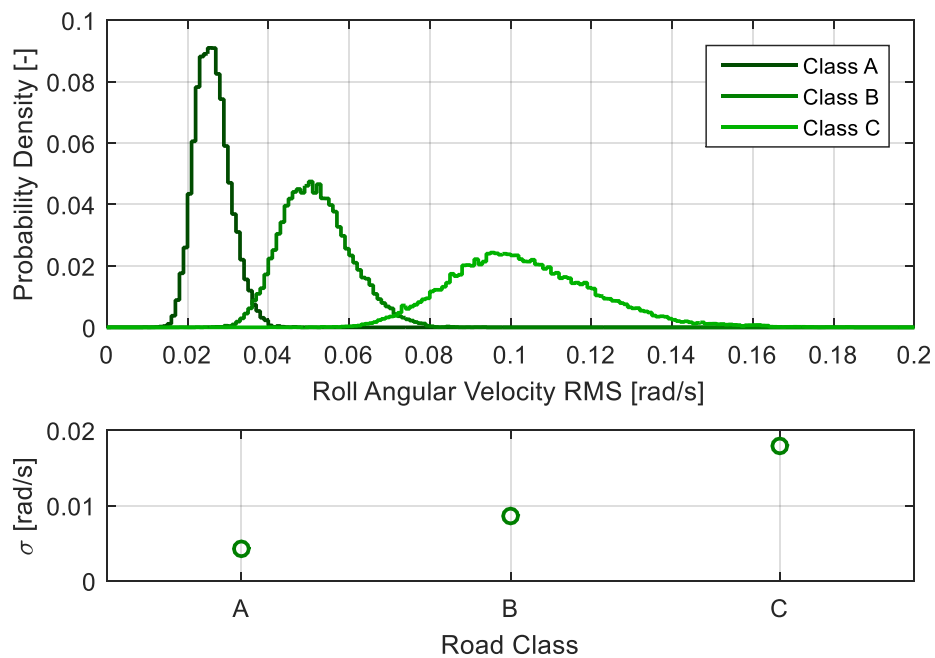


Figure 8-17: A comparison of the of the roll angular velocity moving RMS (2 second window, maximum overlap) PDFs for varying road roughness classes (top) and a comparison of the standard deviation (bottom).

Figure 8-18 shows a comparison of the A-class (left) and C-class (right) heave-pitch bivariate histograms. Most notably, a significant translation towards higher levels of vertical acceleration and pitch angular velocity occurs with the rougher road. The maximum probability density also decreases for the C-class road. The gradient appears similar between the two road roughness classes, fitted linear models support this observation, with the gradient of both histograms being comparable as seen in Table 8-6, which contains a summary of the linear regression performed on the data. The gradient remains similar between all road classes, demonstrating that the gradient is relatively independent of the road surface. The RMSE increases along with the road roughness, the R^2 values remain consistent between the simulations.

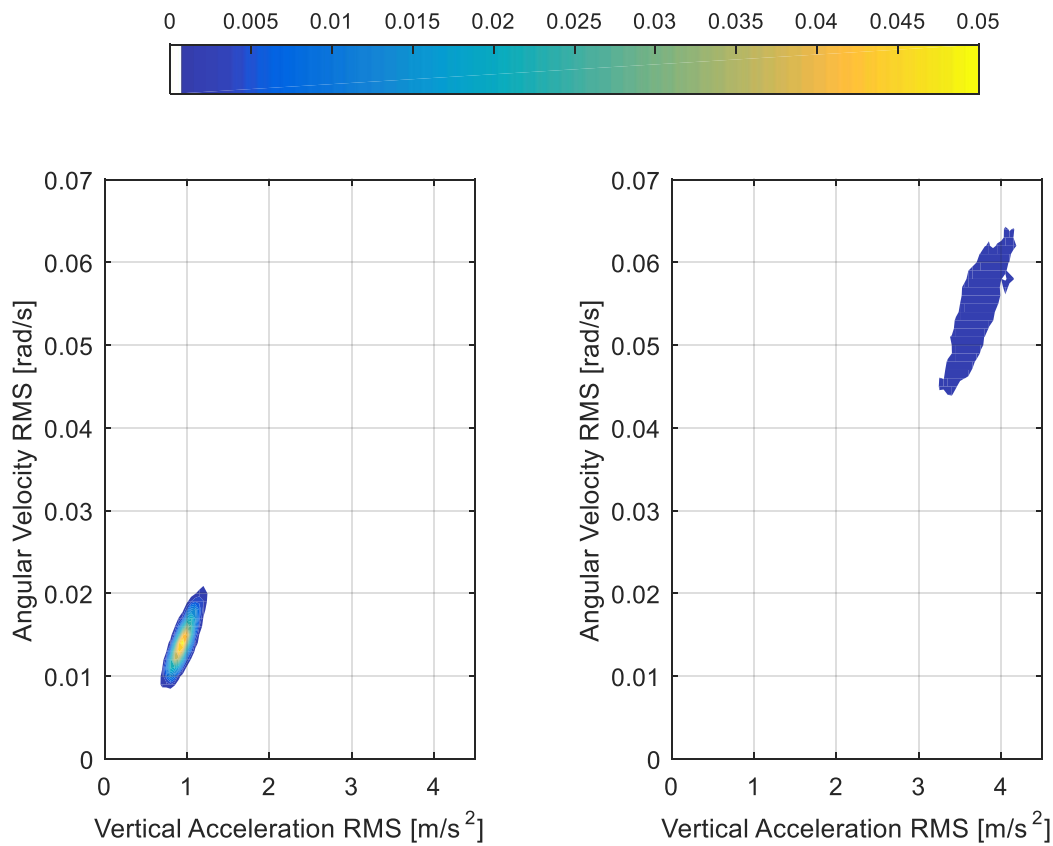


Figure 8-18: Comparison of vertical acceleration-pitch angular velocity bivariate histograms for an A-class road (left) and a C-class road (right).

Table 8-6: A table summarising linear models fit to the heave vs pitch RMS scatter plots.

Road Class	Gradient	Y-Intercept	R^2	RMSE
A	0.0180	-0.0030	0.6486	0.0014
B	0.0180	-0.0059	0.6486	0.0028
C	0.0185	-0.0137	0.6741	0.0056

A comparison of the heave-roll bivariate histograms was not possible as the roll response data became far too dispersed when using the C-class road. This dispersion is best observed in the significantly higher RMSE (Table 8-7) for the C-class road and also within the heave-roll PCA PDF (Figure 8-20)

Table 8-7: A table summarising linear models fit to the heave vs roll RMS scatter plots.

Road Class	Gradient	Y-Intercept	R ²	RMSE
A	0.0000	0.0257	0.0000	0.0043
B	0.0000	0.0514	0.0000	0.0086
C	0.0016	0.0966	0.0015	0.0179

Figure 8-19 displays the distributions of the heave-pitch PCA-adjusted RMS scatter plots for the varying road roughness classes. As the road roughness increases the data becomes substantially more dispersed, resulting in a decreased maximum probability density and an increased standard deviation.

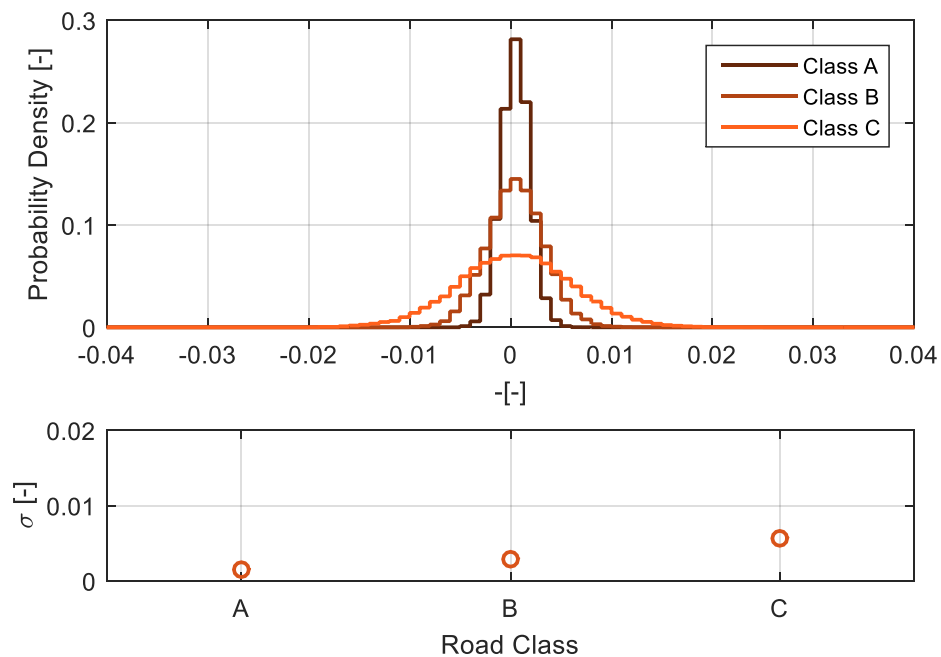


Figure 8-19: A comparison of PDFs taken parallel to the principal axis from the PCA adjusted heave-pitch RMS scatter plots as road roughness is varied (top) and the change in standard deviation (bottom).

The same changes in distribution also occur to the heave-roll PCA-adjusted data, seen in Figure 8-20. As the gradient is effectively zero from the linear models fitted to the RMS scatter plots, the standard deviation from the roll RMS PDFS is equal to the standard deviation of the PCA-adjusted data.

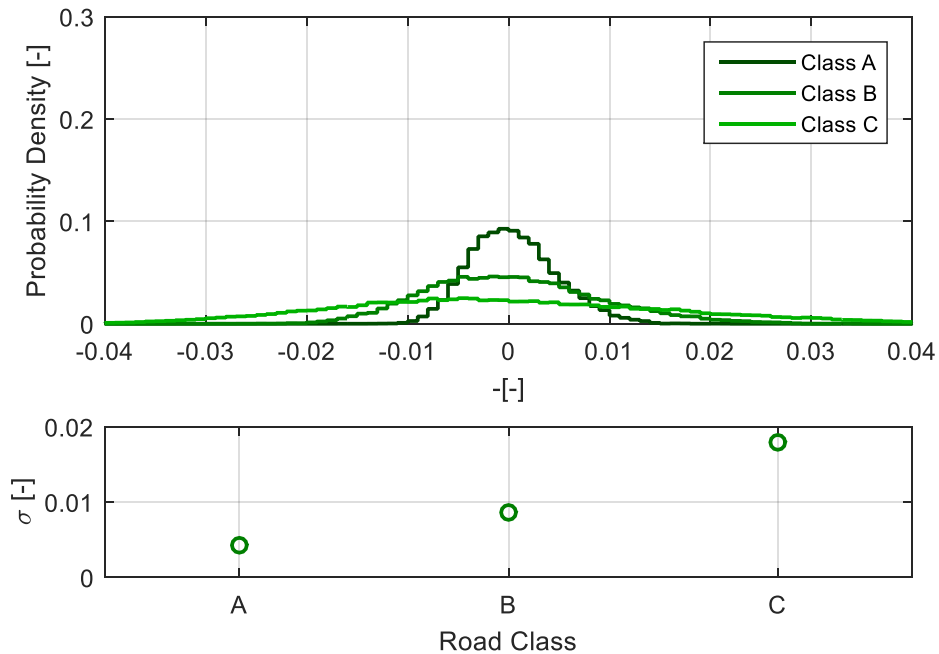


Figure 8-20: A comparison of PDFs taken parallel to the principal axis from the PCA adjusted heave-roll RMS scatter plots as road roughness is varied (top) and the change in standard deviation (bottom).

Figure 8-21, Figure 8-22 and Figure 8-23 contain a comparison of the heave, pitch and roll PSD functions for the different road roughnesses. For each vibratory mode the PSD function is simply translated towards a higher RMS as the road roughness increases. This is expected as the numerical model is linear, and the excitation spectrum shape remains the same for each class, with only the RMS increasing.

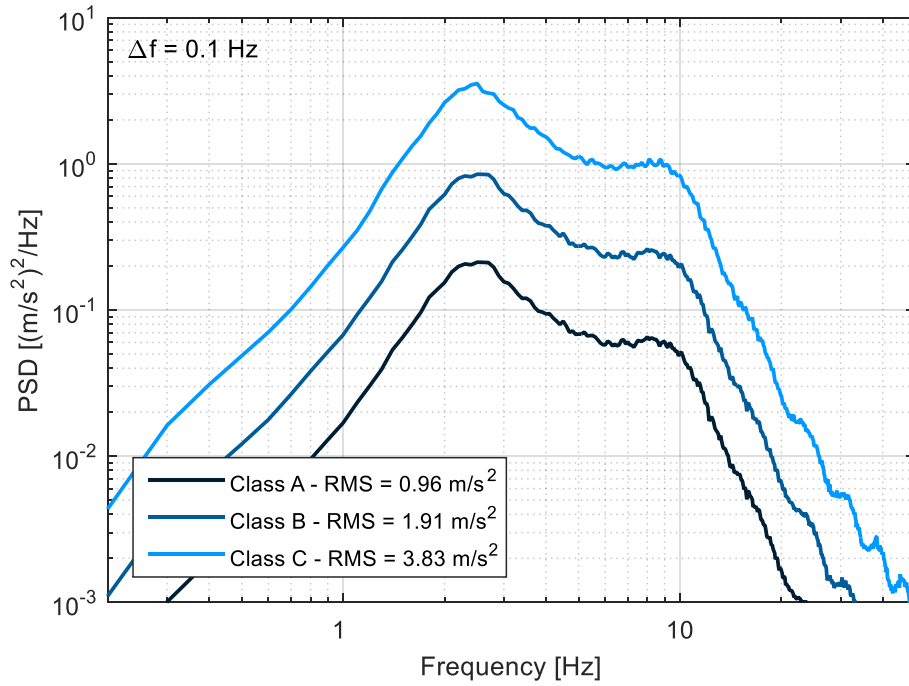


Figure 8-21: A comparison of the vertical acceleration PSD functions at multiple road roughness classes.

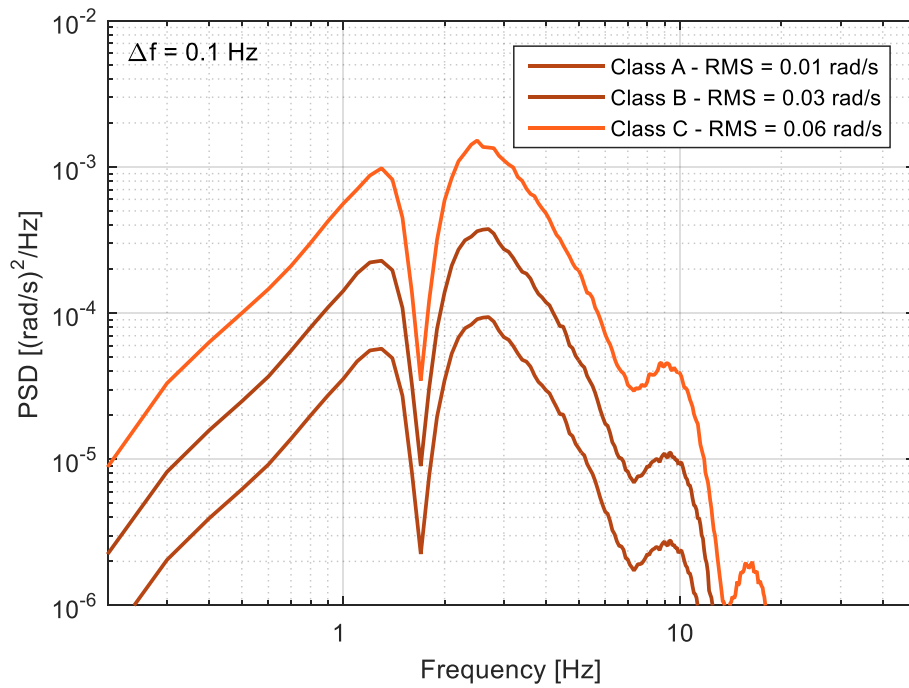


Figure 8-22: A comparison of the pitch angular velocity PSD functions at multiple road roughness classes.

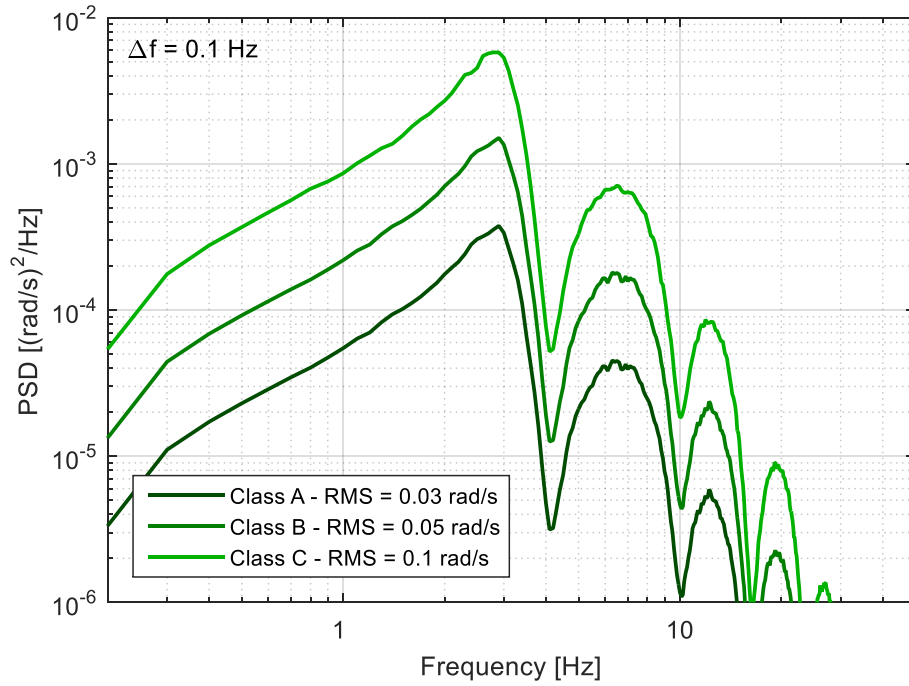


Figure 8-23: A comparison of the roll angular velocity PSD functions at multiple road roughness classes.

The heave-pitch and heave-roll FRFs, shown in Figure 8-24 and Figure 8-25 respectively, remain identical for the simulated roads. The ratio between heave and the other vibratory modes, is independent of the road roughness (provided that the spectral shape remains the same) across the frequency band.

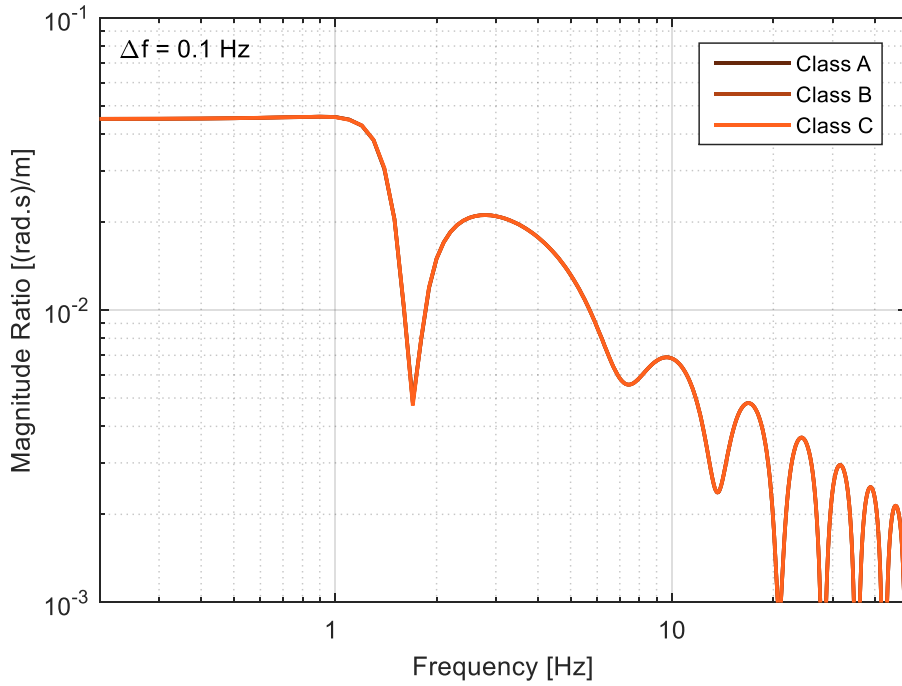


Figure 8-24: A comparison of the frequency response functions between the pitch angular velocity and vertical acceleration as road roughness varies.

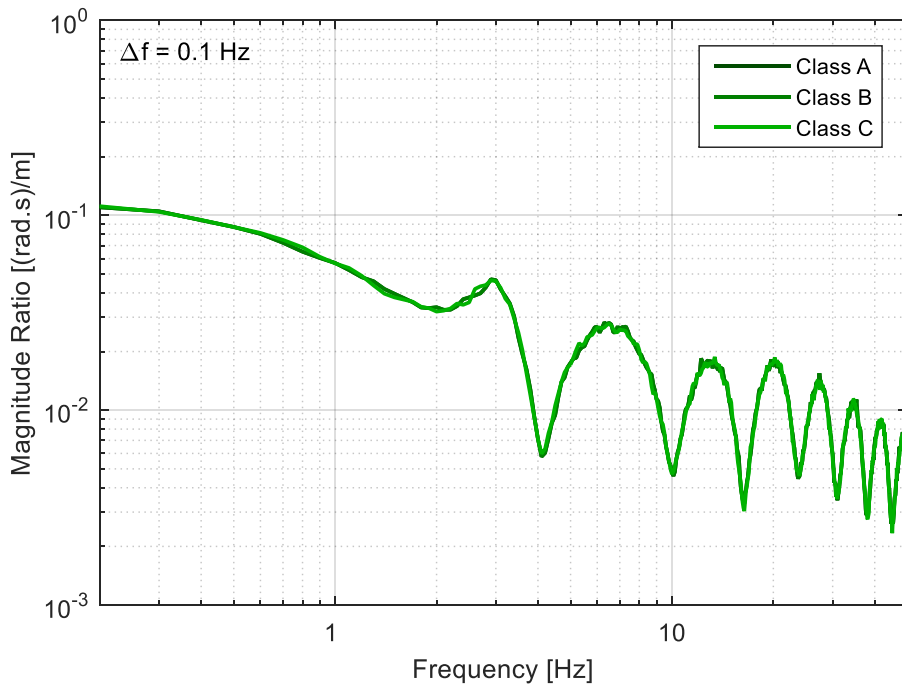


Figure 8-25: A comparison of the frequency response functions between the roll angular velocity and vertical acceleration as road roughness varies.

8.3 On the Effects of Sprung Mass

This section focuses on the effects that variations in the sprung mass, which includes the vehicle body plus any payload carried by the vehicle, has on the vibratory response. This is only possible using a numerical model as the addition of mass in physical experiments alters many other vehicle parameters, most importantly for this study the CG location and MOI.

Five different mass multiplier values were used, allowing for the simulation up to double the original sprung mass, as shown in Table 8-8. The other parameters in the numerical model remained constant. The damping coefficient remained the same between simulations, resulting in a floating damping ratio, which occurs in real life. The sprung mass was not reduced from the base value due to the simulated vehicle already being over damped.

Table 8-8: A table summarising the mass multiplier values and resultant sprung masses used during simulation.

Mass Multiplier	Sprung mass
1	1428 kg
1.25	1785 kg
1.5	2142 kg
1.75	2499 kg
2	2856 kg

Both the pitch-heave and roll-heave RMS ratios increase as the sprung mass increases, as seen in Figure 8-26 and Table 8-9. The vertical acceleration RMS decreases with the increase in sprung mass, believed to be due to the increased damping ratio. The pitch angular velocity RMS increases as the mass is raised, whilst the roll angular velocity remains constant for all sprung mass

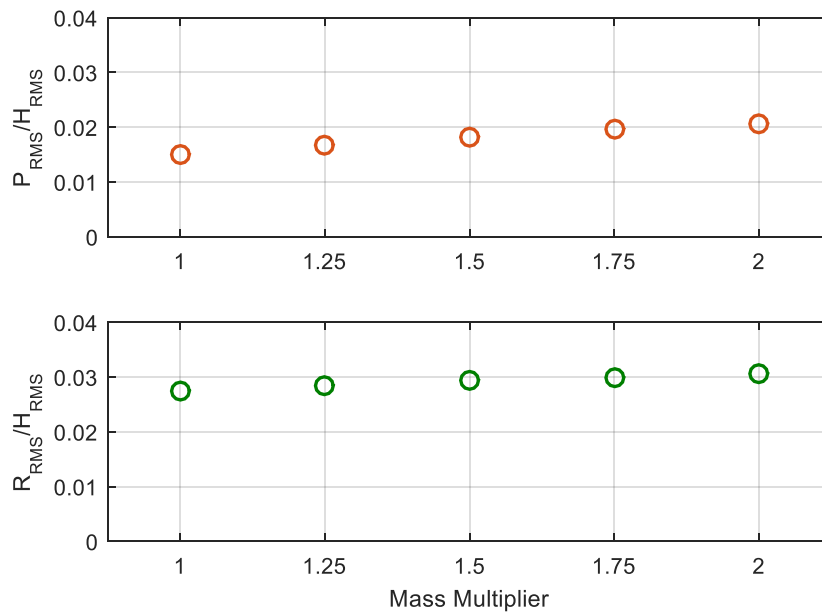


Figure 8-26: The effects of sprung mass on the ratio between the pitch RMS and heave RMS (top) and the ratio between the roll RMS and heave RMS (bottom).

Table 8-9: A table summarising the RMS ratios for the differing sprung masses.

Mass Multiplier	H_{RMS} [m/s ²]	P_{RMS} [rad/s]	R_{RMS} [rad/s]	P_{RMS}/H_{RMS} [(rad.s)/m]	R_{RMS}/H_{RMS} [(rad.s)/m]
1	1.91	2.8×10^{-2}	5.24×10^{-2}	1.50×10^{-2}	2.75×10^{-2}
1.25	1.84	3.05×10^{-2}	5.24×10^{-2}	1.66×10^{-2}	2.85×10^{-2}
1.5	1.79	3.25×10^{-2}	5.24×10^{-2}	1.82×10^{-2}	2.93×10^{-2}
1.75	1.75	3.41×10^{-2}	5.24×10^{-2}	1.95×10^{-2}	3.00×10^{-2}
2	1.71	3.54×10^{-2}	5.24×10^{-2}	2.07×10^{-2}	3.06×10^{-2}

PDFs of the vertical acceleration moving RMS, shown in Figure 8-27, remain a similar shape with the varying sprung mass. The standard deviation reduces slightly as the sprung mass is increased, which is also met with a small increase in the maximum probability density. The mode of the distribution reduces as the sprung mass increases, migrating towards lower RMS levels as the damping ratio decreases.

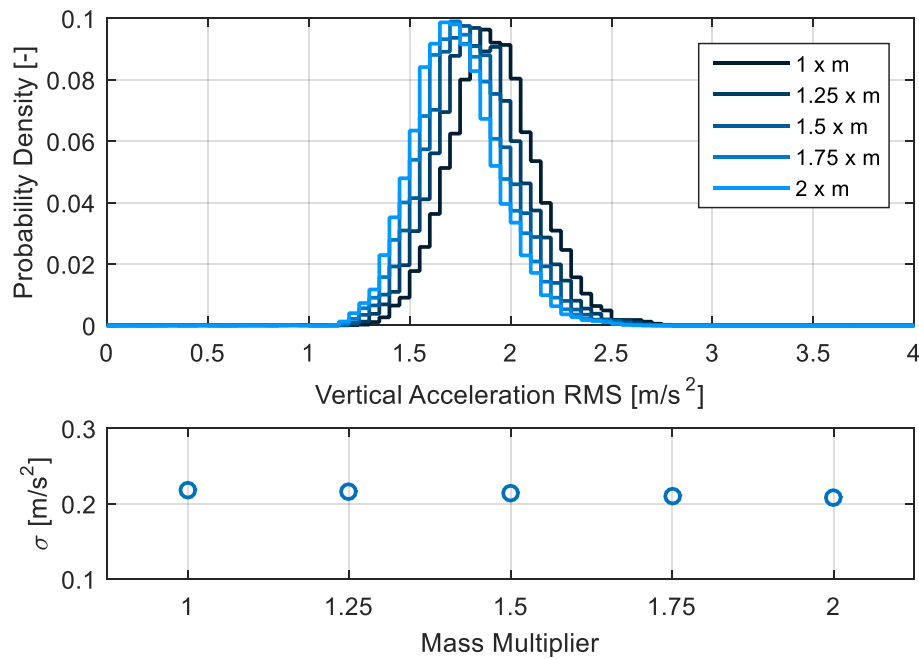


Figure 8-27: A comparison of the of the vertical acceleration moving RMS (2 second window, maximum overlap) PDFs for varying sprung masses (top) and a comparison of the standard deviation (bottom).

Figure 8-28 shows a comparison of the pitch angular velocity moving RMS PDFs. The distributions change significantly as the sprung mass is increased. A reduction in the maximum probability density is met with an increase in the standard deviation, as the distribution becomes more spread out. The pitch response tends towards higher RMS levels as the mass increases, which is indicated by the increasing mode value.

Figure 8-29 shows a comparison of the roll angular velocity moving RMS PDFs. For all sprung masses simulated, the distributions remain almost identical. This was unexpected, however, the distribution of the RMS roll angular velocity in the physical experiments (PAGE NUMBER) did remain similar for the different sprung masses.

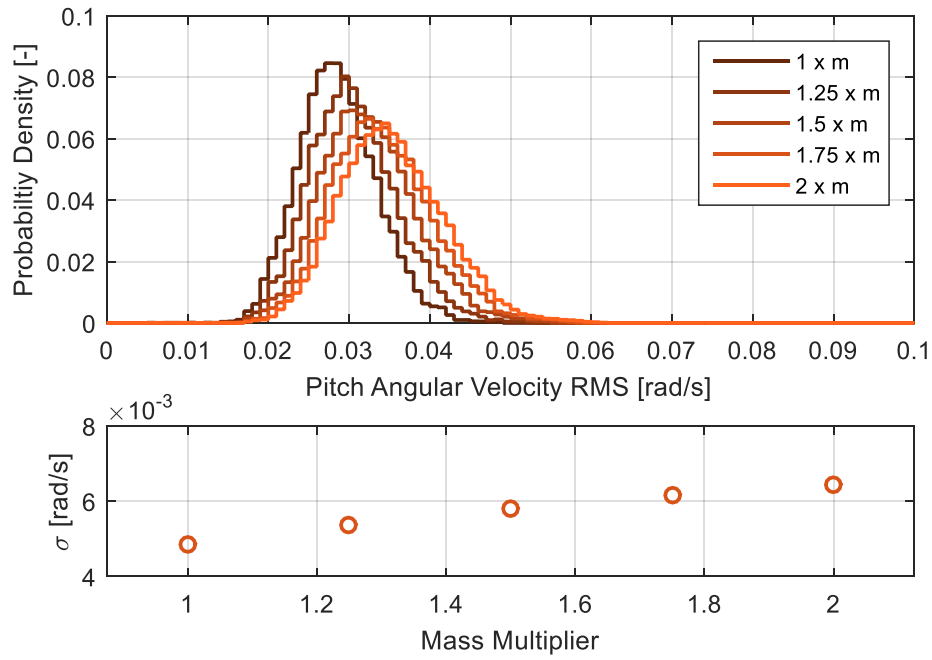


Figure 8-28: A comparison of the of the pitch angular velocity moving RMS (2 second window, maximum overlap) PDFs for varying sprung masses (top) and a comparison of the standard deviation (bottom).

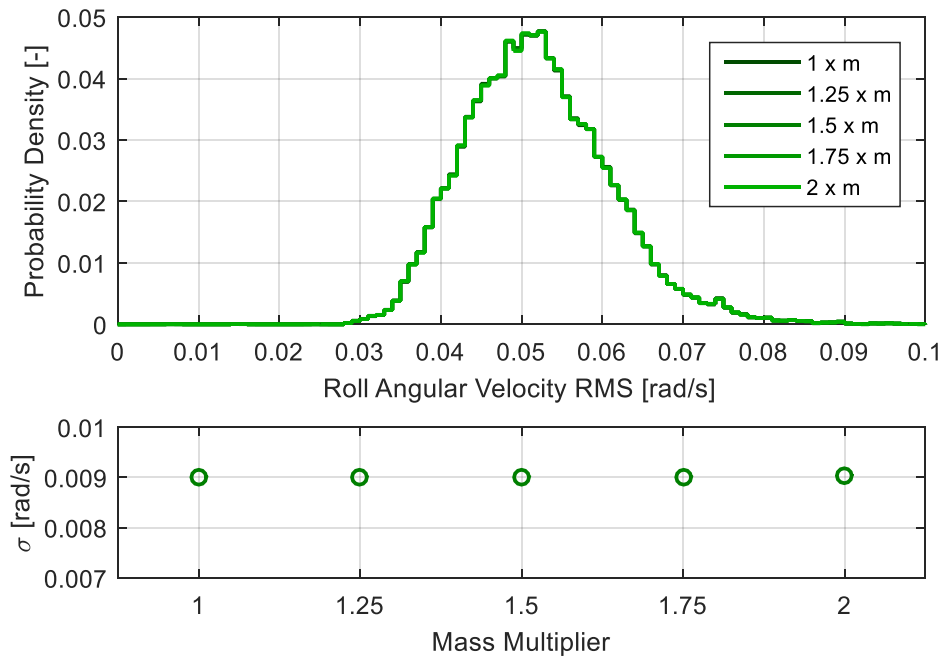


Figure 8-29: A comparison of the of the roll angular velocity moving RMS (2 second window, maximum overlap) PDFs for varying sprung masses (top) and a comparison of the standard deviation (bottom).

Figure 8-30 displays a comparisons of the bivariate histograms at the minimum (left) and maximum (right) sprung masses. A change in slope is observed, with the gradient increasing with the added mass. The data cloud translates towards lower levels of vertical acceleration but to higher levels of pitch angular velocity. The data cloud also spreads as higher levels of pitching motion occur more frequently, causing the gradient to increase.

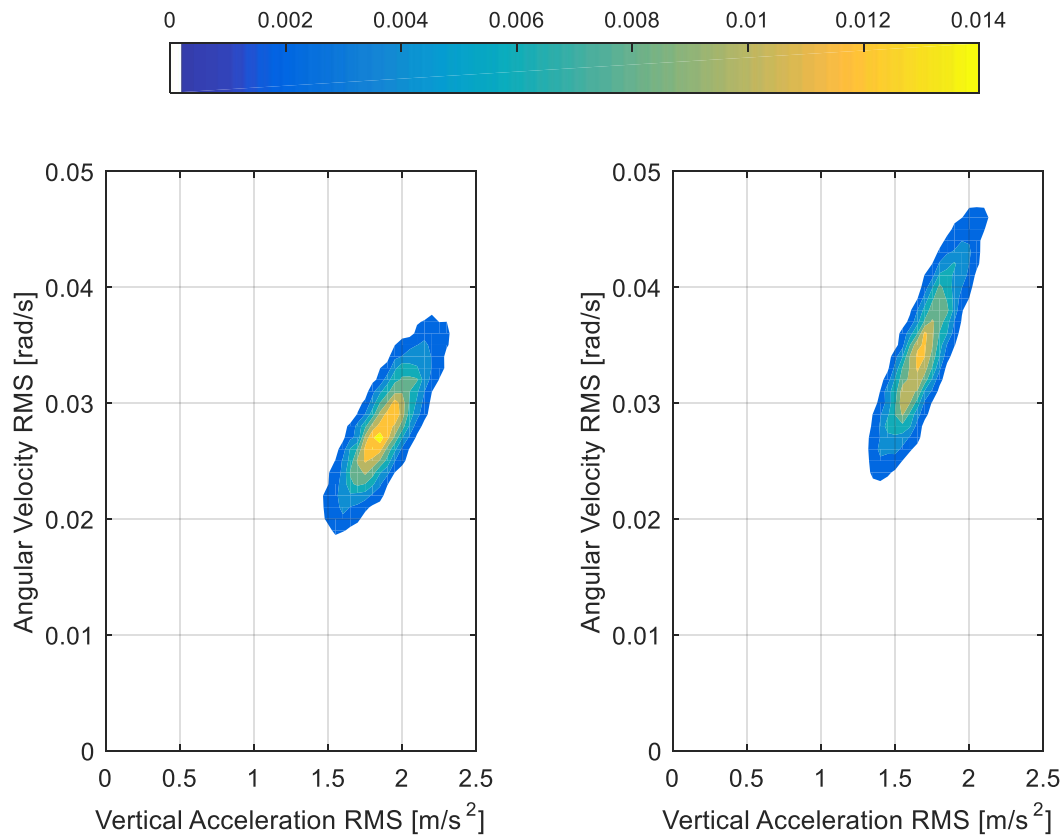


Figure 8-30: Comparison of vertical acceleration-pitch angular velocity bivariate histograms when the sprung mass is 1428 kg (left) and 2856 kg (right).

A summary of the linear models fitted to heave-pitch moving RMS scatter plot is shown in Table 8-10. The gradient increases along with the sprung mass (Figure 8-31), however the change in gradient does not appear to be linear. The strength of the pitch-heave relationship appears relatively independent of the sprung mass as the R^2 and RMSE remain similar.

Table 8-10: A table summarising linear models fit to the heave vs pitch RMS scatter plots.

Mass Multiplier	Gradient	Y-Intercept	R^2	RMSE
1	0.0181	-0.0061	0.6590	0.0028
1.25	0.0212	-0.0087	0.7296	0.0028
1.5	0.0237	-0.0101	0.7570	0.0029
1.75	0.0255	-0.0106	0.7589	0.0030
2	0.0267	-0.0107	0.7506	0.0032

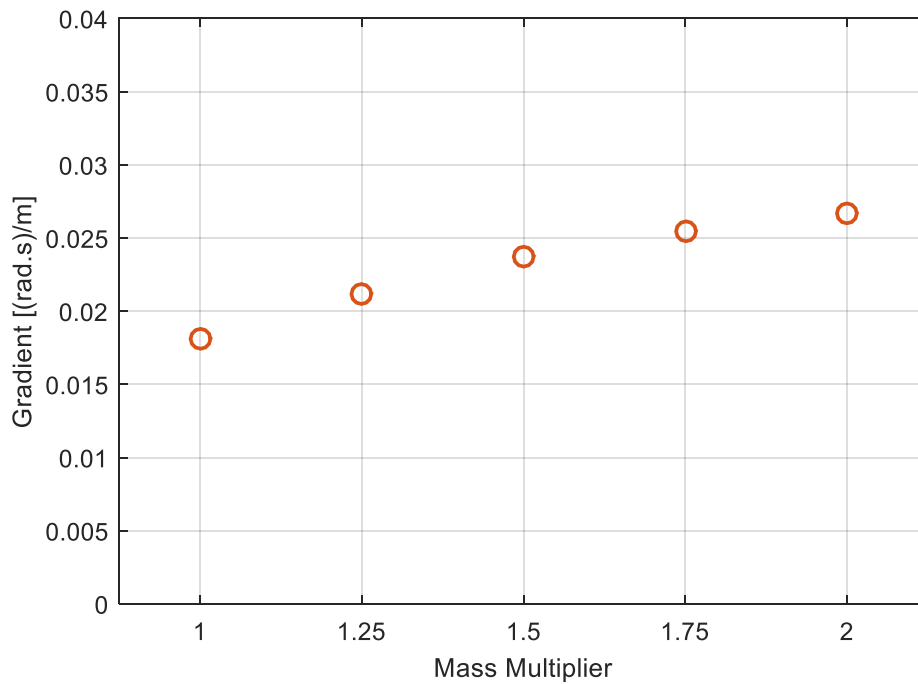


Figure 8-31: A comparison of the heave-pitch RMS scatter plot gradient as sprung mass is varied.

The heave-roll bivariate histograms (Figure 8-32) remain similar between the minimum (left) and maximum (right) sprung mass simulations. The bivariate histograms translate towards higher levels of vertical acceleration, while the roll levels remain the same, due to the roll RMS PDFs being identical. Once again, as with all roll results the fitted linear models return no usable information with the gradient and R^2 equating to approximately zero. A summary of linear models fitted to the heave-roll data is shown in Table 8-11.

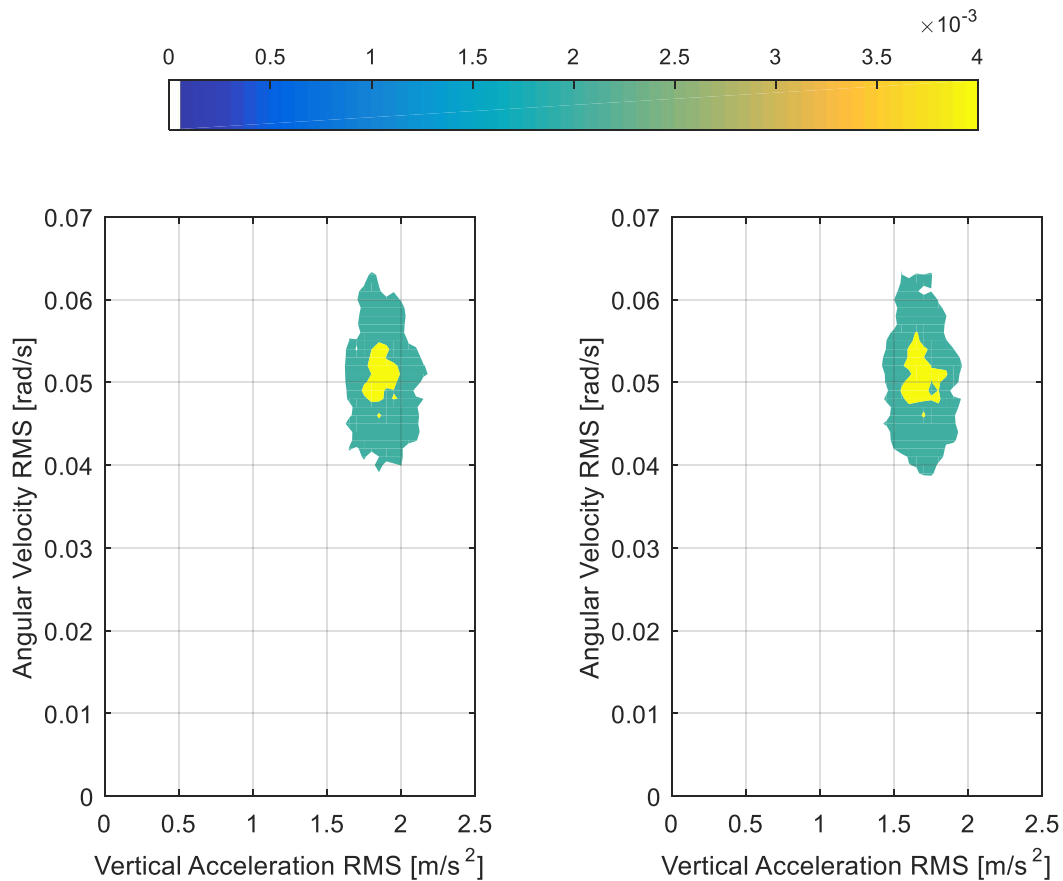


Figure 8-32: Comparison of vertical acceleration-roll angular velocity bivariate histograms when the sprung mass is 1428 kg (left) and 2856 kg (right).

Table 8-11: A table summarising linear models fit to the heave vs roll RMS scatter plots.

Mass Multiplier	Gradient	Y-Intercept	R^2	RMSE
1	-0.0007	0.0530	0.0003	0.0090
1.25	-0.0008	0.0531	0.0004	0.0090
1.5	-0.0009	0.0532	0.0004	0.0090
1.75	-0.0009	0.0532	0.0004	0.0090
2	-0.0009	0.0532	0.0004	0.0090

Figure 8-33 shows a comparison of the PCA-adjusted heave-pitch data PDFs. The pitch distribution remains similar between the differing sprung masses with the standard deviation increasing as the mass is increased, this is met with a decrease in the maximum probability density.

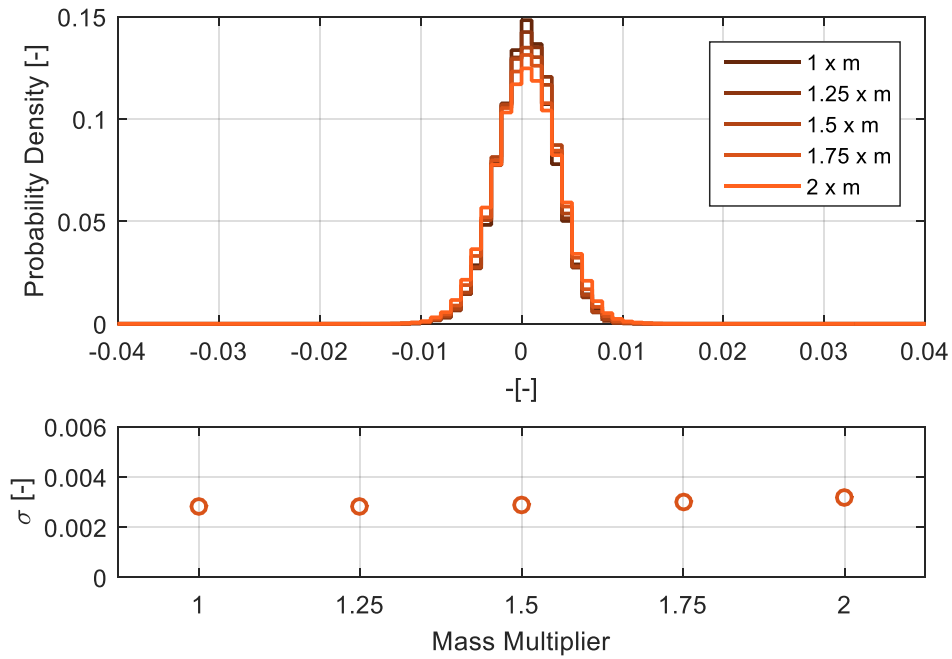


Figure 8-33: A comparison of PDFs taken parallel to the principal axis from the PCA adjusted heave-pitch RMS scatter plots as sprung mass is varied (top) and the change in standard deviation (bottom).

Figure 8-34 shows a comparison of the PCA-adjusted heave-roll data PDFs. The PCA-adjusted heave-roll PDFs remain the same for all sprung masses, remembering that the RMS PDFs also remained the same. As the gradients to the fitted linear models (Table 8-11) are approximately equal to zero the standard deviation of the RMS PDFs end up being equal to those of the PCA-adjusted PDFs (and also the RMSE of the fitted linear models).

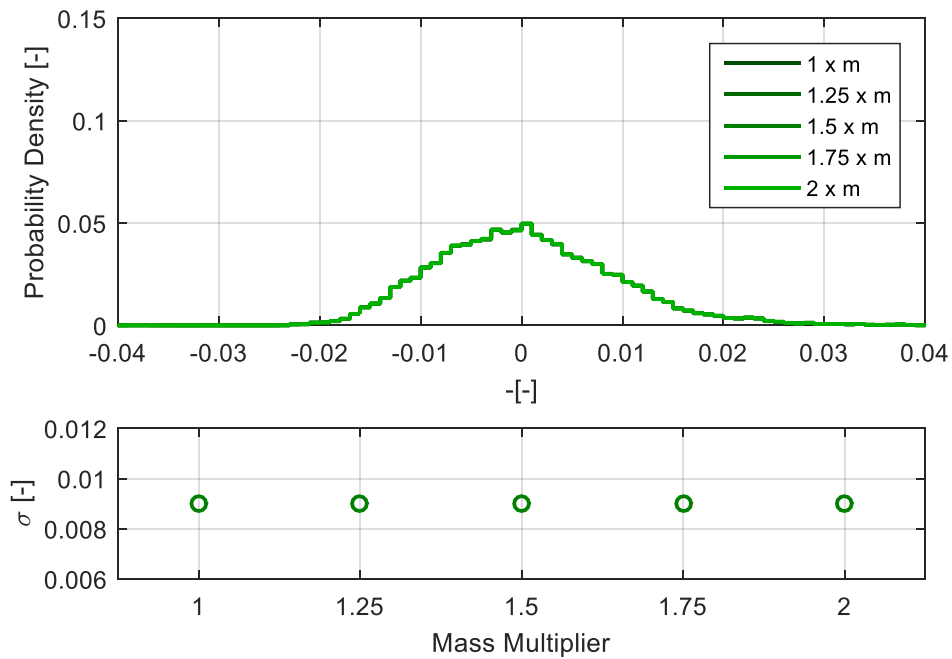


Figure 8-34: A comparison of PDFs taken parallel to the principal axis from the PCA adjusted heave-roll RMS scatter plots as sprung mass is varied (top) and the change in standard deviation (bottom).

Figure 8-35 shows a comparison of the vertical acceleration PSD functions. The RMS decreases as the sprung mass increases, despite this, the PSD functions all have a similar maximum power densities. As the sprung mass is increase the natural frequency of the sprung mass should decrease as the stiff values remained constant. However the point of maximum power density remains at the same frequency for all simulations.

A protrusion from the side of this peak becomes evident as the mass is increased and tends towards lower frequencies. This protrusion, is in fact the peak related to the natural frequency of the heave motion. The other, larger, peak is due to a combination of the vertical acceleration as well as the tangential component of the pitching motion. The vertical component of the pitching motion is amplified due to the simulated measurement point being above the rear axle, creating a 1.9 m lever arm.

Wheelbase filtering effects are evident towards the higher frequencies. As the damping ratio decreases (due to higher sprung mass) the nodes become more pronounced, amplifying the effect.

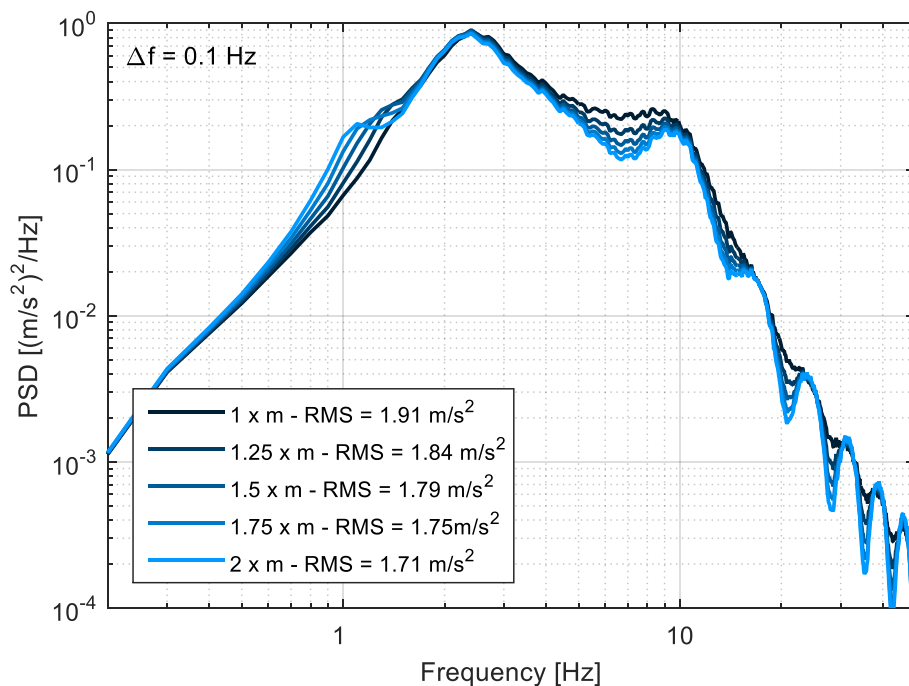


Figure 8-35: A comparison of the vertical acceleration PSD functions as sprung mass is varied.

Figure 8-36 shows a comparison of the pitch angular velocity PSD functions as the sprung mass is varied. The RMS of the pitch PSD functions increases concurrently with the sprung mass. This extra energy is contained within the lower frequencies as above 3 Hz the pitch PSD functions are identical. In the lower frequencies distinct power density levels are observed. At the lowest sprung mass a clear difference can be observed between the peaks is observed, as the sprung mass increases this difference reduces as the peak due to the natural pitching motion (≈ 2.5 Hz) widens. The lower frequency peak 1 Hz is due to the heave natural frequency and its coupling to pitching motion.

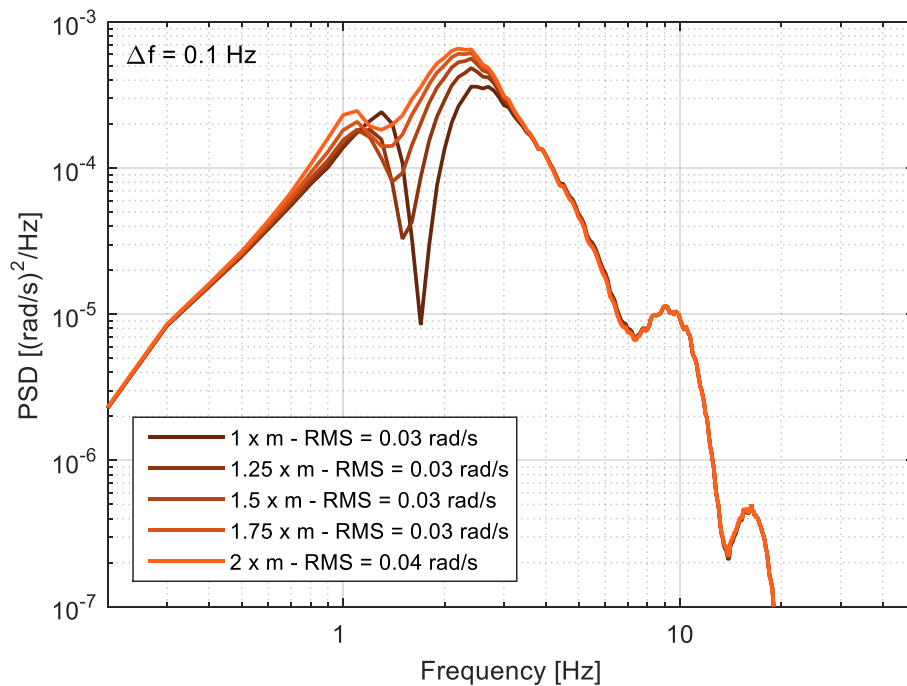


Figure 8-36: A comparison of the pitch angular velocity PSD functions as sprung mass is varied.

The roll PSD functions (Figure 8-37) remain identical for each sprung mass simulated. Once again the coupling between the vibratory modes is reflected by the wheelbase filtering apparent in the roll PSD functions. The nodal frequencies are caused by coupling to the vertical vibration.

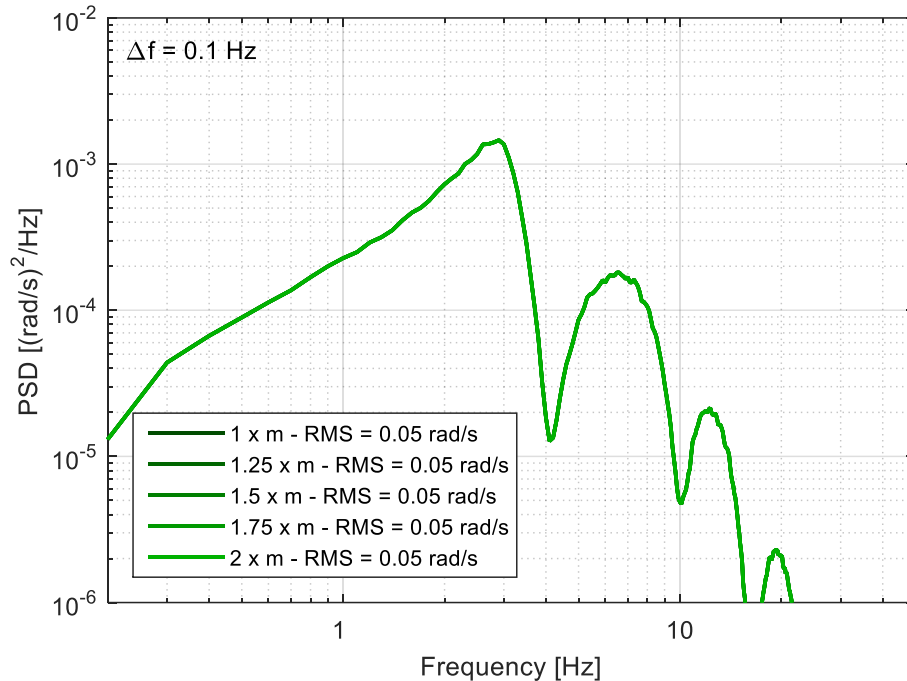


Figure 8-37: A comparison of the roll angular velocity PSD functions as sprung mass is varied.

The heave-pitch and heave-roll FRFs are shown in Figure 8-38 and Figure 8-39 respectively. The horizontal portion at the beginning of the heave-pitch FRF extends until it reaches the natural frequency of the vertical vibration for each of the sprung mass simulations. The drop of is more severe for lower sprung masses due to the narrower pitch natural frequency peaks. The heave-roll FRFs remain similar for all of the simulations. The lower sprung masses are at a higher magnitude ratio for the low frequencies, however this reverses between the wheelbase filtering nodes.

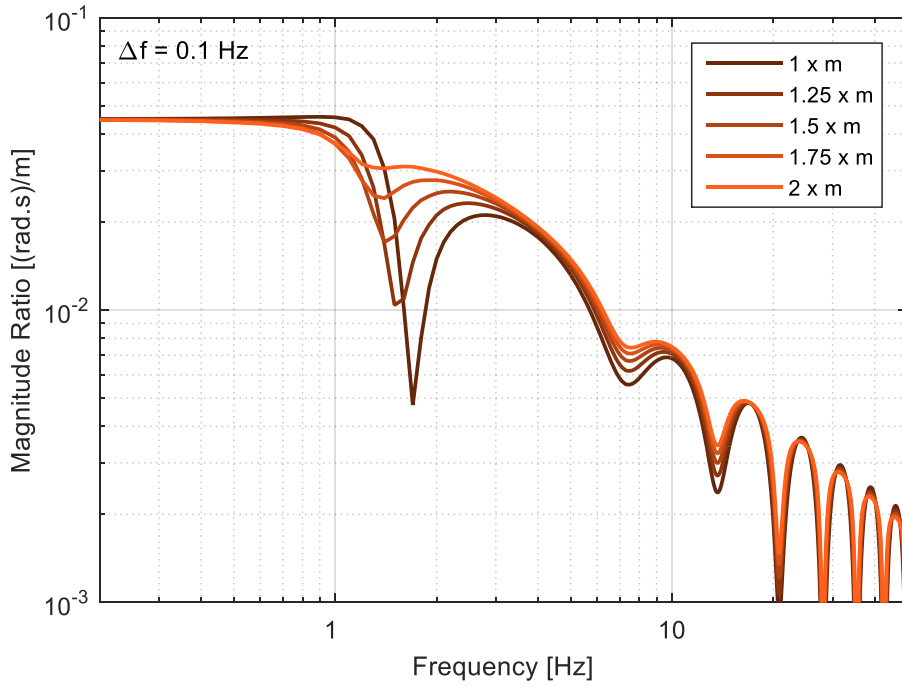


Figure 8-38: A comparison of the frequency response functions between the pitch angular velocity and vertical acceleration as the sprung mass varies.

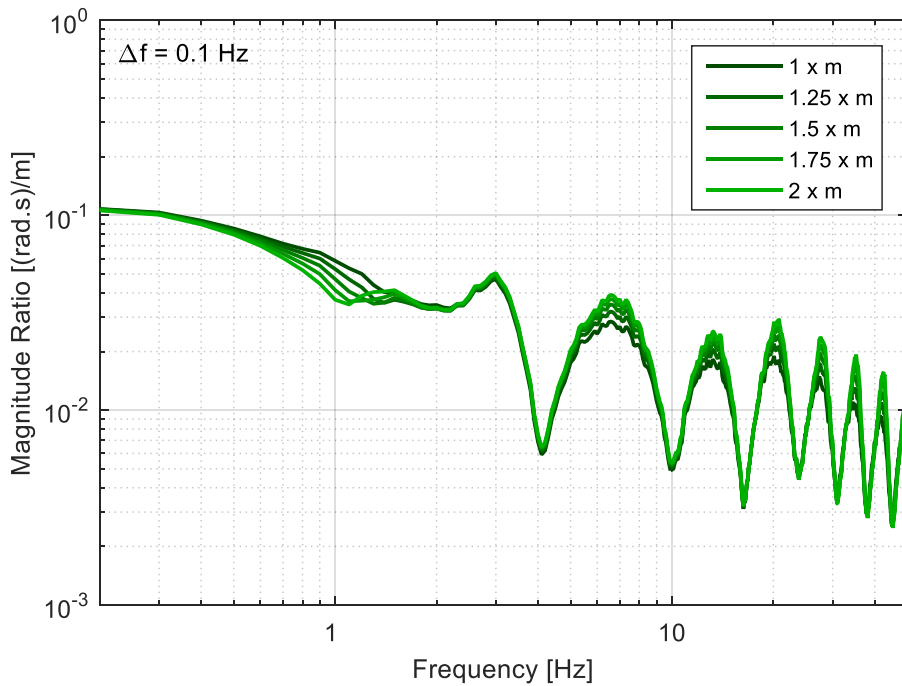


Figure 8-39: A comparison of the frequency response functions between the roll angular velocity and vertical acceleration as the sprung mass varies.

8.4 On the Effects of Moments of Inertia

This section contains the results for simulations in which the vehicles moments of inertia were varied by $\pm 50\%$. The MOI used for the simulations are shown in Table 8-12. For the physical experiments the largest change in the MOI was estimated to be 3 % for the pitch MOI and 13 % for the roll MOI. Initial simulations within these ranges made it difficult to discern changes in the metrics. The CG location and sprung mass remain constant through all simulations.

Table 8-12: A table summarising the MOI used for the simulation series.

MOI Multiplier	Roll I_x [kg.m²]	Pitch I_y [kg.m²]
0.5	237	1341
0.75	356	2011
1	474	2681
1.25	593	3351
1.5	711	4022

Despite the significant change in the pitch MOI the pitch:heave ratio (Figure 8-40) remained similar for all simulations only fluctuating within a small range as seen in Table 8-13. The roll:heave ratio increased with the MOI, however the change was not linear and plateaued for the lower MOI multipliers.

Table 8-13: A table summarising the RMS ratios for the differing MOI.

MOI Multiplier	H _{RMS} [m/s ²]	P _{RMS} [rad/s]	R _{RMS} [rad/s]	P _{RMS} /H _{RMS} [(rad.s)/m]	R _{RMS} /H _{RMS} [(rad.s)/m]
0.5	3.01	4.41x10 ²	6.90x10 ²	1.47x10 ²	2.30x10 ²
0.75	2.31	3.48x10 ²	5.37x10 ²	1.51x10 ²	2.33x10 ²
1	1.91	2.86x10 ²	5.24x10 ²	1.50x10 ²	2.75x10 ²
1.25	1.65	2.46x10 ²	5.35x10 ²	1.49x10 ²	3.25x10 ²
1.5	1.47	2.22x10 ²	5.47x10 ²	1.51x10 ²	3.72x10 ²

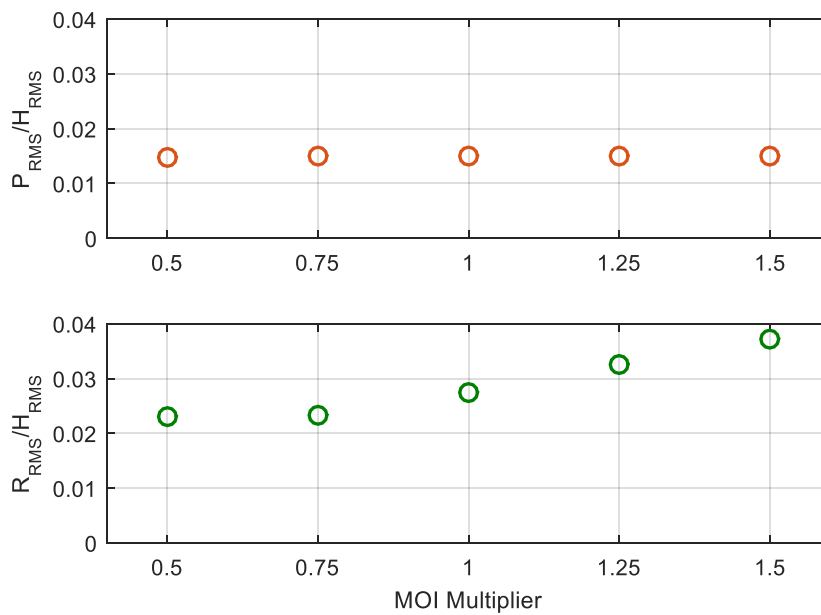


Figure 8-40: The effects of varying the sprung mass's moments of inertia on the ratio between the pitch RMS and heave RMS (top) and the ratio between the roll RMS and heave RMS (bottom).

Figure 8-41 shows a comparison of the vertical acceleration moving RMS PDFs as the MOI are varied. As the MOI are increased the mode of the distribution decreases, although not linearly. Also, as the MOI are increased the maximum probability density increases, which has a corresponding decrease in the standard deviation. The change in standard deviation, mode and RMS ratios all appear to be non-linear despite the linear variation in the pitch and roll MOI.

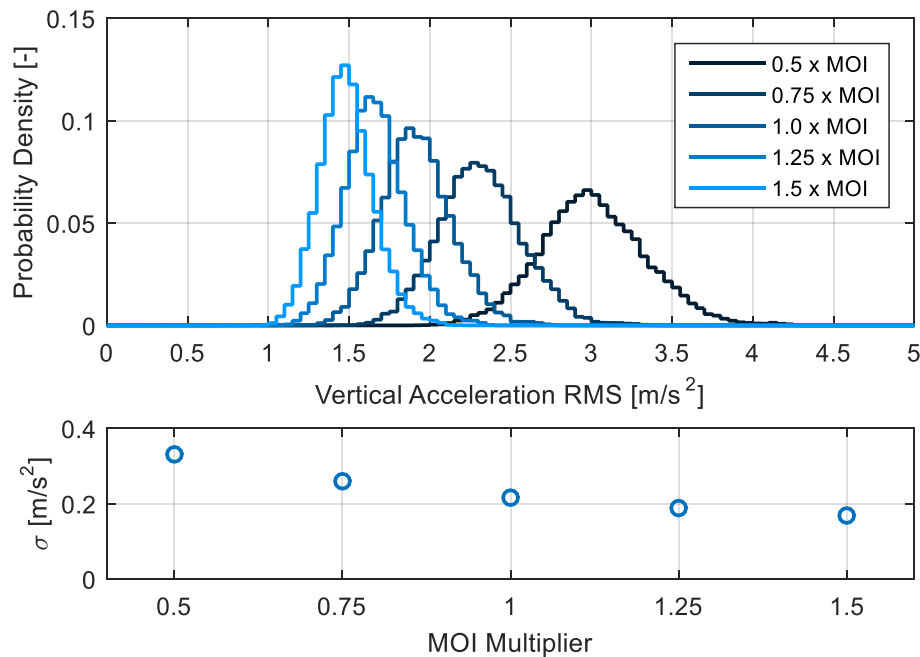


Figure 8-41: A comparison of the of the vertical acceleration moving RMS (2 second window, maximum overlap) PDFs for varying moments of inertia (top) and a comparison of the standard deviation (bottom).

Figure 8-42 shows a comparison of the pitch angular velocity moving RMS PDFs as the MOI are varied. Once more, increasing the MOI reduces the mode non-linearly and increases the maximum probability density. The standard deviation decreases as the MOI increase, also non-linearly.

Figure 8-43 shows a comparison of the roll angular velocity RMS PDFs as the MOI are varied. Significant differences are apparent between the differing MOI. The simulation with the lowest MOI multiplier has a significantly higher mode, whilst the remaining simulations are similar. The maximum probability density and standard deviation also vary. Excluding the 0.5 MOI multiplier the change in standard deviation appears linear. This may indicate an upper limit exists to when the roll MOI no longer effects the mode of the distribution and only varies how dispersed it becomes.

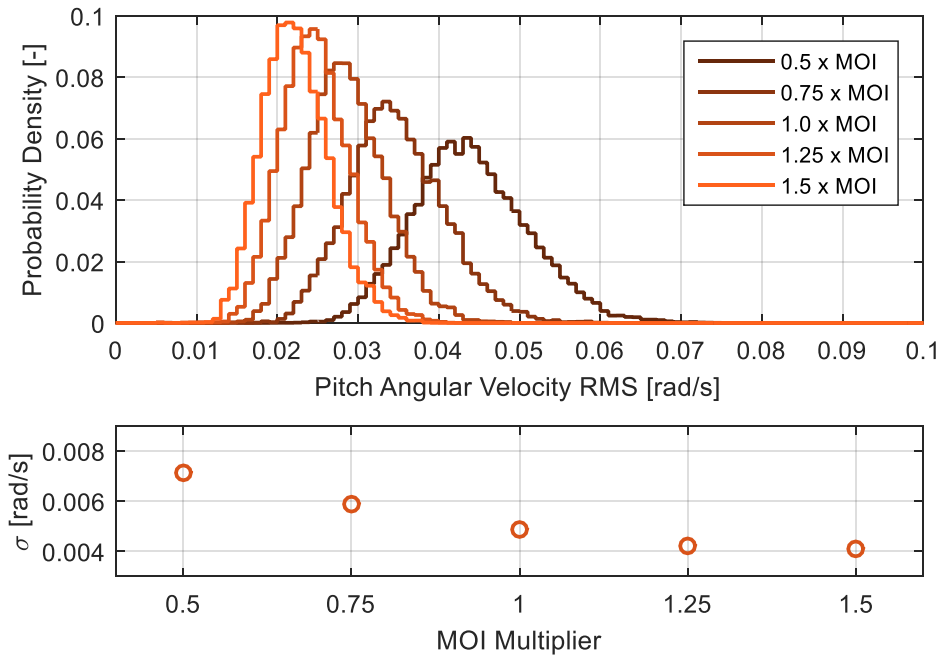


Figure 8-42: A comparison of the of the pitch angular velocity moving RMS (2 second window, maximum overlap) PDFs for varying moments of inertia (top) and a comparison of the standard deviation (bottom).

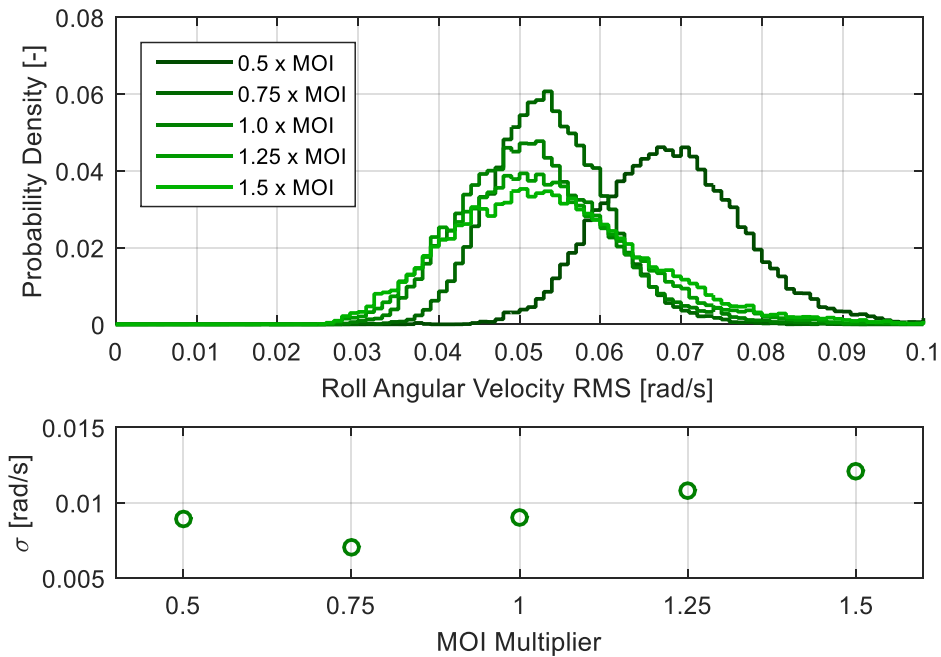


Figure 8-43: A comparison of the of the roll angular velocity moving RMS (2 second window, maximum overlap) PDFs for varying moments of inertia (top) and a comparison of the standard deviation (bottom).

A comparison of the heave-pitch bivariate histograms for the 0.5 (left) and 1.5 (right) MOI multiplier is shown in Figure 8-44. The probability density increase as the MOI is increased. A translation to lower levels of vertical acceleration and pitch angular velocity also occurs. A change in gradient is seen between the two configurations.

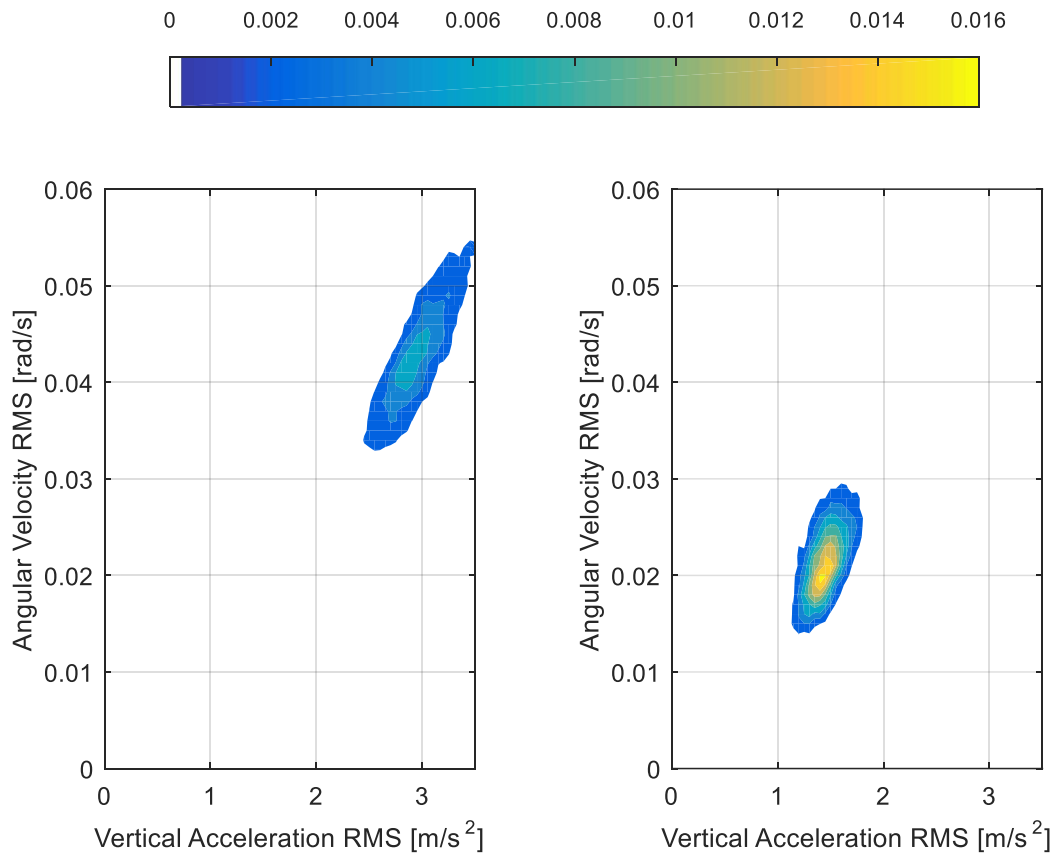


Figure 8-44: Comparison of vertical acceleration-pitch angular velocity bivariate histograms at the minimum MOI (left) and maximum MOI (right).

However, the change in gradient appears random across the different configurations as seen in Table 8-14, which contains a summary of the fitted linear models. Again, excluding the 0.5 mass multiplier, the change in gradient appears linear, as seen in Figure 8-45. The reduction in R^2 is due to the 'shortening' of the distribution along this axis.

Table 8-14: A table summarising linear models fit to the heave vs pitch RMS scatter plots.

MOI Multiplier	Gradient	Y-Intercept	R²	RMSE
0.5	0.0183	-0.0112	0.7250	0.0037
0.75	0.0194	-0.0101	0.7279	0.0031
1	0.0181	-0.0061	0.6590	0.0028
1.25	0.0159	-0.0018	0.5054	0.0030
1.5	0.0136	0.0020	0.3113	0.0034

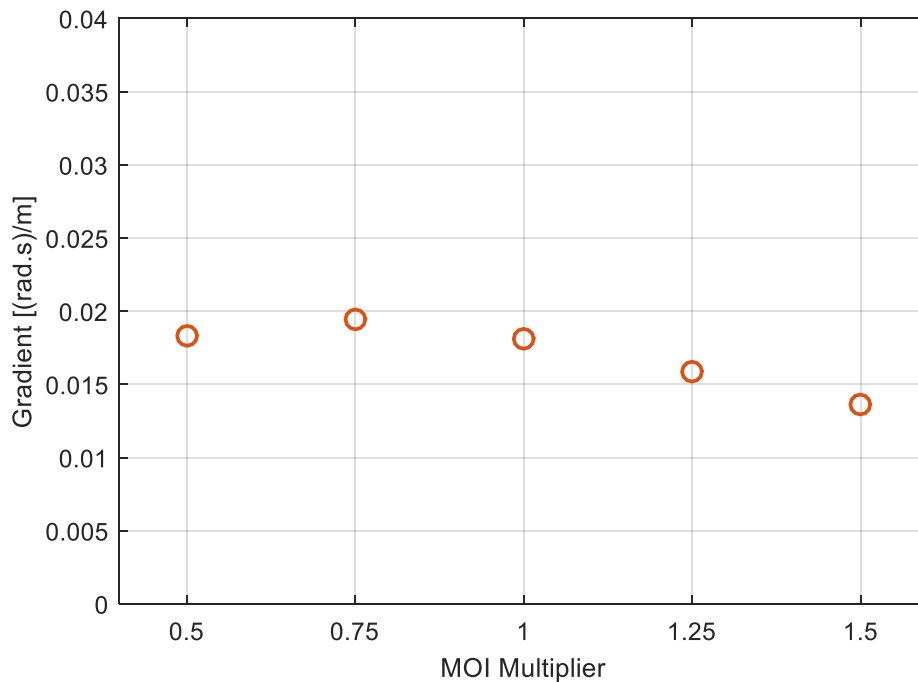


Figure 8-45: A comparison of the heave-pitch RMS scatter plot gradient as the sprung mass's MOI are varied.

Figure 8-46 shows a comparison of the heave-roll bivariate histograms for the 0.5 (left) and 1.5 (right) MOI multipliers. The bivariate histograms translate towards lower levels of vertical acceleration, while the roll levels remain similar, although less dispersed. Once again, as with all roll results the fitted linear models return no usable information with the gradient and R^2 equating to approximately zero. A summary of linear models fitted to the heave-roll data is shown in Table 8-15.

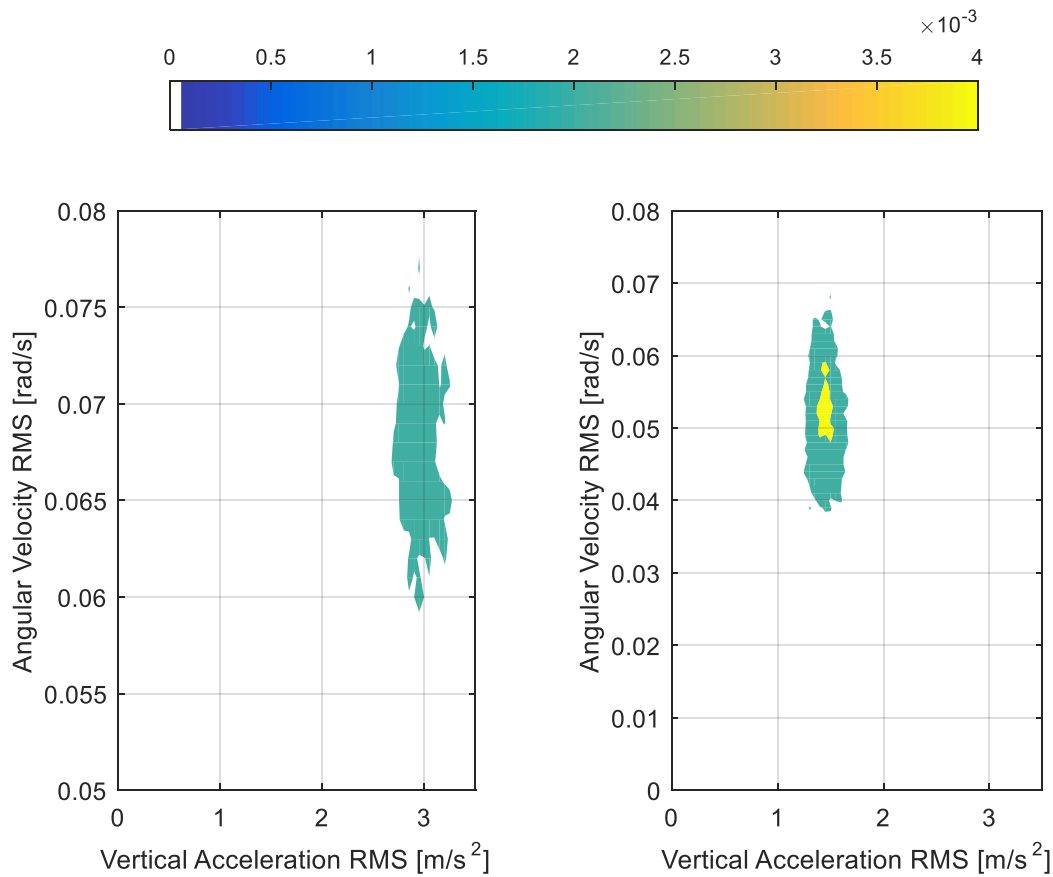


Figure 8-46: Comparison of vertical acceleration-roll angular velocity bivariate histograms at the minimum MOI (left) and maximum MOI (right).

Table 8-15: A table summarising linear models fit to the heave vs roll RMS scatter plots.

MOI Multiplier	Gradient	Y-Intercept	R^2	RMSE
2.5	-0.0003	0.0693	0.0001	0.0089
3	-0.0001	0.0535	0.0000	0.0070
3.5	-0.0007	0.0530	0.0003	0.0090
4	-0.0007	0.0536	0.0001	0.0108
4.5	0.0000	0.0534	0.0000	0.0121

PCA of the heave-pitch data revealed that the distribution parallel to the principal axis remained similar between all MOI simulated, as seen in Figure 8-47. The maximum probability density remains identical. The standard deviation remains similar between the scenarios, fluctuating within a small range. The moving RMS PDFs (Figure 8-42) showed a significant change in the pitch distribution as the MOI varied, with both the mode and standard deviation varying significantly. However these changes had no impact on the on the heave-pitch PCA distribution.

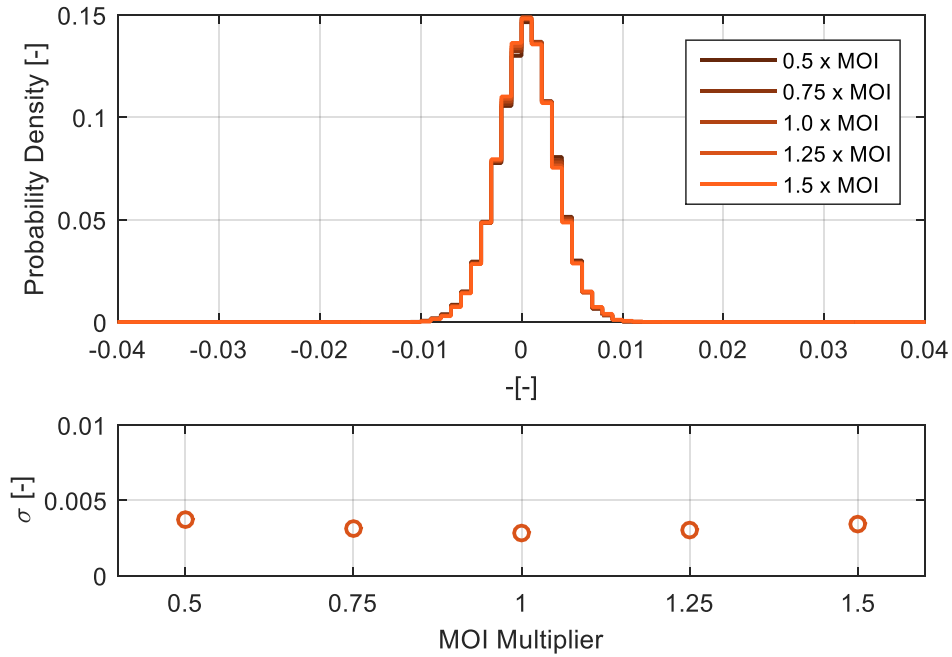


Figure 8-47: A comparison of PDFs taken parallel to the principal axis from the PCA adjusted heave-pitch RMS scatter plots as sprung mass's MOI are varied (top) and the change in standard deviation (bottom).

Unlike its heave-pitch counterpart, the heave-roll PCA PDF did vary with a change in MOI, as seen in Figure 8-48. A reduction in the maximum probability density occurs with the increase in MOI. This is once again coupled to a change in the standard deviation, once more the change in standard deviation is non-linear.

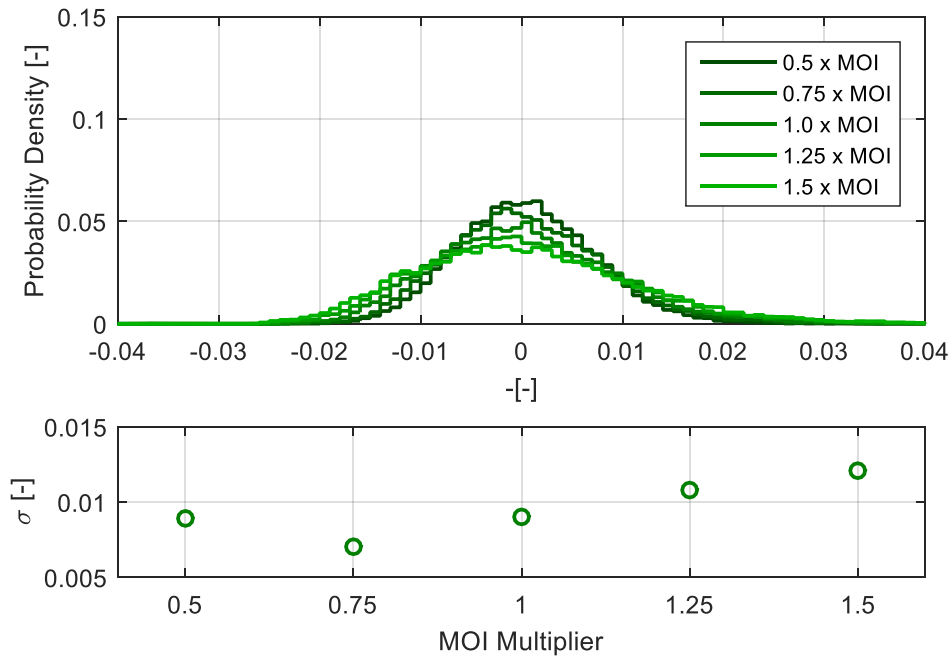


Figure 8-48: A comparison of PDFs taken parallel to the principal axis from the PCA adjusted heave-roll RMS scatter plots as sprung mass's MOI are varied (top) and the change in standard deviation (bottom).

Fourier analysis of the simulation results reveal a significant reduction in the vertical acceleration RMS as the MOI are increased. The vertical acceleration PSD functions, shown in Figure 8-49, showed distinct power density levels between the configurations. The inertial properties also have a significant effect on the severity of the wheelbase filtering effect, with the lower MOI showing the effects to a greater extent.

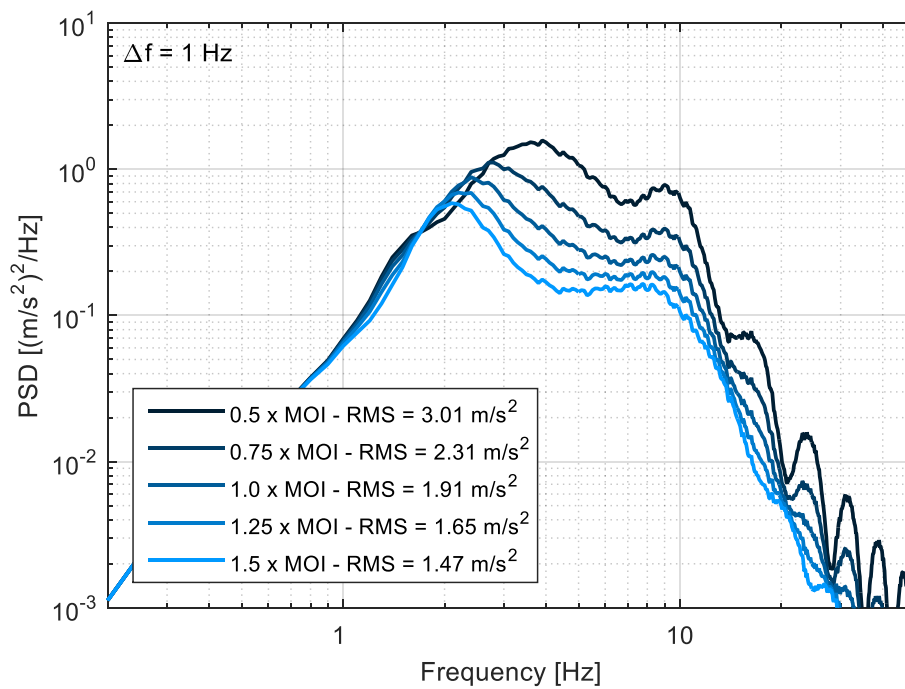


Figure 8-49: A comparison of the vertical acceleration PSD functions as the sprung mass's MOI are varied.

Figure 8-50 shows a comparison of the pitch angular velocity PSD functions. As the MOI are increased the RMS decreases, however at low frequencies the higher MOI contain more energy. This is reversed between the first and second peaks, with the lower MOI containing more energy for the remaining bandwidth.

Figure 8-51 shows a comparison of the roll angular velocity PSD functions. Once again as the MOI are increased the RMS decreases, with the higher MOI containing more energy at low frequencies.

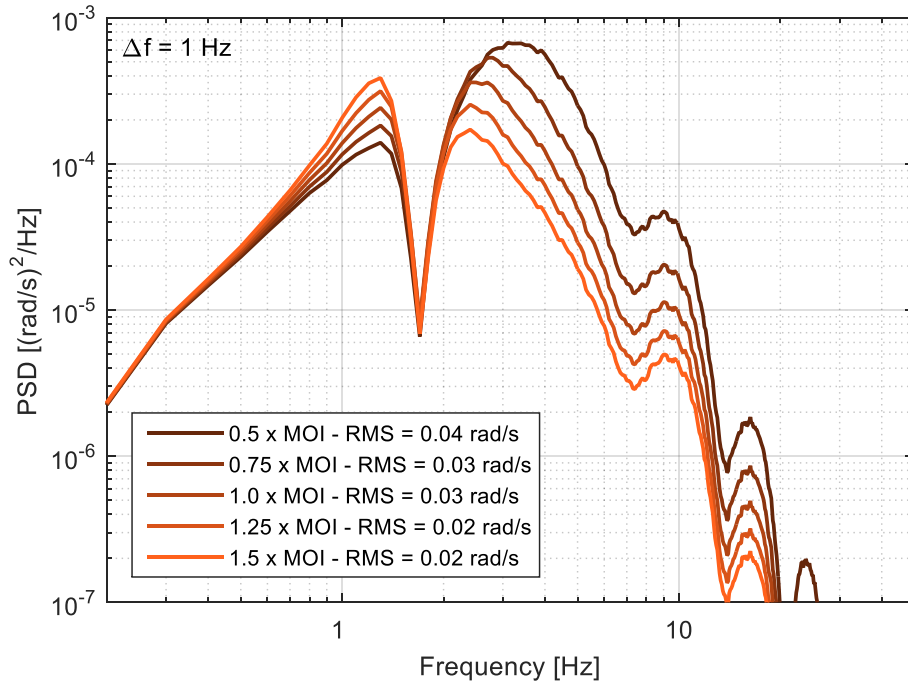


Figure 8-50: A comparison of the pitch angular velocity PSD functions as the sprung mass's MOI are varied.

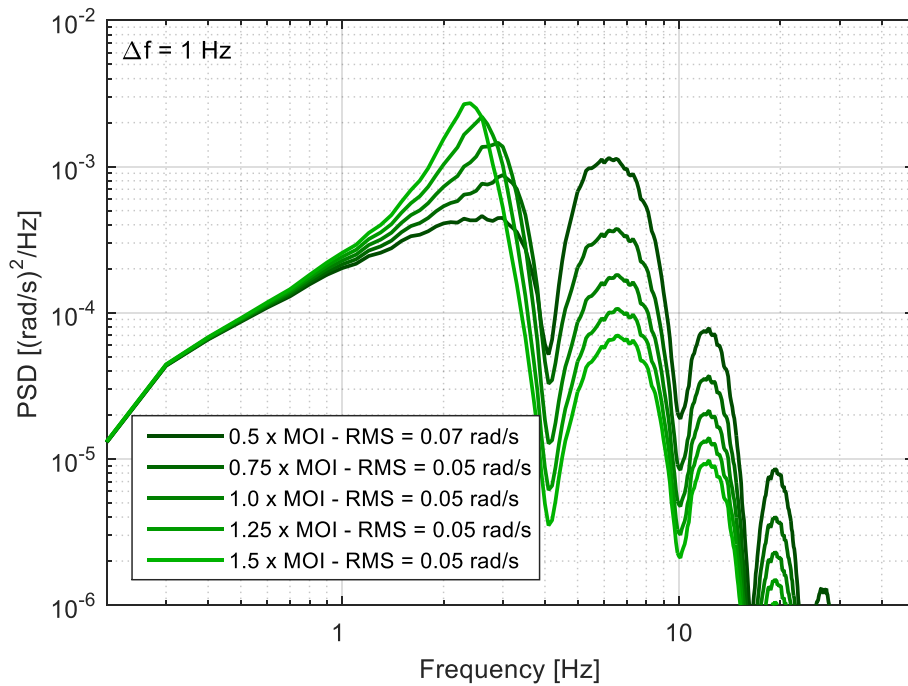


Figure 8-51: A comparison of the roll angular velocity PSD functions as the sprung mass's MOI are varied.

The heave-pitch FRFs, shown in Figure 8-52, reveal that the higher MOI reach a larger magnitude ratio. Although, the smaller MOI have a larger magnitude ratio in the 2-23 Hz bandwidth (approximately).

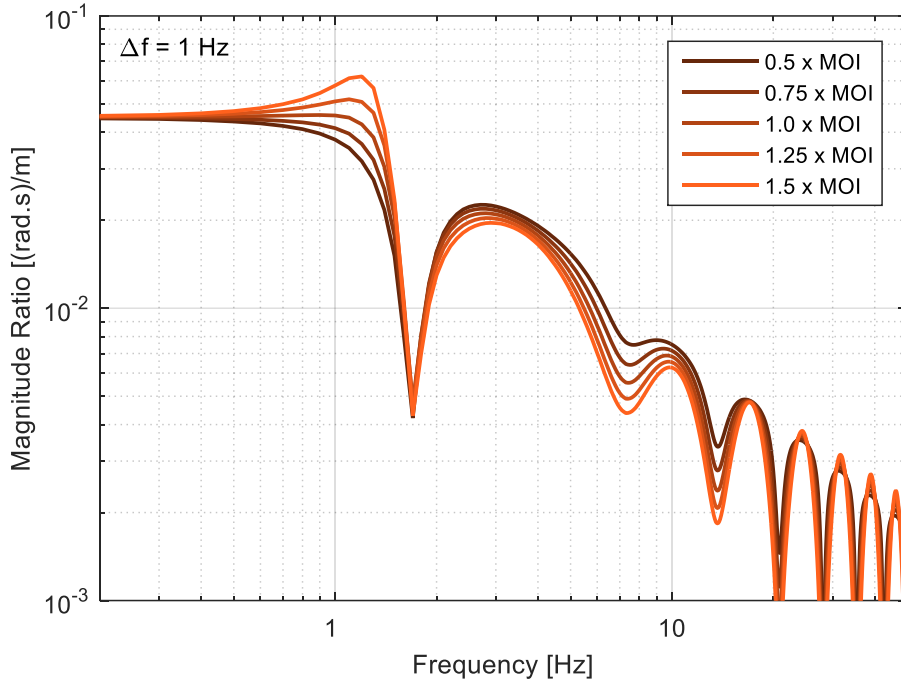


Figure 8-52: A comparison of the frequency response functions between the pitch angular velocity and vertical acceleration as the sprung mass's MOI are varied.

Below 4 Hz the higher MOI values are at a larger magnitude ratio in the heave-roll FRF, shown in Figure 8-53. Above this frequency the lower MOI have a higher magnitude ratio. The effects of wheelbase filtering are highly prominent.

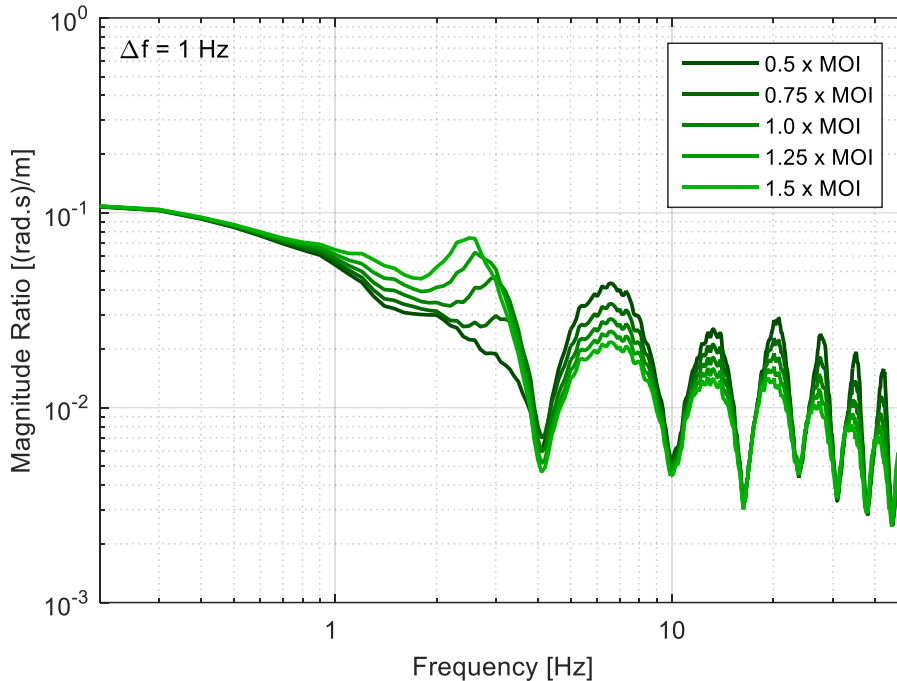


Figure 8-53: A comparison of the frequency response functions between the roll angular velocity and vertical acceleration as the sprung mass's MOI are varied.

8.5 On the Effects of Wheelbase Length

The final vehicle parameter varied was the wheelbase length. The wheelbase was varied between 2.5 and 4.5 m, this range is representative of commercially available utility vehicles. As discussed in section 3.2.2 the wheelbase impacts on the level of pitch vibration. It is also directly related to the wheelbase filter frequencies, as discussed in Appendix B.

For the simulations not only was the wheelbase varied, but also the front to rear CG location so that the front to rear CG location was kept at the same ratio of the total wheelbase for all tests. The CG was located 0.376 times the wheelbase reward of the front axle. This ratio was derived from the vehicle measured in Chapter 7. The measurement location was also taken in the usual position, directly above the rear axle.

The pitch:heave RMS ratio decreases linearly as the wheelbase is increased, as observed in Figure 8-54. The roll:heave ratio also decreases, although it decreases to a larger extent, the decrease is also non-linear.

Table 8-16 contains a summary of RMS ratios, the heave RMS increases with the wheelbase. The pitch RMS also increases with the wheelbase, a part from the 4.5 m wheelbase, where the RMS decreases from the previous 3.5 m value. Similarly the roll RMS show a general decreases as the wheelbase is increased,

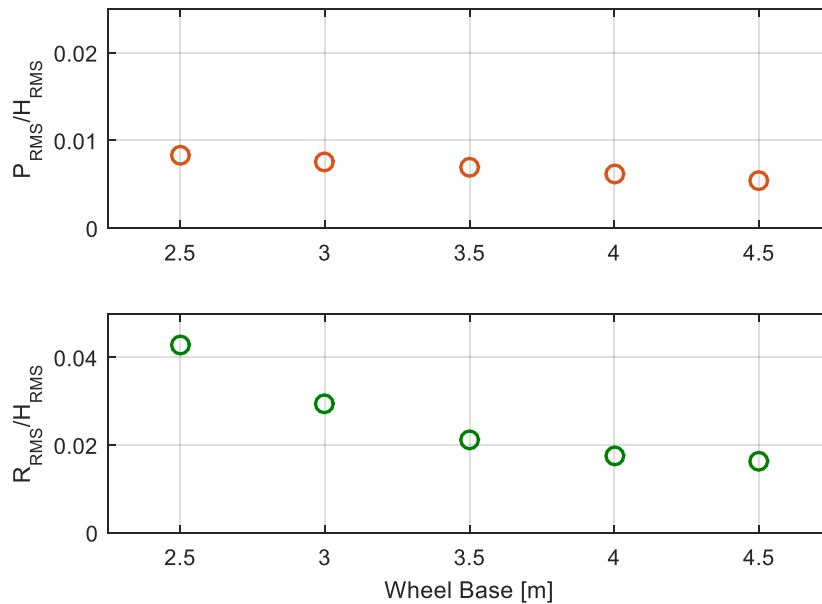


Figure 8-54: The effects of wheelbase length on the ratio between the pitch RMS and heave RMS (top) and the ratio between the roll RMS and heave RMS (bottom).

Table 8-16: A table summarising the RMS ratios for the differing wheelbase lengths.

Wheelbase [m]	H_{RMS} [m/s ²]	P_{RMS} [rad/s]	R_{RMS} [rad/s]	P_{RMS}/H_{RMS} [(rad.s)/m]	R_{RMS}/H_{RMS} [(rad.s)/m]
2.5	1.47	2.46×10^{-2}	6.29×10^{-2}	1.67×10^{-2}	4.28×10^{-2}
3	1.84	2.79×10^{-2}	5.37×10^{-2}	1.52×10^{-2}	2.93×10^{-2}
3.5	2.25	3.14×10^{-2}	4.75×10^{-2}	1.40×10^{-2}	2.11×10^{-2}
4	2.63	3.27×10^{-2}	4.62×10^{-2}	1.24×10^{-2}	1.75×10^{-2}
4.5	3.02	3.21×10^{-2}	4.96×10^{-2}	1.07×10^{-2}	1.64×10^{-2}

Figure 8-55 shows a comparison of the vertical acceleration moving RMS PDFs. As the wheelbase increases the mode also increases consistently. This is the only variation which happens linearly. At the same time, the maximum probability density decreases, which is coupled to an increase in the standard deviation.

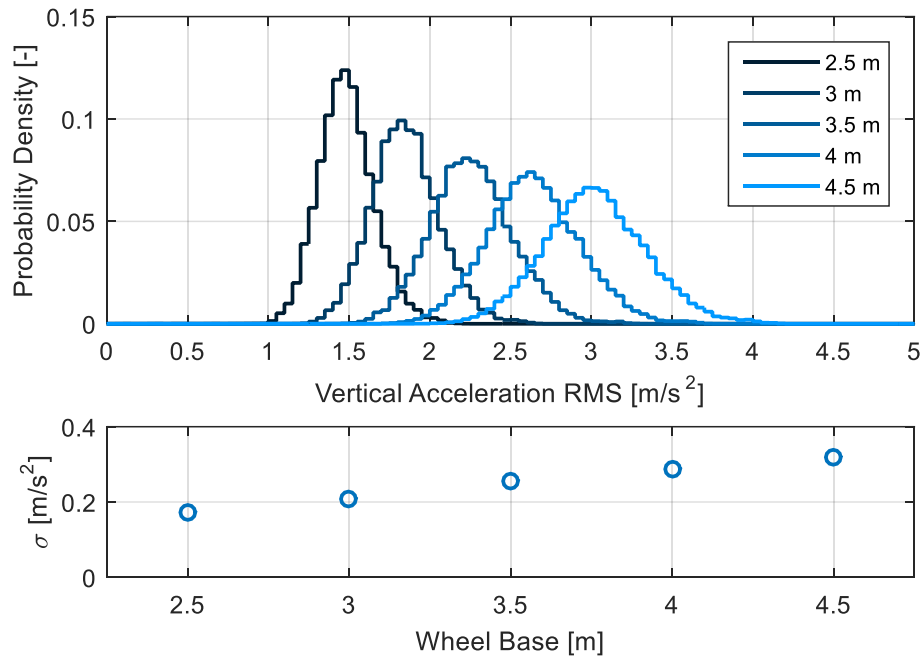


Figure 8-55: A comparison of the of the vertical acceleration moving RMS (2 second window, maximum overlap) PDFs for varying wheelbase lengths (top) and a comparison of the standard deviation (bottom).

Figure 8-56 contains a comparison of the pitch angular velocity moving RMS PDFs. As the wheelbase is increased the mode increases nonlinearly with it. The mode initially increases rapidly for the first three wheelbase values before remaining at this value for the last configurations. The maximum probability density and standard deviation also vary non-linearly as the wheelbase is increased.

Figure 8-57 contains a comparison of the roll angular velocity moving RMS PDFs. As the wheelbase is increased the mode of the distribution decreases non-linearly. As the distributions become less dispersed the maximum probability increase and the standard deviation decreases, once again non-linearly. The RMS range decreases with the wheelbase, however the distributions start at the same RMS values.

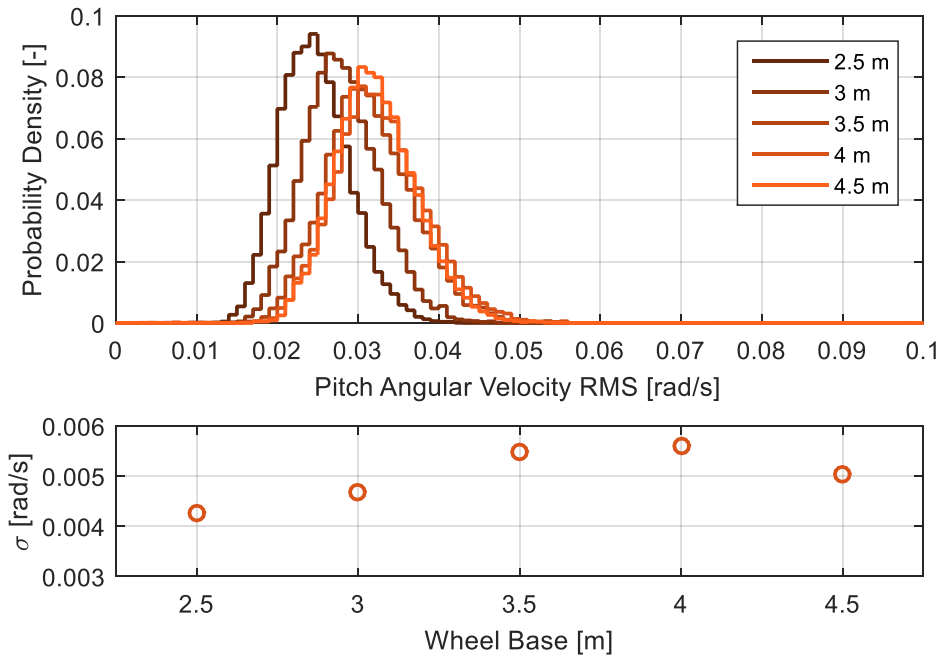


Figure 8-56: A comparison of the of the pitch angular velocity moving RMS (2 second window, maximum overlap) PDFs for varying wheelbase lengths (top) and a comparison of the standard deviation (bottom).

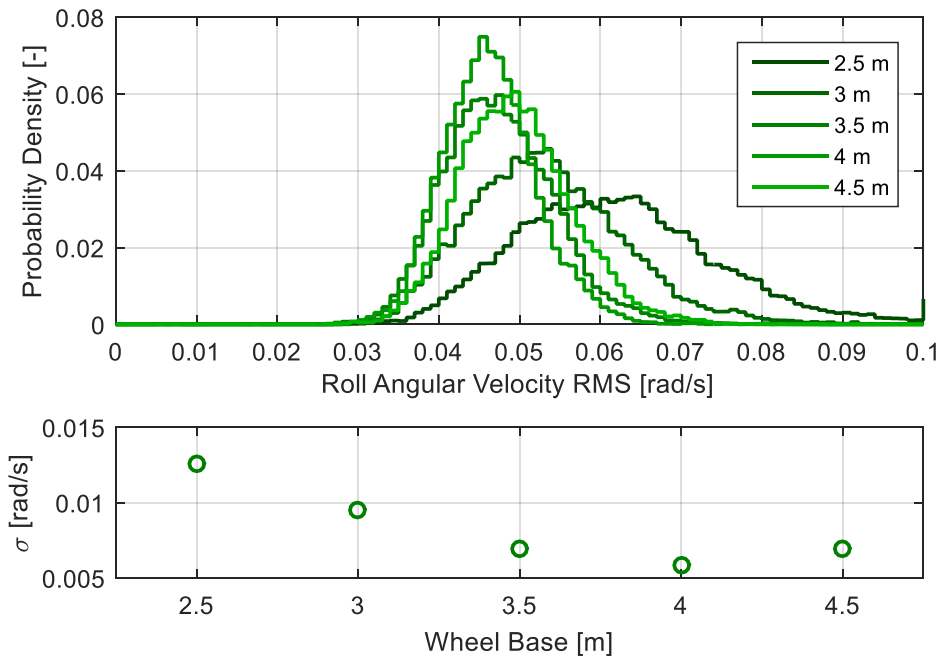


Figure 8-57: A comparison of the of the roll angular velocity moving RMS (2 second window, maximum overlap) PDFs for varying wheelbase lengths (top) and a comparison of the standard deviation (bottom).

Figure 8-58 shows a comparison between the heave-pitch bivariate histograms for the 2.5 m (left) and 4.5 m (right) wheelbase simulations. As the wheelbase is increase the data cloud translates towards higher levels of vertical acceleration and pitch angular velocities. A decrease in the maximum density also occurs. A change in the gradient is evident, with it and the RMSE both varying non-linearly as shown in Table 8-17 and Figure 8-59

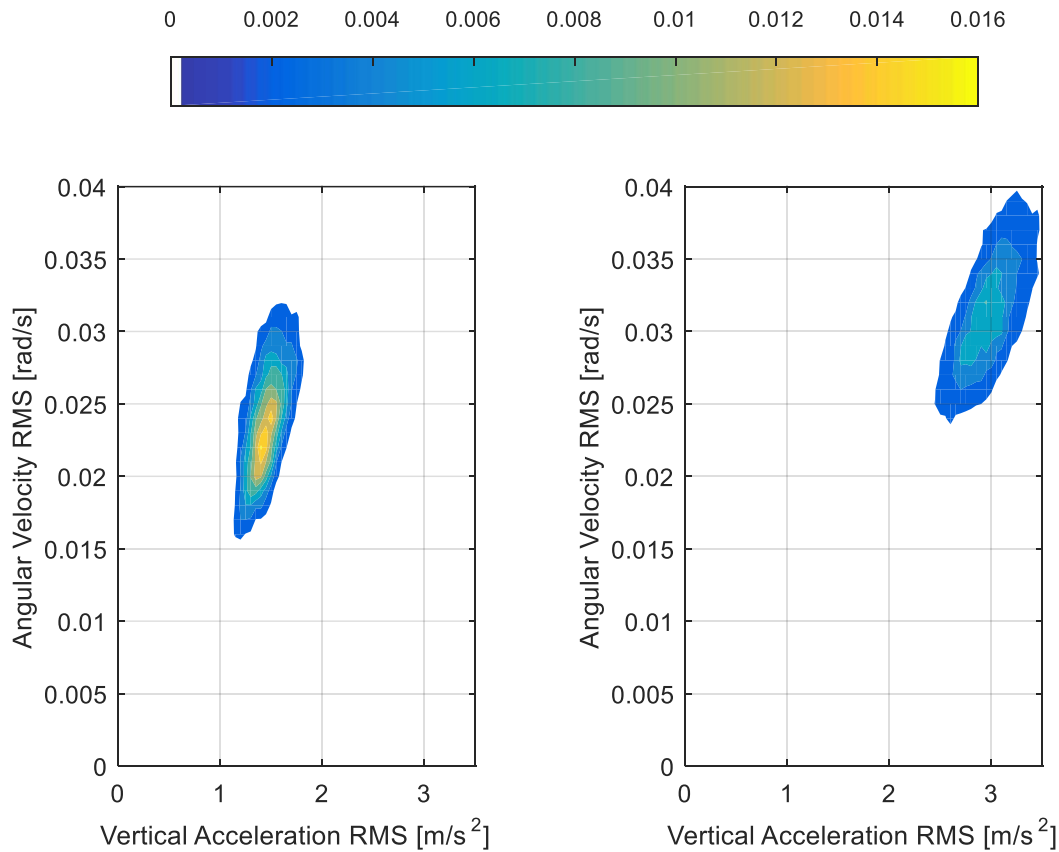


Figure 8-58: Comparison of vertical acceleration-pitch angular velocity bivariate histograms when the wheelbase is equal to 2.5 m (left) and 4.5 m (right).

Table 8-17: A table summarising linear models fit to the heave vs pitch RMS scatter plots.

Wheelbase [m]	Gradient	Y-Intercept	R²	RMSE
2.5	0.0141	0.0036	0.3201	0.0035
3	0.0178	-0.0050	0.6343	0.0028
3.5	0.0180	-0.0094	0.7024	0.0030
4	0.0156	-0.0085	0.6468	0.0033
4.5	0.0114	-0.0025	0.5220	0.0035

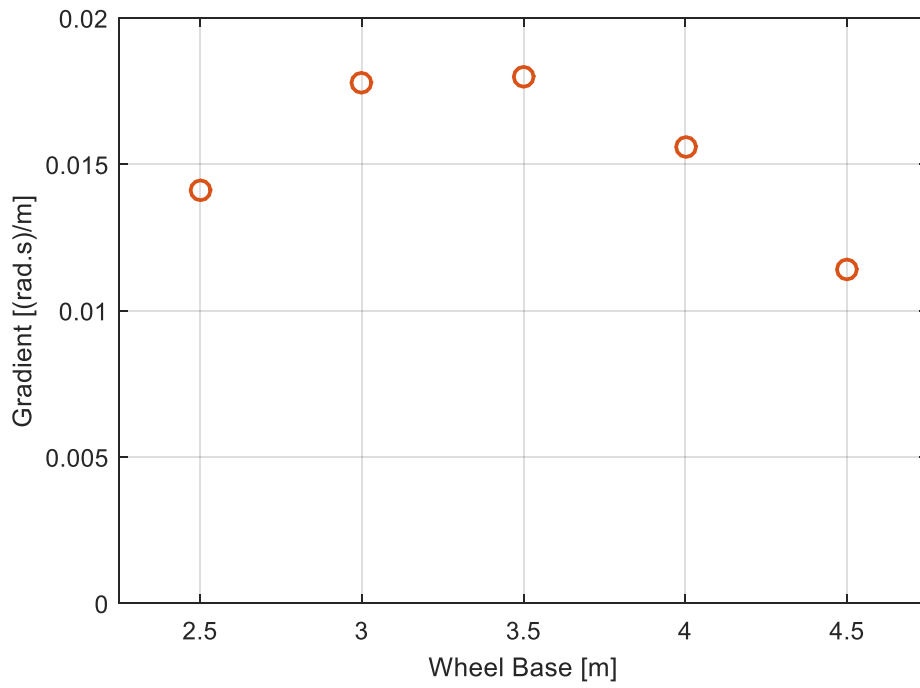


Figure 8-59: A comparison of the heave-pitch RMS scatter plot gradient as the vehicles wheelbase is varied.

Figure 8-60 shows a comparison between the heave-roll bivariate histograms for the 2.5 m (left) and 4.5 m (right) wheelbase simulations. A translation towards higher levels of vertical acceleration occurs whereas the roll angular velocity range decreases. Once again, as with all roll results the fitted linear models return no usable information with the gradient and R^2 equating to approximately zero. A summary of linear models fitted to the heave-roll data is shown in Table 8-18.

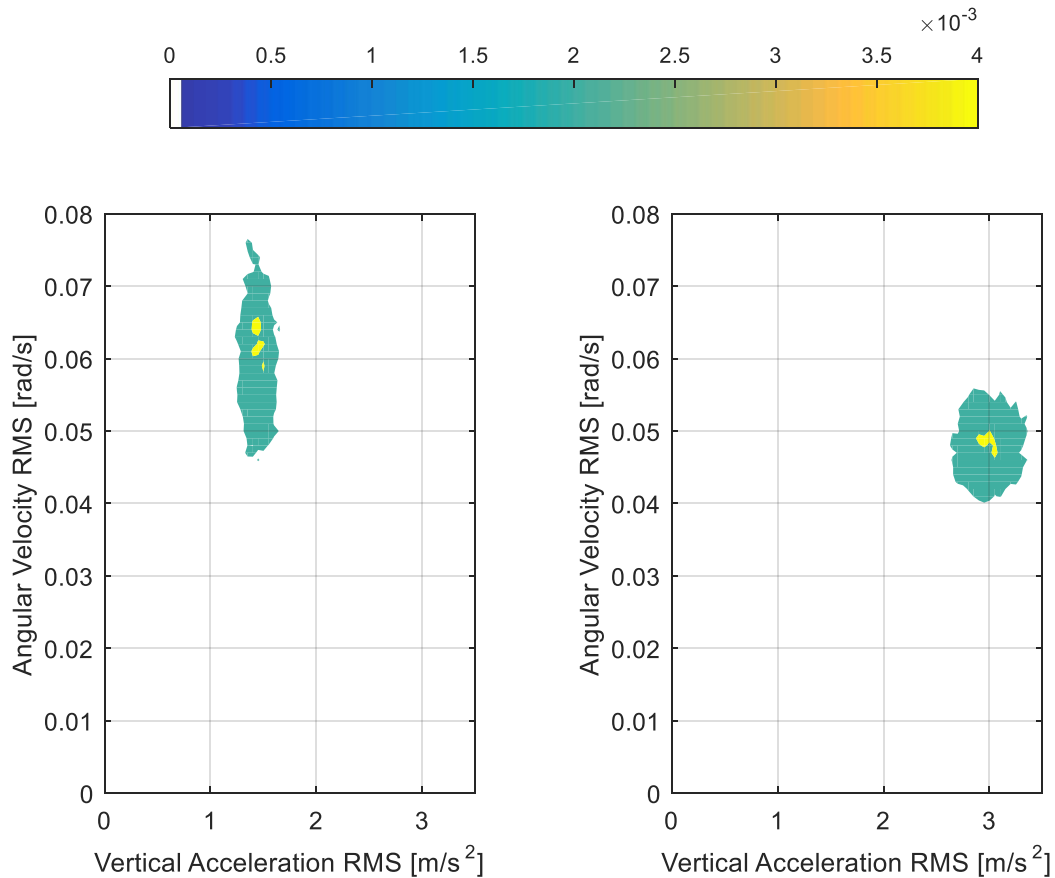


Figure 8-60: Comparison of vertical acceleration - roll angular velocity bivariate histograms of VAN1 traveling along Route 1 and 60 km/h (left) and 90 km/h (right).

Table 8-18: A table summarising linear models fit to the heave vs roll RMS scatter plots.

Wheelbase [m]	Gradient	Y-Intercept	R^2	RMSE
2.5	-0.0025	0.0653	0.0012	0.0125
3	-0.0010	0.0546	0.0004	0.0095
3.5	0.0000	0.0471	0.0000	0.0069
4	0.0002	0.0452	0.0001	0.0058
4.5	0.0002	0.0485	0.0001	0.0069

PCA of the heave-pitch data revealed that the distribution parallel to the principal axis remains similar for the different wheelbases, as seen in Figure 8-61. The standard deviation remains similar between the configurations, whilst the maximum probability density fluctuates randomly. The distribution about the principal axis remains similar despite the large changes to the vertical acceleration a pitch angular velocity moving RMS distributions.

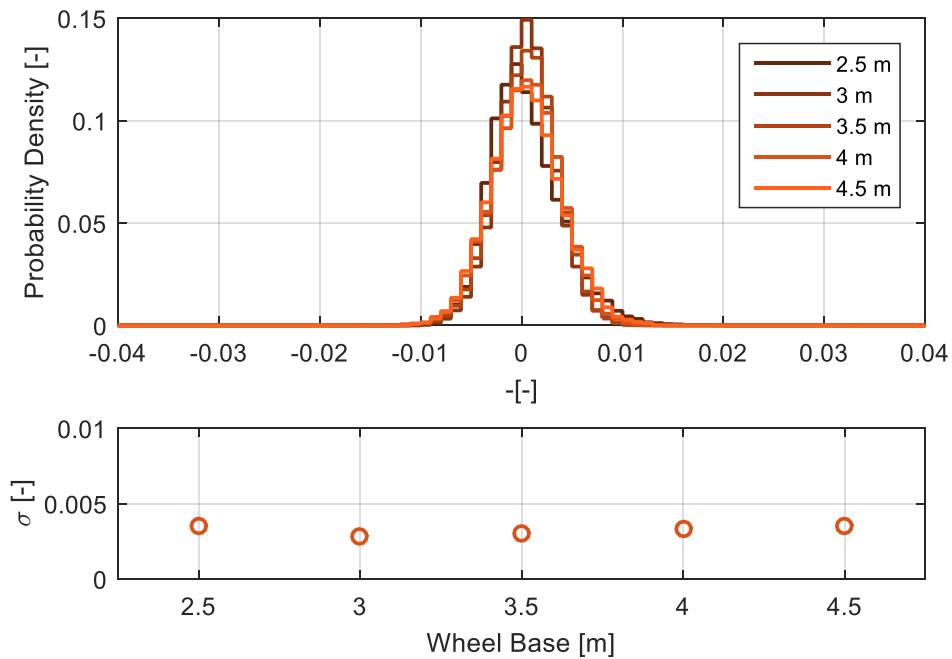


Figure 8-61: A comparison of PDFs taken parallel to the principal axis from the PCA adjusted heave-pitch RMS scatter plots as the wheelbase length is varied (top) and the change in standard deviation (bottom).

A significant change occurs to the PCA-adjusted heave-roll PDF as the wheelbase is increased, as seen in Figure 8-62. The maximum probability density increases as the wheelbase lengthens, which in turn reduces the standard deviation. Again these changes are non-linear despite the linear increments in which the wheelbase was extended.

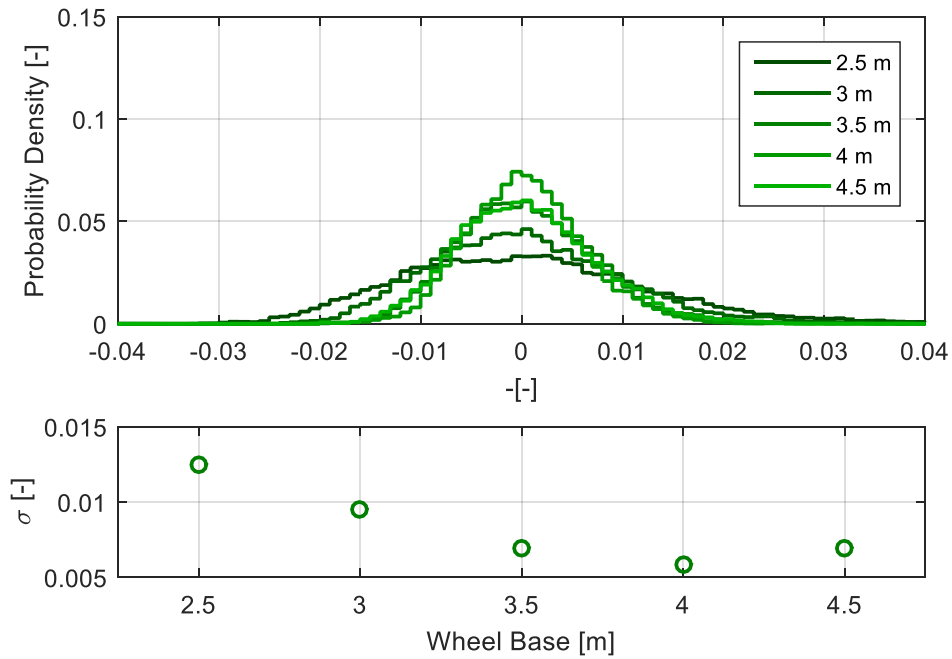


Figure 8-62: A comparison of PDFs taken parallel to the principal axis from the PCA adjusted heave-roll RMS scatter plots as the wheelbase length is varied (top) and the change in standard deviation (bottom).

Figure 8-63 shows a comparison of the vertical acceleration PSD functions as the wheelbase is increased. The total vertical acceleration is equal to the vertical acceleration of the sprung mass plus the tangential (vertical) component of the pitch angular acceleration, increasing the wheelbase increases the lever arm of the rotation which has the potential to increase the vertical acceleration RMS. The changes in the wheelbase filter frequencies is also evident in the PSD functions.

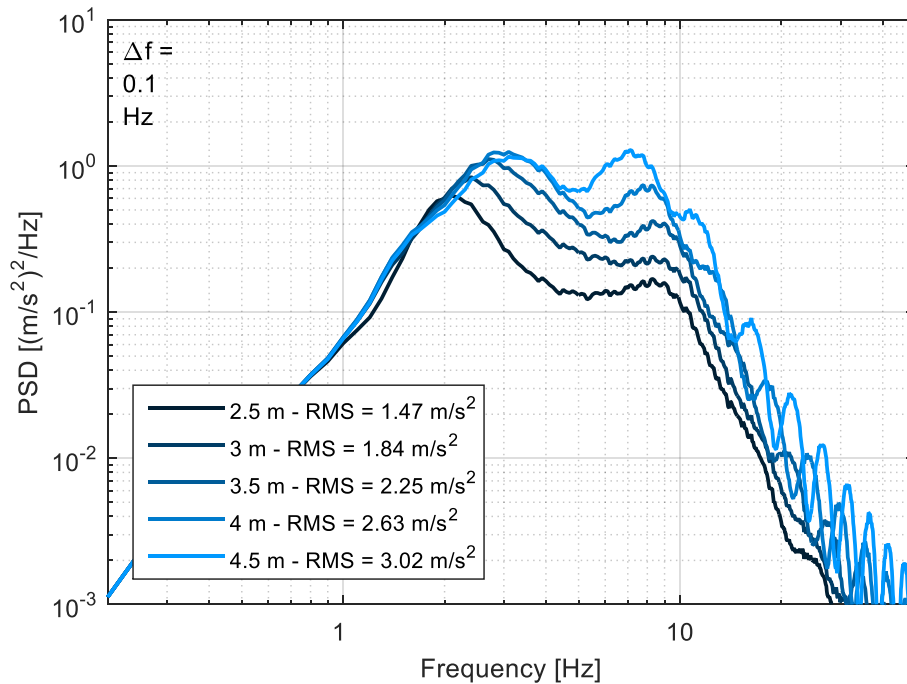


Figure 8-63: A comparison of the vertical acceleration PSD functions as the wheelbase is varied.

Figure 8-64 shows a comparison of the pitch angular velocity PSD functions. As the wheelbase is increased the RMS also increases, however at low frequencies the shorter wheelbases contain more energy. This is reversed between the first and second peaks, with the longer wheelbases containing more energy for the remaining bandwidth.

Figure 8-65 shows a comparison of the roll angular velocity PSD functions. As the wheelbase is increased the RMS decreases, with the short wheelbases containing more energy at low frequencies once more.

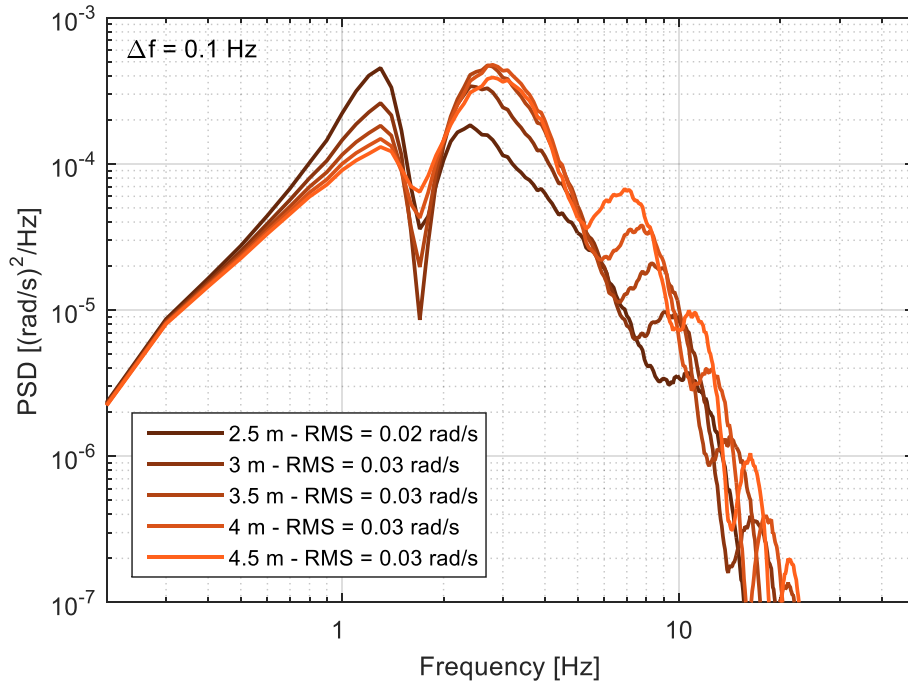


Figure 8-64: A comparison of the pitch angular velocity PSD functions as the wheelbase is varied.

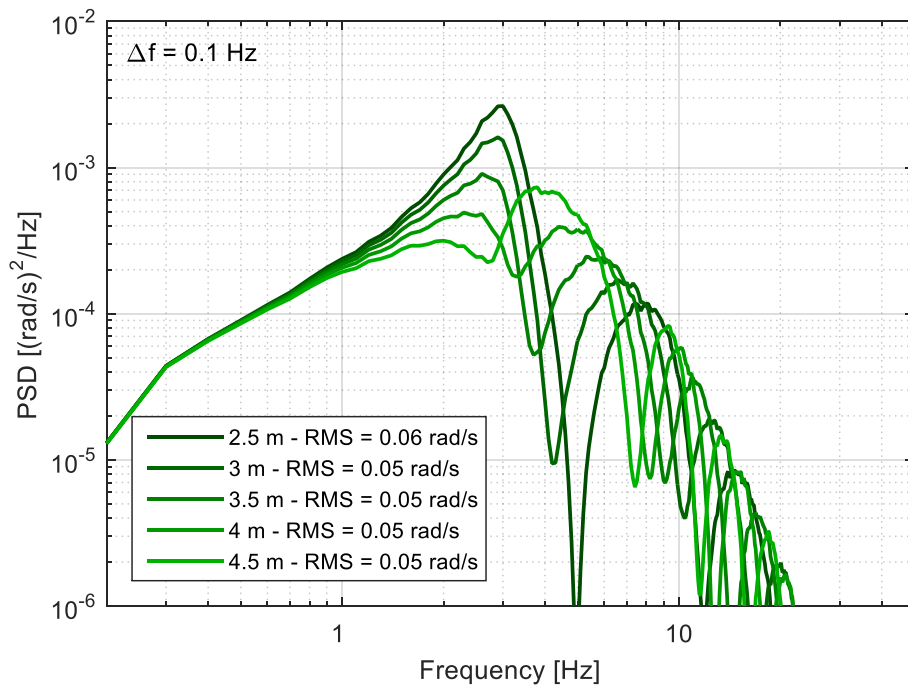


Figure 8-65: A comparison of the roll angular velocity PSD functions as the wheelbase is varied.

The frequency response functions calculated between the vertical vibration and the pitch response are shown in Figure 8-66. The short wheelbase configurations reach a higher maximum magnitude ratio than the longer wheelbases. Although, all FRFs begin at the same magnitude ratio. The wheelbase's effect on the wheelbase filtering nodal frequencies is evident, decreasing as the wheelbase lengthens.

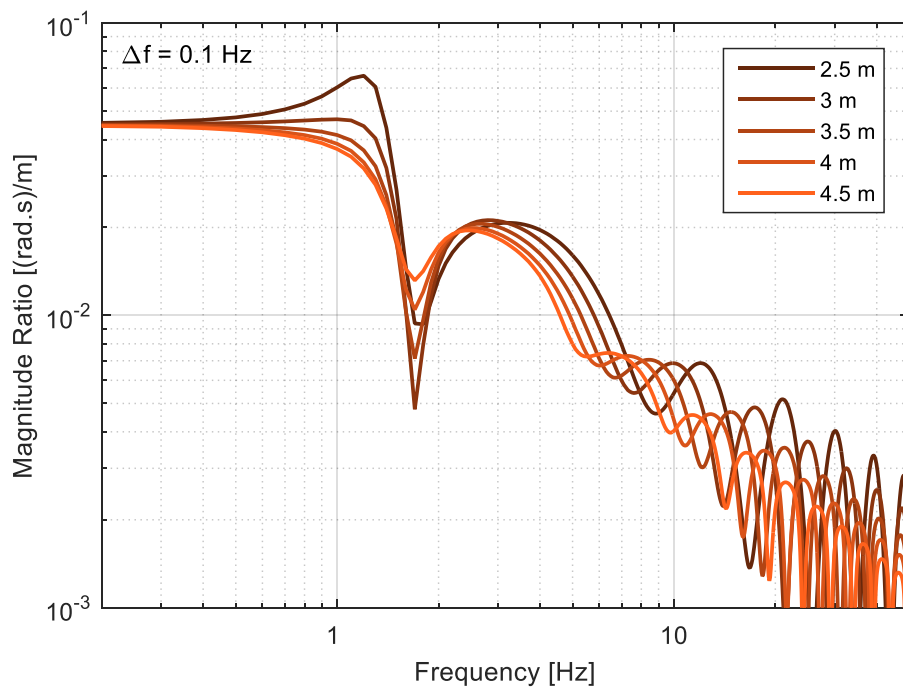


Figure 8-66: A comparison of the frequency response functions between the pitch angular velocity and vertical acceleration as the wheelbase is varied.

Figure 8-67 contains a comparison of the heave-roll FRFs as the wheelbase is varied. Like the heave-pitch FRF the shorter wheelbases reach a higher magnitude ratio than the long wheelbases. Once more, the FRFs all begin at the same initial magnitude ratio.

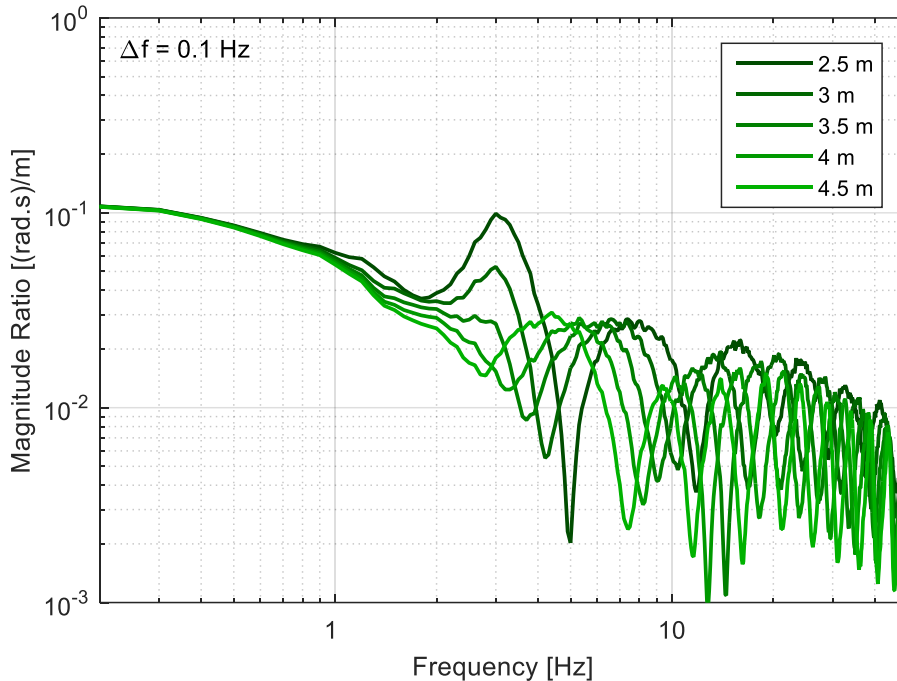


Figure 8-67: A comparison of the frequency response functions between the roll angular velocity and vertical acceleration as the wheelbase is varied.

The effect wheelbase length has on the relationship between heave, pitch and roll appears to be quite complex, from the results. This is due to the coupling between heave and pitch, heave and roll, and therefore pitch and roll (see equations 7-3, 7-4 and 7-5). Furthermore the multi-axial response is also affected by the way the left and right wheel paths are created for the numerical model. In the case of these results, the non-linear coherence function between the wheel paths and the non-linear nature of the road elevation spectra may contribute to some of the less straight forward results.

8.6 Numerical Simulations Summary

This chapter set out to do an in-depth analysis of potential relationships which may exist between the heave, pitch and roll vibratory motion of a four wheeled vehicle. The numerical model simulations returned sensible results thanks to the realistic parameter values obtained in the previous chapter. Several conclusions can be drawn from these results.

The most noteworthy finding, that was evident in all simulations, was that significantly more research needs to be conducted into simulating realistic dual wheel path road elevation profiles. The synthetic road elevation profile used in the simulations returned realistic heave and pitch responses however the roll response was vastly different when looking at the bivariate histograms and PCA distributions. It is believed that introducing a modulated RMS to the road excitation to better represent the non-stationarity of real roads would significantly improve the accuracy of the response characteristics. Further work into the correlation between the left and right wheel paths would be highly beneficial, as a significant gap exists between the literature, standards and actual measurements, to the detriment of numerical simulations.

The idealistic nature of the numerical model was also to its detriment. The effects of wheelbase filtering were highly prominent in the simulation results. The simulations maintain an exactly constant speed which amplifies the effects. Introducing a small random fluctuation in the speed, would reduce the impacts of the response nodes.

Nonetheless, some major findings can be taken from the sensitivity analysis carried out. It was discovered that the vehicle's speed impacts on the RMS ratios and the FRFs, although in contrast, these remain the same when road roughness is varied (if the spectral shape remains the same). For a given frequency range, increasing the vehicles speed has the same effect as increasing the displacement RMS (if the spectrum is linear), however the impacts on a multi-axial vibration are vastly different. The coupling that occurs between different vibratory modes and the roll and pitch excitation means that the changes in roughness are not equivalent to changes in speed.

The coupling between vibratory modes was also responsible for the occurrence of wheelbase filtering in the roll response. This was initially unexpected as it did not appear in the literature or physical experiments. However, the equations of motion contain each vibratory mode therefore some form of coupling will exist. As mentioned previously the perfectness of a numerical model amplifies these effects.

When the sprung mass was increased it was revealed that the largest peak within a vertical acceleration PSD function may not correspond solely to the fundamental frequency of the vertical vibration. When the vertical acceleration is measured away from the centre of gravity the total acceleration measured is a combination of the vertical translation acceleration as well as the tangential component of the body's angular accelerations. When measuring over the rear axle the large distance from the centre of rotation makes the tangential component quite large. This makes the measurement location extremely influential and the analysis quite difficult.

In all simulations parameters were varied linearly, varying by a set amount, despite this many non-linear changes were observed. This was particularly the case when the MOI and wheelbase were varied. In both cases the moving RMS PDFs showed highly non-linear changes in the mode and standard deviation, as well as the gradient of the RMS scatter plots. This results in situations where changing the wheelbase and MOI further may not result in any significant changes to the vibratory response, which is interesting.

This series of numerical simulations was aimed to further study the potential relationships which may exist between the heave, pitch and roll vibratory motion of a four wheeled vehicle. The numerical model simulations returned useful results which has shed light on to the influence that these parameters have on the vibratory motion of transport vehicles.

Chapter 9

Conclusions and Future Work

The preliminary and exploratory nature of this research and the significant number of experiments undertaken make it difficult to draw concise conclusions which completely describe the heave, pitch and roll relationships for all scenarios. Results from the experiments were discussed in detail within the thesis, the conclusion presented here will focus on the more noteworthy results.

The primary hypothesis of this thesis is that a statistical correlation exists between the heave, pitch and roll vibratory motions of a wheeled vehicle traveling over uneven pavements. The research presented herein has found this to be true. A strong relationship was observed between the vertical acceleration and the pitch angular velocity. A weaker, yet still evident relationship was observed between the vertical acceleration and the roll angular velocity.

These relationships were found to exist both in the amplitude and frequency domain, as put forward by the first sub-hypothesis. The second sub-hypothesis stated that these relationships would be a function of vehicle speed, road roughness and dynamic parameters, namely the vehicles geometric properties, vehicle moments of inertia and payload mass, which was also found to be true.

One of the most significant findings of this thesis is that the measurement location of the vertical acceleration response, relative to the centre of gravity of the vehicle has a considerable influence on the data. Whereas pitch and roll angular velocity measurement are fully independent of sensor location. The further the measurement location is away from the centre of gravity the larger the influence of the tangential pitch and roll accelerations. For this reason, it is highly recommended that future publications, dealing with vertical acceleration, estimate the measurement location relative to the vehicle's centre of gravity.

In situations where the vertical acceleration natural frequency is in close proximity to the pitch natural frequency, great care must be taken when stating the 'natural frequency' of the sprung mass. This is especially true when trying to retrieve dynamic properties from the natural frequency estimate.

Numerical simulations are heavily influenced by the effects of wheelbase. The cross talk between the vibratory modes means the wheelbase filtering effects are manifested within the roll response. Little mention of wheelbase filtering is made in the literature, due to it rarely being observed in physical experiments focusing on vertical acceleration. This also relates to the influence of sensor location.

When measuring the away from the centre of gravity, increasing the pitch and roll moments of inertia can reduce the vertical acceleration, due to a reduction in the tangential acceleration of the pitch and roll response.

Current road synthesis techniques are unable to sufficiently replicate road elevation profiles for multi-wheel path simulations. The simulated roll results became unsound due to their non-realistic character.

Road roughness had little effect on the relationships between the vibratory modes. The field experiments showed that there was no significant change in the slope of the moving RMS scatter plot and the FRF's. This was further explored and confirmed with numerical simulations, which allowed for a more controlled testing.

The effect of wheelbase length can be significant on the heave, pitch and roll response. This effect was also shown to be non-linear, due to the hyperbolic nature of road elevation spectra.

Given that this is the first such work on exploring the relationships between the heave pitch and roll vibratory motion, this research has made some significant contributions to this area of knowledge. The results herein provide a good guide for configuring the target PSD functions

and RMS levels for laboratory testing of packaged systems using multi-axis vibration test systems.

9.1 Future Work

Since the research presented in this thesis is the initial stage of a broader effort, there are numerous avenues for further work and investigation. The numerical model developed proved to be an excellent tool for assessing the influence of vehicle and experimental parameters, and can be expanded on in a plethora of ways. The 7DoF light transport vehicle model can be further developed to allow for the analysis of more complex vehicle layouts, including multi-axle rigid trucks and tractor-trailer configurations. These transport vehicle setups are more widely utilised for goods transport.

No matter the complexity of the numerical model it will still be plagued with the same issues that were encountered during this research. Methods to reduce the impacts of wheelbase filtering on the simulations requires further exploration, to better replicate real world results. This could be achieved via small random fluctuations in the speed control or potentially through non-linear suspension.

A better understanding of the road elevation profile is required for the most accurate results. The assumptions of stationarity, isotropy and homogeneity do not hold for all wave lengths and long sections of roads. A method for synthesising dual wheel path road elevation profiles with a user specified coherence function was put forth, however it is still limited to being stationary (constant RMS). The coherence between each wheel path can be specified, but coherence functions put forth in the literature were vastly different than those measured on the actual road. Worse still is that the coherence varies as a function of track width. Significant research needs to be conducted on the synthesis of not only multiple wheel paths but the whole road surface.

The series of physical experiments and numerical simulations revealed that the measurement location (sensor placement) has a large impact on the level of vibration experienced. This, by extension, also influences the vibrations felt by payloads. A significant gap in the literature exists in this area, and would benefit from a thorough investigation.

Finally, more in-depth analysis of the parameters tested would be beneficial, particularly the influence of wheelbase length.

Chapter 10

References

- Ainalis, Daniel (2014), 'Estimating the Dynamic Characteristics of Road Vehicles Using Vibration Response Data', PhD Thesis, Victoria University.
- Ainalis, Daniel, Rouillard, Vincent, and Sek, Michael (2015), 'Issues with the experimental characterisation of automotive shock absorbers for vehicle dynamic simulations', *8th Australasian Congress on Applied Mechanics: ACAM 8*. (Melbourne).
- Allen, R Wade, *et al.* (2003), 'Estimation of passenger vehicle inertial properties and their effect on stability and handling', (SAE Technical Paper).
- Ammon, D and Bormann, V (1991), 'Zur Kohärenz zwischen den Unebenheitsanregungen an linker und rechter Fahrspur', *VDI-Berichte*, 877, 103-18.
- Australian Packaging Covenant (APC) (2014), 'Annual Report', (Sydney).
- APC (2015), 'Australia's Packaging recycling Rate'.
- ASTM (2012), 'ASTM D4728-06: Standard Test Method for Random Vibration Testing of Shipping Containers', (West Conshohocken, PA: ASTM International).
- ASTM (2014), 'ASTM D4169-14: Standard Practice for Performance Testing of Shipping Containers and Systems', (West Conshohocken, PA: ASTM International).
- Batt, G (2010), 'Use of simultaneous three axis vibration in simulation of the transport environment', *International Transport Packaging Forum*.

- Bernad, Carlos, Laspalas, Alberto, and Nt'ifiez, José Luis (2012), 'Development of a Multi-axis Transport Vibration Test', *Eighteenth IAPRI World Packaging Conference* (DESTech Publications, Inc), 364.
- Bernad, Carlos, *et al.* (2010), 'Dynamic study of stacked packaging units by operational modal analysis', *Packaging Technology and Science*, 23 (3), 121-33.
- Bernad, Carlos, *et al.* (2011), 'Transport vibration laboratory simulation: On the necessity of multi-axis testing', *Packaging Technology and Science*, 24 (1), 1-14.
- Bixel, Ronald A, *et al.* (1996), 'Sprung/Unsprung Mass Properties Determination without Vehicle Disassembly', (SAE Technical Paper).
- Bixel, Ronald A, *et al.* (1995), 'Developments in Vehicle Center of Gravity and Inertial Parameter Estimation and Measurement', (SAE Technical Paper).
- Bruscella, Ben (1997), 'The analysis and simulation of the spectral and statistical properties of road roughness for package performance testing', (Victoria University of Technology).
- Bruscella, B., Rouillard, V., and Sek, M. (1999), 'Analysis of road surface profiles', *Journal of Transportation Engineering-Asce*, 125 (1), 55-59.
- Bureau of Infrastructure, Transport and Regional Economics (BITRE) (2010), 'Road freight estimates and forecasts in Australia: interstate, capital cities and rest of state', (Canberra ACT).
- Cebon, David (1989), 'Vehicle-generated road damage: a review', *Vehicle system dynamics*, 18 (1-3), 107-50.
- Cebon, David (1999), *Handbook of Vehicle-road Interaction* (Advances in engineering: Swets and Zeitlinger, Lisse (Netherlands)).
- CEU (1996), 'Council Directive 96/53/EC', The Council of European Communities, (Brussels).
- Charles, Darrel (1993), 'Derivation of Environment Descriptions and Test Severities from Measured Road Transportation Data', *Journal of the IES*, 36 (1), 37-42.
- Chonhenchob, Vane, *et al.* (2012), 'Measurement and Analysis of Vehicle Vibration for Delivering Packages in Small-Sized and Medium-Sized Trucks and Automobiles', *Packaging Technology and Science*, 25 (1), 31-38.
- Cole, Henry A (1968), 'On-line analysis of random vibrations', *Journal of the American Institute of Aeronautics and Astronautics*.
- Cole, Henry A (1973), *On-line failure detection and damping measurement of aerospace structures by random decrement signatures* (2205: National Aeronautics and Space Administration).
- Dodds, C. J. and Robson, J. D. (1973), 'The description of road surface roughness', *Journal of Sound and Vibration*, 31 (2), 175-83.
- Ernst, Matthew, *et al.* (2015), 'Comparison of Electronic Component Durability Under Uniaxial and Multiaxial Random Vibrations', *Journal of Electronic Packaging*, 137 (1), 011009.

- Evans, Merran, Hastings, N, and Peacock, B (2001), 'Statistical distributions', (IOP Publishing).
- Garrott, W Riley, Monk, Michael W, and Chrstos, Jeffrey P (1988), 'Vehicle inertial parameters-measured values and approximations', (SAE Technical Paper).
- Gillespie, Thomas D. (1985), 'Heavy truck ride', (SAE Technical Paper).
- Gillespie, Thomas D (1992), "Fundamentals of Vehicle Dynamics", *Society of Automotive Engineers*.
- Gregory, Dan, Bitsie, Fernando, and Smallwood, D (2008), 'Comparison of the response of a simple structure to single axis and multiple axis random vibration inputs', *79th Shock and Vibration Symposium, Orlando, FL, Oct, 26-30*.
- Griffiths, Katharine (2012), 'An Improved Method for Simulation of Vehicle Vibration Using a Journey Database and Wavelet Analysis for the Pre-Distribution Testing of Packaging', (University of Bath).
- Griffiths, Katharine, *et al.* (2011), 'Simulating the transport environment for packaging testing using a multi degree of freedom method', *International Safe Transit Association, 2011 International Transport Packaging Forum* (University of Bath).
- Heath, A. N. (1988), 'Evaluation of the isotropic road roughness assumption', *Vehicle System Dynamics*, 17 (sup1), 157-60.
- Heath, A. N. (1989), 'Modelling and simulation of road roughness', *IAVSD SYMPOSIUM (11TH: 1989: KINGSTON, ONT) THE*.
- Houbolt, John C. (1962), 'Runway Roughness Studies in the Aeronautic Field', *American Society of Civil Engineers Transactions*.
- Houbolt, John C, Walls, James H, and Smiley, Robert F (1955), 'On spectral analysis of runway roughness and loads developed during taxiing', (National Advisory Committee for Aeronautics).
- IEC (2008), 'IEC 60068: Environmental testing - Part 2-64: Tests - Test Fh: Vibration, broadband random and guidance', (Geneva: International Electrotechnical Commission).
- ISO (1995), 'International Standard 8608: Mechanical Vibration – Road Surface Profiles – Reporting of Measured Data', (Geneva: International Organisation for Standardisation).
- ISO (2001), 'International Standard 13355: Packaging -- Complete, filled transport packages and unit loads -- Vertical random vibration test', (Geneva: International Organisation for Standardisation).
- ISTA (2009), 'ISTA Procedure 3E: Unitized Loads of Same Product', (Michigan: International Safe Transit Association).
- ISTA (2011), 'ISTA Procedure 3H: Performance Test for Products or Packaged-Products in Mechanically Handled Bulk Transport Containers ', (Michigan: International Safe Transit Association).

- Janic, Milan (2007), 'Modelling the full costs of an intermodal and road freight transport network', *Transportation Research Part D: Transport and Environment*, 12 (1), 33-44.
- Kropac, Oldrich and Múčka, Peter (2008), 'Indicators of longitudinal unevenness of roads in the USA', *International journal of vehicle design*, 46 (4), 393-415.
- Kohli, Chiranjeev, Thomas, Sunil, and Suri, Rajneesh (2013), 'Are You In Good Hands?', *Journal of Advertising Research*, 53 (1), 31-42.
- La Barre, RP, Forbes, RT, and Andrew, S (1969), 'The measurement and analysis of road surface roughness', *Technical Report 170/5* (Lindley, Warwickshire.: Motor Industry Research Association).
- Lamb, Matthew J and Parker, Anthony J (2015), 'Monitoring the Condition of Non-linear Packaging Materials Subject to Varying Excitation Levels Using a Reverse Multiple Input/Single Output Based Approach', *Packaging Technology and Science*, 28 (8), 683-93.
- Lamb, MJ, Rouillard, Vincent, and Sek, Michael A (2012), 'Monitoring the evolution of damage in packaging systems under sustained random loads', *Packaging Technology and Science*, 25 (1), 39-51.
- Lépine, Julien, Rouillard, Vincent, and Sek, Michael (2015), 'Review Paper on Road Vehicle Vibration Simulation for Packaging Testing Purposes', *Packaging Technology and Science*, 28 (8), 672-82.
- Marshal, K. D. (2006), 'Tire Noise and Vibration', *The Pneumatic Tire Chapter 9*, 364-408.
- Múčka, Peter (2015), 'Model of coherence function of road unevenness in parallel tracks for vehicle simulation', *International Journal of Vehicle Design*, 67 (1), 77-97.
- National Environment Protection Council (NEPC) (2014), 'Packaging Impacts Decision Regulation Impact Statement'.
- NAVMAT (1979), 'P-9492: Navy Manufacturing Screening Program: Decreased Corporate Costs Increase Fleet Readiness', (Naval Material Command), 6.
- Oestergaard, S. (1991), 'Packaging Goals in Transport Quality', *7th IAPRI World Conference on Packaging Technology and Science* (Utrecht, the Netherlands.).
- Oristep Consulting (2015), 'Global Protective Packaging Market - By Regions and Vendors - Market Trends and Forecasts (2014 - 2020)'.
- Otari, S., *et al.* (2011), 'Statistical Characterization of Acceleration Levels of Random Vibrations during Transport', *Packaging Technology and Science*, 24 (3), 177-88.
- Peterson, C (2012), 'Experimentation at Team Corporation using single and multiple-axis vibration'.
- Quinn, BE and Zable, JL (1966), 'Evaluating highway elevation power spectra from vehicle performance', *Highway Research Record*, (121).

- Riede, Peter M, Leffert, Ronald L, and Cobb, William A (1984), 'Typical Vehicle Parameters for Dynamics Studies Revised for the 1980's', (SAE Technical Paper).
- Root, Dale (1997), 'Six Step Method for Cushioned Package Development', <www.lansmont.com>, accessed 8 April 2014.
- Rouillard, Vincent (2006), 'On the synthesis of non-Gaussian road vehicle vibrations', (Monash University).
- Rouillard, Vincent (2008), 'Generating Road Vibration Test Schedules from Pavement Profiles for Packaging Optimization', *Packaging Technology and Science*, 21 (8), 501-14.
- Rouillard, V and Sek, MA (2000), 'Monitoring and simulating non-stationary vibrations for package optimization', *Packaging Technology and Science*, 13 (4), 149-56.
- Rouillard, V, Sek, MA, and Perry, T (1996), 'Analysis and simulation of road profiles', *Journal of transportation engineering*, 122 (3), 241-45.
- Rozyn, Matthew and Zhang, Nong (2010), 'A method for estimation of vehicle inertial parameters', *Vehicle system dynamics*, 48 (5), 547-65.
- Sayers, M. (1986), 'Characteristic power spectral density functions for vertical and roll components of road roughness', *Proceedings ASME Symposium on Simulation and Control of Ground Vehicles and Transportation Systems, Anaheim, California*.
- Sciulli, Dino (1997), 'Dynamics and control for vibration isolation design'.
- Sek, M.A. (2001), 'Optimisation of Packaging Design Through an Integrated Approach to the Measurement and Laboratory Simulation of Transportation Hazards', *12th International Conference on Packaging (Warsaw, Poland)*.
- Shires, David (2011), 'On the Time Compression (Test Acceleration) of Broadband Random Vibration Tests', *Packaging Technology and Science*, 24 (2), 75-87.
- Singh, S Paul, Antle, John R, and Burgess, Gary G (1992), 'Comparison between lateral, longitudinal, and vertical vibration levels in commercial truck shipments', *Packaging Technology and Science*, 5 (2), 71-75.
- Siviter, R and Pollard, MG (1986), 'Measurement of Railway Vehicle Kinematic Behaviour Using the Random Decrement Technique', *Vehicle System Dynamics*, 15, 537-50.
- United States Department of Defence (2008), 'MIL-STD-810G: Department of Defence Test Method Standard for Environmental Engineering Considerations and Laboratory Tests'.
- Winkler, Christopher B (1983), *Inertial Properties of Commercial Vehicles: Descriptive Parameters Used in Analyzing the Braking and Handling of Heavy Trucks* (2nd Edition, Volume 2).
- WPO (2008), 'Market Statistics and Future Trends in Global Packaging', (Illinois: World Packaging Organisation).

Yam, Kit L (2010), *The Wiley encyclopaedia of packaging technology* (3rd Edition, John Wiley & Sons).

Liu, Xiandong, *et al.* (2015), 'Construction of road roughness in left and right wheel paths based on PSD and coherence function', *Mechanical Systems and Signal Processing*, Issue 60, 668-77.

Appendix A

Validation of the Full Car Numerical Model

The validation of a numerical model is an important process that must be undertaken prior to its use. Due to the complexity of the equations needed for a four wheeled 7DoF vehicle model, it is possible for errors to be made when developing the model. As explained in the following appendix, using an idealised numerical model can lead to results that contain characteristics not seen in measurements made in the real world and, as such, can cause a lot of confusion and doubt about the validity of the model. Several methods for validating the numerical model were employed, including frequency response function comparison and natural frequency calculations using eigenvalues for various parameter sets.

During the validation process several different system excitations were used. The excitation was introduced to the system in different ways to isolate certain motions of the vehicle. Exciting the vehicle with the same signal through all wheels simultaneously eliminates the forced excitation of the pitch and roll modes of vibration. Similarly, different signals were used as left and right wheel paths to excite the roll and vertical vibration modes without exciting the pitch mode. The pitch mode was excited by introducing a time delay between the front and rear wheels.

A.1 2DoF frequency response function fitting

While the 7Dof full car model can appear to be significantly different to the traditional quarter car model, in its most basic form this complex model can respond in the same manner as the 2DoF model. In order to achieve this, the model and excitation must both be symmetrical.

The model is made symmetrical about both the longitudinal and lateral axes, with the front and rear wheels the same distance from the centre of mass. Further to this, the front and rear unsprung masses are made the same, as well as the stiffness and damping of the suspension system and tyres. The system excitation is sent simultaneously through all four wheels, acting as a single input. No pitching or rolling motion is induced in the system this way and moments of inertia and anti-roll bars values can be neglected.

With a symmetrical system the four wheeled vehicle can be transformed into its 2DoF equivalent quarter car model. A vehicle's suspension springs are in parallel with each other, meaning that numerically they can be added together to create an equivalent spring stiffness (k_e). This same process can be done with the stiffness of the tyres (k_{te}), and the unsprung masses (m_{ue}), however the body mass remains the same. The damping coefficients of the suspension (c_e), and tyre (c_{te}) are also added together maintain the same damping ratio overall. The equivalent quarter car model developed is shown in Figure A-1.

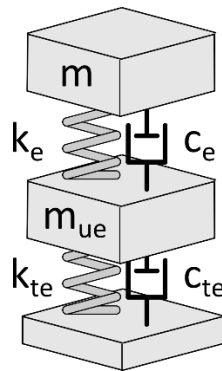


Figure A-1: An illustration of the equivalent 2DoF quarter car model.

Published equations of the theoretical transmissibility function (the type of FRF used) for a 2DoF system (Sciulli 1997) are available due to the prevalence of the quarter car model in vehicle suspension simulation, and shown in equation A-1. The equivalent stiffness and damping values, shown in Table A-1, return a theoretical FRF when input into the equation. Comparisons between the numerical solution FRF and 7DoF numerical model FRF can then be made.

$$TR = \frac{(2\zeta_{te}\omega_{n2}s + \omega_{n2}^2)(2\zeta_e\omega_{n1}s + \omega_{n1}^2)}{\left[s^2 + (2\zeta_{te}\omega_{n2}s + \rho 2\zeta_e\omega_{n1})s + (\omega_{n2}^2 + \rho\omega_{n1}^2) \right] \left[s^2 + 2\zeta_e\omega_{n1}s + \omega_{n1}^2 \right] - \rho(2\zeta_e\omega_{n1}s + \omega_{n1}^2)^2}$$

A-1

Where;

$$\omega_{n1} = \sqrt{k_e / m}$$

A-2

$$\omega_{n2} = \sqrt{k_{te} / m_{ue}}$$

$$\rho = m / m_{ue}$$

Table A-1: Values used in full car vs quarter car vertical vibration FRF comparison

Full car			Quarter car equivalent		
Parameter		Value	Parameter		Value
m	[kg]	1,000	m	[kg]	1,000
m _f = m _r	[kg]	60	m _{ue}	[kg]	240
I _x	[kg.m ²]	800	k _e	[N/m]	40,000
I _y	[kg.m ²]	1,100	k _{te}	[N/m]	800,000
a ₁ = a ₂	[m]	1.5	ζ _e	[-]	0.15
b ₁ = b ₂	[m]	0.75	ζ _{te}	[-]	0.05
k _f = k _r	[N/m]	10,000			
k _t	[N/m]	200,000			
ARB _f	[N.m/rad]	0			
ARB _r	[N.m/rad]	0			
ζ _f = ζ _r	[-]	0.15			
ζ _t	[-]	0.05			

In each case a 50 km class 'A' road was synthesised for the excitation, which was sent to all four wheel simultaneously. The body mass, suspension stiffness, and damping ratio were all varied by ±50%. In the cases where the body mass and suspension stiffness were varied the damping ratio was kept constant, resulting in different damping coefficients for each simulation.

Figure A-2 displays a comparison between the full car numerical model and the 2DoF numerical solution FRFs for various body masses. The numerical solution is found to agree well with the results from the numerical model for all cases (coefficient of determination (R²) of 1.00 for all cases).

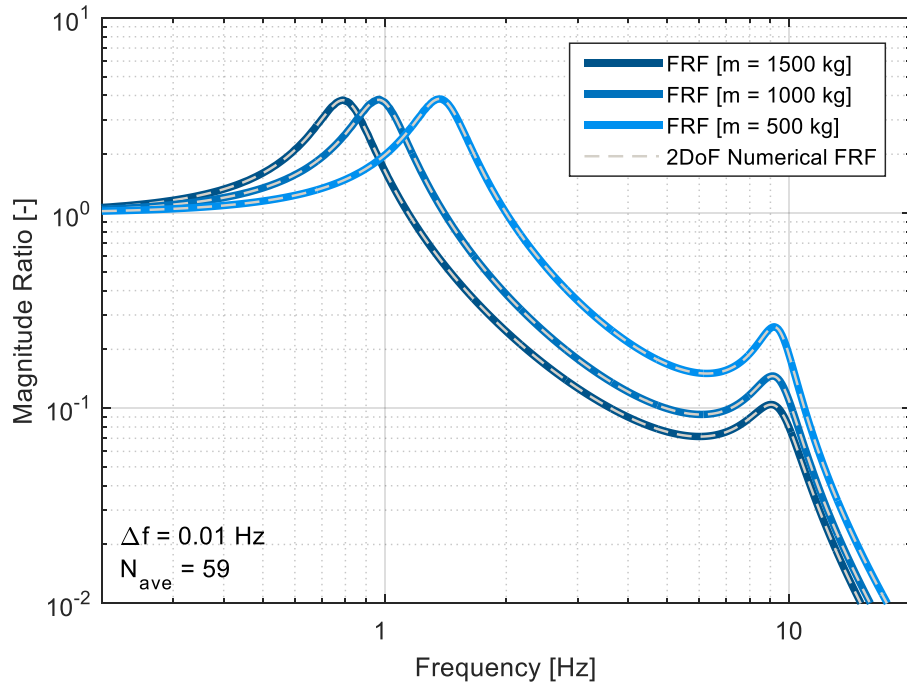


Figure A-2: Frequency response functions for varying body masses overlaid with the results of the 2DoF numerical FRF equation.

Figure A-3 and Figure A-4 show a comparison of the FRFs between the full car numerical model and the 2DoF numerical solution when the suspension stiffness and the suspension damping ratio are varied, respectively. The numerical solution is once again indistinguishable from the numerical model simulation, indicating that the numerical model is valid for these cases.

The results from these comparisons assist in the validation of the numerical model in a multitude of ways, most importantly is that the numerical solution for the 2DoF FRF was from an external source. In each case the natural frequency estimates for both masses correspond to the solution precisely, as does the magnitude ratio. When parameters are varied in the model the results and the numerical solution align, indicating that the equations of motion are implemented correctly.

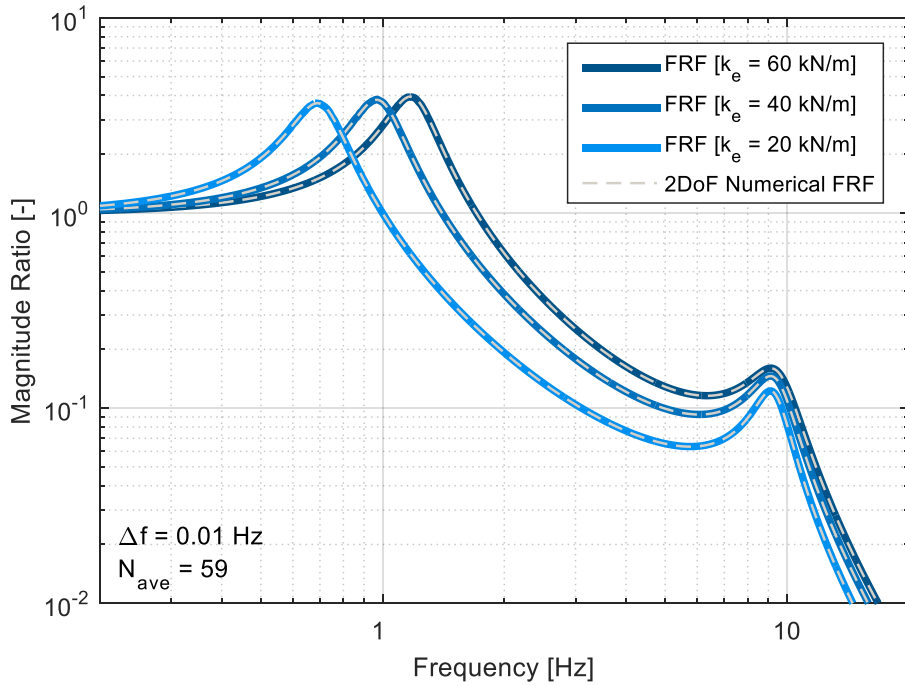


Figure A-3: Frequency response functions for varying effective spring stiffness values overlaid with the results of the 2DoF numerical FRF equation.

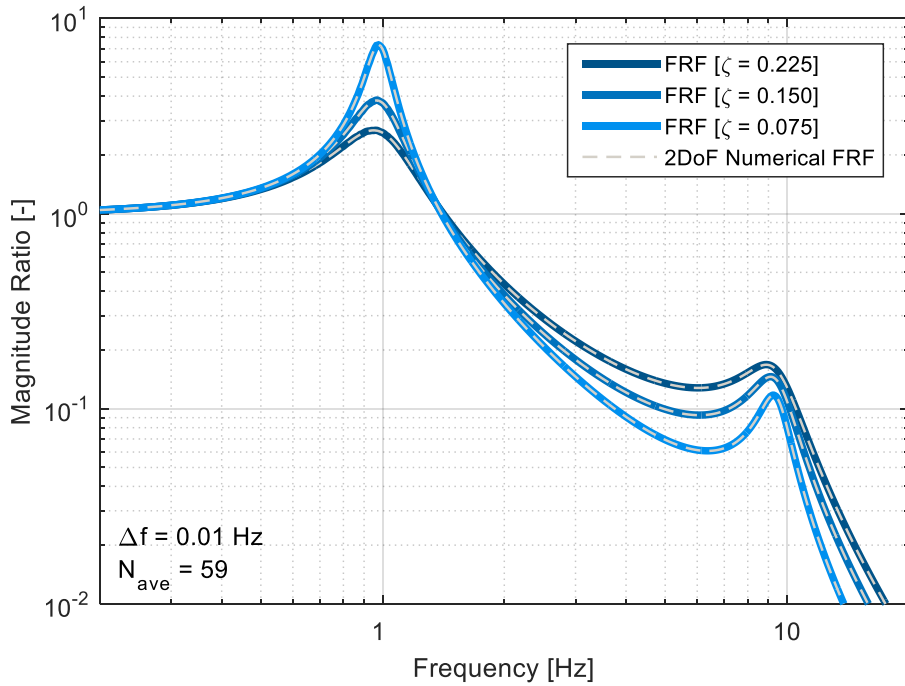


Figure A-4: Frequency response functions for varying effective damping ratios overlaid with the results of the 2DoF numerical FRF equation.

This method of numerical model validation is limited by the significant simplification to the model parameters. There is no way to independently vary the parameters, as this would change the symmetry of the system and it would no longer have any similarity to the 2DoF FRF. Other

parameters, such as the anti-roll bars, cannot be verified using this approach. This method is limited to the vertical vibration motion only, requiring additional approaches to verify the remaining parameters and vibratory modes of the developed numerical model.

A.2 4DoF frequency response function fitting

To test modes of vibration other than vertical, more degrees of freedom are required. The second approach taken to validate the numerical model follows a similar process to the first, however the 2DoF model is replaced by a 4DoF bicycle half car (Figure A-5) FRF numerical solution. This allows for the comparison of both the vertical vibration and pitching frequency response functions. The bike half car FRF numerical solution was calculated from a simplified version of the equations of motion. A Laplace transform was performed on the four equations of motion before the equations were re-written in matrix form and numerical solutions for the vertical vibration and pitching motion of the body mass were found, shown in equations A-9 and A-10, respectively.

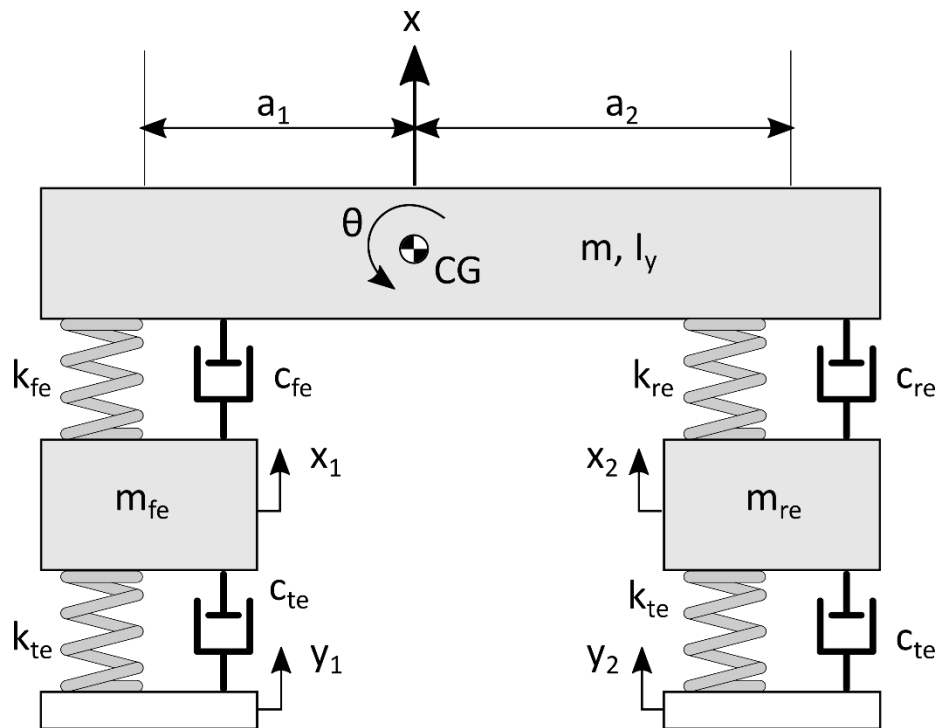


Figure A-5: An illustration of a bicycle half car model.

$$[X] = [H]^{-1} [Y]$$

A-3

Where;

$$[X] = \begin{bmatrix} x \\ \theta \\ x_1 \\ x_2 \end{bmatrix} \quad \text{A-4}$$

And

$$[Y] = \begin{bmatrix} 0 \\ 0 \\ y_1 \\ y_2 \end{bmatrix} \quad \text{A-5}$$

And

$$[H] = \begin{bmatrix} H_{11} & H_{12} & -k_f - c_f s & -k_r - c_r s \\ H_{21} & H_{22} & k_f a_1 + c_f a_1 s & -k_r a_2 - c_r a_2 s \\ H_{31} & H_{32} & H_{33} & 0 \\ H_{41} & H_{42} & 0 & H_{44} \end{bmatrix} \quad \text{A-6}$$

$$H_{11} = k_f + c_f s + k_r + c_r s + m s^2 \quad \text{A-7}$$

$$H_{22} = c_f a_1^2 s + k_f a_1^2 + c_r a_2^2 s + k_r a_2^2 + I_y s^2$$

$$H_{33} = \frac{k_f + c_f s + k_t + c_t s + m_f s^2}{k_t + c_t s}$$

$$H_{44} = \frac{k_r + c_r s + k_t + c_t s + m_r s^2}{k_t + c_t s}$$

$$H_{12} = H_{21} = k_r a_2 - k_f a_1 - c_f a_1 s + c_r a_2 s$$

$$H_{31} = \frac{-k_f - c_f s}{k_t + c_t s}$$

$$H_{32} = \frac{k_f a_1 + c_f a_1 s}{k_t + c_t s}$$

$$H_{41} = \frac{-k_r - c_r s}{k_t + c_t s}$$

$$H_{42} = \frac{-k_r a_2 - c_r a_2 s}{k_t + c_t s}$$

$$s = 2\pi j\omega \quad \text{A-8}$$

$$x = [H]^{-1}_{13} y_1 + [H]^{-1}_{14} y_2 \quad \text{A-9}$$

$$\theta = [H]^{-1}_{23} y_1 + [H]^{-1}_{24} y_2 \quad \text{A-10}$$

In both instances the solutions will work for a MIMO system, however due to the nature of a bicycle half car model, a time delay between inputs will induce wheelbase filtering. As such, it was decided to treat the model as a SIMO system, using the same excitation for the front and rear of the vehicle.

Again, for each case a 50 km stretch of synthesised class 'A' road was used as the excitation, with the same excitation signal input to all four wheels simultaneously. The centre of gravity location, front unsprung mass and the pitch MOI of the body mass were all varied in the following tests. In cases where the front unsprung mass was varied the damping ratio remained constant (requiring different damping coefficients).

Table A-2: Values used in full car vs bike half car vertical vibration FRF comparison

Full car			Quarter car equivalent		
Parameter		Value	Parameter		Value
m	[kg]	1,000	m	[kg]	1,000
m _f = m _r	[kg]	60	m _{fe}	[kg]	120
I _x	[kg.m ²]	800	m _{re}	[kg]	120
I _y	[kg.m ²]	1,100	k _{fe}	[N/m]	20,000
a ₁ = a ₂	[m]	1.5	k _{re}	[N/m]	20,000
b ₁ = b ₂	[m]	0.75	k _{te}	[N/m]	800,000
k _f = k _r	[N/m]	10,000	ζ _e	[-]	0.05
k _t	[N/m]	200,000	ζ _{te}	[-]	0.05
ARB _f	[N.m/rad]	0	I _y	[kg.m ²]	1,100
ARB _r	[N.m/rad]	0			
ζ _f = ζ _r	[-]	0.05			
ζ _t	[-]	0.05			
I _y	[kg.m ²]	1,100			

Figure A-6 displays the frequency response function for three different CG locations. When the distance from the front axle to the centre of gravity (a_1) is equal to 1.5 m the system is symmetrical and the FRF takes the usual 2DoF form. However when the system is asymmetrical, secondary peaks occur. These peaks are also evident in the pitch FRFs shown in Figure A-7. When the system is symmetrical, no pitching motion is induced and therefore the model and numerical solution have no pitch frequency response functions.

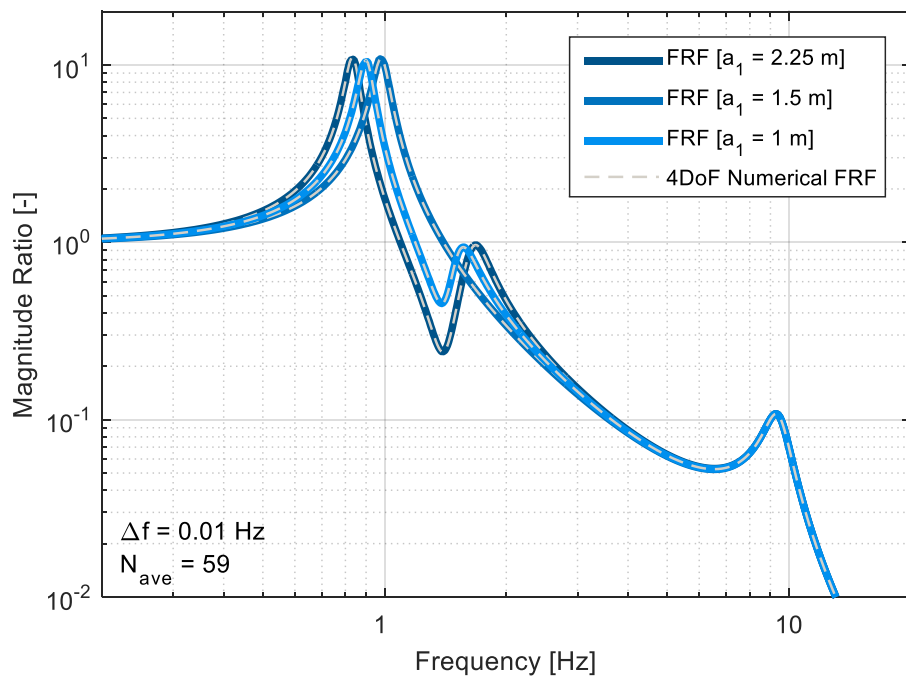


Figure A-6: Vertical vibration frequency response functions for varying centre of gravity locations overlaid with the results of the 4DoF numerical FRF equation.

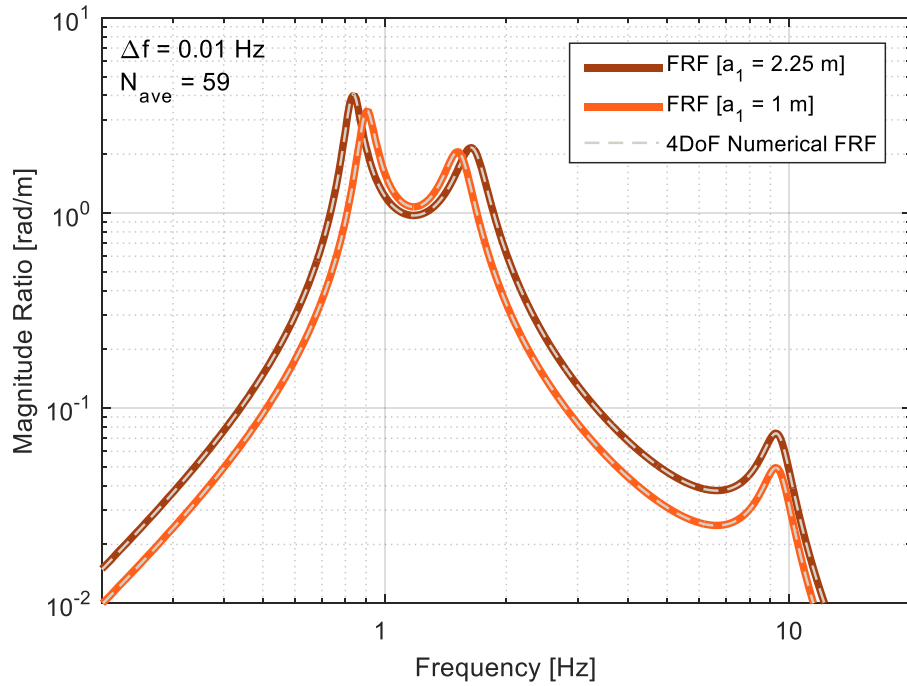


Figure A-7: Pitch vibration frequency response functions for varying centre of gravity locations compared with the results of the 4DoF numerical FRF equation.

Figure A-8 and Figure A-9 show the frequency response functions for the vertical vibration and pitch mode of vibration, respectively. Again, the numerical model is in excellent agreement with the numerical solution. For each case, to induce the pitch mode of vibration, the centre of gravity was set to 2.25 m behind the front axle before the moment of inertia about the lateral axis was varied.

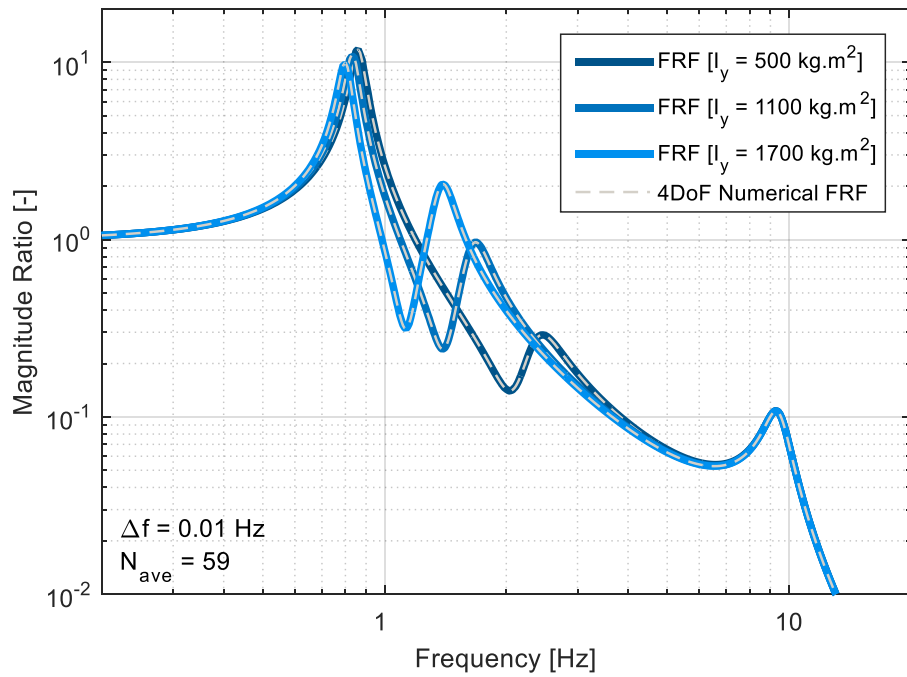


Figure A-8: Vertical vibration frequency response functions for varying moments of inertia compared with the results of the 4DoF numerical FRF equation.

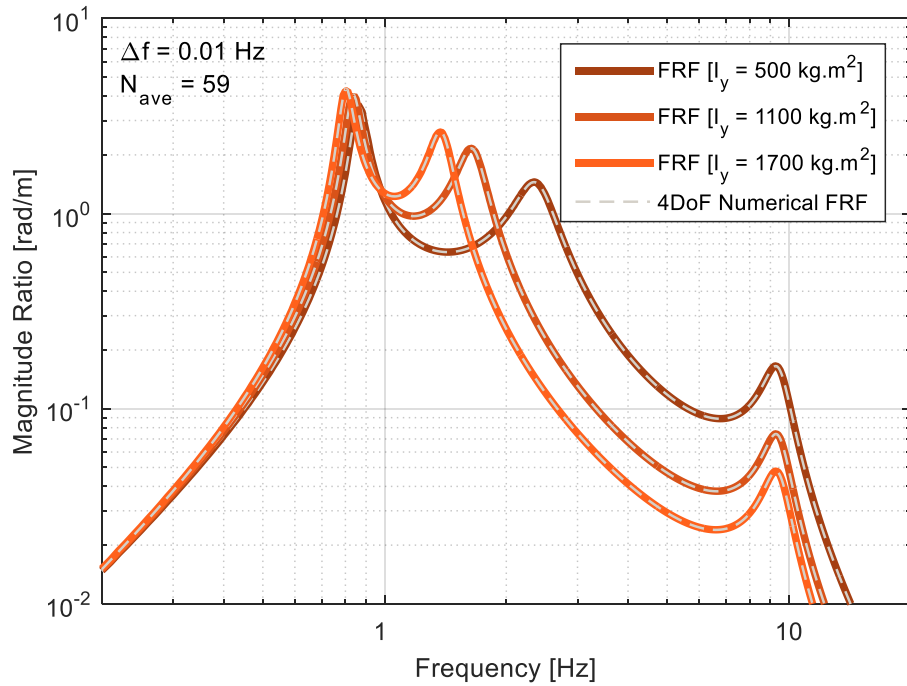


Figure A-9: Pitch vibration frequency response functions for varying moments of inertia overlaid with the results of the 4DoF numerical FRF equation.

For all cases the numerical solutions to the vertical and pitch model vibration frequency response functions of the 4DoF bicycle half car model have shown excellent agreement. Some limitations of the 2DoF FRF fitting process have been overcome with additional degrees of freedom. The method used to create the equations for the numerical solution is applicable to more complex systems, although the difficulty to implement the equations increases. For this reason, a simpler method was used to check the remaining parameters. The process, outlined in the following section, calculates the fundamental frequencies of all the degrees of freedom, enabling the comparison of peak locations to the returned values.

A.3 Eigenvalues

Determining the natural frequencies of the system and comparing them to the numerical model allows for most of the vehicle's parameters to be validated. The method used to estimate the natural frequencies was to calculate the eigenvalues of matrix $[A]$ from equation A-11.

$$[A] = [m]^{-1} [k] \quad \text{A-11}$$

Where;

$$[m] = \begin{bmatrix} m & 0 & 0 & 0 & 0 & 0 & 0 \\ 0 & I_x & 0 & 0 & 0 & 0 & 0 \\ 0 & 0 & I_y & 0 & 0 & 0 & 0 \\ 0 & 0 & 0 & m_f & 0 & 0 & 0 \\ 0 & 0 & 0 & 0 & m_f & 0 & 0 \\ 0 & 0 & 0 & 0 & 0 & m_r & 0 \\ 0 & 0 & 0 & 0 & 0 & 0 & m_r \end{bmatrix} \quad \text{A-12}$$

And;

$$[k] = \begin{bmatrix} k_{11} & k_{12} & k_{13} & -k_f & -k_f & -k_r & -k_r \\ k_{21} & k_{22} & k_{23} & k_{24} & k_{25} & k_{26} & k_{27} \\ k_{31} & k_{32} & k_{33} & a_1 k_f & a_1 k_f & -a_2 k_r & -a_2 k_r \\ -k_f & k_{42} & a_1 k_f & k_{44} & k_{45} & 0 & 0 \\ -k_f & k_{52} & a_1 k_f & k_{54} & k_{55} & 0 & 0 \\ -k_r & k_{62} & -a_2 k_r & 0 & 0 & k_{66} & k_{67} \\ -k_r & k_{72} & -a_2 k_r & 0 & 0 & k_{76} & k_{77} \end{bmatrix} \quad \text{A-13}$$

$$\begin{aligned}
k_{11} &= k_f + k_f + k_r + k_r \\
k_{22} &= b_1^2 k_f + b_2^2 k_f + b_1^2 k_r + b_2^2 k_r + ARB_f + ARB_r \\
k_{33} &= a_1^2 k_f + a_1^2 k_f + a_2^2 k_r + a_2^2 k_r \\
k_{44} &= k_f + k_t + ARB_f \left(\frac{1}{(b_1 + b_2)^2} \right) \\
k_{55} &= k_f + k_t + ARB_f \left(\frac{1}{(b_1 + b_2)^2} \right) \\
k_{66} &= k_r + k_t + ARB_r \left(\frac{1}{(b_1 + b_2)^2} \right) \\
k_{77} &= k_r + k_t + ARB_r \left(\frac{1}{(b_1 + b_2)^2} \right) \\
k_{12} &= k_{21} = b_1 k_f - b_2 k_f - b_1 k_r + b_2 k_r \\
k_{13} &= k_{31} = -a_1 k_f - a_1 k_f + a_2 k_r + a_2 k_r \\
k_{23} &= k_{32} = -a_1 b_1 k_f + a_1 b_2 k_f - a_2 b_1 k_r + a_2 b_2 k_r \\
k_{24} &= k_{42} = -b_1 k_f - ARB_f \left(\frac{1}{b_1 + b_2} \right) \\
k_{25} &= k_{52} = b_2 k_f + ARB_f \left(\frac{1}{b_1 + b_2} \right) \\
k_{26} &= k_{62} = b_1 k_r + ARB_r \left(\frac{1}{b_1 + b_2} \right) \\
k_{27} &= k_{72} = -b_2 k_r - ARB_r \left(\frac{1}{b_1 + b_2} \right) \\
k_{45} &= k_{54} = -ARB_f \left(\frac{1}{(b_1 + b_2)^2} \right) \\
k_{67} &= k_{76} = -ARB_r \left(\frac{1}{(b_1 + b_2)^2} \right)
\end{aligned}$$

Although the stiffness ([k]) and mass ([m]) matrices are of a significant size, they are easily implemented computationally (for instance using MATLAB®). Six different system configurations were evaluated and their results are shown in the following sections. It should be noted that many more configurations were tested to ensure that the numerical model was valid, however only six are presented herein. In all test cases the majority of parameters remained the same, only a combination of unsprung masses, anti-roll bar stiffness and the CG location are varied.

The suspension and tyre damping ratios were set to 0.05 to ensure that all peaks in the PSD functions were well pronounced for identification. Separate random signals were generated for each wheel path, with no correlation at any frequency. No time delay is used between the front and rear wheels, this is done to avoid wheelbase filtering, explained further in the following appendix

For the following investigation, several PSD functions are shown and all have a frequency resolution of 0.1 Hz and 50% overlap.

A.3.1 Case 1: Symmetrical system

The vehicle analysed in the first case is symmetrical about the lateral and longitudinal axes. The parameters used in the first case are shown in Table A-3, and it can be seen that the centre of gravity is located in the centre of the vehicle ($a_1 = a_2$ and $b_1 = b_2$), and that all spring stiffness values are the same in the front and rear. This ensures that the natural frequency estimates for all four unsprung masses should be the same. The parameter values from Table A-3 are used to calculate the [A] matrix, from which the associated eigenvalues are determined.

Table A-3: Parameter values used in numerical model testing Case 1.

Parameter		Value
m	[kg]	1,000
m_f	[kg]	60
m_r	[kg]	60
I_x	[kg.m ²]	800
I_y	[kg.m ²]	1,100
$a_1 = a_2$	[m]	1.5
$b_1 = b_2$	[m]	0.75
$k_f = k_r$	[N/m]	10,000
k_t	[N/m]	200,000
ARB _f	[N.m/rad]	0
ARB _r	[N.m/rad]	0
$\zeta_f = \zeta_r$	[-]	0.05
ζ_t	[-]	0.05

Seven eigenvalues (A-15) are returned from the matrix, resulting in the seven natural frequencies shown in A-16. It has to be noted that the values are listed in ascending order; the order of returned eigenvalues does not correspond to any specific mode of vibration. That is to say that the first value does not always correspond to the natural frequency of the body mass. This makes it slightly more difficult to identify problems with the model, however plotting

response PSD functions from the model's response in conjunction with the estimates of the natural frequency allows for easy comparison.

$$\begin{aligned}
 \lambda_1 &= 5.175 & \text{A-15} \\
 \lambda_2 &= 6.170 \\
 \lambda_3 &= 8.822 \\
 \lambda_4 &= 59.161 \\
 \lambda_5 &= 59.172 \\
 \lambda_6 &= 59.177 \\
 \lambda_7 &= 59.195
 \end{aligned}$$

$$\begin{aligned}
 \omega_1 &= \sqrt{\lambda_1} = 2.275 \text{ rad/s} = 0.824 \text{ Hz} & \text{A-16} \\
 \omega_2 &= \sqrt{\lambda_2} = 2.484 \text{ rad/s} = 0.982 \text{ Hz} \\
 \omega_3 &= \sqrt{\lambda_3} = 2.970 \text{ rad/s} = 1.404 \text{ Hz} \\
 \omega_4 &= \sqrt{\lambda_4} = 7.692 \text{ rad/s} = 9.416 \text{ Hz} \\
 \omega_5 &= \sqrt{\lambda_5} = 7.692 \text{ rad/s} = 9.418 \text{ Hz} \\
 \omega_6 &= \sqrt{\lambda_6} = 7.693 \text{ rad/s} = 9.418 \text{ Hz} \\
 \omega_7 &= \sqrt{\lambda_7} = 7.694 \text{ rad/s} = 9.421 \text{ Hz}
 \end{aligned}$$

The estimated frequencies ω_4 to ω_7 are approximately the same, and therefore represent the four individual unsprung masses. The PSD function returned by the numerical model for the vertical acceleration of the main body has two distinct peaks, reminiscent of a simple 2DoF quarter car model, as shown in Figure A-10.

Both peaks clearly align with the estimates from the calculated eigenvalues, indicating that the EoM have been implemented correctly. The two estimates either side of the first peak correspond to the natural frequency of roll and pitch modes, however from this figure alone we have no way to tell if these estimates are correct.

Figure A-11 presents the PSD function of the roll angular velocity. In this case the primary peak aligns with the lowest natural frequency estimate. Once again the secondary peak aligns with the estimates from the eigenvalues. It is important to note that there is zero correlation between the left and right wheel paths, inducing a large roll excitation into the system at all frequencies.

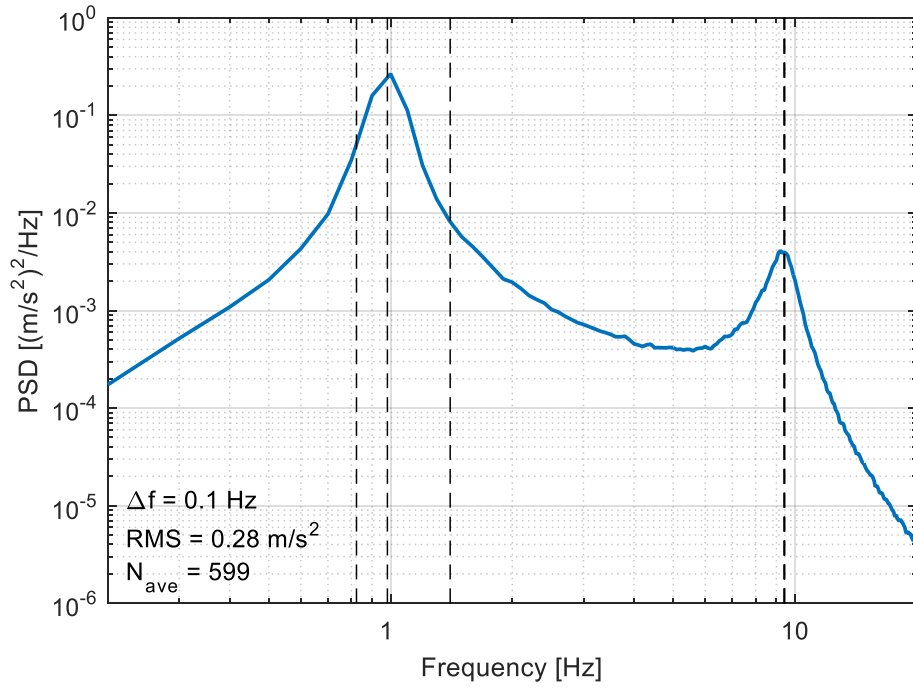


Figure A-10: PSD function of the vertical acceleration (blue) returned from the numerical model for case 1. Vertical black lines represent natural frequency estimates calculated from the eigenvalues.

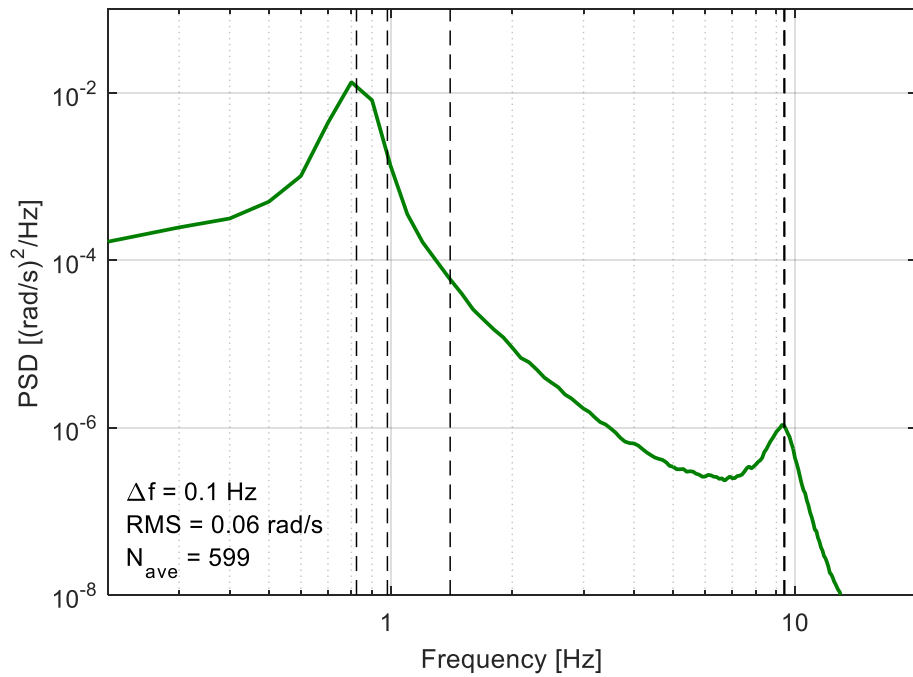


Figure A-11: PSD function of the roll angular velocity (green) returned from the numerical model for case 1. Vertical black lines represent natural frequency estimates calculated from the eigenvalues.

From the first case it is clear that the EoM have been implemented correctly. This case will be used as a reference for the following cases, since it is not only important that the frequency estimates align correctly with the numerical model results, but also that the system changes as expected.

A.3.2 Case 2: Asymmetrical unsprung masses

The second case uses an asymmetrical vehicle model, increasing the front unsprung mass by 150%. All other parameters for the second case remained the same as the first, shown in Table A-4. Increasing the unsprung mass lowers the natural frequency of that degree of freedom, and as such the front and rear unsprung masses will respond differently to the excitation. The different front and rear responses induce a pitching motion in the main body mass.

Table A-4: Parameter values used in numerical model testing Case 2.

Parameter		Value
m	[kg]	1,000
m_f	[kg]	150
m_r	[kg]	60
I_x	[kg.m ²]	800
I_y	[kg.m ²]	1,100
$a_1 = a_2$	[m]	1.5
$b_1 = b_2$	[m]	0.75
$k_f = k_r$	[N/m]	10,000
k_t	[N.m]	200,000
ARB_f	[N.m/rad]	0
ARB_r	[N.m/rad]	0
$\zeta_f = \zeta_r$	[-]	0.05
ζ_t	[-]	0.05

Comparing the frequency estimates returned from the eigenvalues for cases 1 and 2, shown in Table A-5, it can be seen that the first three estimates remain approximately the same for both cases. These estimates correspond to the first resonant frequencies of the vertical vibration, pitch and roll motions of the main body mass. The four remaining estimates are related to the natural frequencies of the four unsprung masses.

Table A-5: Comparison of natural frequency estimates between the cases 1 and 2.

Case 1 [Hz]	Case 2 [Hz]
0.824	0.823
0.982	0.982
1.404	1.404
9.416	5.957
9.418	5.962
9.418	9.417
9.421	9.420

The symmetrical nature of the system evaluated in case 1 saw that the remaining estimates have approximately the same value, however for case 2 these values have separated into two distinct pairs. It was believed at this stage that these values represented the unsprung masses individually, with the estimates at approximately 6 Hz corresponding to the two front unsprung masses. Their higher mass, coupled with the original spring stiffness, causes a reduction in the natural frequency of this DoF, whilst the two rear wheels effectively remain the same.

Three prominent peaks are present in the PSD function for the vertical vibration acceleration of the body mass for case 2, shown in Figure 6-12. This differs from the two peaks observed in case 1 as the three peaks align with estimates from the eigenvalues, with the new peak at approximately 6 Hz.

The PSD function of the roll angular velocity, displayed in Figure A-13, displays three prominent peaks similar to the vertical acceleration. The first peak is again aligned with the 0.8 Hz estimate (as it did in the first case), reaffirming that the estimate corresponds to the first roll resonant frequency. The second and third peaks again align with the estimates from the eigenvalues.

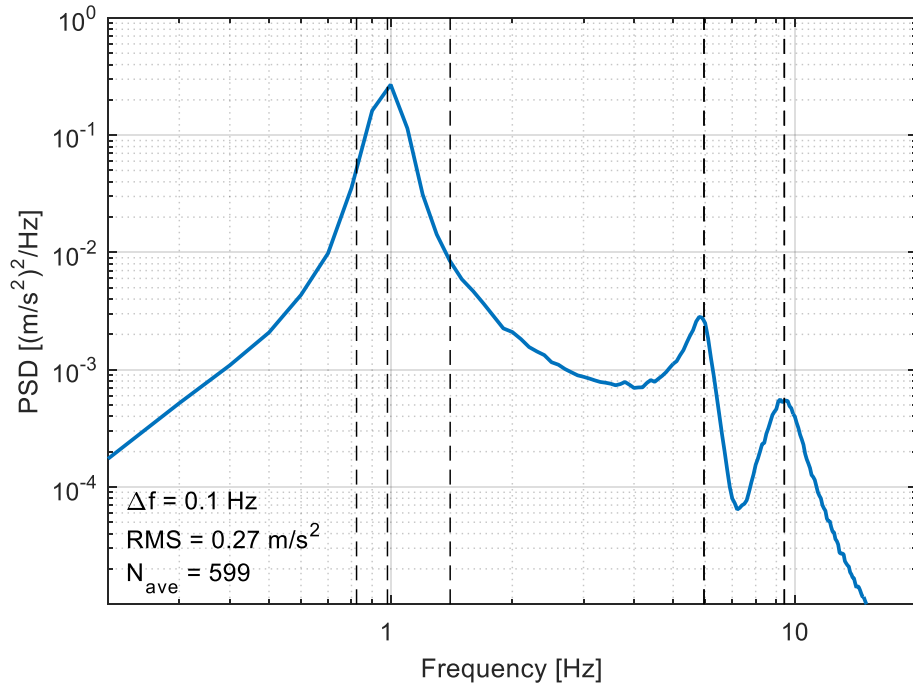


Figure A-12: PSD function of the vertical acceleration vibration (blue) returned from the numerical model for case 2. Vertical black lines represent natural frequency estimates calculated from the eigenvalues.

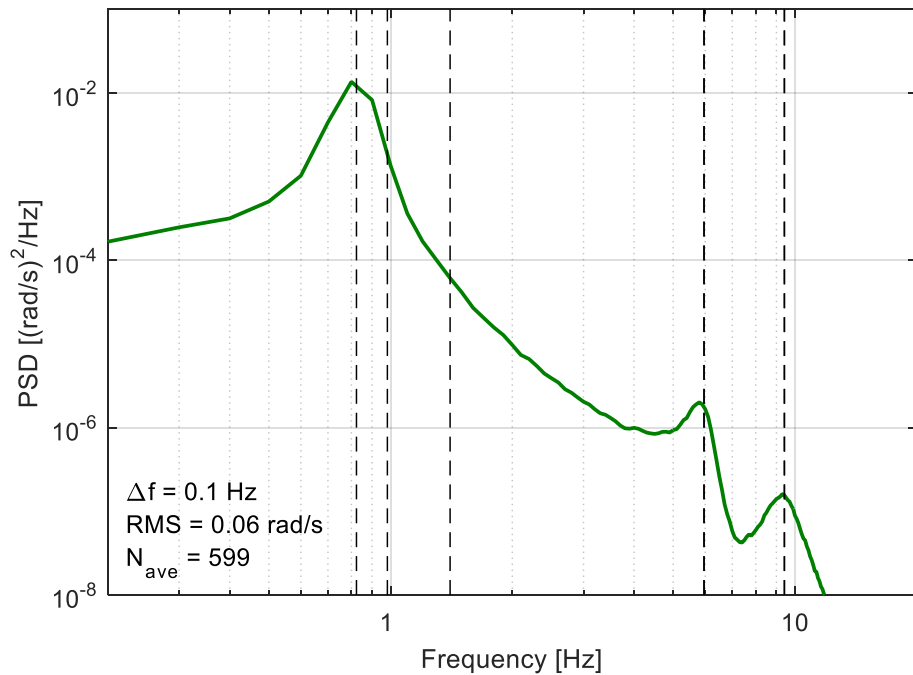


Figure A-13: PSD function of the roll angular velocity (green) returned from the numerical model for case 2. Vertical black lines represent natural frequency estimates calculated from the eigenvalues.

As the front and rear unsprung masses respond differently to the excitation, a pitch mode vibration is induced in the body mass for the first time. The first peak of the pitch angular velocity PSD function, presented in Figure A-14, aligns with the remaining of the lower three

natural frequency estimates obtained from the eigenvalues. It is interesting to note that the second peak has a higher power than the first, it is theorised that this is due to the pitching motion of the main body is being induced due to a difference in response from the unsprung masses. The second peak observed in Figure A-12 has a higher power than the third, resulting in a higher pitching response at this resonance zone.

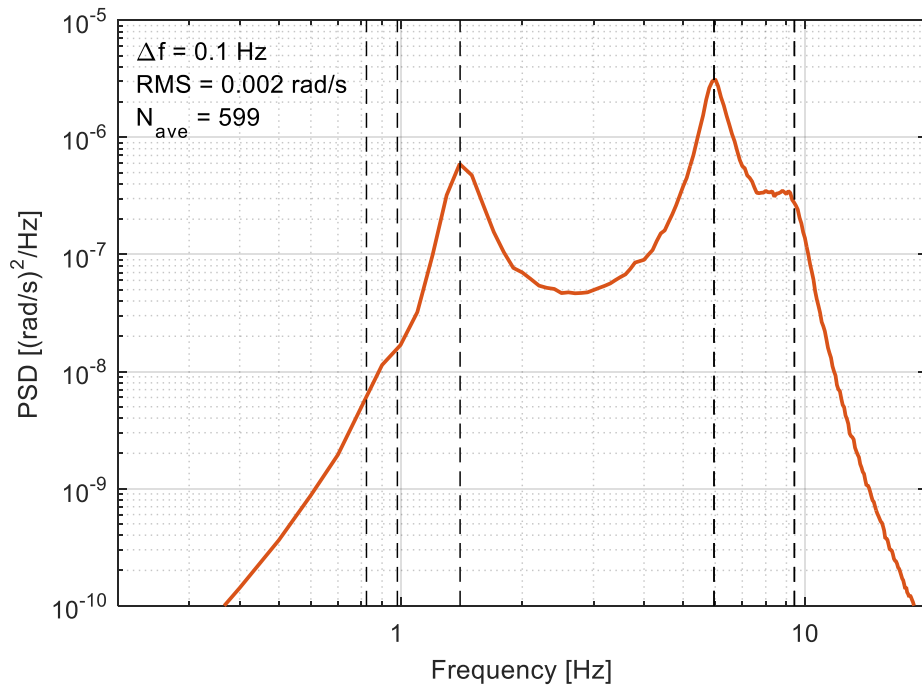


Figure A-14: PSD function of the pitch angular velocity (red) returned from the numerical model for case 2. Vertical black lines represent natural frequency estimates calculated from the eigenvalues.

A.3.3 Case 3: Front anti-roll bar

The third case simulated the addition of a front anti-roll bar to the original set up, the parameters used are shown in Table A-6. The anti-roll bar adds a spring in parallel to the suspension system, increasing the roll stiffness. This increases the roll natural frequency, this shift was exhibited by a change in the predicted roll natural frequency shifting from 0.82 Hz to 2.02 Hz. A comparison of the estimated natural frequencies between cases 1 and 3 is shown in Table A-7.

Table A-6: Parameter values used in numerical model testing Case 3.

Parameter		Value
m	[kg]	1,000
m _f	[kg]	60
m _r	[kg]	60
I _x	[kg.m ²]	800
I _y	[kg.m ²]	1,100
a ₁ = a ₂	[m]	1.5
b ₁ = b ₂	[m]	0.75
k _f = k _r	[N/m]	10,000
k _t	[N/m]	200,000
ARB_f	[N.m/rad]	250,000
ARB _r	[N.m/rad]	0
ζ _f = ζ _r	[-]	0.05
ζ _t	[-]	0.05

Table A-7: Comparison of natural frequency estimates between the cases 1 and 3.

Case 1 [Hz]	Case 3 [Hz]
0.824	0.982
0.982	1.404
1.404	2.016
9.416	9.417
9.418	9.418
9.418	9.421
9.421	13.676

Examining the predicted natural frequencies, some interesting features can be deduced. Firstly, the three lowest estimates correspond to the natural frequencies of the main body mass as before. The four higher frequency estimates still represent the unsprung masses, however three estimates are similar while one is significantly different to the two sets of pairs observed in case 2.

In the previous case the estimates acted in pairs, with two estimates for the front wheels and two for the rear wheels. Looking at case 3, only one pair of estimates remain the same as case 1 (9.418 Hz and 9.421 Hz), which is presumed to represent the rear wheels. The remaining two estimates are vastly different, which was initially a large area of concern. It was expected that the values would remain a pair due to the left/right symmetry of the system.

The PSD function of the vertical acceleration, shown in Figure A-15, has no prominent peak around 13 Hz. Interestingly, it has the same spectral shape and RMS level of the PSD function in case 1, demonstrating that the anti-roll bar has no effect on the vertical acceleration of the system.

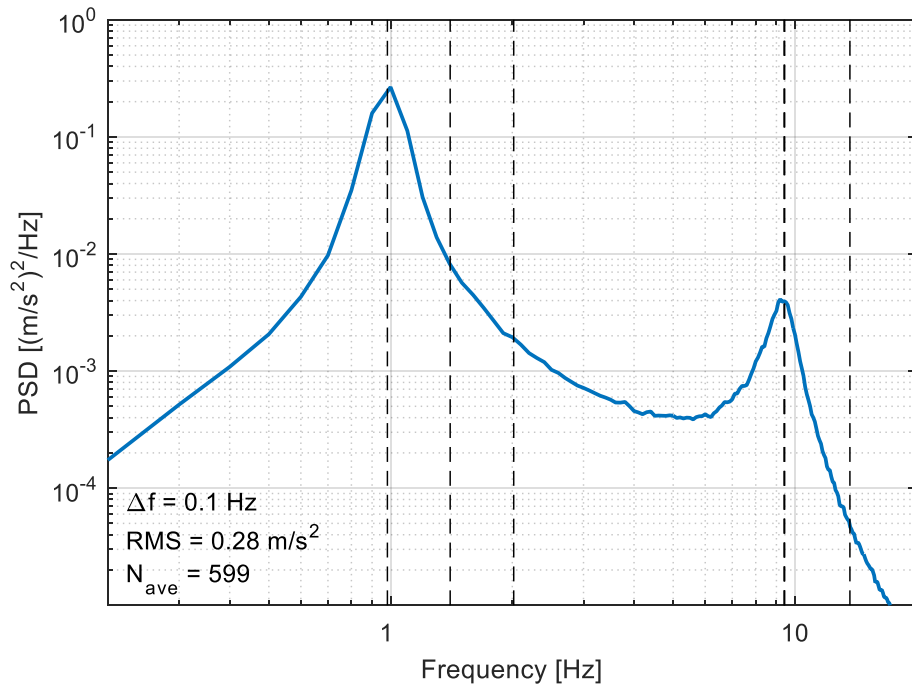


Figure A-15: PSD function of the vertical vibration (blue) returned from the numerical model for case 3. Vertical black lines represent natural frequency estimates calculated from the eigenvalues.

Two prominent peaks are observed in the PSD function of the roll angular velocity, shown in Figure A-16. The first peak corresponds to the body mass at approximately 2 Hz, whereas the second peak aligns with the 13 Hz estimate. A small protuberance is visible around 9 Hz, aligning with the other estimates from the eigenvalues. The significant peak at 13 Hz separates from the previous alignment behaviour between corresponding peaks in the vertical vibration and roll PSD functions.

By increasing the roll stiffness of the vehicle, the body of the vehicle becomes less compliant to the road surface, causing a harsher ride for the occupants and payload. The ride harshness increase is the same as an increase in the RMS level, which was observed when comparing the RMS values of roll angular velocity between cases 1 and 3, growing from 0.06 to 0.14 rad/s.

The diminished peak at 9.5 Hz is the first insight as to what may be the cause of the two separate estimates of the natural frequency for the front unsprung masses. As there is no rear anti-roll bar, the majority of the roll vibration comes from the less compliant front suspension, effectively 'washing' out the peak. This, however, does not completely explain what is occurring.

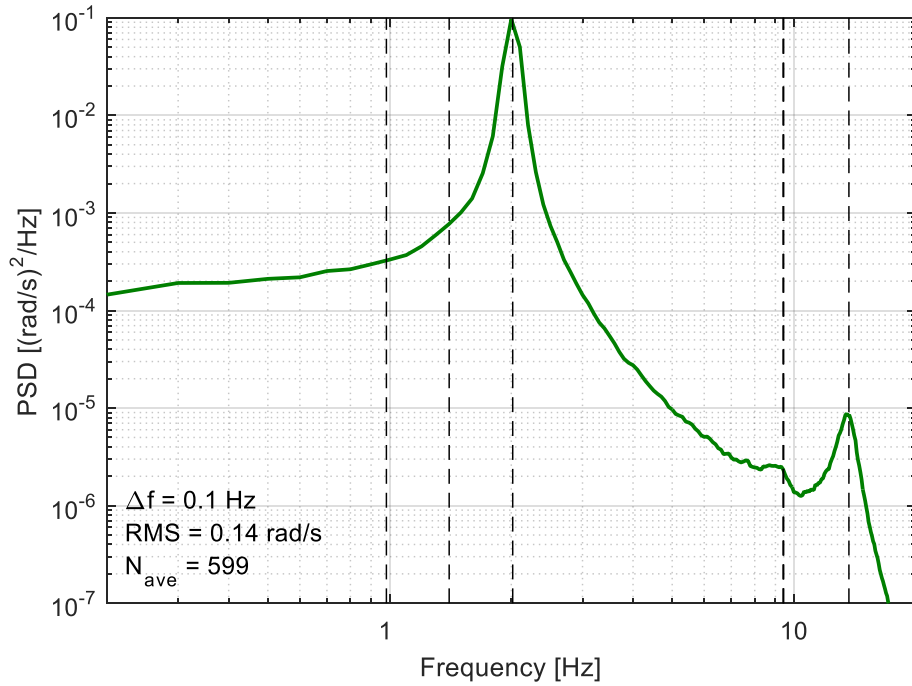


Figure A-16: PSD function of the roll angular velocity (green) returned from the numerical model for case 3. Vertical black lines represent natural frequency estimates calculated from the eigenvalues.

A.3.4 Case 4: Asymmetrical unsprung masses with front anti-roll bar

To further investigate the unexplained natural frequency estimates when an anti-roll bar is added to the system, a combination of cases 2 and 3 was simulated. For this case, both a front anti-roll bar and heavier front unsprung masses were included. The vehicle parameters used for case 4 are shown in Table A-8.

Table A-8: Parameter values used in numerical model testing Case 4.

Parameter		Value
m	[kg]	1,000
m_f	[kg]	150
m _r	[kg]	60
I _x	[kg.m ²]	800
I _y	[kg.m ²]	1,100
a ₁ = a ₂	[m]	1.5
b ₁ = b ₂	[m]	0.75
k _f = k _r	[N/m]	10,000
k _t	[N/m]	200,000
ARB_f	[N.m/rad]	250,000
ARB _r	[N.m/rad]	0
ζ _f = ζ _r	[-]	0.05
ζ _t	[-]	0.05

Examining the natural frequency estimates for cases 1 and 4, shown in Table A-9, an increase of the first roll resonant frequency occurs, as expected. The unsprung natural frequency estimates exhibit the same trait as in case 3, two estimates remain at approximately 9.5 Hz, while the other two shift to new values. This time the first estimate is around 6 Hz, a similar value to case 2, due to the 150 kg front unsprung mass. The second value, at 8.8 Hz is the increased value due to the anti-roll bar. Its proximity to the other estimates is purely a coincidence caused by the system parameters chosen.

Table A-9: Comparison of natural frequency estimates between cases 1 and 4.

Case 1 [Hz]	Case 4 [Hz]
0.824	0.982
0.982	1.404
1.404	1.978
9.416	5.962
9.418	8.814
9.418	9.417
9.421	9.420

Three significant peaks can be observed in the vertical acceleration PSD function shown in Figure A-17, comparable with case 2. The RMS value for the vertical acceleration for case 4 is the same as case 2, providing further confirmation that an anti-roll bar has no measurable impact on the vertical vibration results in these cases.

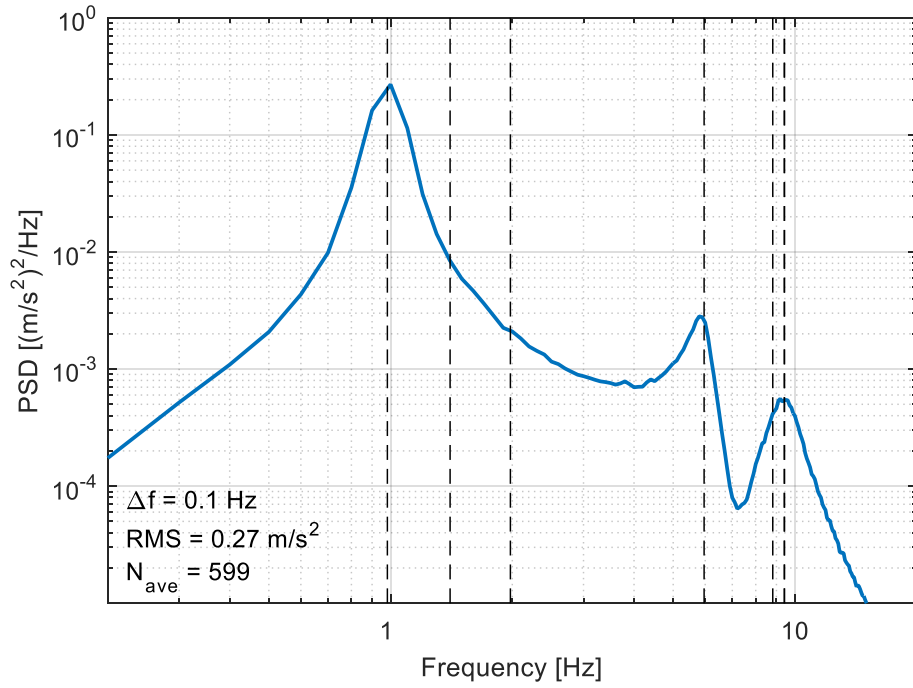


Figure A-17: PSD function of the vertical vibration (blue) returned from the numerical model for case 4. Vertical black lines represent natural frequency estimates calculated from the eigenvalues.

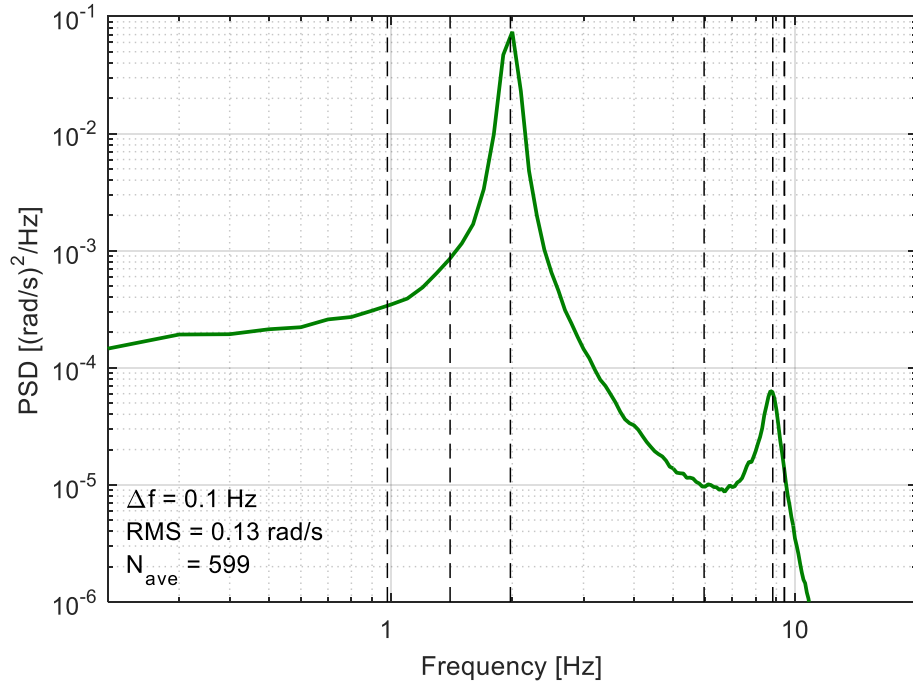


Figure A-18: PSD function of the roll angular velocity (green) returned from the numerical model for case 4. Vertical black lines represent natural frequency estimates calculated from the eigenvalues.

Two distinct peaks are observed in the roll angular velocity PSD function shown in Figure A-18. The second peak aligns with the estimate of 8.8 Hz, with no clear peaks at 6 or 9.5 Hz. It was at this point that an answer to the two estimates for the front unsprung natural frequency was theorised.

An anti-roll bar couples the body and left and right hand side wheels together with a torsional spring. When both wheels travel in the same direction relative to the body of the vehicle no torsional load is input in to the spring, however when the wheels travel in opposing directions the anti-roll bar is twisted. Engaging the anti-roll bar adds its spring stiffness to the system, changing the effective spring rate of each corner. This gives the unsprung masses two natural frequencies, one when the anti-roll bar is engaged and another when it is not.

A.3.5 Case 5: Front and rear anti-roll bars

To further test the hypothesis that the anti-roll bar causes the unsprung masses to have two natural frequencies depending on the excitation, a rear anti-roll bar was added to the heavier front masses and the front anti-roll bar. The values used in the numerical model are listed in Table A-10. For the first time using these parameters, seven different natural frequency estimates are obtained from the eigenvalues as shown in Table A-11.

Table A-10: Parameter values used in numerical model testing Case 5.

Parameter		Value
m	[kg]	1,000
m_f	[kg]	150
m_r	[kg]	60
I_x	[kg.m ²]	800
I_y	[kg.m ²]	1,100
$a_1 = a_2$	[m]	1.5
$b_1 = b_2$	[m]	0.75
$k_f = k_r$	[N/m]	10,000
k_t	[N/m]	200,000
ARB_f	[N.m/rad]	250,000
ARB_r	[N.m/rad]	250,000
$\zeta_f = \zeta_r$	[-]	0.05
ζ_t	[-]	0.05

As with all the previous cases, the first three estimates represent the first resonant frequencies of the vertical vibration, pitching and rolling motions of the main body mass. The remaining four estimates have no corresponding pairs. Meaning that two values should align with peaks in the

vertical vibration acceleration PSD function, with the remaining two aligning with peaks in the roll angular velocity PSD function.

Table A-11: Comparison of natural frequency estimates between cases 1 and 5.

Case 1 [Hz]	Case 5 [Hz]
0.824	0.982
0.982	1.404
1.404	2.647
9.416	5.962
9.418	8.815
9.418	9.420
9.421	13.686

The vertical vibration acceleration PSD function, shown in Figure A-19, displays three prominent peaks. The first peak aligns with 0.98 Hz estimate, whilst the remaining two peaks align with the 5.96 and 9.42 Hz estimates respectively.

As predicted the remaining two unsprung estimates align with the secondary peaks in the roll angular velocity PSD function, shown in Figure A-20. The first roll resonant frequency has increased (relative to the previous case) to 2.6 Hz. This increase is due to the addition of the rear anti-roll bar, resulting in a stiffer system. This also increases the RMS value of the roll PSD function.

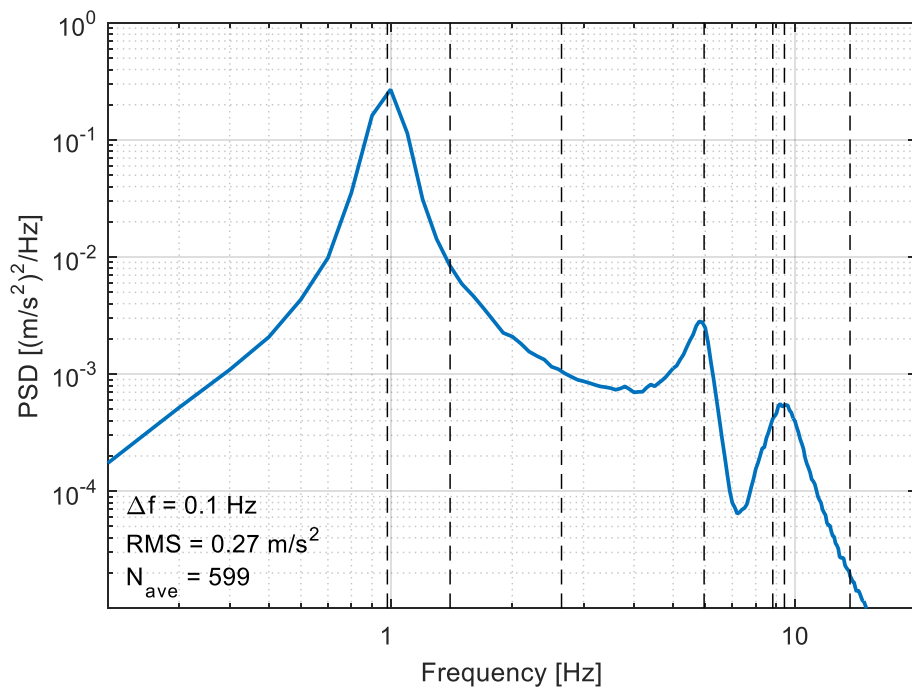


Figure A-19: PSD function of the vertical vibration (blue) returned from the numerical model for case 5. Vertical black lines represent natural frequency estimates calculated from the eigenvalues.

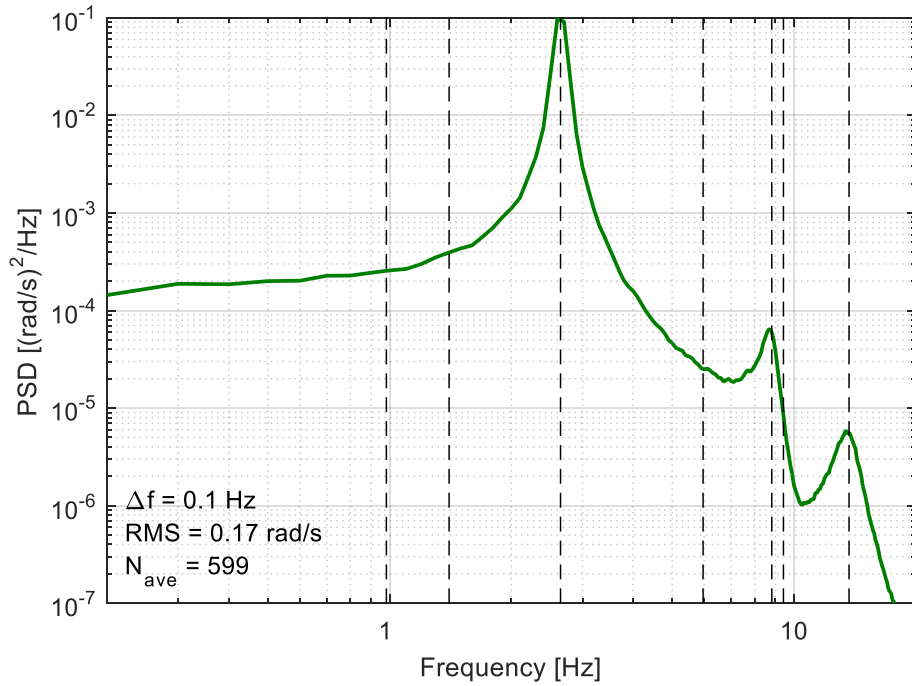


Figure A-20: Power density spectrum of the roll angular velocity (green) returned from the numerical model for case 5. Vertical black lines represent natural frequency estimates calculated from the eigenvalues.

A.3.6 Case 6: Asymmetrical centre of gravity location

All previous cases have dealt with changing only the stiffness and mass values, with the actual geometry of the vehicle remaining constant. The centre of gravity has always been located in the centre of the four wheels, however for case 6 the centre of gravity was moved towards the back of the vehicle by 0.5 m as seen in Table A-12. The moments of inertia were not altered for this simulation.

Table A-12: Parameter values used in numerical model testing Case 6.

Parameter		Value
m	[kg]	1,000
m_f	[kg]	60
m_r	[kg]	60
I_x	[kg.m ²]	800
I_y	[kg.m ²]	1,100
a_1	[m]	2
a_2	[m]	1
$b_1 = b_2$	[m]	0.75
$k_f = k_r$	[N/m]	10,000
k_t	[N/m]	200,000
ARB_f	[N.m/rad]	0
ARB_r	[N.m/rad]	0
$\zeta_f = \zeta_r$	[-]	0.05
ζ_t	[-]	0.05

Interestingly, shifting the CG location only affects the first resonant frequencies of vertical vibration and pitching motion of the main body as seen in Table A-13. It has a drastic effect on the shape of the response PSD functions.

Table A-13: Comparison of natural frequency estimates between cases 1 and 6.

	Case 1 [Hz]	Case 6 [Hz]
	0.824	0.824
	0.982	0.901
	1.404	1.531
	9.416	9.416
	9.418	9.418
	9.418	9.418
	9.421	9.422

Figure A-21 displays the PSD function of the vertical vibration acceleration, and again three distinct peaks are observed. The first peak aligns with the first resonant frequency estimate of vertical vibration. The third peak aligns with the estimated natural frequency of the unsprung masses, however for the first time the second peak aligns with the first resonant frequency of pitch mode vibration.

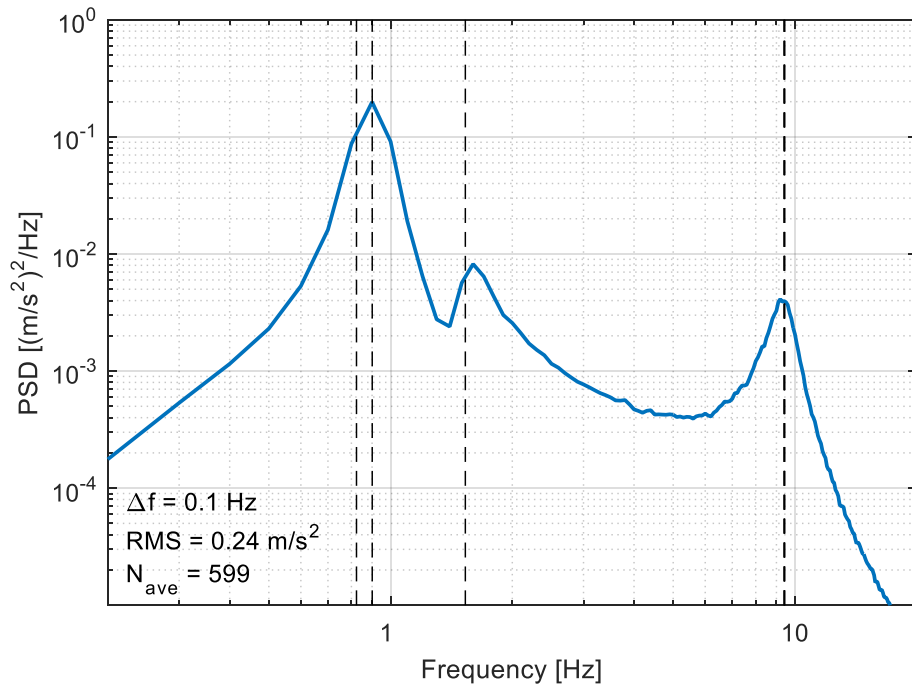


Figure A-21: PSD function of the vertical vibration acceleration (blue) returned from the numerical model for case 6. Vertical black lines represent natural frequency estimates calculated from the eigenvalues.

The excitation signal used for these simulations did not use a time delay between the front and rear wheels to prevent wheelbase filtering impacting the results. Due to this, the pitch mode vibration was only induced by the asymmetry of the model. In the previous cases this was a result of the increased mass of the front unsprung masses. This time the pitch was induced by the centre of gravity being shifted rearward.

Figure A-22 displays the PSD function for the pitch angular velocity results, just like the vertical vibration PSD function significant peaks occur at the natural frequency estimates of vertical vibration and pitch mode vibration. It is of note that the peak aligned with the first vertical vibration resonant frequency estimate is greater than the peak associated with the estimate of the pitch mode vibration. It is assumed that this is because the pitch mode vibration is induced by the asymmetry of the main body, that is to say the vertical vibration is the cause of the pitch mode vibration.

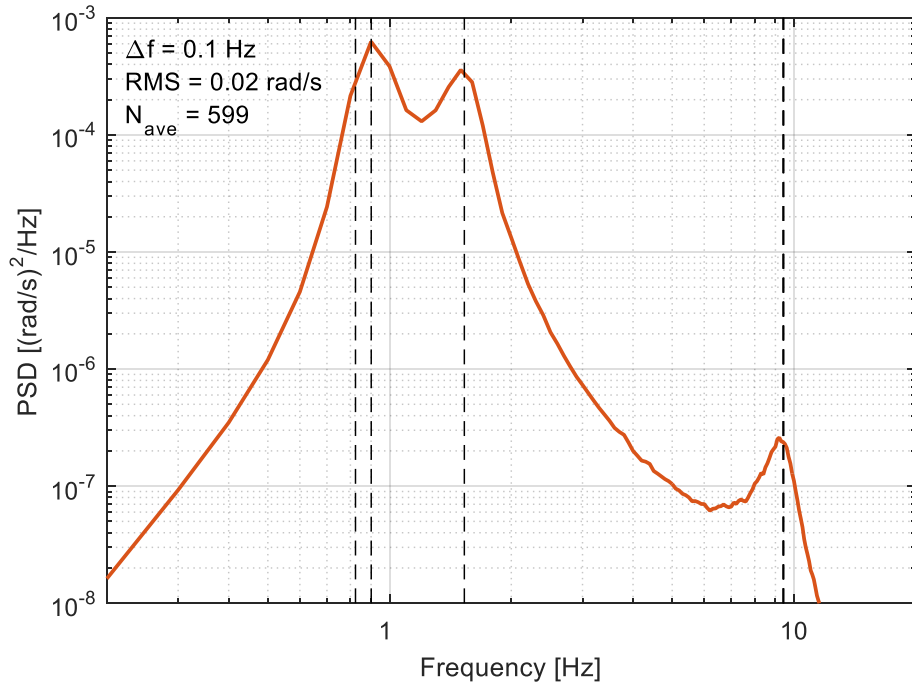


Figure A-22: PSD function of the pitch angular velocity (red) returned from the numerical model for case 6. Vertical black lines represent natural frequency estimates calculated from the eigenvalues.

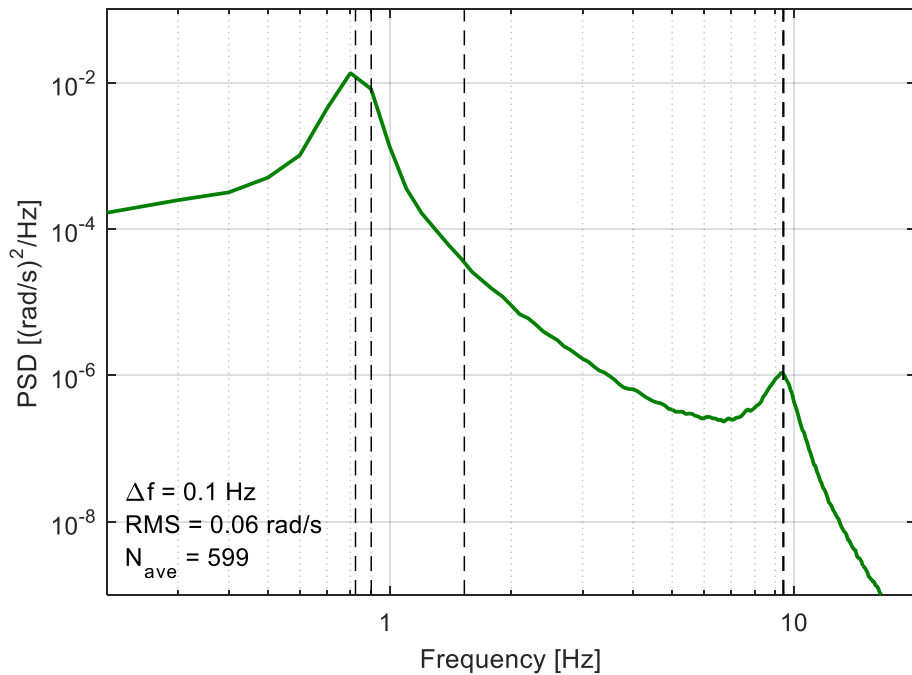


Figure A-23: PSD function of the roll angular velocity (green) returned from the numerical model for case 6. Vertical black lines represent natural frequency estimates calculated from the eigenvalues.

The PSD function for the roll angular velocity (Figure A-23) was not affected by the asymmetry of the system, as it was still symmetrical about the longitudinal axis. The shape and RMS value of the roll angular velocity PSD function remained the same as the results of case 1.

A.3.7 Eigenvalue analysis conclusion

In all of the cases simulated the resonant frequencies predicted by the eigenvalues of the [A] matrix aligned with the resonance zones of the calculated PSD functions. All estimated resonant frequencies were not evident in any single PSD function, however all the estimates were accounted for when all modes of vibration of the main body were considered.

It was established that the estimated resonant frequencies did not correspond directly to a degree of freedom, but was simply a list of all the possible resonant frequencies of the system. A complete list of natural frequencies for each case is shown in Table A-14.

Table A-14: Natural frequency estimates obtained from the eigenvalues of matrix [A] for each case study

Case 1 [Hz]	Case 2 [Hz]	Case 3 [Hz]	Case 4 [Hz]	Case 5 [Hz]	Case 6 [Hz]
0.824	0.823	0.982	0.982	0.982	0.824
0.982	0.982	1.404	1.404	1.404	0.901
1.404	1.404	2.016	1.978	2.647	1.531
9.416	5.957	9.417	5.962	5.962	9.416
9.418	5.962	9.418	8.814	8.815	9.418
9.418	9.417	9.421	9.417	9.420	9.418
9.421	9.420	13.676	9.420	13.686	9.422

This approach has aided in the validation of the numerical model, demonstrating that the equations of motion are implemented correctly. The model responded to changes in its parameters in a realistic and predictable manor; when masses were increased the resonant frequency went down and when the spring stiffness was increased the resonant frequency went up. The addition of an anti-roll bar increased the roll stiffness, increasing the first roll resonant frequency and the RMS value of the roll angular acceleration.

Appendix B

Complexities with Idealised Multi-Axis Vehicle Vibration

As a vehicle traverses the irregular and random surface of a roadway, complex motions are produced that are random. There are, however, certain combinations of the vehicle's geometric properties which, when coupled with the spatial frequency of the roadway, can introduce an interesting phenomenon known as wheelbase filtering. At wavelengths equal to the wheelbase of the vehicle, the vehicle body will experience only vertical motion. Vertical motion also occurs at wavelengths shorter than the wheelbase which have an integer multiple equal to the wheelbase, as well as wavelengths that are considerably longer than the wheelbase (Gillespie 1985), as illustrated in Figure B-1. Concurrent to this, at wavelengths equal to twice the wheelbase only pitching motion is experienced by the vehicle. This also occurs at frequencies shorter than the wheelbase with an odd integer multiple equal to twice the wheelbase.

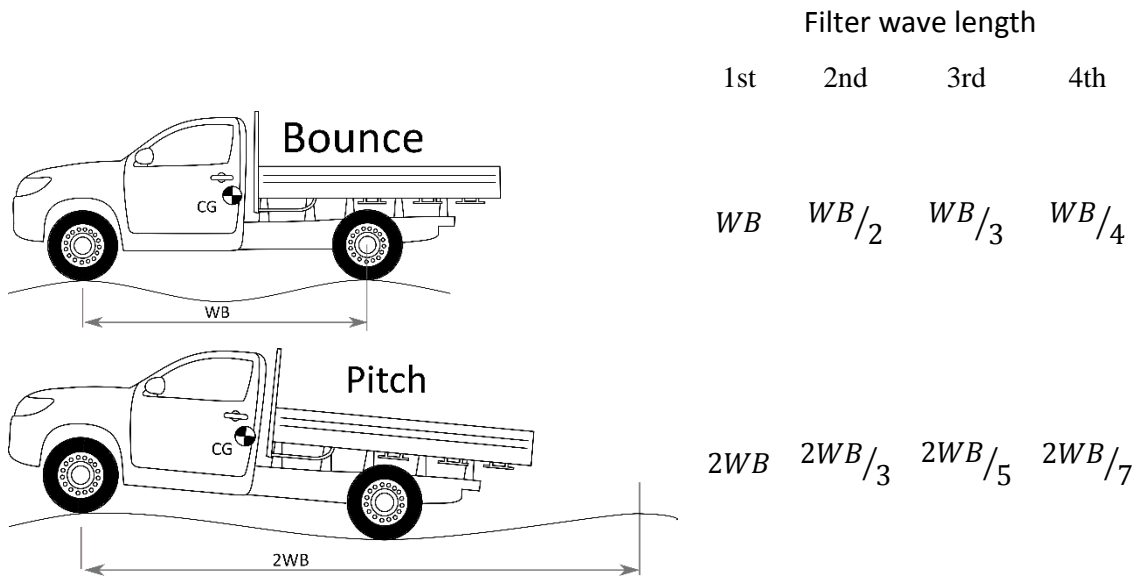


Figure B-1: Illustration of the wheelbase filtering mechanism.

The influence of these filtering effects is best observed in the frequency response function of a simulated bicycle half car vehicle traveling at constant speed, shown in Figure B-2. The light blue line represents the upper boundary of the vertical vibration response. The severe dips, or nodes, in the response corresponded to frequencies where only pitch motion is induced (wheelbase filter).

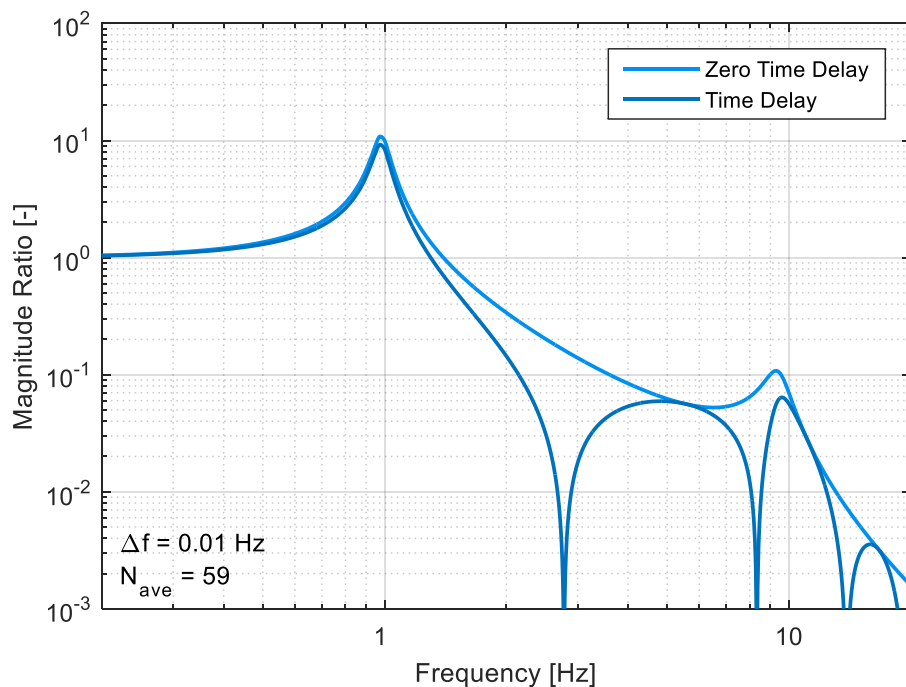


Figure B-2: Illustration of the effects of wheelbase filtering on the vertical vibration of a vehicle traveling at constant speed.

Similar effects are observed in the pitch FRF displayed in Figure B-3. In this case, the nodes correspond to the frequencies where only the vertical vibratory mode is excited.

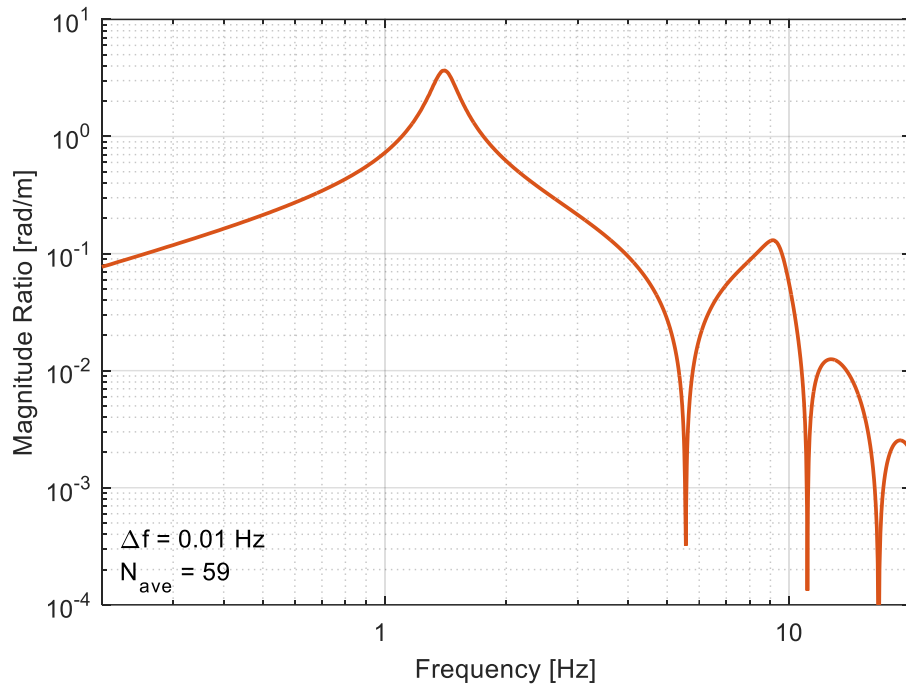


Figure B-3: Illustration of the effects of wheelbase filtering on the pitch frequency response of a vehicle traveling at constant speed.

The effects of wheelbase filtering are not often observed with real world results for many reasons. In the spatial domain, the wheelbase filtering frequencies remain the same, while in the frequency domain the filtered frequencies are dependent on the vehicle's speed. At ambient speeds the response nodes are averaged out in the PSD functions. Nominally constant speed experiments are more susceptible to the effects of wheelbase filtering, however even slight changes in operating speed can reduce or even eliminate the effects.

The second reason that wheelbase filtering is rarely observed in physical experiments is that the effects, particularly for the vertical acceleration, are strongest at the centre of gravity of the vehicle. Mounting a sensor at the centre of gravity is difficult; most measurements are taken directly above the axle as it has long been suggested in the literature that the most severe ride in a vehicle occurs here. As the angular velocity is constant across the entire body it is more likely that the effects of wheelbase filtering will be observed in the pitch response. This was the case for the physical experiments undertaken as part of this research and the effects of wheelbase filtering can be observed in the pitch PSD functions shown in section 6.3.1

Due to the controlled and idealised nature of numerical simulations, they become quite susceptible to the effects of wheelbase filtering. To reduce the impacts of wheelbase filtering the measurement location is moved away from the centre of gravity the total vertical vibration acceleration becomes the sum of the vertical acceleration at the centre of gravity and the vertical component of the pitch and roll angular acceleration.

The vertical component, or tangential acceleration of the pitch and roll angular acceleration, increases as the distance from the centre of rotation increases, and therefore the vertical acceleration experienced is dependent on the measurement location. Towards the centre of gravity, a pitch nodal point, maximum wheelbase filtering effects are observed and the vertical acceleration is affected only by bounce mode. Over the axles, a combination of the pitch and bounce will be present at each frequency and the response will be equivalent to that seen in the quarter-car model (Gillespie 1985).

As the measurement location moves away from the centre of gravity the filtering effects are reduced, as the nodes are filled by the vertical component of the pitch and roll. However the further away the sensor is from the centre of the gravity, the more influential the pitch component becomes. Figure B-4 shows the vertical vibration FRF for varying measurement locations from the front axle. The peak introduced from the pitch component becomes more noticeable as the measurement distance increases. The frequency range where the magnitude ratio is above one is also increased. It is interesting to note that measuring half way between the centre of gravity and rear axle shows the closest match for the primary and secondary peak of an idealised quarter car model.

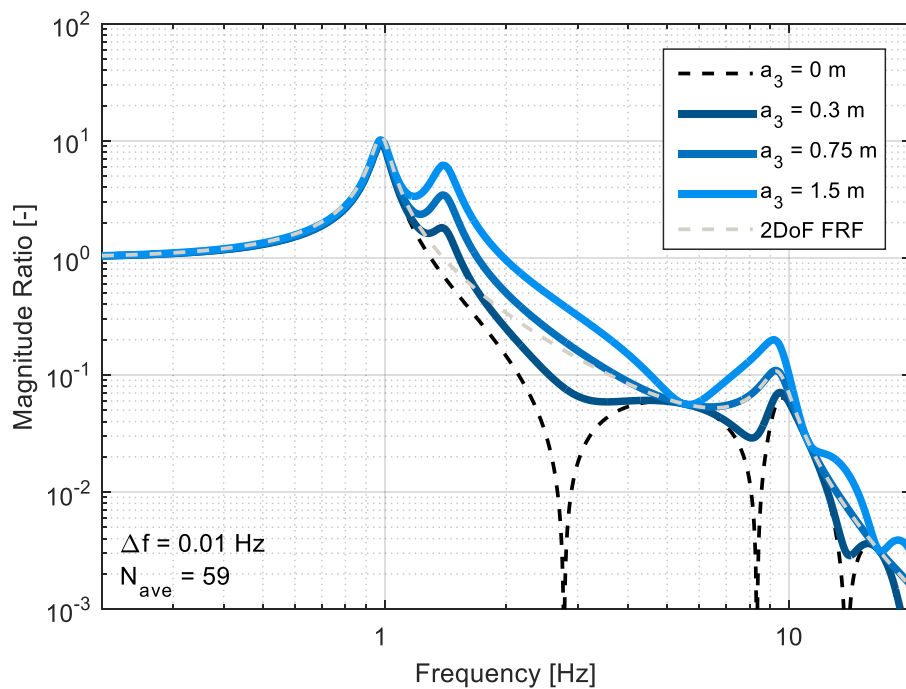


Figure B-4: Effects of measurement location on wheelbase filtering severity. Simulated vehicle with a 3 m wheelbase, CG located half way between the front and rear axle, a_3 is the horizontal distance of the measurement location taken from the CG.

The effects of the measurement location are important and must be considered when conducting physical experiments. Also, it has been shown that selecting a suitable point for simulation is quite ambiguous, and open to interpretation. Compromises must be made between minimising the effects of wheelbase filtering and the effects of the vertical component pitch motion.